MEMS Multi-sensor for Data Storage Tags used in Fisheries Research

Hyldgård, Anders; Lundgren, Bo; Hansen, Ole; Thomsen, Erik Vilain

Publication date:
2008

Document Version
Publisher's PDF, also known as Version of record

MEMS Multi-sensor for Data Storage Tags used in Fisheries Research

PhD Thesis

Anders Hyldgård

November 1st, 2007

DTU Nanotech
Department of Micro and Nanotechnology
Technical University of Denmark

Abstract

This thesis, *MEMS Multi-sensor for Data Storage Tags used in Fisheries Research*, describes the initial steps towards the creation of a new generation of Data Storage Tags (DST) for fish behavioural research. This specifically includes the design and fabrication of a Micro Electro Mechanical System (MEMS) multi-sensor consisting of four sensors and the design and evaluation of a packaging scheme that allows for direct media exposure of all sensors. This leads to a very compact system with high accuracy and fast response times.

DSTs are tiny autonomous measurement systems used in fisheries research to obtain data on the behaviour of fish. These DSTs contain sensors, processor, memory, batteries and, depending on duty cycle, these systems typically operate for around two years and store one million measurements. State of the art DSTs can measure Temperature, Depth and Salinity. This information can subsequently be used to reconstruct fish migration and patterns of fish behaviour.

Fish are caught by the researchers, the system is mounted on the fish which is then released to the ocean. When fishermen eventually re-catch the fish, the DST is returned to the fisheries research institution upon a reward. The data are then retrieved from the tag. By fitting the development in time of the measured data to oceanographic information from other sources the most probable migration route of the fish can be reconstructed.

The performance and usability of current DSTs are limited by the considerable size, low accuracy and/or slow response time of conventional discrete sensor solutions.

The new multi-sensor chip utilizes a piezoresistive silicon pressure sensor, a $TiSi_2$ thermistor, a pn-junction light sensor and a conductivity sensor consisting of four platinum electrodes. The final chip is $3.9 \times 7.3 \times 1.2$ mm^3. The theory of the sensor design and operation is given as well as simple considerations on electronic sensor interfacing. The sensors are designed to operate in the environment range of 1 bar - 21 bar, -2°C - 20°C and 0 psu - 35 psu. A paper on the theory and realization of micro electrode conductivity cells has been published in the *Sensors and Actuators - A physical* journal.

A sensor fabrication process is based on commercial bulk micromachined piezoresistive pressure sensor principles. It is extended to include $TiSi_2$ wires, local oxidation and platinum surface electrodes as well as 3 layer chip stack made from two consecutive anodic bonds. The full fabrication process consists of 10 mask steps and has developed towards a faster and more stable process. This in turn leads to lower price and lower fabrication time

Three different packaging concepts are tested and epoxy potting in a polystyrene tube shows the most promising results for deep sea applications. Investigation of the water penetration processes show that diffusion through the bulk packaging material is sufficiently low for some epoxies.

The water uptake by weight and water diffusion of EpoTek 302-3M is 3% and 1.5×10^{-9} cm^2s^{-1} respectively. However, pressurized testing of the packaging reveals that water is creeping along the interface between the chip and the packaging material. Thus material adhesion to the chip surface is a factor that has to be considered. A paper on the epoxy potting packaging concept has been published in the *Sensors and Actuators - A physical* journal.

The sensors are tested in a laboratory environment and proofs to measure temperature, pressure and salinity with accuracies of ±0.14°C, ±0.05 bar and ±0.5 psu respectively. The quantum efficiency of the light sensor is 40%-70% in the visible domain. The project has included theory, design considerations, microfabrication and characterization and has thus touched on the most important aspects of MEMS research.

Monolithic multi-sensor chips for direct exposure with the use of an epoxy potting packaging concept have the potential of revolutionizing the performance of commercial DSTs in the coming years.

Resumé (In Danish)

Denne afhandling, *MEMS Multi-sensor for dataopsamlingsmærker til brug i Fiskeri Forskning*, beskriver de indledende trin hen imod skabelsen af en ny generation af dataopsamlingsmærker (DST) til forskning i fisks adfærd. Dette involverer design og fabrikation af en Mikro Elektro Mekanisk System (MEMS) multi-sensor bestående af fire sensorer samt design og evaluering af et indpakningskoncept som tillader direkte eksponering af alle sensorerne til det omkringliggende medium. Dette resulterer i et meget kompakt system med høj nøjagtighed og hurtig reaktionstid.

DSTer er små autonome målesystemer der bruges i fiskeriforskning til at indsamle data om fisks adfærd. Disse DSTer indeholder sensorer, processor, hukommelse, batterier og afhængigt af måleinterval kan disse systemer typisk fungere i cirka to år og lagre en million målinger. De mest avancerede DSTer kan i dag måle temperatur, dybde og saltholdighed. Disse informationer kan efterfølgende bruges til at rekonstruere fisks migrationsruter og adfærdsmønstre.

Fisk fanges af forskerne, mærket fæstnes til fisken som efterfølgende slippes fri i havet igen. Når fisken igen fanges, bliver DSTet returneret til fiskeriforskerne mod en dusør. Informationerne bliver da overført fra mærket. Ved at tilpasse tidsudviklingen af de målte data til oceanografisk informationer fra andre kilder kan fiskens mest sandsynlige migrationsrute rekonstrueres.

Brugbarheden af de nuværende DSTer er begrænset af den betydelige størrelse, lave nøjagtighed og/eller langsomme respons tid af de eksisterende løsninger med diskrete sensorer.

Den nye multi-sensor chip består af en piezoresistiv silicium tryksensor, en $TiSi_2$ termistor, en pn-overgang lys sensor og en konduktivitetssensor bestående af fire platin elektroder. Den færdige chip er $3.9 \times 7.3 \times 1.2$ mm^3 i størrelse. Teorien for sensorernes design og funktionalitet bliver gennemgået og der bliver gjort grundlæggende overvejelser om elektronikkens indflydelse på sensorerne. Sensorerne er designet til at fungere i miljøer med parameterrummet 1 bar - 21 bar, -2°C - 20°C og 0 psu - 35 psu. En artikel omhandlende teorien bag og realisering af en mikroelektrode konduktivitetscelle er blevet publiceret i tidsskriftet *Sensors and Actuators - A physical*.

En sensor fabrikationsproces er baseret på kommercielle piezoresistive tryksensor principper med brug af volumenbaserede mikroteknologiske fremstillingsprocesser. Denne proces er udvidet til at omfatte $TiSi_2$ lederbaner, lokal oxidation og platin overflade elektroder såvel som en 3 lags chip sandwich lavet ved to på hinanden følgende anodiske bindinger. Den komplette fabrikations proces består af 10 maske trin og har udviklet sig hen imod en hurtigere og mere stabil proces. Dette medfører i sidste ende en lavere pris og hurtigere fabrikations tid.

Tre forskellige indpakningskoncepter er testet og epoxy støbning i polystyren rør har vist sig som det mest lovende til brug i havet. Undersøgelser af vands indtrængningsprocesser viser at vanddiffusionen gennem materiale volumenet er tilstrækkelig lav i visse epoxyer. Vandoptaget og

vanddiffusionen i EpoTek 302-3M er henholdsvis 3% and 1.5×10^{-9} $cm^2 s^{-1}$. Test af indpakningen under tryk har dog vist at vand trænger ind langs samlingsfladen mellem chip og indpakning. En artikel omhandlende epoxy støbning i polystyren rør som indpakningskoncept er blevet publiceret i tidsskriftet *Sensors and Actuators - A physical*.

Sensorerne er testet under laboratorium forhold og temperatur, tryk og saltholdighed kan måles med nøjagtigheder af henholdsvis ±0.14°C, ±0.05 bar and ±0.5 psu. Kvanteeffektiviteten af lyssensoren er 40%-70% i den synlige del af spektret. Dette projekt har inkluderet teori, design overvejelser, mikrofabrikation og karakterisering og har derfor behandlet de fleste vigtige aspekter i MEMS forskningen.

Monolitiske multi-sensor chips som kan eksponeres direkte til det omkringliggende medium ved hjælp af et epoxy indpakningskoncept har potentialet til at revolutionere ydelsen af kommercielle DSTer i de kommende år.

Preface

This thesis is submitted in partial fulfillment of the requirement for obtaining the Doctor of Philosophy (PhD) degree in engineering at the *Technical University of Denmark* (DTU). The achievements presented in the thesis are a result of work made at the *Department of Micro and Nanotechnology* (NanoTech) under the supervision of Erik V. Thomsen.

The project, "MEMS multi-sensor for Data Storage Tags used in fisheries research", has been carried out in a 3 years period from 2004 to 2007. The project is inspired by the research activities at the *Danish Institute for Fisheries Research* (DIFRES), but is considered entirely a Micro Electro Mechanical System (MEMS) project. The project has been co-financed by NanoTech and DIFRES.

A lot of people have contributed to this project, and the following acknowledgements represent a non-exhaustive list of people to whom I am in dept.

I would like to thank Erik V. Thomsen whose faith, optimism and supervision has been a firm foundation for the project, and associate professor Ole Hansen who often has been a guiding beacon when things got stuck. Also thanks to Dennis Mortensen, Íris Ólafsdóttir, Peter Kastberg Hansen and Peter Schultz whose MSc projects I had the privilege of co-supervising and from whose work I have gained a lot of knowledge. Also thanks to the former and present members of the MEMS-Applied sensor group for inspiring discussions and practical help while keeping the spirits high. In particular Zdenek Ferus and Karen Birkelund for help on electronics and packaging, respectively.

From DIFRES, Ken Haste Andersen, Stefan Neuenfeldt and Bo Lundgren has played an important part of the process of identifying the possibilities and challenges of applying technology to the marine environment.

Special thanks go to Jacob Richter whose daily sparing has been invaluable throughout all my university years.

Last but certainly not least, I thank my wonderful family, especially my lovely wife, whose patience and support has been vital for the completion of the project.

Kgs. Lyngby, Denmark, November 1st, 2007

Anders Hyldgård
DTU NanoTech - Department of Micro and Nanotechnology
Ørsteds Plads, Building 345 East
Technical University of Denmark
DK-2800 Kgs. Lyngby, Denmark

Contents

CHAPTER

1 Introduction

Significant changes in the living conditions of fish have left populations of different species on the edge of endangerment. Excessive fishing and transformation of the environment changes the living conditions of the fish. Large scale regulation programs have been initiated in the European Union in order to preserve the fish populations. However, effective regulation relies on precise knowledge on fish populations size, spawning cycles and migration habits of the fish. It is connected with large difficulties to gain access to such information as the sea is a hostile and inaccessible measurement environment. Traditional methods of population estimation and fish behaviour studies are counting fish from a trawl and sonar scans. Fish caught in a trawl are counted, their stomach contents are examined and their reproduction maturity status is determined. Sonars can be used to estimate size of populations passing by. These methods only give a momentary average of the population size and composition, and the examinations only give information of choice of prey within the last couple of hours and not information of feeding habits, locations, spawning behaviour and individual fish migration. A more extensive knowledge about the individual fish behaviour is needed. Laboratory studies of fish are well known to be partly misleading as fish behaviour changes significant in constrained environments. E.g. the fish tendency to swim in shoals disappears for fish living in small tanks. Tagging of fish has been widely applied to get information about fish migration. However, this only gives information about initial catch site and re-catch site as well as time in between. In recent years electronic tags have been applied to get information to fill the gap in between.

1.1 Data Storage Tags

Electronic tags are autonomous measurement systems that, when applied to a fish, measure parameters in the fish's natural environment. The measured data are then either transmitted or stored in an internal memory. Transmitting tags can either transmit through electromagnetic waves or acoustic waves. The extinction of electromagnetic waves is very high in sea water, due to the high salinity level, and electromagnetic transponder systems are therefore only applied in freshwater environments such as lakes and streams. Acoustic transmitters are used in various experiments in seawater as well [1]. The range is limited to a few hundred meters and true real-environment studies are not easily realized since the fish should be tracked at all times and the behaviour of the fish is initially influenced by the tagging process. The power consumption is also considerable in acoustically transmitting tags. The only viable solution for long time monitoring of sea water fish in their natural environment is Data Storage Tags (DSTs). A DST stores the data

Figure 1.1: Tagging Principle. Fish are caught by the researchers, the system is mounted on the fish which is then released to the ocean. When fishermen eventually re-catch the fish, the DST is returned to the fisheries research institution upon a reward. The data are then retrieved from the tag. By fitting the development in time of the measured data to oceanographic information from other sources the most probable migration route of the fish can be reconstructed.

Figure 1.2: External (*left*) and internal (*right*) tagging of fish with Data Storage Tags (DSTs).

in an internal memory, which can be read out when the fish is re-caught. The re-catch rates in the small seas, such as the Baltic Sea are significant, and for 460 cods tagged from 2003-2005, 40% was returned [2]. The tagging and measurement cycle is illustrated in Figure 1.1. First, the fish is caught and anesthesitized by the researchers. Next, the system is mounted on the fish, either by suturing to the dorsal fin or by surgical insertion of the tag into the peritoneal cavity. The fish is then released to the ocean, where it returns to its natural environment. When fishermen eventually re-catch the fish, the DST is returned to the fisheries research institution upon a reward. The data are then retrieved from the tag.

1.2 Examples of DST use

A large number of individual experiments utilize the use of DSTs for various examinations of the physiology and behaviour of fish. The measured data is used to draw conclusions about various aspects of fish behaviour. Some studies aim at reconstructing the migration route of the fish [3, 4] whereas other studies are trying to gain information about fish physiological and behavioural reactions to changes in the surroundings, such as non-lethal hypoxia conditions and fluctuations in salinity [5, 6, 7].

Reconstruction of the fish migration route (also called geolocation) is the most widely used application of the DST and is therefore the main focus of this project.

Different methods are applied to reconstruct the fish migration, depending on the geographic

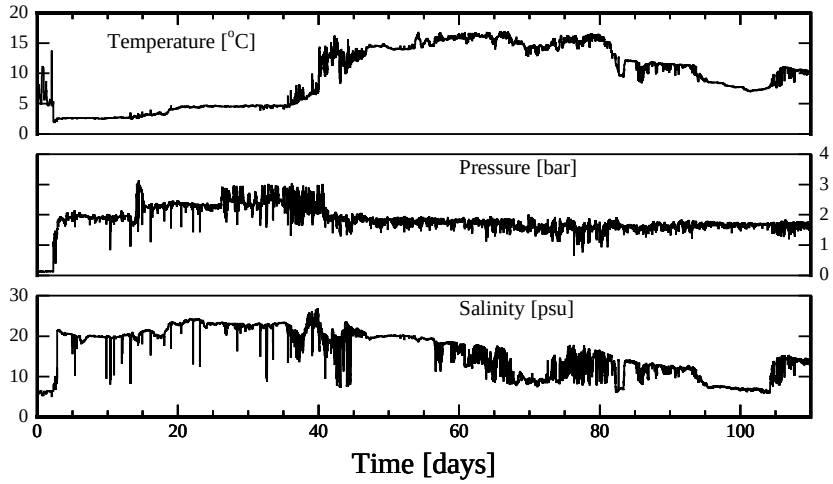

Figure 1.3: Example of measured data using the commercial Star-Oddi DST mounted on a Baltic Cod. The salinity, temperature and depth triplet is used to re-construct the most probable migration route of the fish by making fits to oceanographic data from other sources. Data courtesy of *S. Neuenfeldt.*

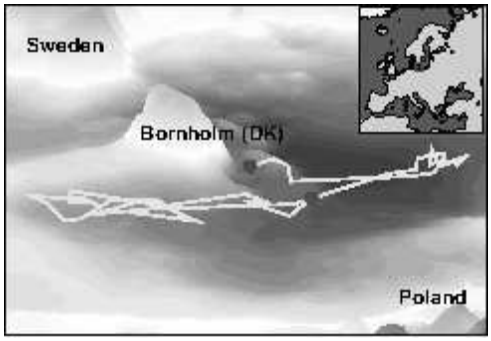

Figure 1.4: Tracked fish migration route from measured DST data of salinity, temperature and depth. Conventional tags only offers information about the location of the red dots, whereas DSTs also supply information about the time in between. Figure courtesy of *S. Neuenfeldt.*

location of the population of the fish. In general the measured parameters are compared to oceanographic data from other sources and statistical methods are applied in order to reconstruct the most probable migration route of the fish.

1.2.1 Geolocation through salinity, temperature and depth in the Baltic Sea

In near coastal waters such as the Baltic Sea, the input of fresh water and local warmup of shallow water creates significant local gradients in salinity and temperature. Additionally the fish is actually constricted by the ocean floor. Thus, the salinity, temperature and depth triplet is locally unique for the different locations in the Baltic Sea, and combined with the maximum swimming speed of the fish the most probable migration route can be reconstructed through statistical fits of the measured data to oceanographical data from other sources. The salinity can be calculated from the conductivity, temperature and pressure (CTD, D for depth) of the water through well established

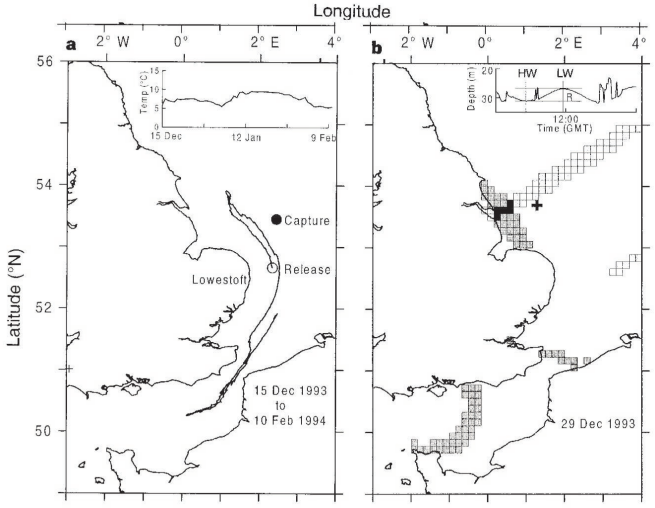

Figure 1.5: Example of geolocation through temperature and tidal variations in the North Sea. For bottom feeding species, such as plaice and cod, the tidal variation can be periodically measured as a pressure induced by a change in water column height above the fish. The left figure shows the migration route of a tagged plaice as reconstructed from the local temperatures (*insert*) and a number of fix-points extracted from tidal variations. The right figure shows the location of such a fix-point based on measurement of tidal range (R) and time of high water (HW) (*insert*). Grey boxes show locations of similar tidal range and white boxes show similar time of high water. Black boxes indicate coincidence. Figure from *Metcalfe and Arnold, Nature*[3]

polynomial fits to empirical data [8](See Appendix A). Figure 1.3 shows the salinity, temperature and pressure as a function of time as measured using a Star-Oddi CTD DST [4]. The reconstructed most likely migration route is shown in Figure 1.4. Clearly, the additional information gained from the DST is tremendous.

1.2.2 Geolocation through temperature and tidal variations in the North Sea

In the North Sea, the timing and magnitude of the local tide varies significantly with the geographic location. Bottom feeding species, such as cod and plaice, spends a large fraction of time on the ocean floor, and the tide can be measured as a variation in pressure which is not induced by fish movement but by a variation in water column above the fish. Figure 1.5 shows the measured temperature and depth as a function of time and the fish locations reconstructed from the temperature and tidal variations.

1.2.3 Other methods of geolocating

Measurement of light intensity is a useful supplement for geolocation. When fish travel over large distances, where information of the locale properties of water is only sparsely available or the variations in the parameters are too small for precise geolocation, the light is used instead. By looking at the light intensity time distribution for a day, the longitude and latitude can by estimated. The distribution for northern Alaska in July is very different from the profile of the Canary Islands. Additionally the light intensity can give indirect information about local phenomena such as cloud coverage or algae in the water.

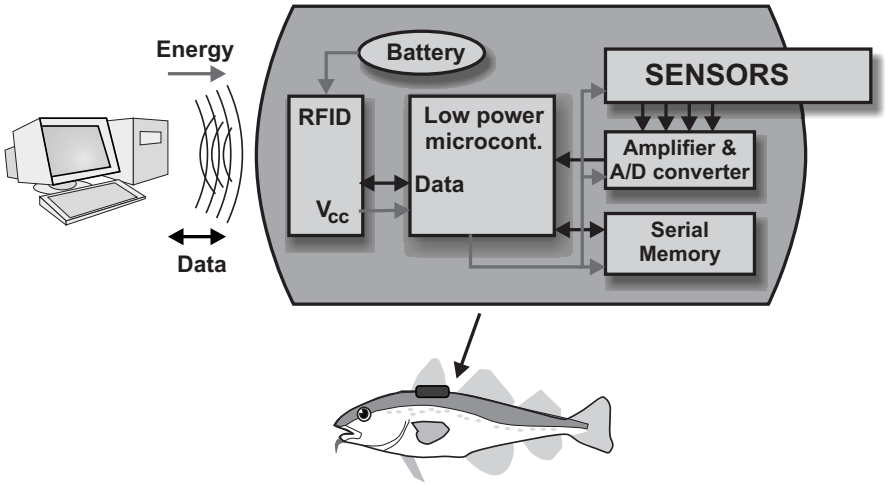

Figure 1.6: Data Storage Tag (DST) system overview. A microcontroller manages the power to and data from the sensors and stores the data in the memory. Batteries power the system. When retrieved, the system can be powered via the wireless interface while data is read out.

Figure 1.7: Commercial Data Storage Tags (DSTs) from Cefas Technology Ltd. [9] (*left*) and Star-Oddi [10] (*middle* and *right*).

Attempts have also been made to implement a GPS transferring technique. The GPS position of fishing vessels are encoded into the sonar signal of the boat. If a DST passes by and detects the signal, the GPS postition is logged in the memory. In this way fix-points are added to the general tracking lowering the uncertainty. However, still the probability of sonar and tag crossing is very low.

1.3 DST Technology

The DSTs consist of sensors, a microprocessor, memory, battery and means of external communication, as shown in Figure 1.6. The micro controller controls the power delivery to the subcomponents in the tag. In this way sensors are momentarily powered and a measurement is converted in the A/D converters and the data stored in the non-volatile memory. Between measurements the system enters a sleep-mode where the power consumption is minute. The data is read out either by wireless communication or through metallic contacts. A number of different manufactures produce DSTs of different kinds. The English company Cefas Technology Ltd. [9] and the Icelandic company Star-Oddi [10] are world-leading in this field. State of the art tags, such as the Cefas G5 tag or Star-Oddi DST-micro tag, have diameters of only 8 mm and have lengths of 30 mm or less.

These tags measure temperature and depth, where as the smallest tag also measuring salinity is 17 mm in diameter and 46 mm in length. Two commercial DSTs are shown in Figure 1.7
The DSTs can, depending on duty cycle, typically operate for around two years and store one million measurements.

1.4 Limitations of current DSTs

The DST technology has developed significantly in the last decade. However, the size, accuracy, number of sensors and sensor response time still does not meet the demands of the fisheries research. The DSTs have insufficiencies in the following fields

- The accuracy of the salinity sensors in current DSTs is not precise enough. As a result, tracking is connected to large uncertainties, e.g. in some cases it cannot be determined whether a fish swims north or south of Zealand (Danish island of 7000 km^2) [2]. An improved accuracy and resolution of the sensors is thus essential for precise geolocation.

- The response time of the DST temperature sensors is too long. This may lead to erroneous salinity measurements as conductivity and temperature are read asynchronously. In conventional tags the temperature is measured in the electronics in the center of the tag. By exposing the temperature sensor directly to the surrounding media the response time is significantly faster, which in turn leads to a more accurate measurement of salinity. Layers in the ocean with rapid changes in temperature (thermocline) and/or rapid changes in salinity (halocline) exist e.g. where fresh water streams into ocean water or where the sun heats up the upper stagnant layer of water.

- The system size is acceptable for investigations of fish of reasonable size, e.g. cod of lengths above 50 cm. For smaller fish the system size should be reduced considerably.

- The price should preferably be lowered in order to increase the number of fish that can be included in a study, hereby improving the statistical foundation.

- Not enough measurements per tag. A natural shrinking of the size of mass storage electronics with time will improve this. Indeed this has been the case through the time of the project.

- When the tag is placed inside the peritoneal cavity the sensors should be placed on a stalk or wire probe that hangs on the fish exterior in order to be exposed to the surrounding media. This tag design sets high demands for a very small sensor system which are not met by current sensor designs.

1.5 Improvement of the current DSTs

There are different possibilities and challenges when improving the DSTs. Essentially there are three main subjects that can be addressed; sensors, packaging and electronics.

Ideally, the tag electronics should be integrated into an Application Specific Integrated Circuit (ASIC) in order to minimize the size and power consumption while meeting the exact demands of the sensors with high performance for a specific sensor configuration. Development of an ASIC is however too costly for a low volume production and is beyond the scope of this project. Though, making clever redesign of conventional discreet electronics may allow for a small gain in size and

power consumption. Some general considerations that are valid for both ASIC and discrete electronics, influence the design of sensors, and should thus be addressed.

A real gain is obtained by designing an integrated multi-sensor, that can be directly exposed to the surroundings. In this way, a very compact system of low power sensors can be realized which allows for direct exposure. Direct exposure of the sensor chip sets high demands for the packaging concept reliability. Simultaneous design of sensor and packaging is necessary to achieve an effective result.

Integration of more sensors into a monolithic chip will lead to the ultimate miniaturization of the sensor size. Adding a new packaging concept will allow for direct exposure, which also means that the sensitivity, accuracy and temporal response of the sensors are potentially improved.

Thus the main task of this project are

- Design and implementation of an integrated multi-sensor capable of measuring temperature, pressure sensor, conductivity and light intensity
- Development of a packaging scheme that allows for direct exposure of the multi-sensor

Additionally the electronics related constraints on the multi-sensor design and DST system has to be investigated.

1.5.1 Integrated multi-sensor system

Central in the design of a new tag is an integrated multi-sensor chip. The new DST will excel over existing DSTs because of the sensor system. Four or more sensors are exposed directly to the surroundings which gives

- high sensitivity as the energy to the sensor is not transferred through the packaging.
- high accuracy as no packaging related offsets will drift over time.
- fast response time as no time delay is introduced from the packaging

A lot of physical and physiological sensors are interesting in connection with fish research. Some, such as temperature sensors, depth sensors, salinity sensors, light sensors and geomagnetism sensors are primarily related to geolocation. Other sensors such as Dissolved O_2 sensors, feeding activity sensors, general activity level sensors, acceleration/tilt senors, travel velocity sensors, electrocardiography (ECG) sensors and electromyography (EMG) sensors are mostly related to fish physiology studies.

The DST multi-sensor should ideally measure all the above parameters continuously. However, size and design complexity limits the number of sensors that are initially combined. The basis implementation is aimed primarily at geolocation, and therefore the multi-sensors implemented in this project utilizes the four sensors that are most obvious for geolocation; a temperature sensor, a pressure sensor, a conductivity sensor and a light sensor.

Combining four sensors on a single chip without compromising the sensitivity and accuracy of the individual sensors calls for an analysis of the different aspects of the sensor functionalities.

1.5.1.1 Temperature

Temperature is considered the primary measurement parameter. It is directly measurable and the determination of temperature is therefore not affected by other parameters. The temperature is

Parameter	Full scale range	Resolution (accuracy)
Pressure/depth (bar/m)	1/0 − 21/200	0.01/0.1 (0.1/1)
Temperature (°C)	(-2) − (+25)	0.01 (0.05)
Salinity	0 − 35	0.01 (0.05)
Light	*As high resolution as possible*	

Table 1.1: Sensible sensor requirements as proposed by The Danish Institute for Fisheries Research (DIFRES).

important mainly for two reasons. First of all, the temperature has high impact on almost every physical and biological process and is thus unavoidable in studies of fish behaviour and living environment. Additionally the temperature has a large influence on the determination of other parameters. This is the case for the indirect measurement parameters, such as the change of conductivity with temperature of water of a given salinity. Additionally, the response of the sensors changes with temperature.

In the multi-sensor design, the temperature is measured using a temperature sensitive resistor as described in Section 2.2.

1.5.1.2 Pressure

Pressure sensors are very useful sensors, because measure of absolute pressure gives an indication of depth in the water and measure of differential pressure can be used to estimate feeding activity or tail beat frequencies. The pressure to depth conversion depends on the mass density of the water column above the fish, which depends on the salinity. This cannot easily be corrected. The accuracy therefore suffers. However, the resolution does not. Density changes with 0.3% for a temperature change of 20°C. Density changes 2.8% for salinity changes of 0 psu to 35 psu. Additionally the density changes with pressure, making the pressure to depth relation slightly non-linear [8]. For a water mass of uniform salinity and temperature the non-linearity is trivial and can be corrected for.

A piezo-resistive pressure sensor is implemented in the multi-sensor design as described in Section 2.3.

1.5.1.3 Electrical conductivity

The measured salinity is used for geolocation but is also an important parameter for fish preferred living habitat. Measurement of the electrical conductivity is the most direct measure of salinity. Salinity, or dissolved salts, is the amount of salts (by weight) dissolved in the water. Ocean water contains about 32‰-38‰ salt of which 90% is NaCl. Oceanographers often refer to the salinity in the unit of psu (practical salinity unit) which is actually equivalent to ppt (parts per thousand), thus 32‰ = 32 psu. The salinity can be determined by drying out samples of seawater and weighing the remaining salts. However, the present, and more practical, salinity definition is based on electrical conductivity, temperature and pressure of the water as defined in UNESCOs "The Practical Salinity Scale" from 1974 [11]. According to this definition the salinity can be calculated from the conductivity, temperature and pressure triplet from well-established polynomial fits to empirical data. Figure 1.8 shows relations between salinity, electrical conductivity, temperature and pressure.

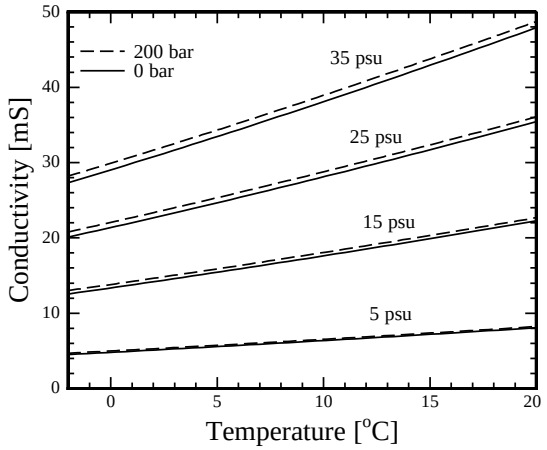

Figure 1.8: Conductivity of saline water as a function of temperature at four different salinities and two different pressures. A precise determination of conductivity and temperature is needed for precise determination of salinity, whereas pressure has a less significant influence.

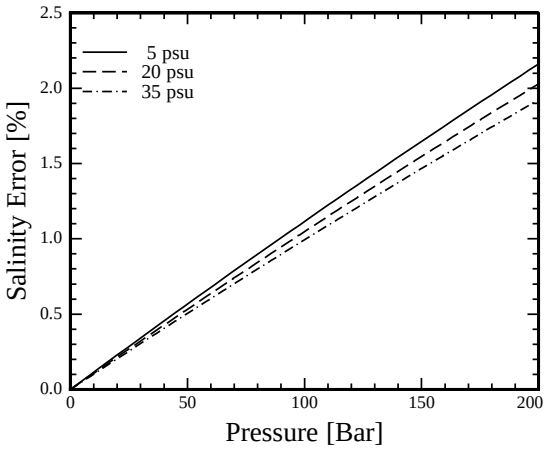

Figure 1.9: The error in salinity determination introduced by pressure if the results are not pressure compensated. The error is 1% at approximately 80 bar corresponding to 800 m depth.

At fixed temperature and pressure the conductivity changes almost linearly with salinity. As seen in Figure 1.8 the temperature has a significant influence on the conductivity whereas pressure plays a less significant role. Thus in all cases a precise measurement of conductivity and temperature is needed in order to make a precise determination of salinity. Because of linearity a 1% (of full scale) accuracy on conductivity is needed for 1% accuracy in salinity determination. Temperatures should be determined with an accuracy better than 0.5°C. Whether pressure compensation is needed depends on the specific measurement conditions and the needed accuracy. The error in salinity determination as introduced by lack of pressure compensation is shown in Figure 1.9. Obviously, if salinity measurements are performed in waters at depths not exceeding 200 m, corresponding to 20 bar, the error would be less than 0.2%, which might be precise enough for some

applications.

Very precise determination of salinity can be made in glass tubes for reference and calibration and high accuracy Conductivity, Temperature & Depth (CTD) profilers are used to investigate seawater parameters at all ocean depths.

Micro system implementation of conductivity sensors is possible. However, in the following chapters it will become evident that precise measurements of conductivity will be complicated by system shrinkage.

Therefore a thorough analysis of a conductivity electrode sensor systems is needed for a significant shrinking of a system without compromising the accuracy. Section 2.1 covers this topic.

1.5.1.4 Light

The light can be used for geolocation, but also as an indirect indicator of the fish environment. In the multi-sensor the light is considered a parameter of secondary importance. A pn-junction is readily available and will thus function as a light sensor, as described in Section 2.4

1.5.2 Packaging scheme that allows for direct media exposure

A new sensor concept allowing for direct exposure of the sensors is essential for improving the current DSTs. A new packaging concept partly defines the form factor of the sensor chips, and the chip and packaging are thus designed simultaneously as a collected system design task. The new packaging concept must fulfill a number of conditions. The most important function is the separation of exposed sensors and the remaining electrical system. This sets high demands for the packaging material with regards to water diffusion and tightness of chemical and mechanical sealing at interfaces. This calls for an investigation of different packaging concepts and materials.

1.6 Main results

In the course of this project three generations of multi-sensors have been designed and fabricated. The designs are made on basis of analytical and numerical modeling of the performance of the four sensors (conductivity, temperature, pressure and light) and considerations of packaging and electronics.

The fabrication process utilize a commercial bulk micromachining pressure sensor process and is extended to include a $TiSi_2$ wiring system, local oxidation and platinum surface electrodes as well as a 3 layer chip stack made from two consecutive anodic bonds. The process sub-steps have been optimized for process stability and prepared for batch processing. A finished multi-sensor chip is shown in Figure 1.10.

Three different packaging concepts have been tested; O-ring sealing, low pressure injection moulding and epoxy potting in a tube. All three concepts rely on a silicon nitride film on the chip to protect the sensors and the $TiSi_2$ wiring system, while polymers or epoxies seal off water from the vulnerable parts of the system. Epoxy potting in a tube shows the most promising results.

The packaged sensors have been characterized in a lab environment for sensitivity, resolution and cross sensitivity.

The results of the project have been presented at the *IEEE MEMS 2005* conference (poster), the *IEEE Sensors 2005* conference (oral presentation), the *Eurosensors 2006* conference (oral presentation) and the *IEEE MEMS 2007* conference (oral presentation). Additionally, the work has resulted in two publications in *Sensors and Actuators - A physical*.

Figure 1.10: Photograph of finished 3rd generation chip. The chip consist of a triple stack of two silicon chips with a pyrex layer in between. The chip dimensions are 3.9 mm × 7.3 mm × 1.2 mm.

1.7 Thesis outline

Motivated by the need for a new generation data storage tags, this thesis describes the design, fabrication and characterization of microtechnology based multi-sensor chips as well as related packaging concepts.

In Chapter 2 the fundamental aspects of the design of the different sensors are described and central design parameters are found through analytical expressions and numerical simulations. This includes a detailed analysis of the conductivity sensor, as salinity sensor performance in extreme system shrinkage is not well known. Additionally, central design parameters are found for the three other sensors.

On the basis of these design considerations, Chapter 3 describes the generations of the micro technology based fabrication process and the related process optimization results. The fabrication process includes 10 lithography mask steps and a number of critical process steps such as local oxidation, dopant pre-deposition and ion-implantation, formation of $TiSi_2$, KOH anisotropic silicon etch and triple stack anodic wafer bonding.

The results of Chapters 2 and 3 is used to design the four sensors. The layouts of three generations of multi-sensor chips are described in Chapter 4.

Chapter 5 seeks to describe the different packaging concepts used in connection with the different chip layouts. An O-ring packaging concept, low pressure injection moulding and epoxy potting is described.

The DST electronics considerations are briefly touched in Chapter 6. The main considerations are sensor interfacing and power consumption and a draft of a test PCB is shown.

The sensor characterization results are presented and compared to theory in Chapter 7. Different aspects of sensor signal stabilities are touched upon and important cross sensitivities are examined.

Chapter 8 summarizes the project results.

CHAPTER

2 Sensor Theory and Design

Combining four sensors on a single chip without compromising the sensitivity and accuracy of the individual sensors calls for an analysis of the aspects of the sensor functionality that is determining for the sensor performance. In the following central design parameters for the four sensors are found through analytical expressions and numerical simulations. A paper on the theory and realization of micro electrode conductivity cells has been published in the *Sensors and Actuators - A physical* journal.

2.1 Conductivity cells

Measurement of the conductivity of an electrolyte is in principle carried out by forcing a current through a sample of the electrolyte and measuring the resulting potential drop. This is most often done with either two or four electrodes exposed to the electrolyte. A number of electrodes combined with a sample of electrolyte is normally referred to as a cell. In the cell, the electrical conductivity κ is ideally related to the measured current I and voltage V as

$$\frac{V}{I} = \frac{K}{\kappa} \tag{2.1}$$

where the cell constant K is geometry dependent. This is discussed in more detail later. Here it is assumed that the electrolyte is behaving purely ohmic and that the polarization ability is negligible. The charge transfer is assumed purely electric and independent of ion-transport. Real

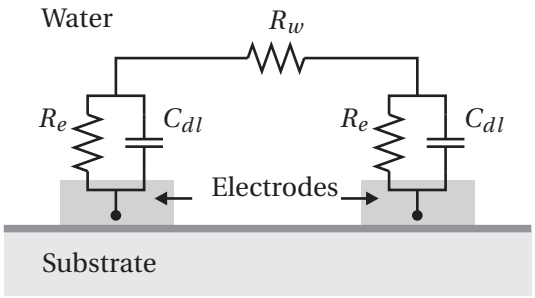

Figure 2.1: Two electrode conductance cell principle. The electrochemical red-ox process is described by the resistance R_e. The electrochemical double layer is described by a capacitance C_{dl}. The equivalent resistance of the water is named R_w. All three parameters change with salinity.

measurements are complicated by the existence of contact potentials in the electrode-electrolyte interface [12]. Charge transfer to and from the interface is a result of either reduction-oxidation (red-ox) processes at the interface or charging of the electrochemical double layer, the charging behaviour of which is much like in a Schottky diode in semiconductor physics. These two processes can simply be modeled as a resistive and a capacitive component in parallel. However, the red-ox reaction resistance is highly nonlinear and the impedance of the double layer capacitance is not exactly inversely proportional to the frequency. The reaction resistance is dependent of the ion-concentration in the electrolyte and highly dependent of the applied potential. The higher the potential, the more red-ox processes are possible. The potential should be kept as low as possible so that no red-ox processes involving the electrode material takes place, hereby minimizing the corrosion of the electrodes. This is naturally of outmost importance in microsystems where the volume to area ratio of the electrodes is low. In a simple estimation of the corrosion rate at a high applied voltage, it is assumed that all charge transfer is caused by red-ox processes involving electrode material. In this case a 800 μm×400 μm (4000 nm thick) electrode dissolves in 16 seconds, assuming 200 μA for 10 V applied potential. For low voltages, e.g. 10 mV, the reaction resistance is easily above 1 MΩ and the corrosive processes are negligible. The double layer capacitance depends on the electrode material and the electrolyte ion concentration. The area specific capacitance is typically in the range of 10-40 μFcm^{-2} [12][13].

2.1.1 Two electrode configuration

A simple equivalent circuit of a two electrode cell can be illustrated as in Figure 2.2. The contribution from the two electrodes is reduced into one effective reaction resistance $R_e/2$ and one effective double layer capacitance $2 \times C_{dl}$. The impedance Z of the cell at medium frequencies, where the reaction resistance, R_e, is negligible, can be expressed as

$$Z = R_w + \frac{1}{j2\omega^{\alpha} C_{dl}} \tag{2.2}$$

where R_w is the cell resistance of the water, ω is the angular frequency, C_{dl} is the double layer capacitance of one electrode and α is an ideality factor which is close to 1 [12]. The magnitude of the impedance can be expressed as

$$|Z| = \sqrt{R_w^2 + \frac{1}{4\omega^{2\alpha} C_{dl}^2}} = R_w \sqrt{1 + \frac{1}{4\omega^{2\alpha} C_{dl}^2 R_w^2}} \tag{2.3}$$

At low frequencies the cell impedance is dominated by the reaction resistance and the conducted current for fixed voltage amplitude is very small. A precise determination of the water

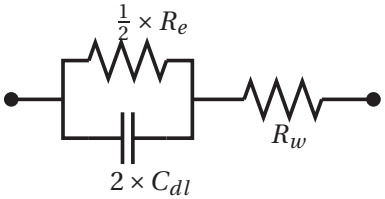

Figure 2.2: Two electrode conductance cell equivalent circuit at low frequencies. The electrolysis resistance R_e is much higher than the water resistance R_w. At higher frequencies the double layer capacitance C_{dl} short circuits and the impedance converges towards R_w.

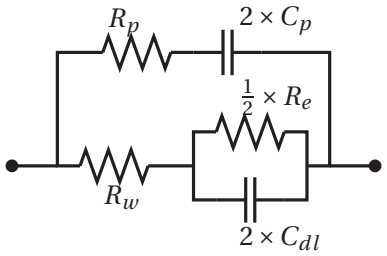

Figure 2.3: Two electrode conductance cell equivalent circuit including parasitic resistance R_p and capacitance C_p. The electrolysis impedance R_e is much higher than the water resistance R_w. The double layer capacitance C_{dl} is higher than the parasitic capacitance C_p

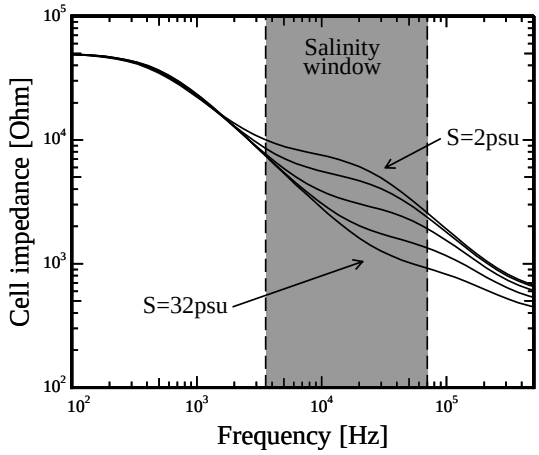

Figure 2.4: Theoretical impedance vs. frequency for a two electrode measurement setup for 5 different salinities (2, 4, 8, 16 and 32 psu) calculated from realistic parameters (C_{dl} = 32 nF, C_p = 5 nF, R_e = 50 kΩ, R_p = 600 Ω, R_w = 1.1 kΩ - 10.5 kΩ and α = 1). At medium frequency the impedance is strongly dependent on salinity. The lower limit frequency is determined by double layer capacitance and the upper limit frequency is determined by parasitic capacitive coupling in the wiring system and substrate.

resistance R_w is thus very difficult. At higher frequencies the double layer capacitance conducts, short-circuiting R_e, and eventually the cell impedance equals the water resistance. In most systems there are upper limits to the operating frequency determined by parasitic capacitances either to a conducting substrate or in the wiring system and measurement equipment.

A more realistic model of the cell behaviour of electrodes placed on a silicon substrate with an insulator in between is illustrated in Figure 2.3. In this case the high frequency impedance is equal to the impedance of the water and the impedance of the substrate in parallel. A theoretical impedance spectrum with realistic parameters (C_{dl} = 32 nF, C_p = 5 nF, R_e = 50 kΩ, R_p = 600 Ω, R_w = 1.1 kΩ - 10.5 kΩ and α = 1) is shown in Figure 2.4. Obviously a frequency interval exists (hereafter named salinity window) in which the impedance is highly dependent of salinity and where the impedance ideally is inversely proportional to the conductivity. The lower frequency limit for the salinity window is determined by double layer capacitance and water resistance at high salinities. Both depend on electrode geometry. The upper frequency limit for the salinity window is determined by the water impedance at low salinities and the parasitic capacitive coupling through the substrate, which is dependent on the dielectric insulation of the electrode system. For metal

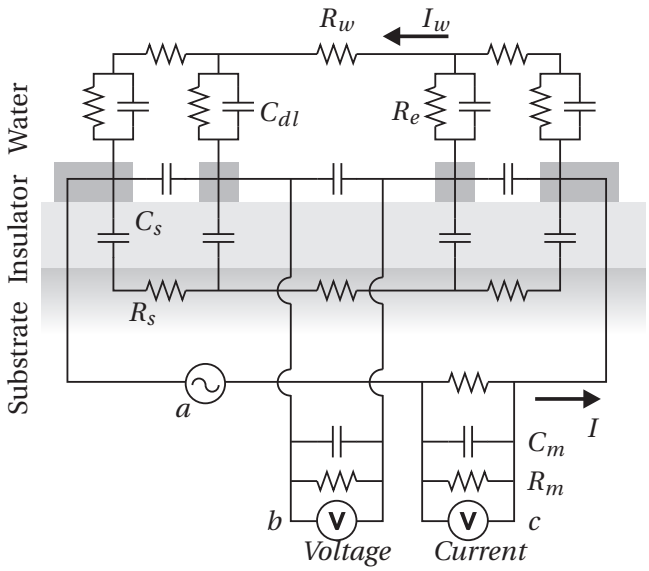

Figure 2.5: An electrical equivalent description of the four electrode conductivity measurement, including cell, source (*a*) and measurement equipment (*b* and *c*). All current I should ideally go through the water and the contact impedance at the voltage electrodes should be much lower than the inner impedance of the measurement equipment.

electrodes placed on silicon dioxide, the upper limit frequency can easily be adjusted by changing the insulating oxide thickness or changing the dimensions of the wiring system. In some cases it is possible to eliminate errors from parasitic or double layer capacitances by calibration. However, the double layer capacitances will most likely change over time due to electrode degradation and/or algae growth.

2.1.2 Four electrode configuration

In order to widen the salinity window and increase system stability a four electrode configuration can be used; in this case the transimpedance Z_T is measured by forcing a current through two (most often outer) electrodes, while the potential is measured between two other (most often inner) electrodes. Ideally the system should give a true measurement of the water resistance for all frequencies lower than the upper frequency limit since all current flow is through the water. This is, however, not always the case.

An equivalent circuit of the system including measurement equipment is shown in Figure 2.5. An AC power source delivers a constant amplitude voltage. The power source is connected to the outer electrodes of the cell through a high precision series resistor used to monitor the current. The current is coupled to the water through the contact impedance. The water resistance is distributed on three resistors the values of which depend on the cell geometry. Unwanted parasitic coupling of the electrodes takes place either as direct capacitive coupling between the electrodes (minor effect) or as capacitive coupling through the dielectric insulating layer into the resistive substrate. The inner impedance of the equipment measuring the cell current and voltage has to be taken into account. Two preconditions need to be fulfilled in order to get a true and stable measurement of the water resistance in the cell; 1) The current I flowing through the outer wire loop (Figure 2.5) should equal the current flowing in the water I_w, and 2) the potential across the voltage measure-

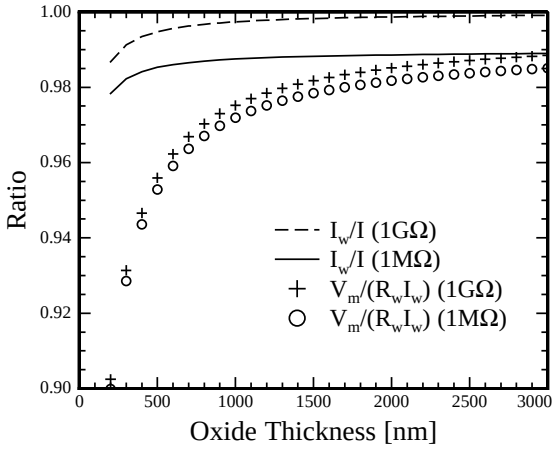

Figure 2.6: Ratio between measurement current I and water current I_w as well as the ratio between measurement potential V_m and the cell water potential $R_w I_w$, with (1 GΩ) and without (1 MΩ) high impedance pre-amplification stage as a function of insulator thickness. The source voltage frequency is 3 kHz. The model parameters are the same as in Figure 2.4.

ment equipment b (Figure 2.5) should equal the potential $I_w R_w$ in the water at the interface of the voltage electrodes. The first precondition is subject to the same upper limit frequency considerations as in the case of a two terminal setup. The second precondition is met, provided that the impedance across the water-electrode interface (contact impedance) of the voltage electrodes is much smaller than the inner impedance of the measurement equipment and the impedance of the substrate coupling. For submillimeter electrodes at low potentials, the contact impedance easily exceeds 1 MΩ in the low frequency domain. This is comparable to the typical input impedance of the AC voltage stage of digital multimeters, such as the Keithley 2000 series (R_m = 1 MΩ, C_m = 100 pF). Simple voltage division predicts a significant measurement error (> 60%) as a result. This can be counteracted by increasing the electrode size and/or increasing the input impedance of the measurement equipment by use of a high impedance instrumentation pre-amplifier stage (such as AD524 with R_m = 1 GΩ and C_m = 10 pF) reducing the error to less than 1%. At medium frequencies the capacitive coupling through the substrate has a significant influence. Figure 2.6 shows the ratio between water current I_w and measurement current I as well as the ratio between cell water potential $R_w I_w$ and measurement potential V_m, with and without instrumental amplifier as a function of insulator thickness (at 3 kHz).

This analysis indicates that a four electrode cell on a 3 μm silicon dioxide insulating layer and a 1 GΩ/10 pF input impedance of the voltage measurement equipments can be used to measure of the water resistance with an accuracy better than ±1%. Increasing the size of the voltage electrodes can further improve the accuracy.

2.1.3 Design

In order to predict the performance of a conductivity cell, the cell constant has to be determined. This can be done by considering the cell as a purely resistive media without any contact potentials under DC conditions. For very simple electrode geometries, such as hemispheres or parallel semi-infinite radial conductors, the cell constant can be evaluated analytically. This can be used to

predict simple scaling properties of the system. For slightly more complicated structures, as generated with planar processing, numerical methods are needed.

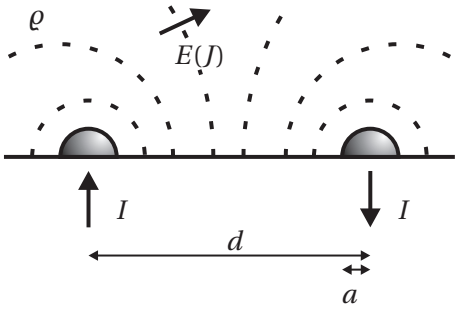

Figure 2.7: Simple analytical approximation to planar and hemispherical electrodes. Two hemisphere electrodes in a semi infinite media of resistivity ϱ. The electrodes carry a current I and $-I$ and the potential drop between the electrodes is found by integrating the resulting electric field distribution $E(J)$ between the electrodes. The approximation is good when the center distance d is much larger than the radius a of the electrodes.

2.1.3.1 Analytical approach

A good two electrode model system consists of a pair of hemispherical electrodes of radius a separated a distance d, immersed in a semi-infinite conductive medium (such as the ocean) with the electrical resistivity ϱ, as shown in Figure 2.7. In a first approximate model the electrodes are considered half space point current sources with the currents $\pm I$. The current density $J(r)$ from a single point source is purely radial, thus

$$J(r) = \frac{I}{2\pi r^2} \tag{2.4}$$

where r is the radial distance from the current source. Thus also the electric E field is purely radial

$$E(r) = -\frac{\partial \Phi}{\partial r} = \varrho J(r) = \frac{\varrho I}{2\pi r^2}. \tag{2.5}$$

Two superimposed point current sources results in the potential Φ

$$\Phi(r_1, r_2) = \frac{\varrho I}{2\pi}\left(\frac{1}{r_1} - \frac{1}{r_2}\right), \tag{2.6}$$

where r_1 and r_2 are the distances from the point sources to the point of interest.

A simple approximate expression for the potential difference V between the hemispheres can be obtained by evaluating the potential, Equation 2.6, at the facing points of the spheres; the result is

$$V = \frac{\varrho I}{\pi a}\frac{d-2a}{d-a} \tag{2.7}$$

and thus the cell constant is

$$K = \frac{V}{\varrho I} = \frac{1}{\pi a}\frac{d-2a}{d-a} \tag{2.8}$$

This simple result is useful for establishing the scaling behaviour, comparison to numerical models, and as an approximate solution to the problem of some planar electrodes separated a large distance. Note, however, that Equation 2.7 and 2.8 are only approximations since the potential, Equation 2.6, does not fulfil the boundary conditions on the hemispherical surfaces.

A potential that fulfil the boundary conditions can be constructed from an infinite sum of point source potentials using the method of images [14]. A set of primary point sources $\pm I_0$ at the centre of the hemispheres must be combined with image point sources $\pm I_1 = \pm I_0 a/d$ displaced a distance $\lambda_1 = a^2/d$ from the centre in order to fulfil the boundary condition on the opposing hemisphere. Now to fulfil the boundary conditions on the opposing hemisphere, these image sources again must be combined with new image sources $\pm I_2 = \pm I_1 a/d_1$ displaced $\lambda_2 = a^2/d_1$ from the centre, and so on *ad infinitum*. Here $d_i = d - \lambda_i$ is the distance from the centre of one sphere to image i in the opposing sphere. The resulting total current becomes $I = \sum_{i=0}^{\infty} I_i$, a sum that converges rapidly except when the spheres nearly touch (it diverges when they touch). The resulting potential difference between the spheres becomes $V = 2\varrho I_0/(2\pi a)$ since the images are arranged for zero potential on the sphere. Finally, the cell constant becomes

$$K = \frac{V}{\varrho I} = \frac{1}{\pi a}\frac{I_0}{I} = \frac{1}{\pi a}\frac{I_0}{\sum_{i=0}^{\infty} I_i} = \frac{1}{\pi a}\mathrm{F}\left(\frac{a}{d}\right), \tag{2.9}$$

where $\mathrm{F}\left(\frac{a}{d}\right)$ is a function exclusively of the ratio a/d. The general trends of the exact and the approximate expressions for the cell constant Equations 2.9 and 2.8 against variation of the geometry are quite similar, except for electrodes which are very closely spaced. Additionally, the analytical expressions are consistent with FEM simulation results obtained in Section 2.1.3.2. The analytical expressions and FEM results are compared in Figure 2.8, thus the simple approximate expression serves as a useful design tool, while the exact solution provides an excellent tool for verification of the accuracy of numerical modeling.

The cutoff frequency of the cell, f_{th}, where the water resistance equals the impedance of the double layer, can be expressed as (using Equation 2.2 with $\alpha = 1$)

$$\begin{aligned} |R_{w,min}| &= |\varrho_{min} K| = \left|\frac{1}{j2\omega_{th} C_{dl}}\right| = \left|\frac{1}{j4\pi f_{th} c'_{dl} A}\right| \\ \Leftrightarrow f_{th} &= \frac{1}{4\pi c'_{dl} A \varrho_{min} K} \end{aligned} \tag{2.10}$$

where $R_{w,min}$ and ϱ_{min} are the water resistance and resistivity at the highest detectable salinity, c'_{dl} is the specific double layer capacitance and A is the electrode surface area. The lowest cutoff frequency is found when the $K \times A$ product is highest. Thus, for semi-spherical electrodes, solving

$$\frac{\partial(K(a,d) \times (2\pi a^2))}{\partial a} = 0 \tag{2.11}$$

gives the best electrode radius (or equivalent square side length) for a given electrode spacing. For a constant outer distance of the electrode of 3800 μm, the lowest cutoff frequency is found at $a \approx 750$ μm which corresponds to $0.33d$.

In the case of two semi-infinite cylindrical electrodes of radius a separated the distance d the potential from two off centre line current sources fulfil the boundary conditions on the cylinder surfaces; this results in the simple exact expression

$$K = \frac{2}{\pi \ell} \operatorname{arccosh} \frac{d}{2a} \tag{2.12}$$

for the cell constant of a cylinder pair of length ℓ. These electrodes each have the area

$$A = \pi a \ell. \tag{2.13}$$

The cylindrical electrode model is a good approximation to long, narrow planar electrodes. Thus it is clear that for these electrodes the product $K \times A$ and hereby the cutoff frequency becomes independent on the electrode length ℓ.
It must be noted that even though Equation 2.11 results in the lowest cutoff frequency, increasing the electrode area also decreases the cell constant and thereby the water resistance. At some point, problems with noise or instrumentation might discourage further enlargement when currents get to high.

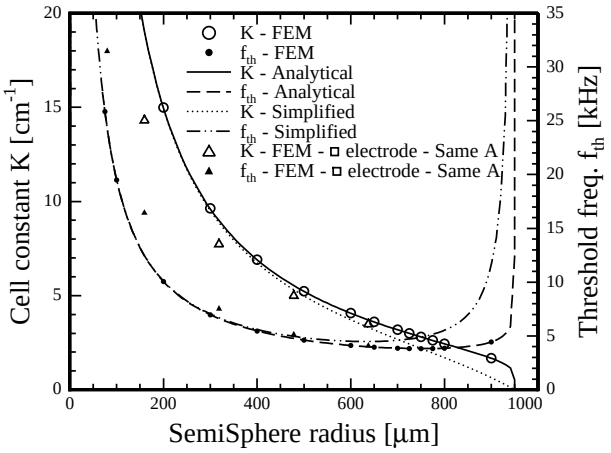

Figure 2.8: FEM verification. The cell constant, K and corresponding threshold frequency, f_{th} for the hemisphere electrodes and for square planar electrodes with the same area. All have same outer distance of 3.8 mm limited by the chip size. The hemisphere FEM results are in good agreement with the analytical solution (Equation 2.9). The simplified approximate solution is only good for electrode radius much smaller than the spacing (Equation 2.8). Medium sized square planar electrodes can be well represented by sphere electrodes of equivalent surface area.

2.1.3.2 FEM analysis

In cases where the electrodes have odd shapes or dimensions that are not easily approximated by simple analytical expressions, a numerical simulation is useful. The cell constants are found numerically using the Finite Element Method (FEM) in the commercial software COMSOL [15]. Generally the potential distribution Φ is found in a cell by solving Laplace's equation

$$\nabla^2 \Phi = 0 \tag{2.14}$$

when applying a current I_a through the outer electrodes while measuring the potential drop V_m on the outer (two electrode configuration) or inner electrodes (four electrode configuration). For unit resistivity the cell constant is equal to the inverse impedance or the inverse transimpedance respectively, e.g.

$$K = Z_T = \frac{V_m}{I_a} \tag{2.15}$$

By means of symmetry the cell is reduced into a half cell, as illustrated in Figure 2.9. The solution to the two electrode configuration problem is easily found by applying a voltage to the electrode and finding the resulting current by integrating the current density across the electrode interface. For the four electrode configuration the solution is found in three steps.
First, the potential distribution Φ_1 is found for a cell with a voltage V_a applied to the outer electrode ($2V_a$ in a full cell) and 0 V applied to the inner electrode. The currents $I_{in,1}$ and $I_{out,1}$ are found for the inner and outer electrode by integrating the current density at the interface of the electrodes. Similarly Φ_2, $I_{in,2}$ and $I_{out,2}$ are found for a case where the electrode voltages are interchanged. Last, the real solution is found as a linear combination $\Phi = \alpha\Phi_1 + \beta\Phi_2$ which also fulfills Laplace's equation. In order to meet the conditions of V_a on the outer electrode and zero current at the inner electrodes it is clear that $\alpha = 1$ and $\beta = -\alpha I_{in,1}/I_{in,2} = -I_{in,1}/I_{in,2}$. Thus the potential measured at the inner electrode is

$$V_m = -2V_a \frac{I_{in,1}}{I_{in,2}} \tag{2.16}$$

and the current flowing in the outer electrode

$$I_a = I_{out,1} - I_{out,2} \frac{I_{in,1}}{I_{in,2}} \tag{2.17}$$

which gives a cell constant of

$$K = \frac{V_m}{I_a} = \frac{-2V_a}{I_{out,1}\frac{I_{in,2}}{I_{in,1}} - I_{out,2}} \tag{2.18}$$

The FEM model is verified by comparing the analytical determined cell constant for the hemispherical electrodes with the FEM calculated cell constant (Figure 2.8). The hemisphere FEM results are in very good agreement with the analytical solution. The approximate solution is only good for electrode radius much smaller than the spacing. The analysis also show that moderately sized square planar electrodes can be described with an accuracy within 15% by using results from hemispherical electrodes of the same surface area.

Figure 2.10 shows the FEM simulated $K \times A$ product of rectangular planar electrodes as a function of the electrode width and length. In conclusion, the electrodes should occupy all available space on a chip of limited size in order to lower the cutoff frequency. However, too closely spaced electrodes results in an increase in cutoff frequency due to very low cell constants.

For the four electrode setup, all the above considerations are also valid, and the voltage electrode should be placed as close to the current electrodes as possible. In the upper limit, the four electrode cell constant is equal to the two electrode cell constant. The size of the voltage electrodes is not important unless the contact impedance becomes comparable to the inner impedance of the measurement equipment as discussed in Section 2.1.

2.1.4 Conductivity sensor summary

The cell constant is central for the determination of electrical conductivity with an electrochemical cell. However, for miniaturized systems on a silicon substrate the operating frequencies have to be considered carefully. On the sensor chip of limitied size the electrodes are made as large as possible with as high a separation as possible. This yields the lowest lower-limit cutoff frequency. The upper-limit cutoff frequency is increased by minimizing the area of the wiring system and increasing the thikcness of the insulators effectively decreasing the parasitic capacitance.

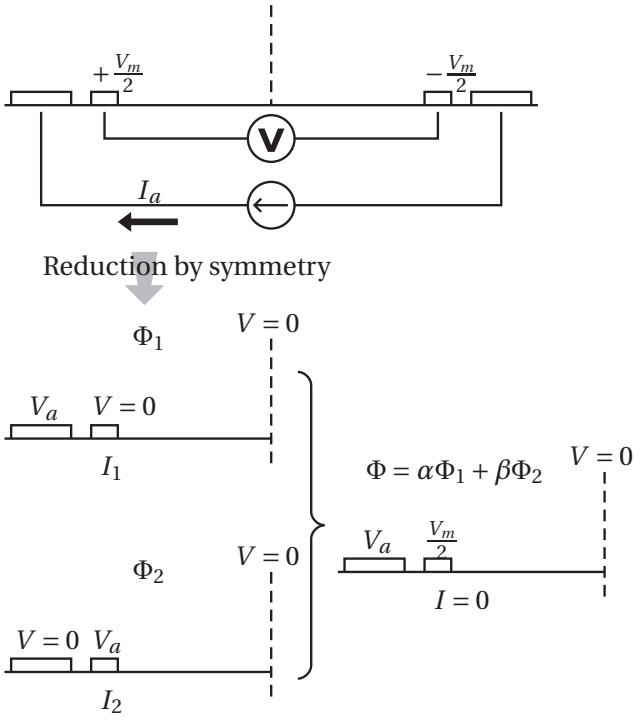

Figure 2.9: Determination of cell transimpedance using FEM. The electrostatic solution is found in two cases; V_a on the outer electrode and $V = 0$ on the inner and then the potentials interchanged. A linear combination of the solutions are found, which fulfills V_a at the outer electrode and $I = 0$ at the inner. The corresponding current in the cell is found by integrating the current density.

2.2 Temperature sensors

Micro fabricated temperature sensors can be implemented in different ways. Most commonly seen are electrical sensors such as noise thermometry, thermodiodes, thermocouples and thermistors. Other sensing principles such as expansion sensors, surface acoustic waves detection sensors and optical sensors can also be applied, but are unsuited for DST applications because of their high demands for data processing and/or power delivery. The same is the case for noise thermometry. Thermocouples suffer from only measuring relative temperatures and can not easily be integrated into a microfabricated design. Remaining are the thermodiodes and thermistors. Both can offer high accuracy, absolute temperature reading and effortless integration.

Thermodiodes and thermal transistors are often used in electronics as the components are readily available. However thermistors have a higher tolerance for changes in fabrication conditions and sets very low demands on interfacing electronics. The performance of a thermodiode varies significantly if traps are introduced etc. As shown in Chapter 7.5.2.1 light is also a significant problem. Implementing thermistor in a metallic or metal silicide material diminishes the problem of carrier generation. Changing material is not an option for thermodiodes. For the above reasons thermistors are used to measure temperature. Another concern is power consumption. As calculations in Chapter 6 shows, a thermistor of reasonable resistance value can be used without significantly affecting the power budget of the complete DST.

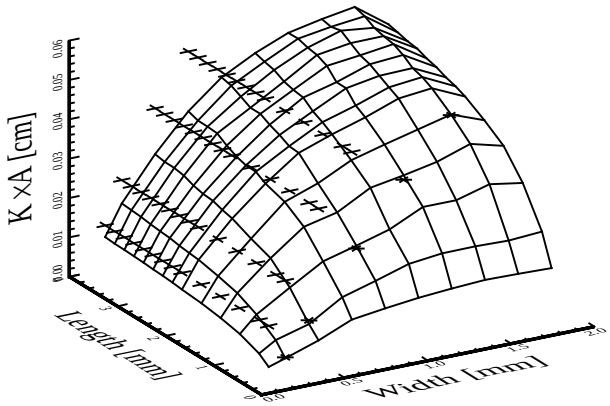

Figure 2.10: $K \times A$ as a function of electrode width and length for and outer electrode spacing of 3.8mm. High $K \times A$ results in low cutoff frequency. The full mesh is FEM results, and the discrete points are the analytical solutions for the hemisphere (Equation 2.9 = $\star$) and semi-infinite conductor (Equation 2.12 = ×) cases for the same electrode area. The mesh color indicates $K \times A$-axis value. Clearly the hemisphere solution fits very well whereas the semiinfinite conductor approximation only gives accurate results for electrodes that are very long and thin compared to their spacing.

2.2.1 Thermistors

The electrical conductivity of all materials is affected by temperature. This is due to changes in ionization and changes in electron scattering mechanisms. For most cases changes in geometry are insignificant. Depending on the type of material the different effects have more or less influence.

2.2.1.1 Doped silicon

The change of conductivity with temperature in a semiconductor is mainly due to changes in ionization and changes in carrier mobility. The Temperature Coefficient of Resistance (TCR), α_R can be expressed as

$$\alpha_R = \frac{1}{\varrho}\frac{\partial \varrho}{\partial T} \tag{2.19}$$

where T is the temperature and ϱ is the resistivity which can be expressed as

$$\varrho = \frac{1}{e(\mu_n n + \mu_p p)} \tag{2.20}$$

where e is the elementary charge and μ_n and μ_p are the carrier mobilities and n and p are the electron and hole concentrations, respectively. The temperature dependence of the intrinsic carrier concentration n_i is known from basic semiconductor theory [16] to be

$$n_i = n_{i,300}\left(\frac{T}{300}\right)^{\frac{3}{2}} \exp\left(\frac{300}{T} - 1\right) \tag{2.21}$$

where $n_{i,300}$ is the intrinsic carrier concentration at 300°C. However, the silicon is doped to a concentration N that is orders of magnitude higher than the intrinsic carrier concentration. Around

room temperature (-50°C - 50°C) the dopants are completely ionized, and the intrinsic concentration is negligible, making the carrier concentration equal to the doping level (independent of temperature). The change in resistance due to change in temperature is thus only coupled to changes in mobility in this temperature range.
Intensive investigation of carrier mobilities has lead to mathematical models describing the mobility as a function of temperature and impurity concentration.
The Klaassen model is build on the simpler Masetti model, which does not account for temperature dependence or second order effects such as electron-hole scattering or ultra-high concentration effects. The simple version of the Klaassen model with temperature dependence is suitable and sufficiently accurate for the purposes of this project. The Masetti expression for the majority carrier mobility μ is

$$\mu = \mu_{min} + \frac{\mu_{max} - \mu_{min}}{1 + (N/N_{ref,1})^{\alpha_1}} - \frac{\mu_1}{1 + (N_{ref,2}/N)^{\alpha_2}} \tag{2.22}$$

The coefficients in equation (2.19) are listed in Table (2.1). The third term is negligible for doping levels below 10^{20}cm^{-3} and will not be discussed further. For low concentrations the mobility goes to

$$\lim_{N \to 0} \mu = \mu_{max} \tag{2.23}$$

which equals the lattice scattering mobility μ_L. By subtracting (2.23) from (2.22) using Matthiesent's rule, the majority impurity scattering remains.

$$\begin{aligned} \frac{1}{\mu} - \frac{1}{\mu_L} &= \frac{1}{\mu_I(N)} \Rightarrow \\ \mu_I(N) &= \mu_N \left(\frac{N_{ref,1}}{N} \right)^{\alpha_1} + \mu_c \end{aligned} \tag{2.24}$$

where

$$\mu_N = \frac{\mu_{max}^2}{\mu_{max} - \mu_{min}} \tag{2.25}$$

and

$$\mu_c = \frac{\mu_{max}\mu_{min}}{\mu_{max} - \mu_{min}} \tag{2.26}$$

The lattice scattering mobility scales with temperature as

$$\mu_L(T) = \mu_{max} \left(\frac{300}{T} \right)^{\theta_i} \tag{2.27}$$

where θ_i is a constant depending on whether the carriers are electrons ($\theta_e = 2.285$) or holes ($\theta_h = 2.247$). The remaining two constants in (2.24) scale with temperature as

$$\mu_N = \frac{\mu_{max}^2}{\mu_{max} - \mu_{min}} \left(\frac{T}{300} \right)^{3\alpha_1 - 1.5} \tag{2.28}$$

and

$$\mu_c = \frac{\mu_{max}\mu_{min}}{\mu_{max} - \mu_{min}} \left(\frac{300}{T} \right)^{0.5} \tag{2.29}$$

Using the models for μ, α_R can be calculated from Equation 2.22. The result is quite complex and the results are plotted in Figure 2.11. It appears from the results that it is possible to make resistors with high and low temperature sensitivity just by changing the doping level. The results also verify

Parameter	As	P	B
$\mu_{max}(cm^2V^{-1}s^{-1})$	1417.0	1414.0	470.5
$\mu_{min}(cm^2V^{-1}s^{-1})$	52.2	68.5	44.9
$\mu_1(cm^2V^{-1}s^{-1})$	43.4	56.1	29.0
$N_{ref,1}(cm^{-3})$	9.68×10^{16}	9.20×10^{16}	2.23×10^{17}
$N_{ref,2}(cm^{-3})$	3.43×10^{20}	3.41×10^{20}	6.10×10^{20}
α_1	0.68	0.711	0.719
α_2	2.0	1.98	2.0

Table 2.1: Constants in the *Klaassen* model.

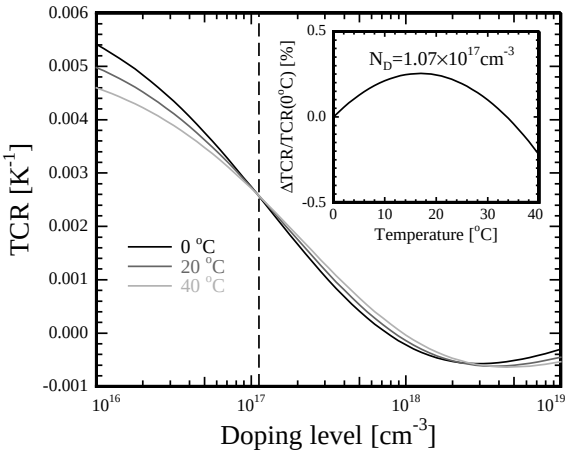

Figure 2.11: Theoretical temperature coefficient of resistance (TCR) of boron doped monocrystalline silicon. The model is in good agreement with literature values [17]. At $N = 1.07\times10^{17}\text{cm}^{-3}$ (dashed line) the TCR is almost constant over the measurement temperature interval. Insert shows the relative change in TCR at $N = 1.07\times10^{17}\text{cm}^{-3}$ as a function of temperature.

that the TCR changes with temperature. Similarly, a high degree of linearity between ρ and T can be obtained by seeking a doping concentration where

$$\frac{\partial^2\rho}{\partial T^2}\rightarrow 0 \tag{2.30}$$

for all values of T in the measurement interval.
The TCR of p-type single crystalline silicon as function of doping concentrations at 0°C, 20°C and 40°C is shown in Figure 2.11. Evidently the TCR depends strongly on the doping level. At $N = 1.07\times10^{17}\text{cm}^{-3}$ the TCR is almost constant over the measurement temperature interval. In this case the temperature can simply be found from measured resistance values through the exponential expression

$$R(T) = R_0\exp[\alpha_R(T-T_0)] \tag{2.31}$$

A higher degree of linearity can be achieved by choosing a doping level which gives a TCR that decreases with temperature. The best relative linearity is found for doping levels above of N=5×10^{18} cm^{-3} for the -2°C to 20°C interval. However, for these doping levels, the temperature dependence of the resistance is very weak.

For polycrystaline silicon much higher TCR's can be achieved. However, the sensor performance is very vulnerable to variations during fabrication. Changes in the polycrystaline film quality such as variations in grain size and oxygen contamination strongly affect the behaviour.

2.2.1.2 Metals and metal silicides

In order to eliminate the influence from light, the semiconducting silicon can be substituted with metallic or metal silicide materials. In thermistors, platinum is most often used, but many metals are good candidates too. The Bloch-Gruneissen formulation can be used to describe the resistivity of metals.

$$\varrho(T) = \varrho_0 + A\left(\frac{T}{T_D}\right)^n \int_0^{T_D/T} \frac{t^n}{(e^t-1)(1-e^{-t})} dt \tag{2.32}$$

where T_D is the Debye temperature and n is an integer depending on the type of scattering mechanism:

1. n = 5 implies that the resistance is due to scattering of electrons by phonons (as it is for simple metals)
2. n = 3 implies that the resistance is due to s-d electron scattering (as is the case for transition metals as Ta)
3. n = 2 implies that the resistance is due to electron-electron interaction.

For low temperatures, T_D/T becomes large and the integral converges to a constant value. This means that in the low temperature limit the resistivity scale with T^n.
Looking at the integrand small values of t, the series expansion gives us

$$\frac{t^n}{(e^t-1)(1-e^{-t})} = \frac{1}{t^2}t^n + \frac{1}{12}t^n + O(t^n) \tag{2.33}$$

which gives the approximate evaluation of the integral

$$\int \frac{t^n}{(e^t-1)(1-e^{-t})} dt = \int t^{n-2} = \frac{t^{n-1}}{n-1} \tag{2.34}$$

In the high temperature limit, i.e. where T is comparable to or larger than T_D, the resistivity can then be expressed as

$$\varrho(T) \approx \varrho_0 + A\left(\frac{T}{T_D}\right)^n \left[\frac{t^{n-1}}{n-1}\right]_0^{T_D/T} \tag{2.35}$$

$$= \varrho_0 + A\left(\frac{T}{T_D}\right)^n \frac{1}{n-1}\left(\frac{T_D}{T}\right)^{n-1} \tag{2.36}$$

$$= \varrho_0 + \frac{A}{n-1}\frac{T}{T_D} \tag{2.37}$$

Thus a linear relation between ϱ and T is obtained regardless of the value of n.

A high degree of linearity and low sensitivity to light is a high motivation for realizing the temperature sensor using metals or metal silicides. As later shown, metal thermistors are incompatible with the fabrication process of the multi-sensor. The thermistors are therefore implemented by using a metal silicide (a metal - silicon compound, see Section 3.2). The temperature behaviour of metal silicides is not well documented, but as the general electrical behaviour is metallic, the temperature dependence is also expected to be so. The reported TCR for $TiSi_2$ is $\alpha_R = 4.3 \times 10^{-3}$ K^{-1} [18], which is somewhat higher than that of platinum $\alpha_R = 3.9 \times 10^{-3}$ K^{-1}.

2.2.1.3 Noise

The theoretical detection limit or resolution of the temperature sensor is set by noise. The Johnson noise or thermal noise can be expressed as

$$v_{noise} = \sqrt{4k_B T R \Delta f} \tag{2.38}$$

where Δf is the bandwidth, k_B is the Boltzmann constant, T is the temperature and R is the resistance. For a DC measurement ($f < 100$ Hz) at room temperature on a 10 kHz resistor the noise is 0.13 μV which corresponds to a temperature change of 10 μK. Obviously, Johnson noise in the resistor is not a problem in order to obtain 0.01°C resolution.

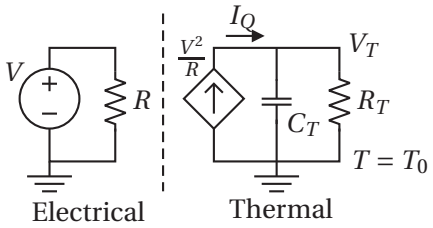

Figure 2.12: A simple lumped element equivalent model of the heating of an electrical resistor. The electrical circuit (left) dissipates a power V^2/R which in the thermal domain (right) is represented with the heat current I_Q. The heat capacity of the resistor is represented by the capacitor C_T, and heat is transported from the resistor to an ideal thermal reservoir (ground) through the thermal resistance R_T. The thermal voltage V_T exhibits an exponential decay with time towards the steady state temperature $I_Q R_T$.

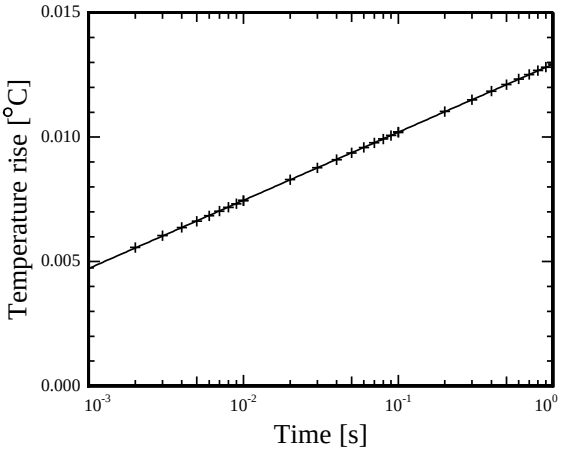

Figure 2.13: The temperature rise due to self-heating as a function of time of a 3 cm long, 10 μm wide and 110 nm thick $TiSi_2$ wire. The simulation results are worst case maximum heating where the surrounding water is completely stagnant and all heat transport is due to diffusion.

2.2.1.4 Self-heating

In normal operation the dissipated power in the resistor gives rise to an offset error, the so-called self-heating. The power makes the temperature of the resistor rise and then the heat is transported

from the resistor through thermal diffusion. The process is described by the heat-flow equation. The general heat-flow equation for a homogeneous region where the heat capacity and thermal conductivity are constant is found from the continuity equation and the linear flux equation in the temperature domain. The heat-flow equation is expressed as

$$\frac{\partial T(\mathbf{r},t)}{\partial t} - \frac{\kappa}{C}\nabla^2 T(\mathbf{r},t) = \frac{1}{C}P'(\mathbf{r},t) \tag{2.39}$$

where T is the temperature, $\mathbf{r}$ is the spatial position, t is the time, C is the heat capacity per unit volume, κ is the thermal conductivity and P' is the heat generation rate per unit volume. The equation can be solved using numerical methods or approximated using lumped-element equivalent models.

A simple lumped-element equivalent model is shown in Figure 2.12. The temperature in the resistor is seen as uniform and the heat-flux is linearly dependant on the temperature corresponding to a condition of steady state diffusion to an ideal thermal reservoir. The transient solution for such a model is easily found. Using the formalism from electrical circuits the heat current can be expressed as

$$I_Q = \frac{V_T}{R_T} + C_T\frac{dV_T}{dT} \Leftrightarrow \tag{2.40}$$

$$\frac{dV_T}{dT} = \frac{I_Q}{C_T} - \frac{1}{R_T C_T}V_T \tag{2.41}$$

which is an ordinary first order differential equation. Giving the boundary conditions

$$V_T(t=0) = 0 \tag{2.42}$$

$$\frac{dV_T}{dt} = 0 \text{ for } t \to \infty \tag{2.43}$$

the thermal voltage can be found as

$$V_T = I_Q R_T\left(1 - \exp\left(\frac{-t}{R_T C_T}\right)\right) \tag{2.44}$$

for $t \geq 0$. Clearly the self-heating is time dependent. Thus shortening the actual duration of the measurements lowers the effect of self-heating. The results are of course dependent on the boundary conditions and for complex geometries a good approximate value of R_T is not easily found.

A more accurate description can be made using finite element simulations. The heat-flow equation is solved using COMSOL where the power is dissipated in a small crossectional resistor element connected to a large half-plane heat conducting media of a size that emulates an semi-infinite media for short transient times. This means that $T \to 0$ for large distances from the resistor. The structure also includes the thin film layers and a substrate. The 2D simplification is feasible since the length to width ratio is very high.

The simulated temperature rise due to self-heating as a function of time of a 3 cm long, 10 μm wide and 110 nm thick $TiSi_2$ wire is shown in Figure 2.13. The simulation is carried out using the values listed in Table 2.2 and the properties of $TiSi_2$ is calculated as a 1:2 ratio of the properties of titanium and silicon. The simulation results are worst case maximum heating where the surrounding water is completely stagnant and all heat transport is due to diffusion. Conversely, if the water is moving fast the water acts as an almost ideal reservoir giving a much larger heat transport from the surface. In the diffusion case, the measurement time should be faster than 100 ms in order to achieve an accuracy better than 0.01°C. Alternatively the constant voltage driven resistor should be made longer in order to reduce the power dissipation per unit length.

Material	κ W/(m K)	C_p J/(kg K)	C_v 10^6 J/(m^3 K)	ϱ kg/m^3
Silicon	124.0	702	1.63	2328
Silicon nitride	30.1	710	2.26	3184
Silicon dioxide	1.4	1000	2.10	2100
Pyrex	1.1	750	1.67	2230
Water	0.6	4180	4.18	1000

Table 2.2: Table of thermal properties of different materials.

2.2.2 Temperature sensor summary

Both doped semiconductors and metallic resistors can be used as thermistors. The lower sensitivity to light and high level of linearity makes metallic resistors the material of choice. When considering thermal noise and self-heating of $TiSi_2$, a 0.01°C accuracy can be achieved by making 3 cm long, 10 μm wide resistors and limiting the measurement time to 100 ms.

2.3 Pressure sensors

Most pressure sensors rely on detecting the mechanical deformation of a body when it is exposed to a pressure. Piezoresistive, capacitive, inductive, piezoelectric and optical effects can be used, but in microtechnology piezoresistive and capacitive sensors are dominating in commercial sensors. This is mainly due to their compatibility with microfabrication technologies and their high accuracy. Capacitive sensors can also be fabricated by post-processing on top of CMOS technology. Micromechanical pressure sensors are successfully fabricated commercially and the Grundfos pressure sensor fabrication process, which inspired the first version of Fish & Chips, promises very accurate pressure sensors. These pressure sensors rely on bending of a membrane due to a pressure difference from one side of the membrane to the other. The bending causes stress to resistors build into the membrane which due to the piezoresistive effect changes resistance value as a function of stress. The strengths of this technique are the simplicity of the fabrication and the measurement principle. The weakness is the power consumption which normally is higher for resistive sensors than for capacitive sensors.
Piezoresistive pressure sensors are chosen since their reliable fabrication process serves as a platform for the remaining sensors. In future versions of a multi-sensor chip the capacitive pressure sensor could be an attractive alternative. This is commented in Section 3.0.1.

2.3.1 Stress in silicon

In anisotropic materials, such as silicon, the resistivity cannot in general be considered a scalar [19]. The electric field vector, $\boldsymbol{E} = (E_x, E_y, E_z)$, and the current density vector, $\boldsymbol{J} = (J_x, J_y, J_z)$, are coupled through the resistivity tensor, $\underline{\varrho}$ as

$$\boldsymbol{E} = \underline{\varrho}\boldsymbol{J} \tag{2.45}$$

where the i'th element of the vector $\boldsymbol{E}$ can, using the Einstein summation convention, be written as

$$E_i = \sum_{j=1}^{3} \varrho_{ij} J_j \equiv \varrho_{ij} J_j \tag{2.46}$$

In stress free silicon, the off diagonal components of the resistivity tensor, ϱ_{ij}, are equal to zero, and the diagonal elements, ϱ_{ii}, are all equal to the average resistivity $\bar{\varrho}$ i.e.

$$\bar{\varrho} = \varrho_{11} = \varrho_{22} = \varrho_{33} \tag{2.47}$$

This means that the individual directional elements of the field vector are dependent only on the same directional element in the current density vector, e.g. $E_x = \varrho_{xx} J_x$. This makes the silicon behave isotropically when it is not stressed.
For a stressed material, the resistivity changes as a function of stress, which can be expressed with a series of stress components of increasing order. For small stress values, only the first order linear stress is of importance and it can be written as

$$\varrho_{ij} = \varrho^0_{ij} + \bar{\varrho}\pi_{ijkl}\sigma_{kl} \Rightarrow \frac{\Delta\varrho_{ij}}{\bar{\varrho}} = \pi_{ijkl}\sigma_{kl} \tag{2.48}$$

where π_{ijkl} are the piezo resistive coefficients in the fourth rank piezo tensor. In a similar way the stress matrix is coupled to the strain matrix through the fourth rank stiffness tensor as

$$\sigma_{ij} = c_{ijkl}\epsilon_{kl} \tag{2.49}$$

		[10^{-11}Pa^{-1}]		
		π_{11}	π_{12}	π_{44}
n-type	(11.7 Ωcm)	-102.2	+53.4	-13.6
p-type	(7.8 Ωcm)	+6.6	-1.1	+138.1

Table 2.3: The three independent piezo resistive coefficients π_{11}, π_{12} and π_{44} in n-type and p-type silicon at 300K [21][22].

Silicon is a cubic crystal with diamond structure. Due to symmetry in the crystal structure, the symmetry related piezo and stiffness tensors simplify and only three independent piezo resistive coefficients as well as three independent stiffness coefficients remain in the tensors. The independent coefficients of equations 2.48 and 2.49 are in six-vector notation written as π_{11}, π_{12} and π_{44}, and c_{11}, c_{12} and c_{44}, respectively [20]. The piezo resistive coefficients for 300K and low doping are listed in Table 2.3. The piezo coefficients depend on doping level and temperature and should be corrected in accordance with Figure 2.14 [21][22].
In the specific case where a silicon crystal experiences a uniaxial stress σ directed along the <110> crystal direction on a (100) substrate, the description simplifies further. The relative change in resistance of a resistor with current flowing in the same direction as the stress reduce to

$$\frac{\Delta R}{R} = \frac{\Delta \rho}{\rho} = \frac{\sigma}{2}(\pi_{11} + \pi_{12} + \pi_{44}) = \sigma \pi_l \tag{2.50}$$

For a resistor with current flowing perpendicular to the stress direction the relative resistance change reduces to

$$\frac{\Delta R}{R} = \frac{\Delta \rho}{\rho} = \frac{\sigma}{2}(\pi_{11} + \pi_{12} - \pi_{44}) = \sigma \pi_t \tag{2.51}$$

where π_l and π_t are named the longitudinal and transversal piezo resistive coefficients. From Table 2.3 it is clear that π_{11} and π_{12} are very small compared to π_{44} in p-type silicon. This means that π_l an π_t have almost the same value but with opposite sign.

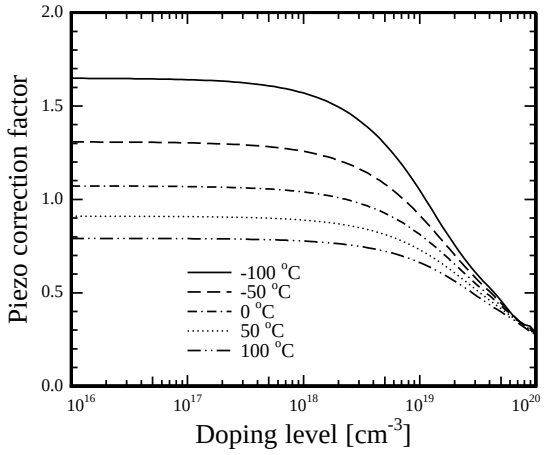

Figure 2.14: Piezo correction factor. The piezo resistive coefficients change with temperature and impurity concentration. The plot is made from standard fits to empirical data [21].

2.3.2 Stressed membranes as pressure sensors

Numerical and analytical examination of stress in membranes show that the maximum stress in square membranes is found in the middle of the side edge. For small deflections the maximum stress is related to the pressure p as

$$\sigma_{max} = 0.294\left(\frac{l}{t}\right)^2 p \tag{2.52}$$

where l and t is the side length and thickness of the membrane [23]. Although the stress in the resistor area is not homogeneous and uniaxial, the average uniaxial stress of σ_{max} is a good approximation, if the resistor is small compared to the side length of the membrane.

Piezoresistors are placed in the maximum stress sites as shown in Figure 2.15. As a result resistors with current flowing in the primary stress direction experience an increase in resistance whereas resistors with current flowing perpendicular to the primary stress direction experience a decrease in resistance of the same magnitude, as predicted in Equations 2.50 and 2.51. This is exploited by placing resistors in a Wheatstone bridge. The output from a Wheatstone bridge for small changes in resistance can be expressed as

$$V_{out} = \frac{V_{in}}{2}\frac{\Delta R_2 - \Delta R_1}{R} \tag{2.53}$$

The output voltage as a function of the maximum stress is found by combining Equation 2.50, 2.51 and 2.53 to get

$$V_{out} = \frac{V_{in}}{2}\left(\frac{\Delta R_l}{R} - \frac{\Delta R_t}{R}\right) = \frac{V_{in} P \sigma_{max}}{2}(\pi_l - \pi_t) \tag{2.54}$$

$$\approx (17.7 \times 10^{-11}\ \mathrm{Pa}^{-1}) V_{in}\left(\frac{l}{t}\right)^2 p \tag{2.55}$$

where the piezo coefficients are corrected with the piezo correction factor P of 0.87 for a doping level of 5.2×10^{18} cm^{-3}. Besides having a simple voltage output, the Wheatstone bridge has the advantage of being very tolerant to changes in temperature if the resistors are doped to the same level. A small temperature related increase in resistance in all the resistors is balanced out. More details on temperature dependence in resistors are given in Section 2.2.

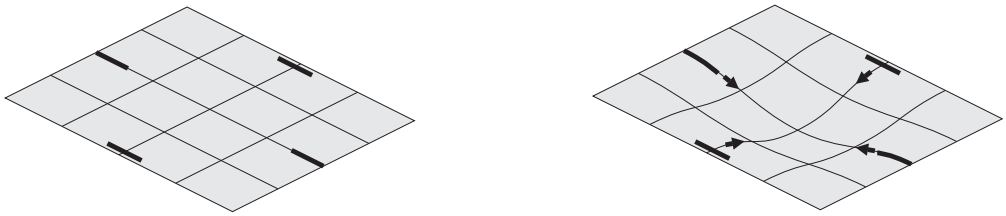

Figure 2.15: Pressure sensor membrane. Resistors are placed on the middle of the membrane sides where the stress is highest. Two resistors are placed in the primary stress direction and two are placed perpendicular to the primary stress direction to give positive and negative resistance response. (*left*) No pressure, membrane is not flexing. (*right*) Pressure, membrane is flexing. Black arrows indicate the primary stress direction.

2.3.2.1 Sensor dimensioning

From Equation 2.54 it is clear that a high l/t ratio gives high signals. The upper limit for l/t is set by the maximum allowed stress in the membrane. Although the tensile strength of silicon is 7 GPa, a safe limit often used is 500 MPa. By rearranging Equation 2.52 the maximum l/t is found to be

$$\frac{l}{t} < \sqrt{\frac{500 \text{ MPa}}{0.294 \cdot 2 \text{ MPa}}} = 29.2 \tag{2.56}$$

This gives a sensitivity S of

$$S = \frac{V_{out}}{V_{in} p} = (17.7 \times 10^{-11} \text{ Pa}^{-1})(29.2)^2 = 1.5 \times 10^{-7} \text{ Pa}^{-1} \tag{2.57}$$

The thermal noise in the pressure sensor piezoresistors is calculated from Equation 2.38. For a 30 kΩ resistor with a 10 kHz bandwidth the thermal noise is 2.2 μV. This gives a theoretical resolution of

$$p = \frac{2.2 \ \mu\text{V}}{3 \text{ V} \cdot 1.5 \times 10^{-7} \text{ Pa}^{-1}} \approx 5 \text{ Pa} = 0.05 \text{ mbar} \tag{2.58}$$

which corresponds to a water depth change of 0.5 mm. However, the sensor is temperature dependent. Temperature dependence of the resistors are canceled out in the Wheatstone bridge and temperature compensation of the piezo resistive coefficients can be done with the precision of the temperature measurement, i.e. approximately 0.01°C. This gives an uncertainty in the piezo correction factor and thus on the sensitivity of 0.0026%. This gives an accuracy of the pressure measurement of 0.5 mbar at 20 bar. The uncertainty of the resistor values assuming that half the Wheatstone bridge changes and the other does not of approximately 1 mbar corresponding to 1 cm. In practice, piezoresistive pressure sensors offer an accuracy of 0.1% of the full operating scale which gives a 20 cm accuracy of a 20 bar sensor (which is on the scale of the height of a fish). The above accuracies are post-calibration accuracies as variations in fabrication process parameters and misalignment of masks will result in variations in offset and sensitivity.

2.3.3 Pressure sensor summary

A piezoresistive pressure sensor is chosen, and the Wheatstone arrangement of resistors gives a voltage signal output that is proportional to the pressure. In order to get a high signal to noise ratio the membrane sidelength to thickness ratio is increased to the limit of safe operation without membrane fracture.

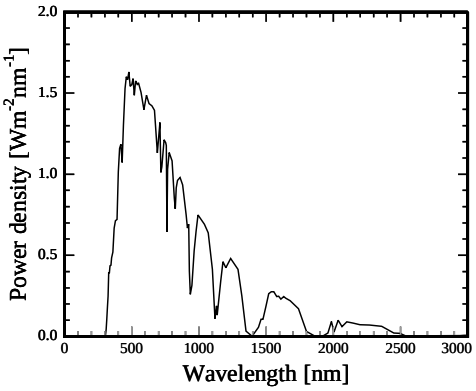

Figure 2.16: Solar power density as a function of wavelength for a AM1.5g standard sun. (AM1.5g = average sun passing through 1.5 times the atmosphere of a sun in zenith on a clear day.)

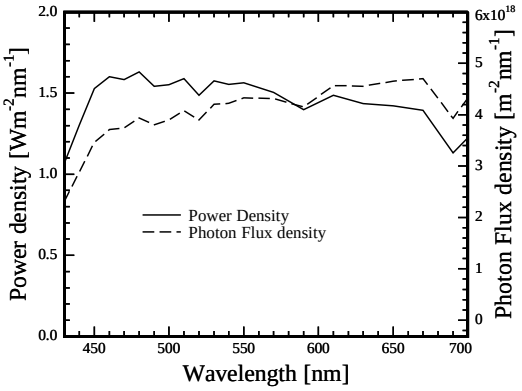

Figure 2.17: Solar power density and photon density in the visible part of the light spectrum. The power is almost uniformly distributed from 450 nm to 700 nm. The spectral distribution changes when the light goes through water.

2.4 Light sensors

The light sensor consist of a pn-junction made from ion-implantation of boron into a 10^{15} cm^{-3} phosphorous doped silicon substrate. The result is a single sided pn-junction with p-type peak concentration of 10^{18} cm^{-3} and a junction depth of 500 nm. The light sensor is not optimized since the fabrication process parameters are fixed by other sensors. However, this section describes the processes that influence the signal obtained with the sensor in the ocean, and the expected performance is evaluated.

2.4.1 Sun light

The sun irradiates a large amount of energy, whereof a fraction hits Earth. Depending on the geographical location, the time, time of year and local air composition, the light intensity varies. If the sun is close to the horizon, the rays have to pass through a larger mass of air, than if the rays came from directly above. On midday in Denmark, the sun passes through 1.2 times (summer) to 5.2 times (winter) the amount of air, it would pass if the sun was in zenith. In the following the standard sun radiation spectra for sun passing through 1.5 clear atmosphere (AM1.5g) is used. The full spectrum is depicted in Figure 2.16 and the visible part in Figure 2.17. Furthermore, the surface suffers a reduction in incoming photons due to the inclination angle. On average this will correspond to a 44% reduction in photons at 56°C northern latitude.

The total solar-radiation power P can be expressed as

$$P = \int_0^\infty p(\lambda)\, d\lambda \tag{2.59}$$

where p is power density as a function of wavelength (Figure 2.16 and 2.17). From the power density distribution p the photon flux density ϕ can be calculated as

$$\phi(\lambda) = \frac{p(\lambda)}{E_{ph}(\lambda)} = \frac{p(\lambda)\lambda}{hc} \tag{2.60}$$

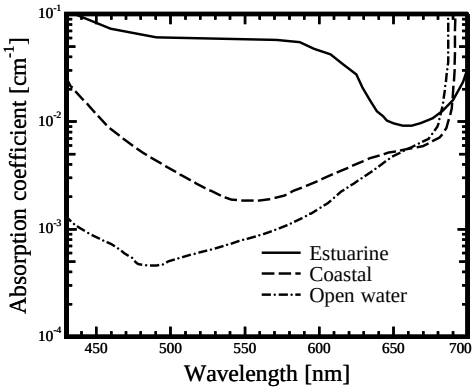

Figure 2.18: Absorption coefficient of light in seawater. Ultraviolet and infrared light is absorbed rapidly below the surface whereas blue light is transmitted into large depths.

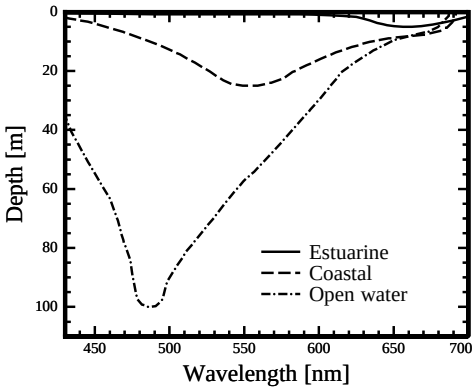

Figure 2.19: Transmitted light in seawater. The graph shows at which depth 1% of incoming photons remain. Ultraviolet and infrared light is absorbed below the surface whereas blue light is transmitted into large depths.

where E_{ph} is the photon energy, h is Planck's constant and c is the speed of light. $\phi(\lambda)$ is shown in Figure 2.17.
Example ($\lambda = 500$ nm):

$$\phi(500\text{ nm}) = \frac{1.55\text{ Wm}^{-1}\text{nm}^{-1} \times 500\text{ nm}}{6.625 \cdot 10^{-34}\text{ Js} \times 3 \cdot 10^{8}\text{ ms}^{-1}} = 3.9 \cdot 10^{18}\text{ m}^{-2}\text{s}^{-1}\text{nm}^{-1} \tag{2.61}$$

meaning that $3.9 \cdot 10^{18}$ photons with a wavelength of 500 ± 0.5 nm hit a surface of 1 m^2 per second.

When the sunlight hits the ocean surface, approx 50% of the photons are reflected depending on the inclination angle and the surface roughness. The seawater then absorbs photons as the light passes through and photon flux density decreases exponentially with depth. The absorption coefficient for photons in seawater α_w as a function of wavelength is shown in Figure 2.18. Ultraviolet and infra-red light is absorbed very quickly at the surface, and not surprisingly the blue light is transmitted very well. As shown in Figure 2.19, 1% of the photons with wavelengths around 490 nm still remain even at 100 m depth. The remaining photon flux density ϕ at depth d is given by the Lambert-Beer's absorption law [24],

$$\phi(\lambda, d) = \phi(\lambda, 0) \cdot \exp(-\alpha_w(\lambda) \cdot d) \tag{2.62}$$

When the remaining photons hit the photo-sensor surface some photons are reflected. The transmitted photons are then absorbed in the silicon substrate, either by exiting electrons and creating electron-hole pairs or by other crystal related processes which do not create carriers.

The quantum efficiency expresses the fraction of photons that generate a carrier which contributes to current generation. The quantum efficiency is normally divided into the internal quantum efficiency (IQE) and the external quantum efficiency (EQE). The IQE covers the efficiency when photons have entered the actual sensor area, i.e. the silicon substrate in this case. The EQE also includes the losses arising from packaging and the absorption/reflection related to surface films. Commercial photodiodes have EQEs of above 90% in the visible domain.

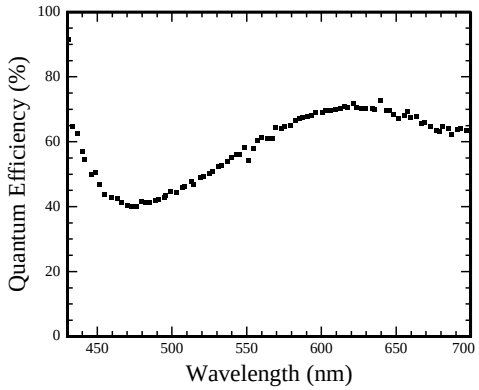

Figure 2.20: Measured external quantum efficiency of a silicon pn-junction photo-diode. The quantum efficiency is limited by poor transmission trough the protective films and recombination processes in the substrate.

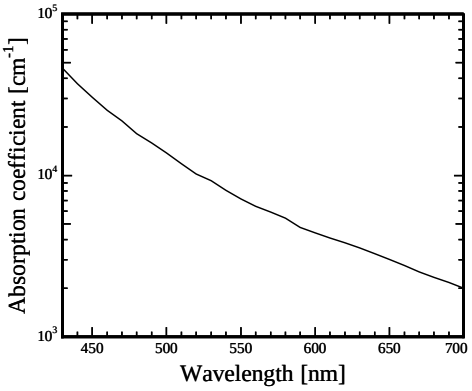

Figure 2.21: Absorption coefficient for photons in silicon. The fast increase in absorption from 400nm to 360nm is caused by the presence of a direct bandgap transition that begins excitation at these energies.

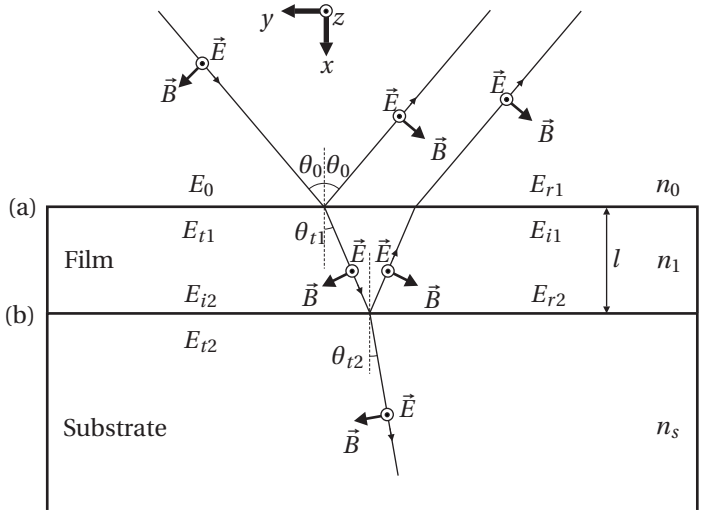

Figure 2.22: Optical reflectance from a thin film coating. A substrate with refractive index n_s covered with a thin film of thickness l with refractive index n_1. Light is incident from a media with refractive index n_0. The formalism used for deriving the optical properties is shown on the figure, where $\vec{E}$ and $\vec{B}$ is the direction of the electric and magnetic field respectively (the symbol $\odot$ is indicating a vector pointing "out of the paper"), the magnitudes of the electric field, E, and magnetic field, B are given on either side of the interfaces (a) and (b).

2.4.2 Surface film filters

The reflectance of thin films and media transitions is well described in literature. A simple description is by use of transfer matrices [25] calculated from the index number of the material, the thickness of the film and the wavelength, and is valid for thin transparent films.

In the following, the formalism is deducted for electric fields perpendicular to the plane of

incidence. However, for normal incidence the case of perpendicular and parallel electric field are equivalent, and the results can be generalized. Using the notation in Figure 2.22 and the boundary conditions for the electric and magnetic fields, i.e. the tangential component of the resultant fields are continuous across the media interfaces, a *transfer matrix* can be derived relating the electric fields, E_a and E_b, and magnetic fields, B_a and B_b, at the two interfaces

$$\begin{bmatrix} E_a \\ B_a \end{bmatrix} = \begin{bmatrix} \cos\delta & \frac{i\sin\delta}{\gamma_1} \\ i\gamma_1\sin\delta & \cos\delta \end{bmatrix} \begin{bmatrix} E_b \\ B_b \end{bmatrix} \tag{2.63}$$

where γ_1 is a prefactor related to the refractive indices n_x and angles θ_x as

$$\gamma_0 = n_0\sqrt{\epsilon_0\mu_0}\cos\theta_0 \tag{2.64}$$

$$\gamma_1 = n_1\sqrt{\epsilon_0\mu_0}\cos\theta_{t1} \tag{2.65}$$

$$\gamma_s = n_s\sqrt{\epsilon_0\mu_0}\cos\theta_{t2} \tag{2.66}$$

and δ is the phase difference that develops due to one traversal of the film,

$$\delta = k_0\Delta_1 = \left(\frac{2\pi}{\lambda_0}\right)n_1 t\cos\theta_{t1} \tag{2.67}$$

where k is the wave number and Δ is the optical path difference, $\Delta = n_1 l\cos\theta_{t1}$ between the two beams.
The transfer matrix in Equation 2.63 can generally be represented as

$$\underline{M} = \begin{bmatrix} m_{11} & m_{12} \\ m_{21} & m_{22} \end{bmatrix} \tag{2.68}$$

and adding more layers yields an overall transfer matrix M_T of

$$\underline{M}_T = \underline{M}_1\underline{M}_2\underline{M}_3\cdots\underline{M}_N \tag{2.69}$$

where M_1 and M_N is the transfer matrix of the first and the last layer respectively.
The reflection coefficient and transmission coefficient for the field are defined as

$$r = \frac{E_{r1}}{E_0} \qquad \text{and} \qquad t = \frac{E_{t2}}{E_0} \tag{2.70}$$

Combining Equations 2.63, 2.68 and 2.70 the transmission and reflection coefficients are found as

$$t = \frac{2\gamma_0}{\gamma_0 m_{11} + \gamma_0\gamma_s m_{12} + m_{21} + \gamma_s m_{22}} \tag{2.71}$$

$$r = \frac{\gamma_0 m_{11} + \gamma_0\gamma_s m_{12} - m_{21} - \gamma_s m_{22}}{\gamma_0 m_{11} + \gamma_0\gamma_s m_{12} + m_{21} + \gamma_s m_{22}} \tag{2.72}$$

The reflectance R, which determines the reflected irradiance, is defined by

$$R = |r|^2 \tag{2.73}$$

and the transmission is given by

$$T = 1 - R \tag{2.74}$$

In this way, transmission and reflectance of various combinations of films and thicknesses as a function of wavelength can be calculated. The transmittance T of a 120 nm silicon nitride and 200 nm oxide on top of silicon is shown in Figure 2.23.

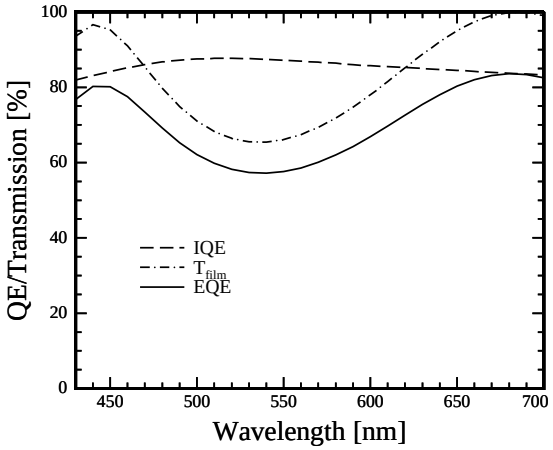

Figure 2.23: Internal quantum efficiency (IQE), surface film transmission (T_{film}) and external quantum efficiency (EQE= T_{film}×IQE) of a 120 nm silicon nitride film and 200 nm oxide film on top of silicon substrate. The internal quantum efficiency is determined by the absorption light and diffusion of carriers to the depletion region of the pn-junction diode as described in Section 2.4.3. The surface film transmission is determined by the layer composition and thicknesses of the surface layers and is calculated from equations 2.64 trough 2.74.

2.4.3 Internal quantum efficiency

Photons that are transmitted to the Si substrate are absorbed according to Lambert-Beer's absorption law (Equation 2.62) with the absorption coefficient of Si, α_{Si}, shown in Figure 2.21, assuming that the absorption is independent of doping level. The number of photons absorbed per unit length is expressed as

$$-\int_0^\infty \frac{\mathrm{d}\phi(\lambda,x)}{\mathrm{d}x}\mathrm{d}\lambda = \int_0^\infty \alpha_{Si}(\lambda)\exp(-\alpha_{Si}(\lambda)x)\mathrm{d}\lambda \tag{2.75}$$

where x is the distance from the surface.

The pn-junction is located 500 nm from the silicon to SiO_2 interface. A simple estimation of the quantum efficiency is made by assuming that the doping level on the p-side is uniform although the ion-implanted doping profile is Gaussian shaped. The depletion region extends approximately 950 nm into the n-type substrate while it only extends 1 nm into the p-side due to the high ratios between the doping level on the two sides. The minority carrier lifetimes and diffusion constants are approximately $\tau_n = 4$ μs and $D_n = 38$ cm^{2}s^{-1} for the electrons on the p-side and $\tau_n = 200$ μs and $D_n = 12$ cm^{2}s^{-1} for the holes on the n-side respectively [26][27].

The excess carrier concentration δn is found by solving the steady state continuity equation [24]

$$D_n\frac{\partial^2\delta n(x)}{\partial x^2} + \Big(G_n(x) - U_n(x)\Big) = 0 \tag{2.76}$$

where G_n is the electron generation rate found from Equation 2.75 and the electron recombination rate U_n is expressed as

$$U_n = \frac{\delta n(x)}{\tau_n} \tag{2.77}$$

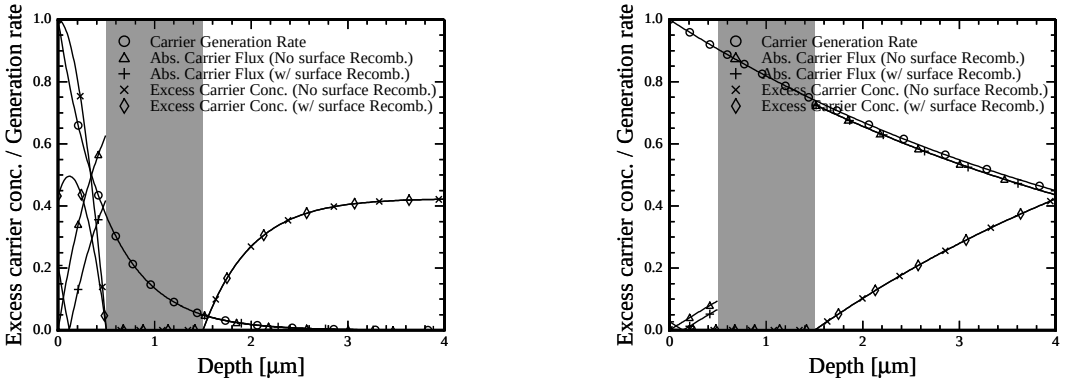

Figure 2.24: Normalized excess carrier generation, flux and concentration in a pn-junction light sensor illuminated with 480 nm (*left*) and 700 nm (*right*) light, with and without surface recombination. 32% of the photons are absorbed and generating carriers inside the depletion region when the light is 480 nm whereas only 16% are absorbed inside the depletion region for 700nm. The remaining current comes from carriers generated outside the depletion region and diffusing to the depletion region. The flux from the substrate is low for 480 nm and high 700 nm, as few and many carriers are generated below the depletion region respectively. The bulk carrier lifetime is long in the lightly doped substrate and the carrier flux from the substrate is not significantly affected by the backside surface recombination. The relatively high surface flux of 480 nm is affected by the surface recombination rate. The quantum efficiency is approximately 78% and 98% with and without surface recombination for 480 nm and 95% and 98% with and without surface recombination for 700 nm.

and similar for holes. It is assumed that every carrier generated in or diffusing to the depletion layer is instantly caught in the electric field and contributes to the photo current. Carriers outside the depletion region either diffuse to the depletion region or to the surface of the silicon substrate. At the surface a finite surface recombination rate lower the quantum efficiency. However, the surface recombination rate at Si-SiO_2 interfaces is very low [28].

Figures 2.24 and 2.25 show the excess carrier generation, concentration and flux in four different cases; 480 nm and 700 nm light on a normal silicon wafer and a 3 μm device layer SOI wafer. These simulations give an IQE of 78%/98% for 480 nm light with/without surface recombination and 95%/98% for 700 nm light in a normal silicon substrate. The IQE does not change significantly for 480 nm light when changing to an SOI wafer, whereas the IQE decreases to 34%/45% for 700 nm light. The surface recombination velocity is set to 10^4 m/s.

A full simulation can be made using commercial software packages such as ATHENA and ATLAS from Silvaco [29], where the implantation profiles, depletion layer variation, surface recombination and doping dependant bulk recombination rates are taken into account. A simple estimate is made with the assumption of 80% of the carriers generated outside the depletion region are diffusing to the depletion layer. The estimated IQE along with the calculate surface film transmission as well as the resulting EQE for a normal silicon wafer are shown in Figure 2.23.

If the pn-junction is reverse biased the photo current is

$$I(d) = eA\int_0^\infty EQE(\lambda,d)\phi(\lambda,d)d\lambda = eA\int_0^\infty IQE(\lambda,d)T(\lambda,d)\phi(\lambda,d)d\lambda \tag{2.78}$$

where e is the electron charge and A is the sensor area [24]. Assuming 50% reflection on the seawater-sensor interface the photocurrent for a 800 μm × 800 μm sensor should be 15 μA at 10 m

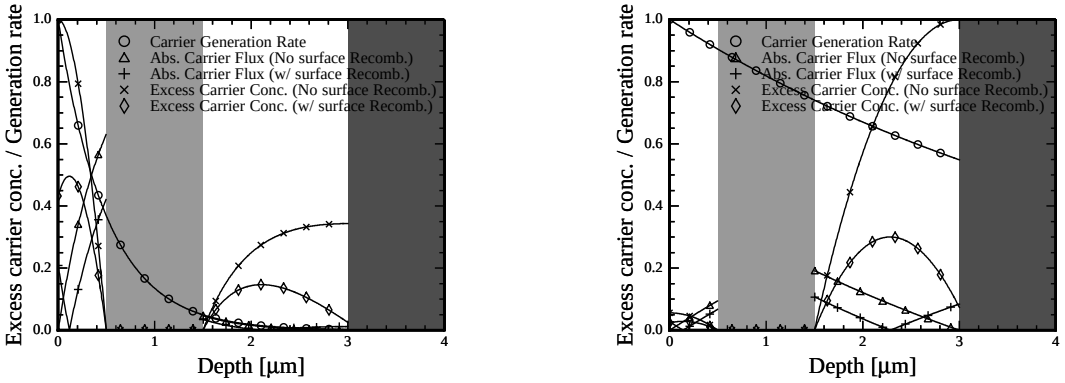

Figure 2.25: Normalized excess carrier generation, flux and concentration in a pn-junction light sensor in an SOI device layer illuminated with 480 nm (*left*) and 700 nm (*right*) light, with and without surface recombination. The depletion region generation and the surface flux is equivalent to the normal substrate case in Figure 2.24. Almost all light (>99%) is absorbed above the buried oxide for 480 nm light. Only 45% of the 700 nm light is absorbed above the buried oxide, while the remaining photons are lost, assuming zero reflection on the oxide. The carrier flux from the device layer below the depletion region is affected by the buried oxide surface recombination rate. The quantum efficiency is approximately 77% and 99% with and without surface recombination for 480 nm light and 34% and 45% with and without surface recombination for 700 nm light.

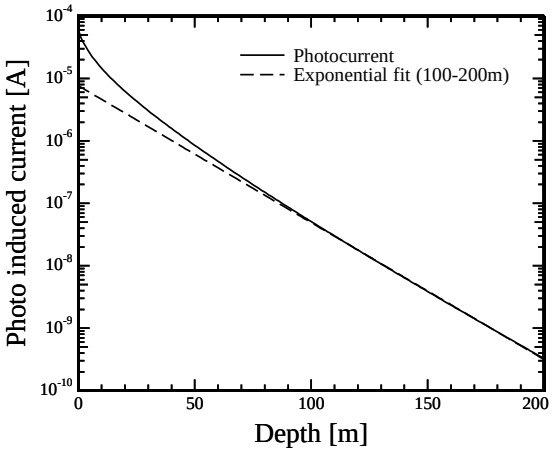

Figure 2.26: Photocurrent as a function of depth. The relation is not completely exponential because the absorbtion coefficient varies with with wavelength, so the spectral distribution changes with depth.

and 50 nA at 100 m which are detectable currents. However, different noise sources such as clouds, algae, seaweed or shadows from the packaging may decrease the signal significantly. The signal at depths closer to the surface should however be good. The expected photocurrent as a function of depth is shown in Figure 2.26.

The actual detectable light intensity is limited by the leakage current of the diode. This varies much between diodes, but generally it scales with the diode area, as does the signal. The signal to

noise ratio is thus mainly effected by the quantum efficiency.

2.4.4 Light sensor summary

A p-n photo diode is used as a light sensor. Silicon shows high photon absorbtion for the wavelengths that are transmitted in sea water, and calculations have shown that the light intensity transmitted in clear water is sufficient to give a 50 nA signal at 100 m depth. However, the leakage current limits the minimum detectable light intensity.

2.5 Summary

Central design parameters have been found for the four sensors through analytical expressions and numerical simulations. No contradicting constrains have been localized and the sensors can be combined on a single chip while meeting the needed precision of the sensors.

CHAPTER

3 Sensor fabrication

Designing a new complex fabrication process is very challenging. Even just adding a few extra lithography mask steps and process steps will add profoundly to the complexity. Every additional process step has to be evaluated against all existing steps to avoid unwanted influence on existing functionality; e.g. high temperature processes that make dopants redistribute or a changing of surface topology that makes protective films less conformal. Even just keeping the defect density low and thereby the yield high is problematic in a manual process with many lithography steps.
This chapter describes three generations of fabrication processes, going from the extension of an existing process, through process optimization to a batch process preparation.
The initial Fish & Chips fabrication process is inspired by a commercial pressure sensor process.

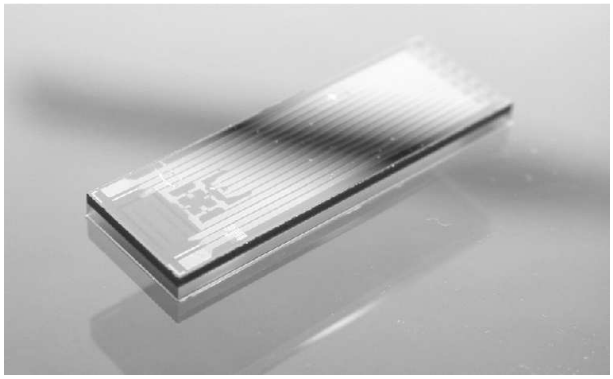

Figure 3.1: Photograph of finished 2nd generation chip. The chip consist of silicon chip with a pyrex glass backside. The chip dimensions are 4 mm × 12 mm × 0.85 mm.

The sensor is fabricated on a silicon substrate using conventional bulk micromachining. When choosing the fabrication technology, the main concerns are the surrounding media and the sensor integration. The sensor system is exposed directly to the seawater, which calls for a protective coating. In our case a LPCVD Si_3N_4 film is chosen because of its excellent chemical stability, its low water diffusivity (less than $10^{-18}cm^2s^{-1}$ [30]) and its well established fabrication technology. In order to electrically connect the sensors to the electronics, a wiring system, which is isolated from the water as well, has to be applied. Because of the high thermal budget of the Si_3N_4 fabrication, a metal film is not an option. Highly doped silicon paths can be used, but the high density of wires, the relatively high resistivity (compared to metals) and the high capacitance to the substrate make doped silicon wires unattractive. An excellent alternative is titanium disilicide ($TiSi_2$) [31], which

offers high thermal stability, a low resistivity (~ 10 times lower than highly doped silicon) and manageable processing. In addition the $TiSi_2$ can be used as thermistor material with a relatively high sensitivity to temperature and insignificant sensitivity to light (compared to doped silicon thermistors). The electrode material should be chosen from criteria of good electrochemical coupling to the electrolyte and chemical inertness. Platinum electrodes are preferred in many applications, and are also used in our sensor.

Other alternative processes have been considered, e.g. exchanging the piezo resistive pressure sensor with a capacitive pressure sensor. However, emphasis has been put on design freedom, process reliability and former experience within the research group, all of which favors the piezo resistive system.

3.0.1 The pressure sensor

The pressure sensor is in all three generations made from KOH etching of silicon to form a membrane. Boron-doped silicon piezoresistors and the highly doped p-type and n-type substrate conductors/contacts are all made by ion-implantation in the 1st and 2nd generation. In the 3rd generation substrate conductors/contacts are made by diffusion while piezo resistors are still made by ion implantation. The measurement pressure range can easily be changed by altering the membrane thickness. Even for a low pressure range (0-20 bar) the membrane will typically be quite thick (>20 μm). This is realized in a timed KOH etch. The piezo resistors are thin compared to the membrane thickness meaning that they are positioned at the maximum stress site for a given pressure, far from the neutral axis of the membrane.
When the substrate is changed to an SOI wafer, the buried oxide can be kept thin compared to the membrane thickness. The buried oxide will thus not significantly influence the stiffness of the membrane.
Capacitive pressure sensors have been considered as an alternative, and indeed the power consumption can be very low for capacitive sensors. However, high demands on interface electronics and fabrication process complexity have discouraged the use of capacitive sensors.

3.0.2 The temperature sensor

The temperature sensor was initially designed as a doped silicon thermistor. A high TCR and a high resistivity made it seem attractive for small thermistors with a high resistance value. However, such sensors are very sensitive to light as a significant number of carriers are generated from incoming light. If the sensors are furthermore isolated from a substrate contact through a pn-junction, the carriers will contribute to a photo-induced current. As the chip is exposed directly to the surrounding media, all light shielding must be implemented on-chip. Using $TiSi_2$ as a masking layer has proven to be insufficient (see Section 7.5.2.1) and [32] has reported the insufficiency of metal films as effective light shielding.
Consequently, the doped silicon thermistor has been exchanged with a $TiSi_2$ thermistor in the 2nd and 3rd generation. $TiSi_2$ shows a very linear response between resistivity and temperature with a reasonable temperature coefficient of resistance (TCR = 4.2×10^{-3} K^{-1}) and a very low sensitivity to light (see Section 7.5.2.1). The low resistivity of $TiSi_2$ will however call for a very long and thin structure in order to keep the resistance high and thereby the power consumption and self heating low (see Section 2.2).

3.0.3 The light sensor

The light sensor is a simple pn-junction photo diode. As the pressure sensor fabrication already includes a medium dose ion-implantation, a standard pn-junction diode can be made with little extra effort. However, as neither the substrate defect density or the surface thin films thicknesses are designed primarily for the light sensor, the quantum efficiency is not optimized. The layer thicknesses, however theoretically allows for approximately 70-80 % transmission from 450-500 nm light. Even the presence of a buried oxide layer (under the 3 μm SOI device layer) does not affect the performance significantly as most photons in the blue part of the spectrum are absorbed very close to the silicon surface.

3.0.4 The conductivity sensor

The conductivity sensor consists of four electrodes exposed to the surrounding and contacted by the $TiSi_2$ wiring system through holes in the silicon nitride. The electrode material should be chosen from criteria of good electrochemical coupling to the electrolyte and chemical inertness. Platinum electrodes are preferred in many applications, and are also used in our sensor. In some cases the platinum surface is processed to form a porous structure, so-called platinum black, in order to increase the effective area. However, this method is unfit for marine applications since the rough surface is a catalyst for bio-fowling, e.g. algae growth. Platinum has a very poor adhesion to silicon nitride and a 10 nm titanium layer is therefore used as an adhesion layer. It is not ideal, since two metals in contact exposed to the same electrolyte is an electrochemical cell, which could lead to corrosion. The contact area of the titanium is, however, so small that this effect is not expected to pose a problem.
The oxide thickness under the electrodes and the wiring system should be as thick as possible, in order to get the best capacitive decoupling of the electrode system from the substrate. For that reason a 3 μm local oxidation process step is introduced in the 3rd generation fabrication process.

3.1 Fabrication process overview

3.1.1 The 1st generation

An outline of the 1st generation Fish & Chips fabrication process is shown on Figure 3.2. The process proceeds as follows:

Fig. 3.2 a)

A 100 nm wet thermal oxide is grown (T=1150°C) on a 350 μm double-side polished (100) Si n-type (10 Ω-cm) substrate. Alignment marks are made by opening windows in the oxide followed by further thermal oxidation resulting in 200 nm oxide.
Ion implantations masked with 2.2 μm AZ5214e resist layers are used to form the thermistors (^{11}B, 4×10^{12} cm^{-2}, 150 keV), the piezoresistors (^{11}B, 5×10^{14} cm^{-2}, 50 keV), the substrate conductor (^{11}B, 10^{15} cm^{-2}, 150 keV) and the substrate contact (^{31}P, 6×10^{15} cm^{-2}, 150 keV).

Fig. 3.2 b)

The implanted resistors are contacted via a self-aligned $TiSi_2$ wiring system [31]. This is done by deposition and structuring of 100 nm polysilicon (LPCVD at 620°C and wet etch in HF and HNO_3) followed by deposition of 44 nm Ti and a two step RTP annealing process at 600°C for 5 min and 850°C for 60 s to form the stable C54 phase of $TiSi_2$.

Fig. 3.2 c)
Both sides of the wafer are coated with a 120 nm LPCVD silicon nitride deposited at 800°C.

Fig. 3.2 d)
Holes are opened in the nitride on the backside using Reactive Ion Etching in a SF_6/O_2 plasma (32:8 sccm, 80 mTorr). Holes are opened in the underlying oxide in HF and a timed KOH etch (at 80°C) is performed to form the 30 μm membrane of the pressure sensor.

Fig. 3.2 e)
The nitride on the backside is then removed in H_3PO_4 at 160°C. The nitride on the front side works as a protective coating for the sensors and is thus protected by a 600 nm PECVD oxide during the etch. This oxide is subsequently removed along with the backside oxide.

Fig. 3.2 f)
Contact holes through the nitride is formed by reactive ion etching in a SF_6/O_2 plasma. The etch has to be timed well, as it has poor selectivity between nitride and $TiSi_2$.
Two lift-off process are used to define the 100/10 nm Pt/Ti layer used for the conductivity electrodes and the 200/10 nm Au/Ti layer used for the bonding pads respectively.

Fig. 3.2 g)
Finally, a 500 μm pyrex wafer is anodically bonded to the backside of the wafer (at 375°C) at low pressure forming the reference cavity for the pressure sensor.

3.1.2 The 2nd generation

The process is subsequently optimized and the second generation utilizes the same steps as above, only without the thermistor implantation. The boron doped silicon thermistors are substituted with titanium disilicide thermistors. This increases the temperature to resistivity linearity and eliminates effects of carrier generation from incoming light.
The chip layout is also radically changed (See Section 4.3).

3.1.3 The 3rd generation

The third generation fabrication process utilizes more functionality, while preparing more substeps for batch processing. First of all, the process implements different silicon dioxide thickness for substrate sensors (pressure and light) and for surface sensors (thermistor and electrodes). This allows for high thermal and electrical insulation of the surface sensors from the substrate while ensuring low steps heights in the contact holes for the substrate sensors. In this way electrical contact can be established across a step with a thin film that is not completely conformal. The substrate has additionally been substituted with a Silicon On Insulator (SOI) wafer which allows for total electrical isolation of the individual sensors when the local oxidation extend through the full thickness of the device layer.
In order to speed up the process and lower the price, the boron and phosphorous doped contacts are realized using a diffusion process instead of ion-implantation.
A design variation also utilizes a second silicon substrate which is anodically bonded to the backside of the pyrex allowing for double sided sensors in a silicon-pyrex-silicon triple stack. In this way the active sensor area can be doubled without significantly changing the form factor of the chip. This could be used for more sensors or to increase the area of existing sensors, e.g. a light sensor

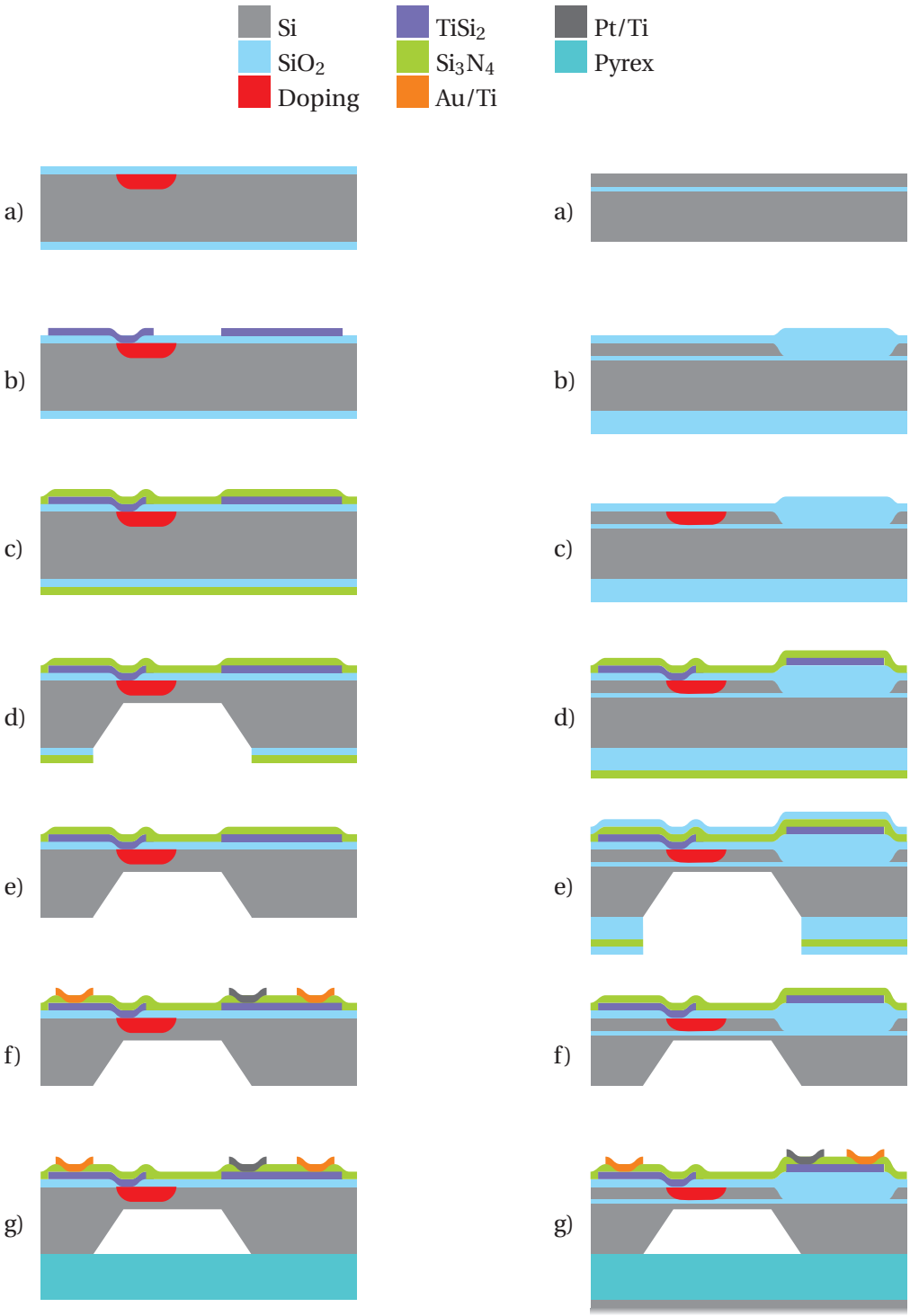

Figure 3.2: 1st generation fabrication process. The steps are described in Section 3.1.1

Figure 3.3: 3rd generation fabrication process. The steps are described in Section 3.2

where the signal amplitude is proportional to the sensor area.

3.2 Detailed 3rd generation process desription

The third generation Fish & Chips process is shown in Figure 3.3. A detailed description of the 3rd generation fabrication process will be given in the following.

3.2.1 Local oxidation (LOCOS)

The base substrate is an SOI wafer with a 3 μm $\pm$0.5μm device layer and 1 μm buried oxide (Figure 3.3 a). Preferably the thickness variation should be small, as the maximum thickness determines the total oxidation time for the LOCOS process and the minimum thickness limits the active depth of the light sensors. In addition, the quality of the bonding of the SOI wafer is very important. Wafers acquired from Ultrasil has shown a tendency to break apart in the bond interface when exposed to the high temperature of the LOCOS process. Colleagues in the industry have had similar problems with wafers from the same vendor.
The local oxidation (Figure 3.3 b) is carried out in a couple of iterations. First, a 130 nm LPCVD Si_3N_4 film is deposited, followed by a 400 nm TEOS. Standard lithography using AZ5214e resist defines the structure. Then openings are etched in the TEOS using BHF and photoresist as the mask. Subsequently openings are made in the nitride using H_3PO_4 at 160°C and the TEOS layer as the mask. The TEOS is then removed in BHF.
The local oxidation is made in a thermal oxidation furnace at 1150°C in four runs of 11 hours, where in between all oxide is removed in BHF. Alternatively the oxidation would take up to 100 hours due to the parabolic grow rate. The nitride is also oxidized during the process [33][34]. A too thin or permeable silicon nitride would result in fatal oxidation of the device layer under the nitride. The silicon nitride thickness should in principle have a thickness of 360 nm. However, the thermal expansion of silicon, silicon dioxide and silicon nitride are very different. Therefore, increasing the nitride thickness will increase the possibility of delamination due to excessive stress in between the films. A successful LOCOS step is shown in Figure 3.4. After the LOCOS process, the nitride film is removed in H_3PO_4.

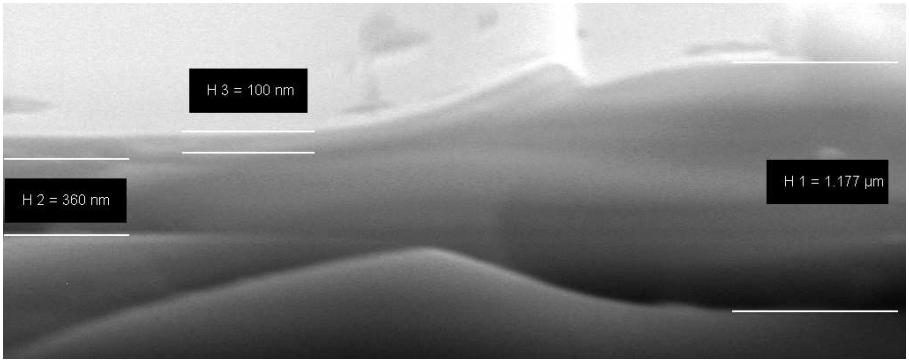

Figure 3.4: LOCOS crossection with the characteristic "birds beak" formation. A 100 nm Si_3N_4 is used to mask the oxidation. Scanning Electron Microscope - 10 kV acceleration voltage.

Process		Sheet resistance		Roughness		
Recipe	Parameters	Measured	σ_M	R_{max}	R_a	σ_{R_a}
	Pre dep/Cool down	Ω/□		nm		
Blank				1.34	0.0942	0.0088
1: BP1000	Gas flow: N_2:?.?/?.? O_2:?.?/?.?	4.2	0.087	2.02	0.0962	0.0161
2: BP1000	Gas flow: N_2:?.?/?.? O_2:?.?/?.? wet??? 90min	3.1	0.050	1.66	0.0888	0.0104

Table 3.1: Phosphorous pre-deposition. Boron doped (100) substrate wafers

3.2.2 Boron and phosphorous pre-deposition

After the initial oxidation of the surface, two consecutive diffusion processes makes highly doped n-type and p-type contacts respectively. The two processes follow the same sequence. First, an oxide layer is grown. For the first process this is already done (LOCOS). Then openings are made to the substrate using standard lithography and BHF etch. Finally the dopants are diffused into the substrate by thermal diffusion (Figure 3.3 c). For the p-type diffusion, solid boron seed wafer sources are used whereas n-type diffusion is made from a gaseous phosphorous source.
As a result of the diffusion process, a phase layer of the specific dopant will be present at the surface, which is unwanted. This layer is therefore normally oxidized and subsequently removed. There are different approaches to this, which influence the final result. A number of experiments are performed to investigate the properties of different diffusion processes. The results are summarized in Tables 3.1 and 3.2. The ideal diffusion process has a low sheet resistance and a low surface roughness, which is needed for subsequent coverage by thin films.
The phosphorous process delivers excellent results and does not need optimization. The diffusion takes place at 1000°C and the result is a sheet resistance of 3.1-4.1 Ω/□ without an increase in surface roughness when compared to blank silicon wafers.
For boron diffusions, higher temperature clearly result in lower sheet resistance. This is not surprising since the profile is much deeper than for processes of the same time and lower temperatures as seen in Figure 3.6. The surface roughness is however 20 times higher than for the best low temperature process. The phase layer thickness of the high temperature process is very large and is difficult to remove (See Figure 3.5).
Process 4 gives the most satisfactory results. The diffusion takes place at 950°C and 5 sccm H_2 and 0.2 sccm O_2 is added to the ambient during deposition but no O_2 is present while cooling. Afterwards, the top layer is removed in HF and an additional oxidation of the top layer followed by HF removes the phase layer.
There are a number of advantages of diffusion processes over ion-implantations. Diffusion gives a high doping concentration with a deep junction. A similar profile would require ion-implantations at varying energy and very long implantation time. The ion-implantation is a single wafer process, whereas diffusion is a batch process. The diffusion process is therefore faster and less expensive when used in production. The disadvantage is the lack of flexibility in the doping concentration. A diffusion profile initially always has a surface concentration equal to the solid solubility. The lateral diffusion under the mask is also higher for diffusion processes.

Process		Sheet resistance		Roughness		
Recipe	Parameters	Measured	σ_M	R_{max}	R_a	σ_{R_a}
	Pre dep/Cool down	Ω/□		nm		
Blank				1.34	0.0942	0.0088
1: Boron975	Gas flow: N_2:5.0/0.0 O_2:0.2/5.0	35.2	10.105	4.01	0.2676	0.0846
2: Boron975	Gas flow: N_2:5.0/5.0 O_2:0.0/0.0 Dry950 30min	16.2	1.106	18.0	1.3350	0.5762
3: Boron975	Gas flow: N_2:5.0/5.0 O_2:0.2/0.0	13.4	0.699	3.97	0.1490	0.0736
4: Boron975	Gas flow: N_2:5.0/5.0 O_2:0.2/0.0 HF,Wet800 30min	14.0	0.493	3.72	0.2475	0.1109
5: Boron975	Gas flow: N_2:5.0/5.0 O_2:0.2/0.0 Wet800 30min	14.4	0.483	15.2	0.3648	0.1471
6: Boron1125	Gas flow: N_2:5.0/4.5 O_2:0.0/0.5	2.0*	-	53.4*	4.70*	-

Table 3.2: Boron pre-deposition. Phosphorous doped (100) substrate wafers. *[35]

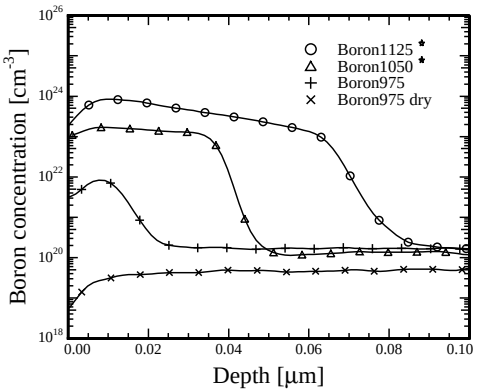

Figure 3.5: Secondary ion mass spectroscopy (SIMS) profile at shallow depth. The solid solubility of boron in silicon is exceeded for high temperatures making a boron phase layer at the surface.

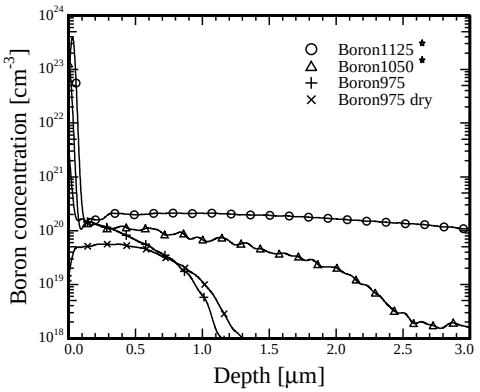

Figure 3.6: Secondary ion mass spectroscopy (SIMS) profile at larger depth. The profile extends further into the substrate for higher temperatures than for low temperatures due to higher diffusion.

3.2.3 Ion implantation

A better control of the doping profile is achieved using ion-implantation. A 2.2 μm lithography step defines implantation areas. The resist is burned at 250°C for 30 minutes. Charged dopant ions are accelerated towards the surface of the silicon. The ions penetrate into the silicon with a gaussian concentration profile which peak depth, peak concentration and width is determined by the energy of the ions. A medium high peak concentration of 5.2×10^{18} cm^{-3} at 500 nm depth is achieved with a dose of 5×10^{14} cm^{-2} and an energy of 50 keV. This gives an approximate junction depth of 1.5 μm. The dopants will activate and redistribute in the subsequent high temperature

processes.

3.2.4 Titanium disilicide ($TiSi_2$) formation

Silicides are compounds between silicon and more electropositive elements, but in microtechnology the term silicides is normally used for transition metal silicides. These silicides are usually inert to most aqueous solutions of everything but hydrofluoric acid. Silicides of titanium, cobalt and nickel are often used in IC processes as interconnect materials due to the combination of their high temperature stability, low electrical resistivity (16-20 $\mu\Omega$cm) and low barrier height to both n-type and p-type substrates. $TiSi_2$ is used in the Fish & Chips processes, because it is the only transition metal silicide which may be post-processed in the LPCVD silicon nitride furnace which is available. A piranha clean (H_2SO_4(80):H_2O_2(20)) is mandatory prior to post-processing in the LPCVD furnace, and substitutes the RCA clean normally used.

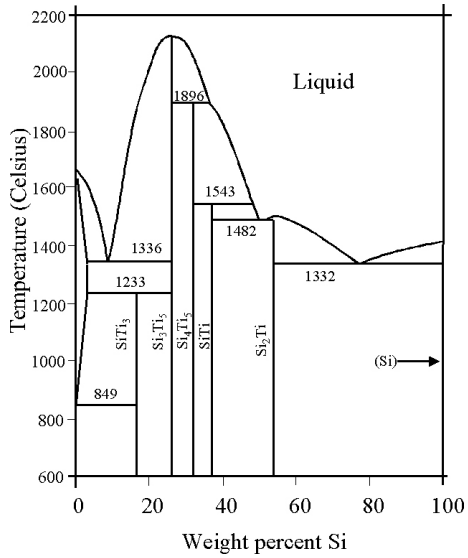

Figure 3.7: Binary phase diagram for silicon and titanium. Taken from [36]

The $TiSi_2$ is made from films of polycrystalline silicon and titanium annealed at high temperature in a Rapid Thermal Annealing furnace. Ideally the elements should be present at an atomic ratio of 1:2 giving a thickness ratio of 1:2.27 depending on the polycrystalline silicon structure. The resulting thickness is 1.11 times the initial polysilicon thickness. Figure 3.7 shows the binary phase diagram of titanium and silicon [36]. Evidently $TiSi_2$ is electrochemically stable in a large temperature interval, and a slight unbalance in the mixing ratio will just produce more TiSi or pure Si respectively [37]. Neither excess TiSi nor pure Si will significantly increase the resistivity or lower the stability. Finite diffusion sources (such as films) at the right ratios forms a single uniform phase, given sufficient diffusion and formation time. However, $TiSi_2$ forms two different phases; C49 which forms at low temperatures (350°C-700°C) and C54 which forms at temperatures above 700°C [38]. Since C54 has a much lower resistivity than C49 (15-20 $\mu\Omega$cm compared to 60-80 $\mu\Omega$cm [38]), C54 is preferred in a wiring system. Annealing silicides below 650°C or above 980°C will make the resulting resistivity sensitive to oxygen contamination during silicidation. At temperatures above 900°C the formation is unstable resulting in large variations in resistivities [39]. Consequently the C54 silicides are annealed between 650°C and 900°C.

However oxygen contamination is always an issue [40]. Oxygen in the silicide will affect the surface topology and the contact resistance, even if the resistivity is not affected. Thus, precautions have to be taken in all aspects of the silicide formation process in order to minimize oxygen contamination. Nitrogen in the silicide annealing ambient can have a smoothing effect on the surface topology and can prevent unwanted silicon diffusion [41]. However, nitrogen will react to form TiN, and the nitrogen concentration should therefore be kept at a minimum.

When using silicides as wiring system, care has to be taken in order to make good ohmic contacts. The metal behaviour of the silicide makes the silicide form Schottky barriers with silicon unless a highly doped silicon layer ensures tunneling and thereby a good ohmic contact. However, dopants present in the silicon contact areas will diffuse into the forming $TiSi_2$. Due to a high segregation constant (Estimated from the solid solubilities [42]) and a low diffusivity of dopants in the silicide, dopants will accumulate heavily on the interface inside the silicide, and the silicon contact will deplete, ruining the contact. Several precautions can be taken in order to prevent this from happening [41]; a) Keeping a low temperature-time product will limit the actual diffusion. However, as the segregation process is most dominant in the beginning it might not be as effective. b) Minimizing the silicide thickness will most likely not be effective either since it is mainly an interface effect. c) A higher initial concentrations and a deeper profile will make more dopants available and make a higher concentration remain after migration. Using in-situ doped poly crystalline silicon for silicide formation will also minimize the depletion. However, the effect on formation kinetics of dopants present during annealing is not known in detail. The contact resistance is in literature reported as low as 66.4 Ωcm^2 [43].

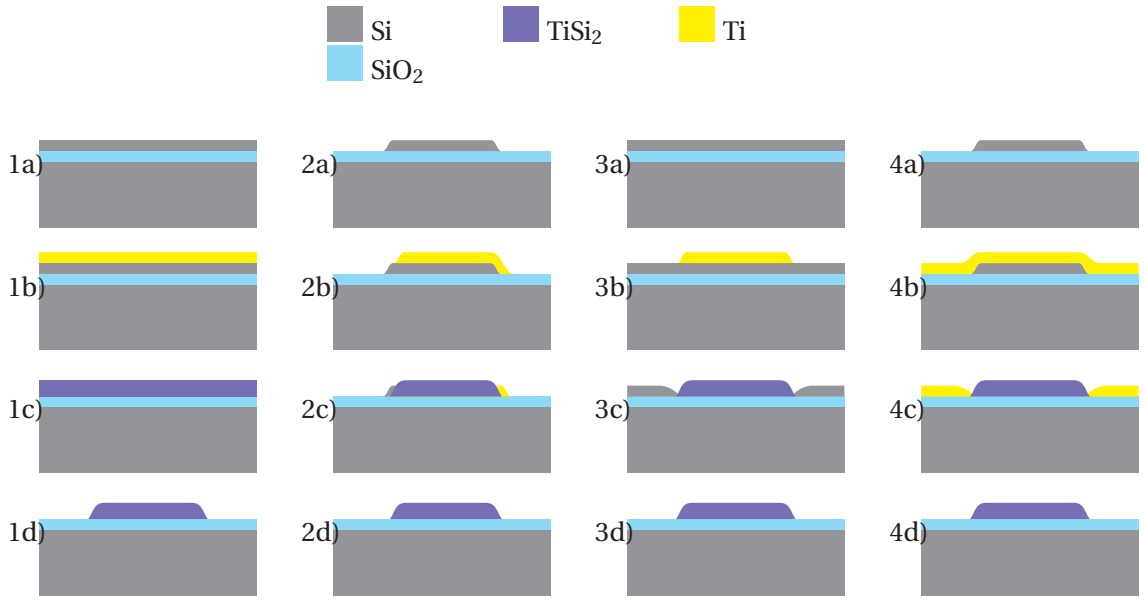

Figure 3.8: Silicide fabrication scheme 1-4. The steps are described in Section 3.2.5

.

3.2.5 $TiSi_2$ fabrication

Different fabrication schemes can be applied, when structuring $TiSi_2$. Figure 3.8 shows the four possible fabrication schemes (assuming titanium on top of silicon), which are:

1. Neither titanium or silicon are structured prior to annealing. An etch with high selectivity to $TiSi_2$ compared to SiO_2 is needed. Neither HF nor a physical reactive ion etch achieve this.

2. Both titanium and silicon are structured. Silicon can be etched in poly-etch and titanium can be structured in a lift-off process. However two consecutive lithography steps are needed. This makes misalignment possible, with formation of TiO_2 as the result, this is shown in Figure 3.9.

3. Titanium is structured. An etch with high selectivity to polysilicon compared to $TiSi_2$ and SiO_2 is needed. Etchants containing HF are not an option. XeF_2 would possibly work, but is not available.

4. Polysilicon is structured. An etch with high selectivity to titanium compared to $TiSi_2$ and SiO_2 is needed. Titanium has a high etch rate in piranha (240nm/min) [44] and a very low etchrate in $TiSi_2$ and SiO_2.

The self-aligned nature of scheme 4 and the high selectivity of the etch involved makes it the obvious choice. The annealing has to be carried out in two steps. First, a low temperature pre-anneal forms C49 $TiSi_2$. Then, excess titanium is removed in piranha. A second high temperature anneal transforms the $TiSi_2$ to the low resistivity C54 phase. If the annealing is otherwise made in a single step, titanium is not removed from the surrounding oxide prior to the high temperature annealing. SiO_2 then reacts with titanium to form TiO_2 and $TiSi_2$. These products cannot be removed in a subsequent piranha and the $TiSi_2$ short circuits the full wafer surface (See Figure 3.10). This is observed in [45] and verified in this project.

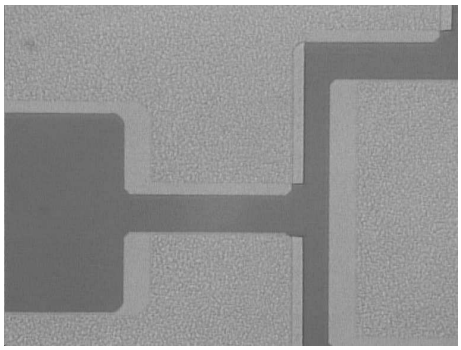

Figure 3.9: Misalignment between the two masks steps involved in the formation of $TiSi_2$ corresponding to Subfigure 2b in Figure 3.8. Misalignment is avoided by applying a self-aligned fabrication scheme.

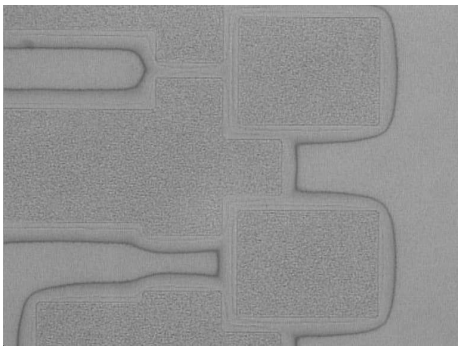

Figure 3.10: Unsuccessful self-aligned silicide formation. The titanium reacts with the underlying SiO_2 due to too high pre-annealing temperature. This result in the whole wafer surface becoming conducting.

The fabrication process for titanium disilicide is as follows (Figure 3.3 d). A 100 nm polycrystalline silicon film is deposited in an LPCVD process at 620°C. The quality of the film is vital to the successful formation of silicide. Poor pressure control has shown to have an impact but no definite connection has been proven.

A 2.2 μm AZ5214E positive photoresist is spun on, and is structured in a conventional UV photo lithography process. The structures are developed in a AZ351B developer. The resist has very low etch rates in the poly etch. Thus, resist residues in the developed areas have a high impact on the uniformity of the subsequent etch. This is critical since the selectivity between polysilicon and the underlying SiO_2 is not high. Photoresist residues are therefore removed in an oxygen plasma at 1000 W for 4 minutes. Four wafers are put in the asher at a time, because experiments show that a larger number of wafers yield a higher density of resist residues on wafers placed in the middle of the wafer carrier.

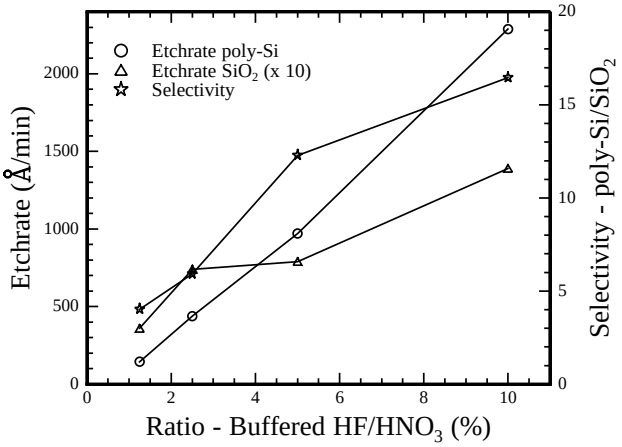

Figure 3.11: Poly silicon etchant selectivity. The selectivity between poly silicon and silicon dioxide increases with relative BHF concentration. The etchrate in both poly silicon and silicon dioxide increases as well, making the exact etch depths harder to control.

The polysilicon is then etched in a HNO_3:H_2O:HF solution. The etchrate and selectivity has been optimized by measuring the etch rate at different HF concentrations (See Figure 3.11). A higher HF concentration gives a higher selectivity, but the high etch rate makes process monitoring more critical. For boron doped polysilicon, the etchrate is very high even for low HF concentrations, and selectivity is not an issue.
Titanium is deposited in an Alcatel electron beam evaporation system. Prior to deposition each wafer is dipped in BHF for 15 seconds to remove any native silicon dioxide on the polysilicon, and a 5 minutes dummy evaporation is carried out to remove any oxidized titanium from the top of the melt. Each wafer is then transferred directly to the RTA furnace. A 12 hour delay between metallization and pre-annealing has shown a 2 times increase in silicide resistivity, possibly due to oxygen contamination. When the wafer is pre-annealed it is much less sensitive to oxygen exposure.

Prior to annealing, a high temperature bakeout of the RTA chamber and carrier is performed. A number of nitrogen purging and evacuation cycles at high temperature removes water vapor from the chamber walls. When the wafer is placed in the chamber, the chamber is also purged and evacuated to remove all oxygen contaminants. Unfortunately, this process has a tendency to make the wafer slide off the carrier resulting in an uneven heat distribution across the wafer, giving varying silicide quality. In future, a carrier with a small recess should be made to counteract this. The annealing layer is facing the carrier, as it gives a more uniform heat distribution and thus a more

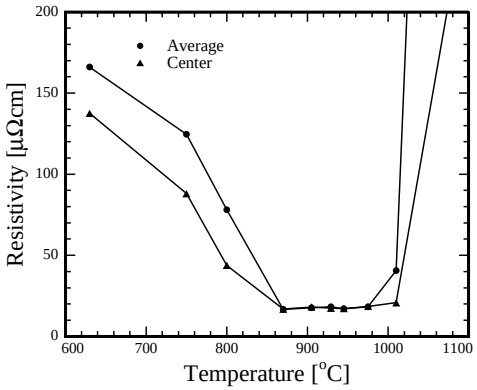

Figure 3.12: Measured $TiSi_2$ resistivity as a function of final annealing temperature. The center resistivity is measured as 16.8 $\mu\Omega$cm - 18.6$\mu\Omega$cm.

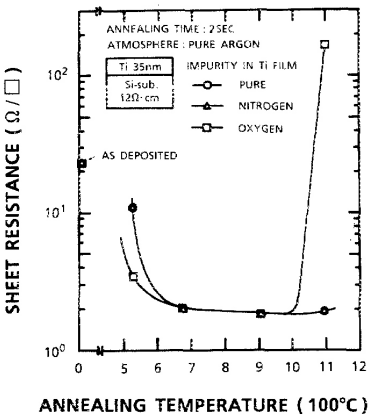

Figure 3.13: Literature values of $TiSi_2$ resistivity as a function of final annealing temperature. [39]

uniform silicide. This, however, complicates the temperature control. The temperature is either measured from the backside of the carrier through a thermocouple or by a pyrometer aimed at the top side of the carrier (wafer backside). Both measure temperatures that are different from the temperature in the annealing layer. A calibration is thus necessary. Figure 3.12 shows the resistivity of the $TiSi_2$ after second annealing as a function of temperature. The low temperature limit for the low resistivity C54 phase formation is shifted up in temperature compared to literature values (Figure 3.13) which is verified through COMSOL simulations. This calibration will however depend strongly on substrate thickness and layer composition.

The wafers are pre-annealed at 600°C for 40 minutes forming the C49 $TiSi_2$ phase. After the pre-anneal, the excess titanium is removed in piranha (H_2SO_4(8):H_2O_2(2)) for 10 minutes. The wafers are annealed a second time at 850°C for 1 minute using the same procedure as for the pre-anneal. This forms the low resistivity C54 $TiSi_2$ phase. After the silcidiation process, the wafers are again cleaned in piranha for 10 minutes, preparing them for LPCVD nitride.

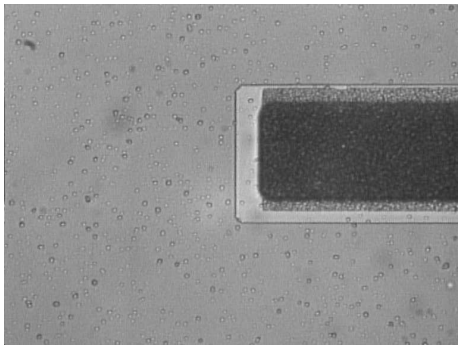

Figure 3.14: Pinholes in the silicon nitride film. The pierced film is inefficient as masking material for bulk silicon etch in KOH.

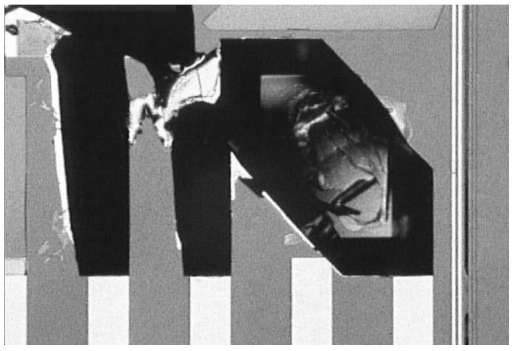

Figure 3.15: Destroyed sensor surface due to nitride failure during etching in KOH.

3.2.5.1 LPCVD Silicon Nitride and KOH etch

The 120 nm silicon nitride film is deposited at 850°C in an LPCVD furnace (Figure 3.3 d). The high temperature ensures a dense film with few cracks. A non-permeable film is vital when it functions as a masking material in the subsequent KOH etch. The conformity of the film is good and the sharp 110 nm steps of the $TiSi_2$ can be covered.
As in the LOCOS process, the nitride is covered with a TEOS, lithography defines the structure and a BHF, H_3PO_4 and BHF etch sequence leaves openings in the nitride (Figure 3.3 e). The KOH etch is performed at 80°C and the etch rate (approx 1.2 μm/min) is measured after approximately half the total etch time. The etch is stopped on time to give the desired membrane thickness. An etched membrane is shown in Figure 3.16.
Unfortunately, the Si_3N_4 process available at the DANCHIP cleanroom facility is of varying quality. Often, the film is full of contaminating particles of a size that is visible in an optical microscope, meaning that they most likely pierce the film full of pinholes. A pinholed surface is shown in Figure 3.14. The result in the subsequent KOH etch is a large number of trenches etched in silicon which at best lower the yield, but in worst case ruin the wafer. Especially if the pinhole density is high on the frontside. For this reason no 3rd generation chips are successfully realized with pressure sensor membranes. A destroyed device after KOH as shown in Figure 3.15.
Further protection of the frontside can be applied in form of a single wafer carrier which is mechanically fastened to the wafer sealing it from the etchant. However, this process makes a large fraction of the wafers break, and should therefore be avoided as much as possible.
After the KOH etch, the frontside is protected with photoresist layer. A BHF, H_3PO_4 and BHF etch sequence removes the oxides and the nitride on the backside while keeping the nitride on the front side, which works as a protective coating for the sensors. In this way a perfectly smooth silicon surface is prepared for annodic bonding on the backside (Figure 3.3 f).

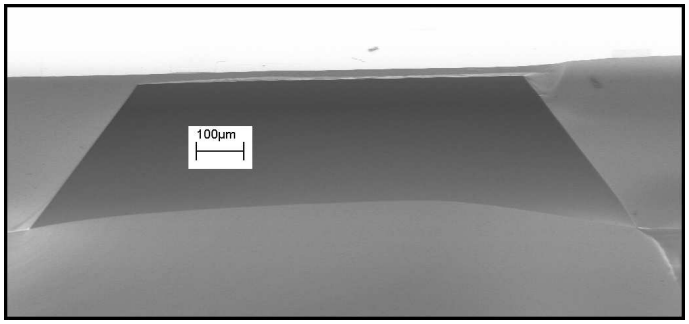

Figure 3.16: Crossection of membrane and cavity realized by KOH etch of silicon. A pyrex wafer is anodically bonded to the backside. The apparent curved shape of the pyrex is the fracture edge of the amorphous pyrex. Scanning Electron Microscope - 4 kV acceleration voltage.

3.2.5.2 Contact holes and metallization

Contact holes through the nitride are etched using a F_6/O_2 plasma (32:8 sccm, 80 mTorr) plasma. The selectivity between the nitride and the underlying $TiSi_2$ has not been measured but is not better than 1:1 which means that great care has to be taken in order not to remove the $TiSi_2$ completely. A 30 second overetch into the $TiSi_2$ is normally acceptable and will not affect the contact resistance. The contact holes are then metalized in two separate lift-off processes with 100/10 nm Pt/Ti and

200/10 nm Au/Ti respectively. First, positive photoresist is spun on, and standard mask exposure is performed, only with approximately half the normal exposure time. Then, the photoresist is heated to 120°C for 100 seconds on a hotplate, which inverts the polarity of the photoresist. The photoresist is then flood exposed for 30 seconds without a mask. After development the photoresist will have opposite polarity than the mask and opposite slopes of the sidewalls compared to normal positive photoresist lithography. This makes it easier to lift off the metals as more photoresist is exposed to the solvent.
The metals are deposited using electron beam evaporation with deposition rates of 1 Å/sec. The lift-off is carried out in an acetone bath with applied ultrasound for approximately 10 minutes (Figure 3.3 g).

3.2.5.3 Anodic bonding of Pyrex

Finally, a pyrex wafer is anodically bonded to the backside of the silicon wafer (Figure 3.3 g). The wafers are bonded by increasing the bonding voltage from 200-400 V in steps of 100 V for 10 minutes each at 320°C in a near vacuum environment. The temperature is kept well below the Au-Si eutectic temperature of 363°C[46], as the Au contacts will otherwise delaminate. The bonding strength increases with temperature. However, the average increase is only from approximately 22 Nmm^{-2} to 26 Nmm^{-2} when increasing the temperature to 400°C, which is a typical bonding temperature [47]. The bonding at 320°C is thus still very strong.
The bonding is made with a slower increase in voltage, if an additional silicon device wafer is to be bonded to the backside. Tests show that a fast increase to high voltages will result in the formation of clusters at the pyrex wafer backside. These clusters will discharge the pyrex wafer, destroying the silicon wafer in the process. A triple stack is successfully bonded by bonding the first two wafers increasing the bonding voltage from 200-250 V in steps of 50 V for 10 minutes each at 320°C, whereafter the third wafer is bonded by increasing the bonding voltage from 200-400 V in steps of 50 V for 10 minutes each at 320°C. The low bonding voltage of the first bond results in a 80% decrease in bond strength. The bonding voltage of the first bond can probably be increased slowly to gain a higher bond strength.

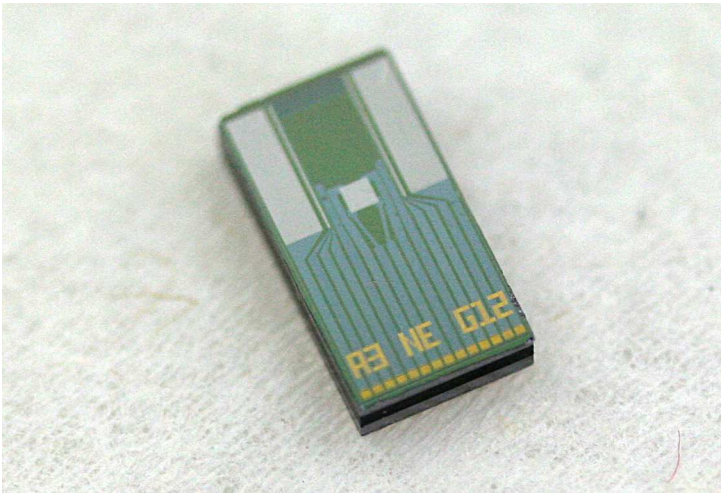

Figure 3.17: Photograph of finished 3rd generation chip. The chip consist of a triple stack of two silicon chips with a pyrex layer in between. The chip dimensions are 3.9 mm × 7.3 mm × 1.2 mm.

3.3 Summary

The full fabrication process consist of 10 mask steps, and a number of processes including local oxidation, dopant diffusion, ion implantation, wet and dry etch, film deposition and metallization. The fabrication process has developed towards a faster and more stable process. This in turn leads to lower price and lower fabrication time. An estimate of the fabrication time and price is given in Appendix B. The fabrication of 10 wafers in the local cleanroom is estimated to cost €24,700, using a lab technician price of €70/hour for 150 hours. This would result in a chip cost of €16.4 for a 100% yield. However, the price is very much dependent on batch size and the production foundry used.

CHAPTER

4 Multi-sensor Design

Based on the theoretical considerations in Chapter 2 and the fabrication processes outlined in Chapter 3, three generations of multi-sensor chips have been designed. In this chapter some general design considerations are given. Then follows a qualitative description of the three chip generations, in which theoretical key values of the sensor performance are estimated.

4.1 General design issues

In general, all the structures on every generation are designed with a 10 μm design rule, meaning that wherever it is possible, the design has a 10 μm tolerance to misalignment between two masks. This precaution is especially important when making electrical connections, this being with metals, silicides or doped silicon areas. Contact holes from metal to silicide and silicide to buried conductor are made 10 μm smaller than the conductors so that the contact resistance stays invariant to misalignment. A processing tolerance between consecutive doping steps is applied by making the doping overlap where ever possible. However, in the sensor areas the tolerance is limited by the small space between implanted structures. Lateral diffusion of carriers set the minimum safe distance.

All sensors are contacted through a $TiSi_2$ wiring system. The conducting wires are kept wide in order to get small series resistances. The $TiSi_2$ is also used as light shielding in the first two generations.

Ultimately the upper design limit for any sensor is the sensor chip size. As one of the main goals of the project is to minimize the size of the complete system, the chip size is made as small as possible without compromising the performance.

4.1.1 Pressure sensor

Pressure sensors are dimensioned so that the size of the piezoresistor areas are much smaller than the dimensions of the membrane, and so that the membrane width to thickness ratio is in accordance to the calculations in Chapter 2. The sheet resistance of the piezoresistor implanted area is so low that the piezoresistors have to be realized by making a series of resistors placed in one direction and conductor implanted cross-connections (see Figures 4.1 and 4.2) in order to ensure a high resistance. The longitudinal and transverse piezoresistor are made in the same way but rotated 90° relative to the membrane side length edge (Figures 4.1 and 4.2).

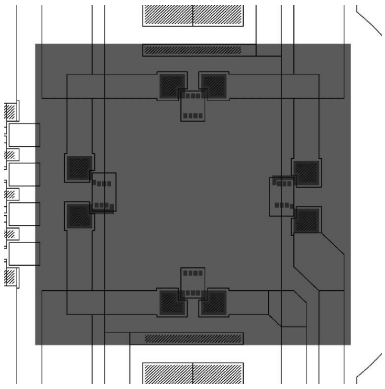

Figure 4.1: Pressure sensor layout for the 1st generation multi-sensor. The square represents the backside opening resulting in a membrane on the front side aligned with the smaller red squares. The membrane is 800×800 μm^2.

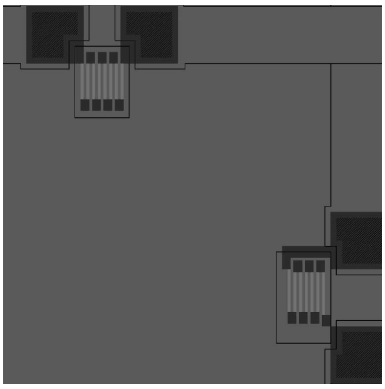

Figure 4.2: Zoom of the 1st generation pressure sensor. The piezoresistors are placed in the direction of the primary stress direction and perpendicular to the primary stress direction. The resistors are made longer by combining a series of parallel resistors.

Figure 4.3: Layout of the temperature sensors of the 1st and 2nd generation multi-sensor. The 1st generation on the left utilize two ion-implanted resistors with negative TCR and two ion-implanted resistors of a different doping level and with a positive TCR. The resistors are arranged in a Wheatstone bridge configuration. The 2nd generation temperature sensor on the right is made as a $TiSi_2$ meander structure which resistance can be measured using a four point technique.

4.1.2 Temperature sensor

The temperature sensor is coupled through four silicide wires. The temperature sensor is placed as far from the packaging as possible, in order to improve the temporal response of the sensor. For thermistor structures with high length to width ratios, the temperature sensor is implemented in a meander structure as shown in Figure 4.3.

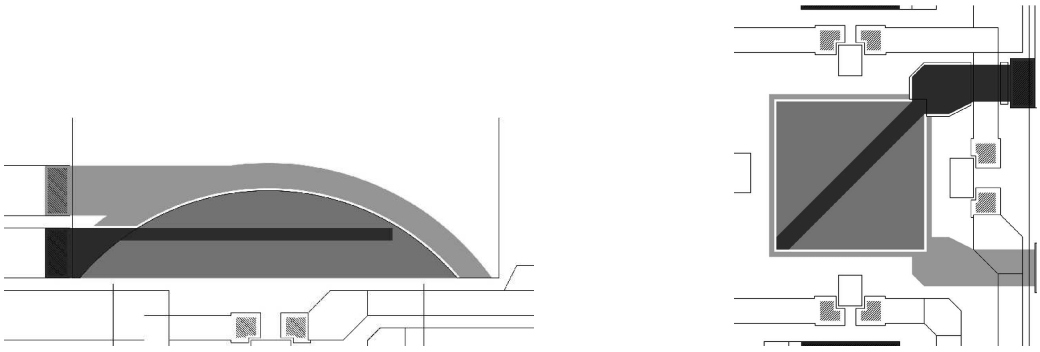

Figure 4.4: Layout of two variations of the light sensors of the 1st generation multi-sensor. The sensor on the left is made to fit the inner diameter of the packaging O-ring. The sensor on the right is placed centrally on the chip in the O-ring center.

4.1.3 Conductivity sensor

The conductivity sensors are made as two pairs of platinum electrodes that are separated as much as possible to ensure a high cell constant. The two outer current carrying electrodes are wider than the inner voltage measuring electrodes. All electrodes are of equal length.

4.1.4 Light sensor

The light sensor generally occupies as much of the remaining space from the other sensors as possible. The light sensor is a large ion-implanted p-type area, which forms a light-sensitive pn-junction diode with the n-type substrate. The active pn-junction area is connected to the $TiSi_2$ wiring system by conductors of highly doped p-type areas and highly doped n-type areas as shown in Figure 4.4. In this way a relatively low series resistance is obtained in the diode.

4.2 1st version - Based on a commercial pressure sensor design

In the 1st generation the chip is dimensioned to fit in a O-ring packaging concept (See Section 5.1) as used by the Danish company Grundfos. The O-ring has an inner diameter of 2 mm and an outer diameter of 4 mm. The minimum size of the chips is thus 4×4 mm^2. However, in order to leave space for two rows of electrical contacts the chip size is set to 4×6 mm^2, as shown in Figure 4.5. A $TiSi_2$ wiring system connects the sensors to the wire bonding pads in the two ends of the chip respectively. The wire bonding pads are of equal size and spacing in order to prepare them for manual as well as automatic probing. The sensors occupy the remaining 3.14 mm^2 surface area inside of the O-ring. The sensors do not extend under the O-ring, even where the O-ring and chip do not touch.

The pressure sensor occupies the 800×800 μm^2 center square and the pressure sensor connectors makes the whole pressure sensor take up 1000×1000 μm^2 plus the size of the wires which goes under the O-ring. The pressure sensor is positioned centrally in order to ensure a symmetric contribution from the O-ring induced stress. The O-ring is compressed 20% in order to withstand pressures of more than 20 bar and a considerable stress is transferred to the chip substrate. This stress has a stress-tail that reaches away from the actual contact surface [48]. The piezoresistors meanders take up 70×70 μm^2 of space and are placed at the maximum stress location of the membrane. With a membrane length to thickness ratio of 27 and a peak doping concentration of 8.9×10^{18} cm^{-3} in the piezoresistors, the expected pressure sensor sensitivity is 1.4×10^{-7} bar^{-1}.

On opposing sides of the pressure sensor, two pairs of electrodes form the four-electrode conductivity cell. The 1st generation electrodes are dimensioned with more consideration to the available space and surrounding sensors than to the performance of the cell as the size influence on performance had not yet been fully theoretically investigated. The current carrying outer electrodes are 400×100 μm^2, the inner voltage measuring electrodes are 400×50 μm^2 and the center spacing of the outer electrodes is 1500 μm. These geometries yield a double layer capacitance of 16 nF and a 2-electrode cell constant of 36.8 cm^{-1} giving a theoretical 2-electrode lower limit frequency of 6.5 kHz for 35 psu.

On a third side of the membrane is the temperature sensor comprising of two pairs of ion implanted resistors placed in a Wheatstone bridge. One pair is designed with a peak doping concentration of 8.9×10^{18} cm^{-3} (similar to the piezoresistors) giving a negative temperature coefficient of resistance (TCR) of -0.4×10^{-3} K^{-1}, and the other to 5×10^{16} cm^{-3} giving a positive TCR of 3.6×10^{-3} K^{-1}. This should give an effective sensitivity of the bridge of V_{out}/V_{in}=2×10^{-3} K^{-1}.

On the fourth side of the membrane a pn-junction light sensor occupy the remaining space giving an active surface area of 0.4 mm^2. In a design variation the light sensor is placed on the pressure sensor membrane knowingly that cross sensitivities will most likely be introduced.

The active pn-junction areas of the pressure sensor and the temperature sensor are covered with $TiSi_2$ in order to shield out light. However, carriers generated in the substrate will still result in a significant cross sensitivity to light.

4.3 2nd generation

The 2nd generation multi-sensor (shown in Figures 4.6 and 4.7) is very different from the 1st generation. The sensors are now not constricted by an O-ring but the whole of one end of the chip is exposed directly to the seawater, while the other end is placed within the packaging material (see Chapter 5). In this way the chip width is maintained while the chip surface available for sensors is increased significantly from 3.14 mm^2 to 16 mm^2. However, as all wires connect to the same end of the chip, the wires cannot be routed as efficiently as in the O-ring design, whereby the wires occupy relatively more space.

The pressure sensor is still placed centrally on the chip to get the highest degree of symmetry. It has the same dimensions and theoretical sensitivity as in the 1st generation.

The conductivity sensor electrodes are increased in size and moved further apart in order to widen the salinity sensitive frequency window. The outer and inner electrodes have a size of 800×400 μm^2 and 800×50 μm^2 respectively, and the outer electrode center spacing is 3500 μm.

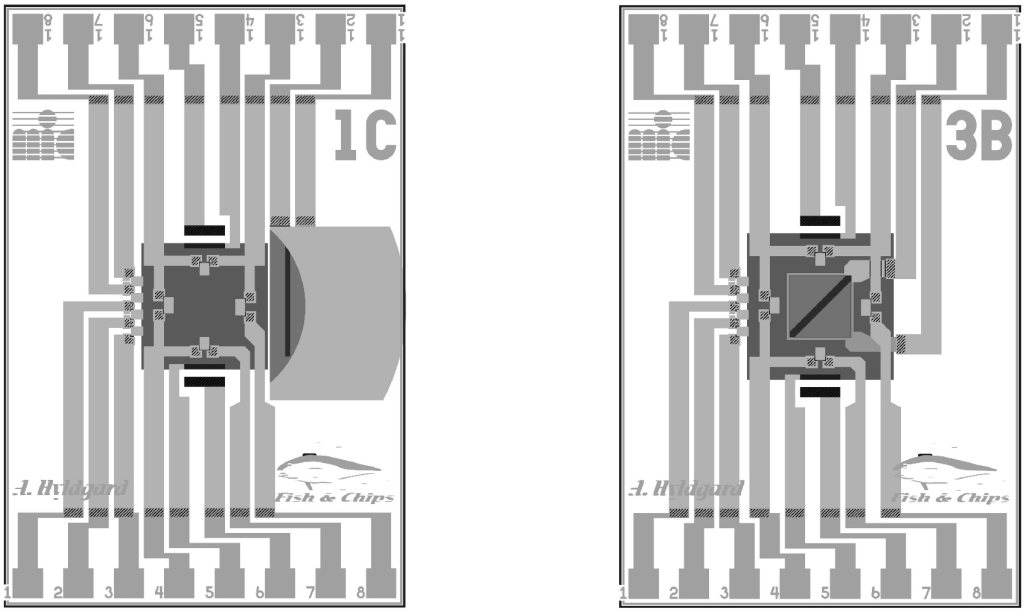

Figure 4.5: Layout of two variations of the 1st generation multi-sensor. Both chips are made to fit the inner diameter of the packaging O-ring. The sensors are electrically connected to the bonding pads at the ends of the chips through the $TiSi_2$ wiring system. The pressure sensors are placed centrally on the chip and the temperature sensors are placed to the left. The conductivity electrodes pairs are placed on opposing sides of the pressure sensor. For design 1C (*left*), the light sensor is placed on the inner rim of the O-ring where as the light sensor is placed on the pressure sensor membrane in design 3B (*right*) The chips are 4×6 mm^2.

This gives a theoretical double layer capacitance of 128 nF, a 2-electrode cell constant of 14.0 cm^{-1} and a theoretical 2-electrode lower limit frequency of 2.1 kHz for 35 psu.

The temperature sensor is made as a $TiSi_2$ thermistor, in order to get a better reproducibility of the resistivity and the TCR. Additionally, the $TiSi_2$ is far less sensitive to light than doped silicon thermistors. A 10 μm wide 12 mm long $TiSi_2$ meander structure gives an effective resistance of 1.7 kΩ. The TCR of $TiSi_2$ is approximately 4.2×10^{-3} K^{-1} which gives a 0.07 Ω change in resistance for a 0.01°C change in temperature. The remaining space on the chip is occupied with the pn-junction light sensor which has an active junction area of 2 mm^2.

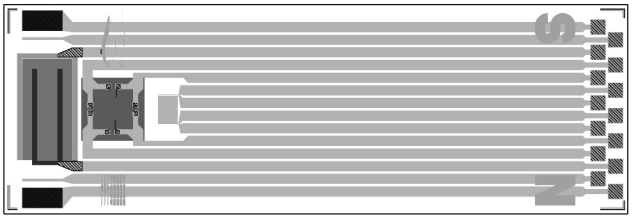

Figure 4.6: Layout of the 2nd generation multi-sensor. The active sensor area in one end of the chip is exposed directly to the water where as the other end is totally encapsulated. The sensors are electrically connected to the bonding pads at the end of the chip through the $TiSi_2$ wiring system. The chips are 4×12 mm^2.

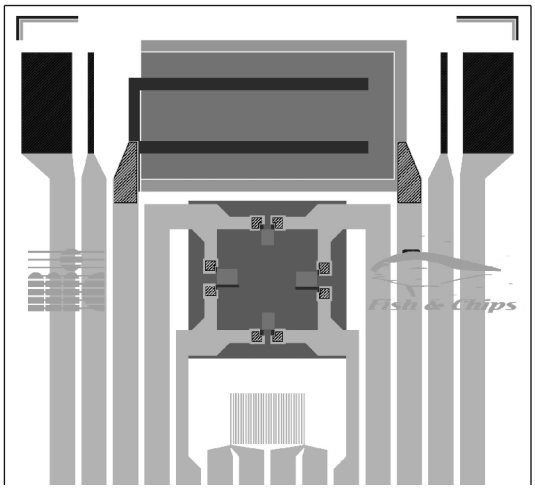

Figure 4.7: Zoom of the active sensor area of the 2nd generation multi-sensor. The pressure sensors are placed centrally on the chip and the temperature sensor is placed closer to the packaging. The conductivity electrodes pairs are placed on opposing edges of the chip with the light sensor in between.

4.4 3rd generation

The 3rd generation multi-sensor chip (shown in Figure 4.8) relies on the same packaging concept as the 2nd generation. The sensors are still placed in one end while the wire bonds are protected inside the packaging in the other end. However, the chip size is reduced due to better control of the packaging process. The sensing principles have not changed although the sensor dimensions and placement have changed.

A major change is the use of an SOI substrate instead of a pure silicon substrate. This allows for a complete dielectric isolation between the individual sensors and to the substrate. Local oxidation removes the entire device layer everywhere except in the location of the pressure sensor and the light sensor. In this way the effective thickness of the oxide under the electrode system is very thick (above 3 μm) and the light sensitivity of the pressure sensor is reduced significantly as no carrier generated in the substrate will diffuse to the pn-junction of the pressure sensor piezoresistors. In a design variation the pressure sensor is further shielded from light by adding a titanium-platinum metal stack on top of the pressure sensor.

The pressure sensor membrane is decreased in size to 400×400 μm^2, which is made possible by shrinking the piezoresistor dimensions and by thinning the pressure sensor membrane. In principle this should leave the sensitivity unaffected.

The temperature sensor $TiSi_2$ meander is increased in length to 34.5 mm, which gives a resistance of 4.8 kΩ.

The light sensor active area remains 2 mm^2, but as the sensor is now disconnected from substrate the effective area is decreased.

The conductivity sensor electrodes are increased in size but the outer electrode center spacing is reduced as the outer limitation from the chip size is actually reduced slightly from 4 mm to 3.9 mm. The outer and inner electrodes have a size of 3200×970 μm^2 and 3200×50 μm^2 respectively, and the outer electrode center spacing is 2800 μm. This gives a theoretical double layer capac-

itance of 1.2 μF, a 2-electrode cell constant of 3.4 cm^{-1} and a theoretical 2-electrode lower limit frequency of 900 Hz for 35 psu.

In a design variation a silicon-pyrex-silicon triple stack is used. The one pair of the conductivity electrodes is moved to the opposite side of the pyrex wafer, i.e. a current and a voltage electrode on one chip and the same applies for a chip bonded to the other side of the pyrex. This effectively increase the cell constant to 5.4 cm^{-1} while keeping the same double layer capacitance. This decreases the theoretical 2-electrode lower limit frequency to 600 Hz.

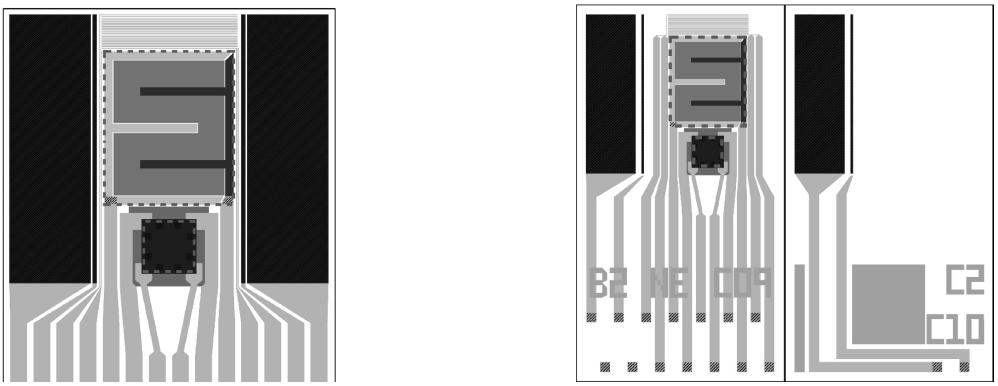

Figure 4.8: Layout of two variations of the 3rd generation multi-sensor. On the left is a zoom of the active sensor area with large conductivity electrodes with temperature sensor, light sensor and pressure sensor in between. On the right is the double sided layout with the conductivity electrodes placed on both sides of the the triple stack. The vacant space on the backside can be used for additional sensors.

Gen.	Chip dimension [mm^2]	Membrane dimension [μm^2]	Thermistor l/w ratio	Electrode dimensions [μm^2]	Light sensor junction area [mm^2]	Lower limit frequency [kHz]
1	4 × 6	800 × 800	100 & 6	400 × 100 400 × 50	0.4	6.5
2	4 × 12	800 × 800	1200	800 × 400 800 × 50	2	2.1
3	3.9 × 7.3	400 × 400	3450	3200 × 970 3200 × 50	2	0.9 (0.6)

Table 4.1: Overview of the chips.

4.5 Test Structures

Test structures are implemented on the wafer, in order to determine process parameters such as resistivity or contact resistance. The test structures include:

- Van der Pauw structure which is a four terminal electrical structure that is used to accurately find the sheet resistance as a simple relation between a voltage and a current.

- 6-terminal Kelvin structure, which is an electrical test structure used to find the contact resistance between different layers. This can be done for both the front end and the back end of the contact area, as well as an average over the contact area.
- Thin lines with varying spacing that are etched on the backside using KOH. If the mask is misaligned to the crystal directions the KOH etch will etch under the mask. The under-etch and thereby the misalignment can be found by inspecting which lines are no longer separated and form one hole.
- Thin top layer stripes made in the different masks that are easy to find and can be used to make surface step profiles.
- SIMS/EDX areas of dimensions fit for SIMS or EDX characterization.

Details on test structure principles can be found in [49].

4.6 Summary

Three generations of multi-sensor chips have been designed. The 1st generation is designed for an O-ring packaging concept whereas the 2nd and 3rd generation rely on a moulding or potting packaging concept. The conductivity sensor electrodes are gradually increased in size, whereas the pressure sensor in the 3rd generation multi-sensor is decreased in size. The length to width ratio and thereby the resistance of the temperature sensor is increased as a result of increasing reliability of the fabrication process. The light sensor occupy the remaining space. Key values from the three generations are summarized in Table 4.1. Test structures have also been implemented.

CHAPTER

5 Packaging

In this project, the aim is a very compact and reliable system capable of measuring the parameters very accurately with a high sensitivity and short response time. This calls for a packaging scheme that allows for direct exposure of a silicon sensor to the surrounding environment. Proper isolation of the sensing area from the packaging material also implies that the sensors are stress de-coupled from the packaging. This in turn allows for pre-packaging wafer scale calibration, hereby significantly lowering the overall cost.
The main function of the packaging is to connect sensor to electronics and batteries while protecting the system from negative influence from the seawater environment. Parts of the sensor must be exposed directly to the surrounding environment, which calls for a very tight sealing, as the distance between the vulnerable, such as electronics, and the exposed parts of the sensor is very small. This has proven to be a difficult task.
Different packaging concepts can be applied. This chapter describes three different packaging concepts that has been tested; O-ring sealing, low pressure injection moulding and epoxy potting in a tube. All three concepts rely on a silicon nitride film on the chip to protect the sensors and the $TiSi_2$ wiring system, while polymers or epoxies seal off water from the vulnerable parts of the system. The water uptake and diffusion in polymers and epoxies has been investigated in [50][51][52][53] but an investigation of the specific material in this system is needed in order to ensure that it meets all the requirements set by the harsh system environment. Determination of water uptake and diffusion in three epoxies as well as test of water penetration along chip-packaging interfaces are presented in the end of this chapter. A paper on the epoxy potting packaging concept has been accepted for publication in the *Sensors and Actuators - A physical* journal.

5.1 Compressed O-ring concept

In commercial pressure sensors from Grundfos [54] the membrane of the pressure sensor is exposed directly to the surrounding media though an O-ring seal, as shown in Figure 5.1. This concept successfully seals off the interface electronics from medias at temperatures up to 80°C and pH values up to 14. A precondition for this tight seal is a 20% compression of the O-ring material in a cavity with smooth surfaces. This promising concept has been tested on the 1st generation multi-sensor chips which has a lateral design fitting the dimensions of the O-ring. The O-ring has an inner diameter of 2 mm, an outer diameter of 4 mm and it is made from Nitrile Rubber (NBR).
A laser-ablated PMMA housing was heat bonded with chip, O-ring and wiring inside. The housing consist of three parts as shown in Figure 5.2. These parts were structured using a 50 W CO_2 laser

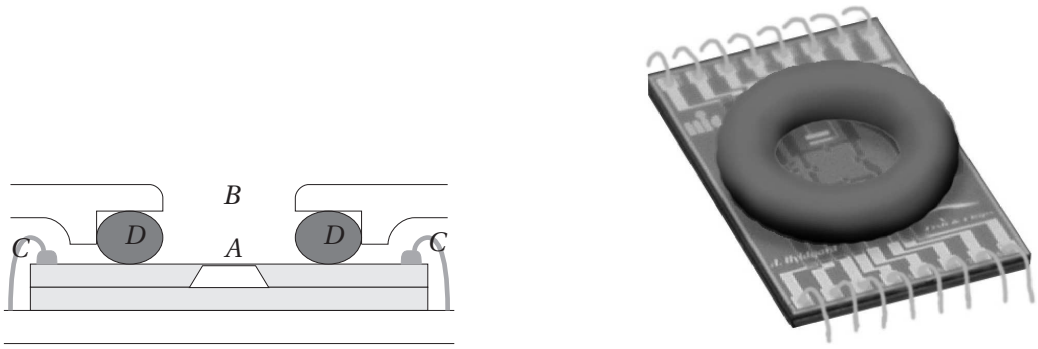

Figure 5.1: O-ring packaging concept. The sensors *A* are directly exposed to the water *B*. The the wire bonds *C* and other vulnerable parts of the systems are isolated from the water by an O-ring *D*. A 20% compression of the O-ring and a smooth surface are needed for a tight seal.

(1.9 kWmm^{-2}), with a 110 × 110 mm^2 size working area [55]. The parts are laser-ablated with the O-ring cavity placed in the center of the laser working areas, hereby minimizing the beam angle error.

The silicon chip is placed in a cavity in the middle part fitting the dimensions of the chip. A flex-print [56] with conducting wires is placed in the bottom part, fed through a hole in the middle part, and glued on to the middle part adjoining the silicon chip, only separated by a sub-millimeter separator in the PMMA. A second flex-print is glued on to the middle part adjoining the chip on the opposite side. Wirebonds are made between the flex-prints and the contact areas on the chip. The flex-print wires consist of a tin-lead alloy, which makes wirebonding very difficult. Alternative an electroplating process can be applied to coat the wires with a metal, that is more suitable for wirebonding. This has however not been tested. Finally, the O-ring is put in a cavity on the top part and the three parts are assembled. PMMA has a glass transition temperature of 105°C [57], and heating the PMMA stack, while applying pressure from a load, will make the PMMA bond. The approximate force needed for bonding is 200 N corresponding to a pressure of 1.5 bar. The actual bonding temperature is evaluated in Figure 5.3. The bonding yield is estimated through visual inspection. It is clear that a high bonding yield is obtainable with temperatures above 110°C. There are two problems arising from this. Firstly, the flexprints are only stable below 105°C. Above this temperature the wires curl up and electrical connection is lost. Secondly, a prolonged exposure to pressure at elevated temperature makes the package deform to a degree where either wirebonds are destroyed or the O-ring is forced out of position. A force that decreases with time or with deformation of the stack is needed. Some successful bonds have been achieved using a spring clamp, though the yield is low.

Successful testing of the sensors has been performed using the O-ring packaging concept. However, when the system is exposed to saline water for hours, the electrical connection to the sensors is lost. Water is clearly observed inside the packaging when Phenol Red is added to the water prior to experiments. The O-ring is evidently not making a tight seal, either because it is not compressed sufficiently or because of the PMMA surface roughness.

Despite the problems described here, sealing of sensors using O-rings is used successfully in industry. However, some case specific issues have to be taken into consideration; first of all, even if the O-ring is mechanically tight, water will still diffuse through the packaging and condense in the empty cavity inside the packaging. This is not the case with the Grundfos O-ring packaging

concept that relies on ventilation of the dry side of the packaging to remove water vapor [54]. Condensing can partly be avoided by filling the void with liquid silicone. However, most important is the accumulation of debris in the O-ring cavity. In the ocean, the O-ring will almost certainly fill up with organic and inorganic debris, which lower the sensitivity and introduce offsets. As there is no effective way of preventing this, it is concluded that the O-ring packaging concept is not well suited for the Fish & Chips application.

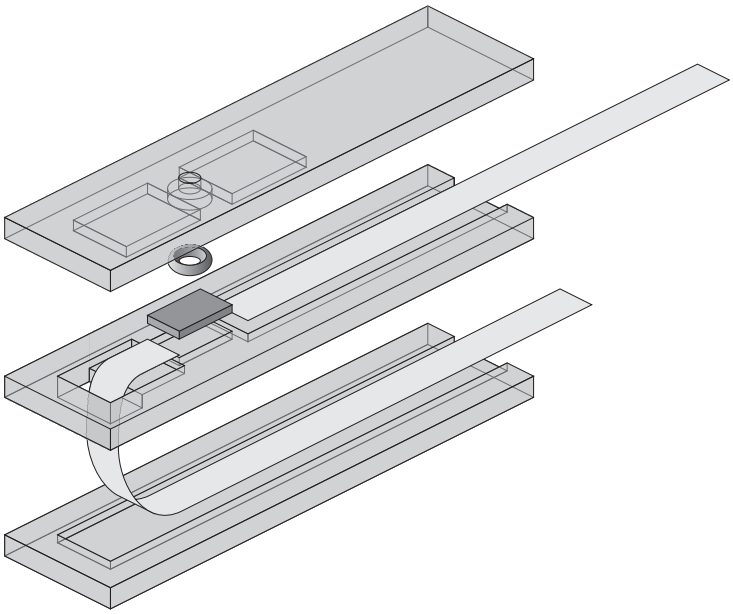

Figure 5.2: Laser-ablated PMMA housing. The three PMMA pieces are shaped using laser ablation. The sensor chip and flex-prints are fastened to the middle part and wire bonds connect the two. An O-ring makes the seal between chip and PMMA, and the three PMMA pieces are thermally bonded.

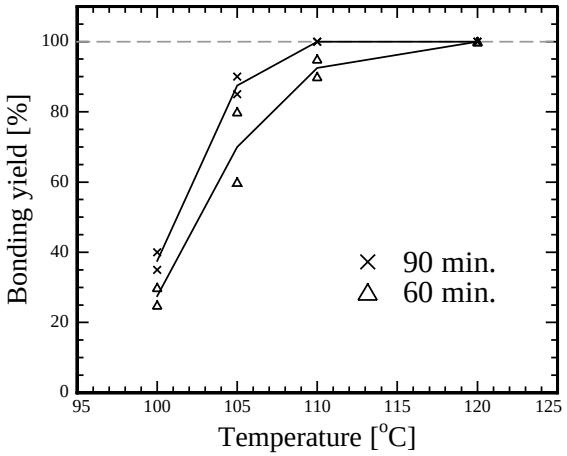

Figure 5.3: PMMA thermal bonding yield as estimated through visual inspection. For temperatures above the glass transition tempearture of PMMA (105°C) a 100% bonding yield is obtained for 90 min. bonding.

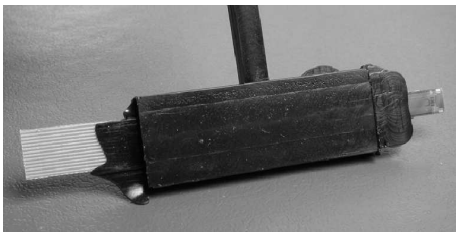

Figure 5.4: Chip packaged using Low pressure injection moulding of Macromelt. The chip is wirebonded to a PCB and placed in a mould. The mould is filled with melted thermoplast at pressures of 3-6 bar.

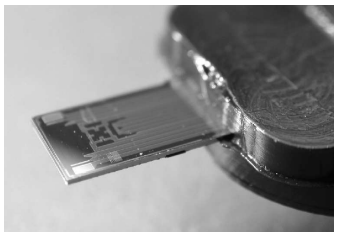

Figure 5.5: Chip sticking out of the Macromelt packaging. The vulnerable wirebonds are inside the packaging. The softness of the Macromelt material makes the system fragile as the wirebonds detach when the packaging is bent.

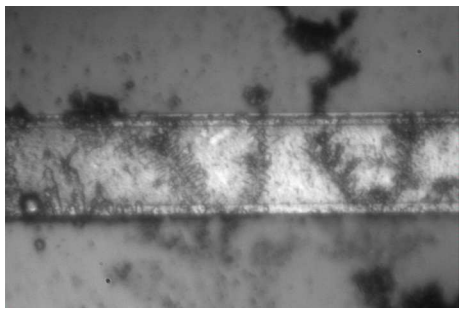

Figure 5.6: Part of a platinum electrode after exposure to a growing algae culture for 4 weeks. Clearly organic debris are left behind. The attachment is however loose and rinsing removes the debris. A higher flow of water over the surface might prevent organic material from attaching to the surface.

5.2 Low pressure injection moulding using Macromelt®

In order to minimize the accumulation of debris in the sensor area, the chip layout is changed to the elongated design as described in Section 4.3. In the new design only inert silicon nitride and inert platinum electrodes with very low surface roughness are exposed to the surroundings. In this way, the possibility of organisms or particles attaching to the surface is minimized.
The new sensor layout calls for a new packaging scheme. Injection moulding is an obvious possibility as the process leaves no voids inside the packaging and it can make tight seals to objects of most shapes. However, high pressure injection moulding as used in industry, is relatively expensive and very time consuming for a low volume production. A less expensive and more accessible alternative is low pressure injection moulding. The process is similar to that of injection moulding, only performed at much lower pressure. The object that needs encapsulation is placed in a two-part (or more) custom made mould with an inlet for the thermoplast and one or more air outlets. A molten thermoplast is then injected into the mould at a pressure of 3-6 bar. The inlet and the outlet dimensions are designed to allow for complete filling of the mould before the thermoplast solidifies. The properties of the thermoplast, such as the glass transition temperature and viscosity, as well as the dimensions of the objects and needed tolerances, influence the level of optimization needed. A standard Macromelt thermoplast [58] is used to test the 2nd generation Fish & Chips design. An aluminum mould has been manufactured using manual drilling and milling, and the

chips are attached to custom made printed circuit boards (PCBs). The process is optimized using a semi-transparent version of macromelt, so that voids can be observed. The same Macromelt is also available with added black dye, which can be used if the contents of the tag has to be shielded from light. A chip encapsulated using low pressure injection moulding is shown in Figures 5.4 and 5.5. The encapsulated chips are exposed to saline water with growing algae culture. Figure 5.6 shows an electrode on a chip after 3 weeks of exposure. Clearly, some debris has accumulated but the extend of coverage is not fatal for the sensors. The water in the test solution is also almost still, which is not the case for a moving fish.
The packaging is tight on a short timescale where the packaged chips are exposed to saline water. However, after days of exposure to saline water some sensors fail. The diffusion length is too long for a sufficient quantity of water to penetrate to the surface by diffusion alone. The only plausible failure mechanism are mechanical failure of the wirebonds caused by the high flexibility of the packaging material or water penetrating to the wirebonds along the chip-packaging interface. This has not been investigated in detail. However, it is well known that thermoplasts shrink slightly ($\sim 1-2\%$) [59] when cooled and the adhesion to Si_3N_4 is poor. Penetration along the interface of a Si-Epoxy interface is investigated in Section 5.4. The low stiffness and the material contraction of the available moulding materials, motivate a new 3rd generation packaging scheme.

5.3 Potting of Epoxy

The 3rd generation packaging scheme relies on the same basic chip design as in the 2nd generation. The chip is sticking out of a completely filled encapsulation.
In the 3rd generation, the chip is packaged using a potted tube packaging concept. The sensors and PCB are placed in a Polystyrene tube which is subsequently filled with two-component epoxy leaving one end of the sensor exposed to the surroundings. The potting process is illustrated in Figure 5.7 and a potted chip is shown in Figure 5.8.
DST manufacturer CEFAS Technology Ltd. [9], uses a potting packaging system in their G5 tag. This system does not expose the sensors directly but relies on internal sensors coupled to the surrounding environment through the packaging. The G5 tag shows that potting using a two-component fill combined with glob-topping can be used in systems for yearlong exposure to seawater.
The silicon-epoxy interface is in principle stronger than for the case of injection-moulded thermoplasts, that tends to shrink slightly when cooled.

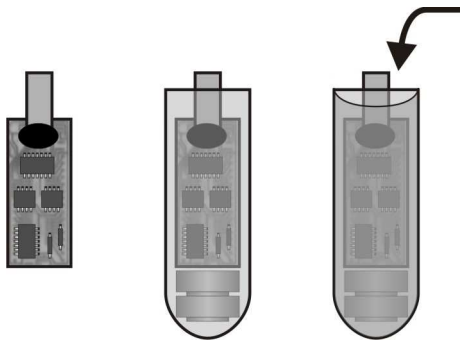

Figure 5.7: Packaging scheme. The sensor chip is mounted on the PCB and the wire-bonds are glob-topped. The PCB and batteries are connected and put in a polystyrene tube. The tube is filled with glue (potted) covering the system while leaving one end of the sensor chip exposed.

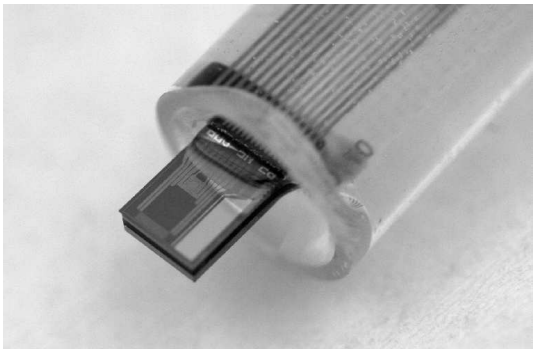

Figure 5.8: The potted chip. The sensor part is exposed to the surrounding seawater while the electronics and batteries are protected inside the packaging. Electrical connection is made through $TiSi_2$ paths on the chip surface which are covered by a Si_3N_4 film.

The most important requirements for the potting material that has to be considered are

- Chemical stability
- Adhesion
- Water solubility & diffusion
- Viscosity
- Glass transition temperature (T_g)
- Electrical insulation
- Curing temperature

Additionally a zero buoyancy mass of the system is sought, as well as neutral colors making the fish no more visible than usual.

Three transparent epoxies listed in Table 5.1 on page 77 are considered. The epoxies all have a specific weight at approx 1.1g/cm^2, good electrical insulation properties and a T_g well above the working temperature range.

The potting process is very simple and if the epoxy curing process temperature is kept below 70°C, then batteries, electronics and the sensor chip are compatible with the potting process. Many epoxies are typically cured at temperatures above 80°C for 1-3 hours, but when curing larger amounts, the exothermic process plays an important role. To ensure that the temperature does not rise above 70°C while curing a PT100 element has been encapsulated in test tubes, and the temperature has been monitored while approximately 3 cm^3 epoxy cures. The curing temperature profiles for the different epoxies are shown in Figure 5.9. In the case of curing EpoTek 302-3M [60] the temperature rise is insignificant as long as the epoxy is cured at a temperature below 40°C. If the curing temperature is increased to 45°C the temperature inside the tube increases to about 56°C within 15 min. An alternative to the heat curing epoxies is UV-curing glues. The Dymax 1180 and Dymax 3069 UV-glues show high exothermicity even at constant low power illumination (pot center temperature > 80°C). UV-glues also have to be cured from the bottom and up in order to avoid trapped bubbles in the tube, which further complicates the potting process. Due to the high temperature during curing, the UV glues are discarded for use in the current application.

In conclusion, the investigated thermosetting epoxies all meet the requirements for processing, whereas the UV-curing glues fail due to excessive temperatures while curing.

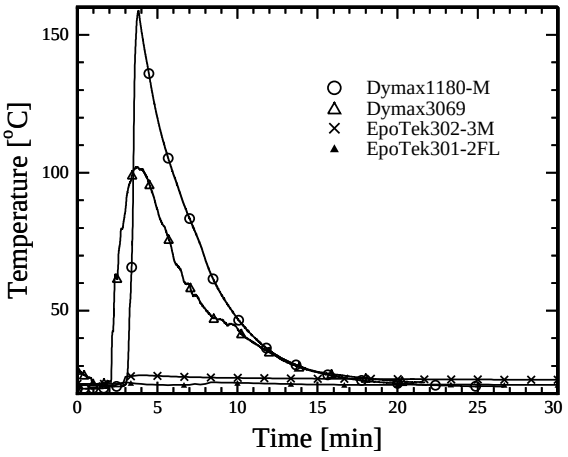

Figure 5.9: Encapsulation center temperature as a function of time as measured with potted PT100 elements. For constant low power illumination the Dymax UV-curing glues show high exothermicity giving rise in temperatures to above 100°C. The heat curing epoxies cure in 24 hours without significant temperature rise. Accelerated curing can be performed at intermediate temperatures (45°) without compromising the tube content.

5.4 Experimental evaluation of packaging concepts

5.4.1 Water uptake and diffusion

Obviously the main purpose of the packaging is to protect the contents of the tag from the surrounding water. A good packaging material is chemically inert and prevents water from being present at critical sites inside the package. In the following it will become clear that water will diffuse to the center of the package within a limited period of time, and the presence of water will then be limited only by the water saturation level. If the system undergoes temperature changes, the water solubility in the filling will change, and excess water will be transferred to the surface of the filling volume.

The water uptake of most epoxies is listed as being very low (<1%) [60]. However, these data are based on very different experimental conditions and the real absolute water uptake is most often significantly higher and has to be measured. Rough estimates, of how much water can be accepted within the packaging, can be made from assumptions of corrosion mechanisms and water flux consideration [61]. However, the final evaluation should be made empirically and measures of water uptake and diffusion should work as comparison only. The water uptake in the most resistant epoxies is expected to have no significant impact on the performance of the packaging and the embedded system. Completely filling also results in a mechanically robust packaging.

The total water uptake as well as the diffusion coefficient is found by measuring the gain in weight of 50x50x1mm^3 sheets of epoxy after submersion in salt water at room temperature. The choice of epoxy obviously has a huge influence on the amount of water that the packaging can contain, for these epoxies a variation from 3% up to 15%. The EpoTek 305 [60], that had the high-

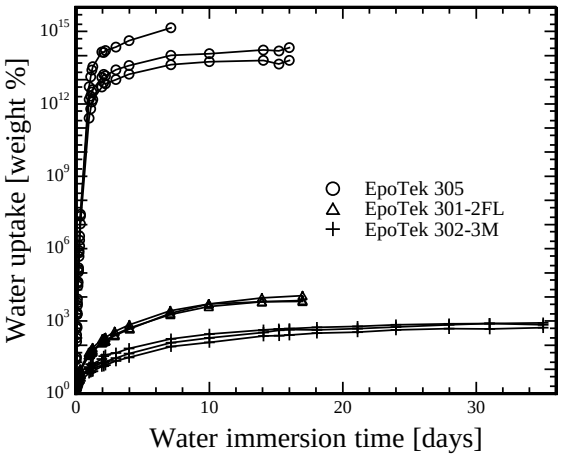

Figure 5.10: Relative water uptake (by weight) in three epoxies as a function of time of sample immersion. Three samples are measured for each epoxy. For true Fickian diffusion, the uptake should saturate when a uniform saturation level is reached through the whole sheet. Non-Fickian diffusion, such as polymer redistribution or reaction with incoming water make the water uptake continue. The lowest uptake is found in EpoTek 302-3M that saturates at approx 2.9%.

est water uptake, got brittle and broke during handling. The amount of water that will condense in possible small cavities within the packaging depends on the water concentration at the cavity interface. The water diffusion into the sheets is considered as a one-dimensional diffusion from two sides. The concentration profile and time development is found from Fick's law under the assumption of a constant diffusion constant

$$\frac{\partial C(x,t)}{\partial t} = D\frac{\partial^2 C(x,t)}{\partial x^2} \tag{5.1}$$

where C is the concentration, D is the diffusion constant, t is the time and x is the distance within the sample normal to the surface. The well known one sided diffusion problem with boundary conditions

$$C(x,0) = 0 \tag{5.2}$$
$$C(0,t) = C_s \tag{5.3}$$
$$C(\infty,t) = 0 \tag{5.4}$$

where C_s is the solid solubility of water in the sample, yields the error function solution [62]

$$C(x,t) = C_s\left(1-\mathrm{erf}\left(\frac{x}{2\sqrt{Dt}}\right)\right) \tag{5.5}$$

As the maximum of absorbed water will be C_sL where L is the thickness of the sample the total water uptake per unit area $M(t)$ is expressed as

$$M(t) = \frac{4}{\sqrt{\pi}}C_s\sqrt{Dt} \tag{5.6}$$

and the relative water uptake as

$$\frac{M(t)}{M_{max}} = \frac{4}{\sqrt{\pi}}\frac{\sqrt{Dt}}{L} \tag{5.7}$$

where M_{max} is the water content at saturation. For short times, where the diffusions from the two sides of the sample is uncoupled, the diffusion constant can be found from the linear relation between the relative water uptake and square root time as expressed by Equation 5.7. The short time water uptake is shown in Figure 5.12. It shows the expected linear relation and the diffusion constants are calculated and listed in Table 5.1. The measured values are on the same order as literature values [53], and the one sided diffusion is thus measurable for short times.

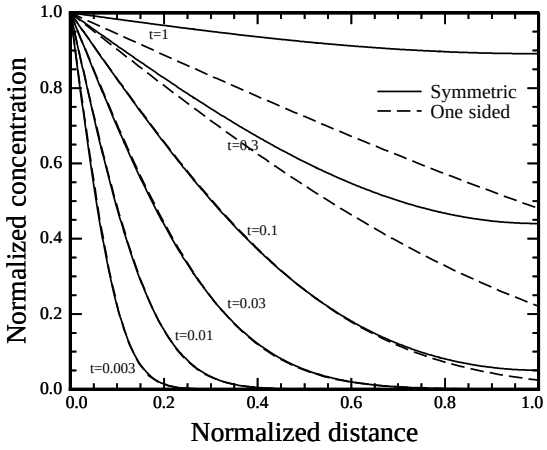

Figure 5.11: Normalized diffusion for the symmetric diffusion (full) and the one sided diffusion for 6 different times (dashed). For short times the two profiles are identical, whereas the difference is significant for longer times.

In order to analyze the long term measurements it is necessary to consider that the diffusion profiles from the two sides overlap. Hence, the exact solution to the double sided diffusion problem must be used. The exact solution can be found with the boundary conditions

$$C(x,0) = 0 \tag{5.8}$$

$$C(0,t) = C_s \tag{5.9}$$

$$C(L,t) = C_s \tag{5.10}$$

by using the method of separation of variables. The exact one-dimensional solution can then be expressed as an infinite series [61][62][63]

$$M(t) = M_{max}\left(1 - \frac{8}{\pi^2}\sum_{n=0}^{\infty}\frac{1}{(2n+1)^2}\exp\left[\frac{-D(2n+1)^2\pi^2 t}{L^2}\right]\right) \tag{5.11}$$

For short times the solution equals the simple solution given by Equation 5.6. For long times the two symmetrical error functions meet at the center plane of the sheet and the water uptake will be approaching total saturation as an exponential decay. All the exponential terms will be dominated by the $n = 0$ term which gives the simple long time expression

$$1 - \frac{M}{M_{max}} = \frac{8}{\pi^2}\exp\left(-\frac{Dt}{L^2}\pi^2\right) \tag{5.12}$$

Thus, a logarithmic plot of the long time relative water uptake as a function of time has a slope proportional to the diffusion constant. Figure 5.13 shows such plots for the water uptake of the

investigated epoxies. As expected from Equation 5.11, straight lines are seen, from which the diffusion coefficients of water is determined and results are listed in Table 5.1.

The water diffusion constants for short time and long time diffusion calculations show very similar results and clearly the variation in diffusion and water uptake is strongly dependent of the choice of epoxy.

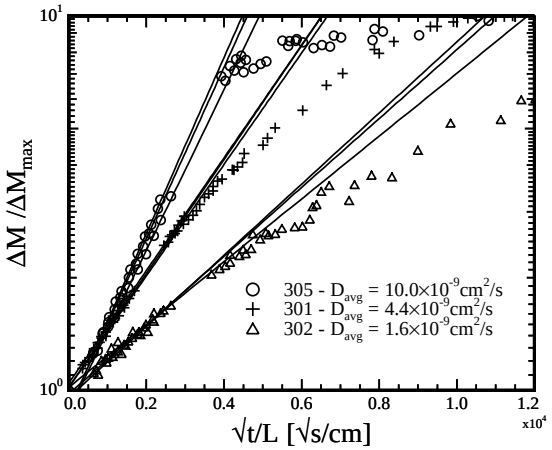

Figure 5.12: Relative water saturation (by weight) in three epoxies as a function of the square root of time of sample immersion normalized with the sample thickness. Three samples are measured for each epoxy. For short times, the diffusion coefficient is proportional to the slope of the graph. The diffusion is 6 times faster in the EpoTek 305 than in the EpoTek 302-3M. Diffusion constants fit very well with literature values [53].

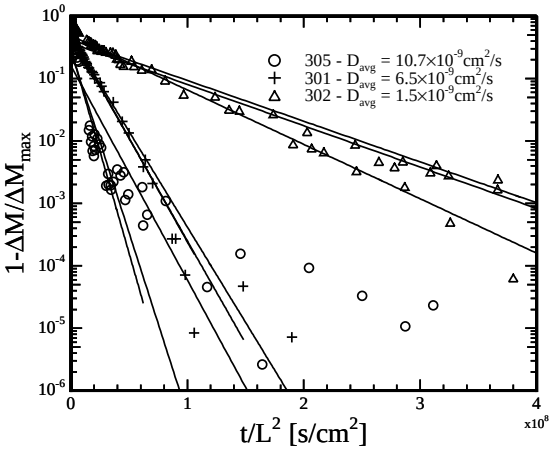

Figure 5.13: Logarithm of the relative water saturation (by weight) in three epoxies as a function of time of sample immersion normalized with the sample thickness squared. Three samples are measured for each epoxy. For long times, the diffusion coefficient is proportional to the slope of the graph. The diffusion is 6 times faster in the EpoTek 305 than in the EpoTek 302-3M. Fitting between 60%-99.9% saturation gives diffusion constants which match very well with the short time diffusion values found in Figure 5.12. Points below 10^{-4} are subject to large relative uncertainties due to water residues on the samples during weighing.

Name	Supplier values		Measured values			
	Viscosity	T_g	T_{max}	Water uptake	D_{H_2O} - short	D_{H_2O} - long
(EpoTek [60])	[cPs]	[°C]	[°C]	[weight %]	[10^{-9} cm^{2}s^{-1}]	[10^{-9} cm^{2}s^{-1}]
302-3M	800-1600	65	26.6	2.9	1.6 +/- 0.8	1.5 +/- 0.2
301-2FL	125	60	24.1	4.0	4.4 +/- 0.4	6.5 +/- 0.2
305	100-300	30	-	14.4	10.0 +/- 0.4	10.7 +/- 2.7

Table 5.1: Key properties of three EpoTek epoxies. The low water uptake and diffusion of EpoTek 302-3M makes it the epoxy of choice. A T_g well above working temperature range, a low curing temperature and a moderate viscosity is also fulfilled.

5.4.2 Leakage test

A second failure process is water penetrating along the interface between the silicon chip and the packaging. This process is difficult to distinguish from diffusion, as the quantity of water entering this way is very low compared to the diffusion process. However, the penetration time can be much shorter.

In an attempt to detect leaking water, a test chip with sacrificial aluminum wires is fabricated. The aluminum wires are parallel coupled and connected to Au contacts in one end of the chip. The chip is then encapsulated using the potting packaging scheme, with one end sticking out, while the resistance of the wiring system can be monitored from connectors in the opposite end.

The chip is emerged in saline water almost filling a pressure chamber. Air pressure is applied through a pressure controller and electrical feed-throughs allow for electrical measurements (See Figure 5.14).

When the saline water leaks along the interface of the chip, the wires corrode changing the resistance of the aluminum wiring system. The change in resistance with time is shown in Figures 5.15 and 5.16 for Epotek 305 and Epotek 302-3M respectively. Two out of three 305 samples lose all wires within less than 5 hours while two out of three 302-3M maintain contact for more than 17 days. This corrosion process cannot be caused by diffusion of water alone. The solubility of water in Epotek 302-3M is approximately 3% corresponding to 1670 mol m^{-3}. Assuming that it takes one water molecule to corrode one aluminum atom, it will take 1 mol m^{-2} to corrode a 100 nm aluminum film. A simple 1-dimensional diffusion calculation on a 5 mm packing at steady state, where the chip surface flux is highest (worst case), will give a flux F of

$$\begin{aligned} F &= -D\frac{\partial C}{\partial x} = -1.6\times10^{-13}\ \text{cm}^2\text{s}^{-1}\frac{-1670\ \text{mol m}^{-3}}{0.005\ \text{m}} \\ &= 5.3\times10^{-8}\ \text{mol m}^{-2}\text{s}^{-1} \end{aligned} \tag{5.13}$$

giving the total corrosion time t of

$$\begin{aligned} t &= \frac{1\ \text{mol m}^{-2}}{5.3\times10^{-8}\ \text{mol m}^{-2}\text{s}^{-1}} \\ &= 1.8\times10^{7}\ \text{s} \approx 7\ \text{months} \end{aligned} \tag{5.14}$$

where D is the diffusion constant, C is the concentration, and x is the distance from the surface. Thus, the failure process observed in Figures 5.15 and 5.16 is water penetrating along the sensor-packaging interface. The longest time of 17 days is much to short for the Fish & Chips application where the total exposure time will exceed 2 years at even higher pressures. According to [64] and

[65] the failure is due to delamination at the interface or microcracks arising in the polymer due to swelling. A better adhesion of the epoxy to the surface may lower the leakage due to delamination. Better adhesion may be accomplished using a thin film with better adhesion properties or a surface treatment changing the topology. Polymers with low water uptake results in fewer cracks at the interface.

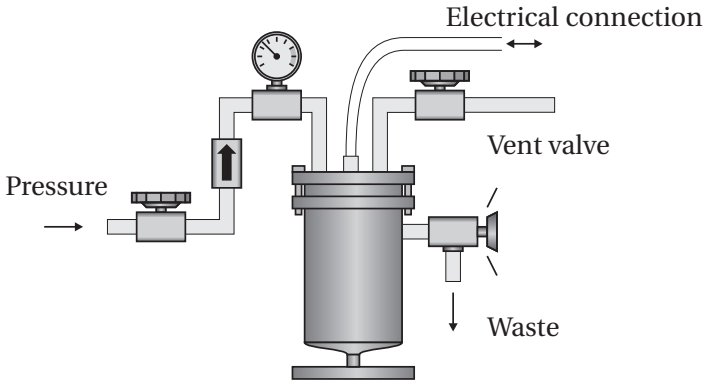

Figure 5.14: Packaging test chamber. The chamber is filled with saline water and pressurized to 5 bar using a pressure controller. The air valves are closed and the setup is left under pressure. Electric connections to the chip is made through electrical vias in the chamber lid.

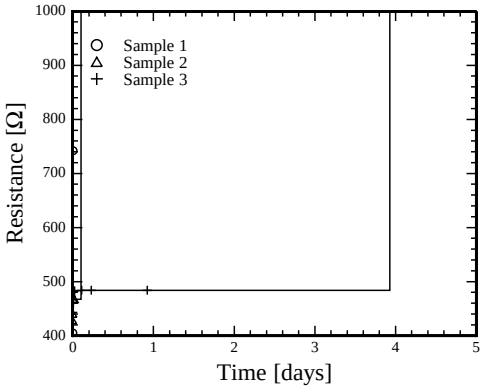

Figure 5.15: Test of water penetration along the chip-packaging interface for the EpoTek 305. The test-chip aluminum wire system resistance is monitored while the chip is exposed to saline water. As saline water reaches the aluminum wires the wires are corroded and the parallel resistance increase. All electrical connection is lost within four days.

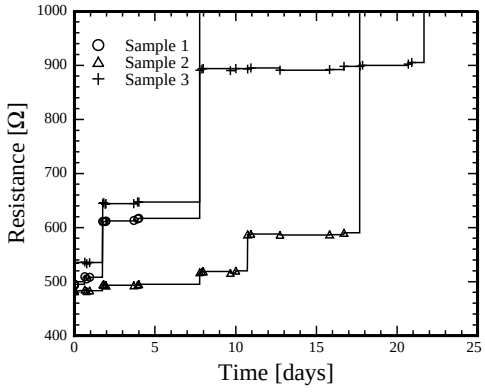

Figure 5.16: Test of waterpenetration along the chip-packaging interface for the EpoTek 302-3M. The water penetrates much slower compared to EpoTek 305 in Figure 5.15. However, all electrical connections are still lost within 8-22 days. Much improvement of the interface seal is needed for real ocean applications.

5.5 Summary

A number of properties has to be taken into account when choosing potting material [63]. The low water-uptake and diffusion constant of EpoTek 302-3M makes it the epoxy of choice. How-

ever, 302-3M has the highest viscosity of the three (0.8-1.6 Pa×s compared to 0.1-0.3 Pa×s), which again makes the chance of bubble formation higher. However, even with the EpoTek 302-3M bubble formation was not observed. A T_g well above working temperature range ensures a low plastic deformation over time and a low curing temperature and a moderate viscosity makes the epoxy practical for potting. The electrical insulating properties are not listed by the supplier, but similar epoxies are listed with electrical resistivities higher than $10^{13}\Omega$cm. In addition to the above investigations, mechanical stress has to be considered as a significant failing process. Stress from the curing process or stress induced by polymer swelling can result in excessive force on wire-bonds or allow water to penetrate along the surface of the chip. This in turn can result in loss of electrical contact as wire-bonds are torn off or etched away. Choosing an epoxy with low water-uptake can minimize problems with polymer swelling. Clever design of the exact shape of the packaging may also limit the stress coupled to the interfaces and surface treatment may result in better adhesion.

Potting shows promise of a compact and reliable packaging scheme that allows for direct year-long exposure of a silicon sensor to the surrounding environment with a high degree of protection of the vulnerable parts of the system. However, further testing and significant improvements are still needed.

CHAPTER

6 Electronic interfacing of the multi-sensor

The main constraint on a DST is size. A derived constraint is power consumption as power storage is very space consuming. When making an autonomous microsystem for long time operation without supply of external energy, the main concerns for the interface electronics are the therefore size and power consumption. This eliminates many otherwise attractive commercial IC's for use in the system as they have a very large package size or a significant power consumption. Even with a very compact surface mounted die (SMD) layout, the electronics will take up considerable size. The only real good solution is the design of a ultra low power Application Specific Integrated Circuit (ASIC). This is a very costly solution for a low volume production, and will not be considered here. Both a discrete electronic solution and an ASIC should contain the same main components. A schematic view of a data storage tag electronics design is shown in Figure 6.1. The sensors are connected to conditioning circuits for signal input and output. Sensor output signals are fed to an A/D converter (ADC) trough a multiplexer (MUX) or to multiple ADCs either internally in a microcontroller (MCU) or as discrete components. Size, pin-out and power considerations will determine the best suited solution. The digital data is stored in a non-volatile memory. Communication is carried out through direct electrical connections or via a wireless protocol such as RFID or Bluetooth. The battery supplies the microcontroller directly and the microcontroller manages the power supply to the remaining electronic components and sensors.

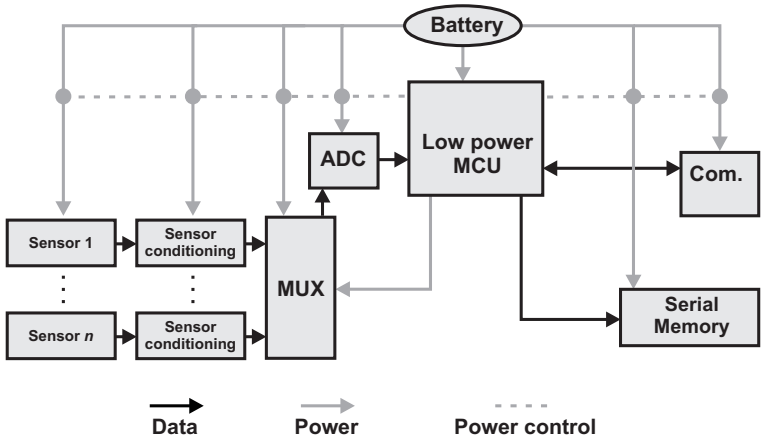

Figure 6.1: Schematic layout of the suggested electronics. Sensors are connected to an ADC through conditional circuits and a multiplexer. The ADC digital result is stored in a serial memory. Communication to and from the micro controller is carried out through direct electrical connections or via a wireless protocol.

Some considerations are made about sensor power consumption and signal conditioning. A power budget is made on basis of an MSP430F2013 micro controller from Texas Instruments and and AT45DB041D Serial Flash memory from Atmel. These components are combined in a SMD draft PCB design which accommodates one pressure sensor for testing purposes.

6.1 General considerations on electronics

6.1.1 Memory

The DST should make as many measurements as possible and data should be readable even if the DST runs out of power. Therefore the data is stored in a non-volatile memory. If the size of the memory is in the mega byte (MB) range Flash RAM is preferred prior to EEPROM as the Flash is a lot smaller in physical size. The Flash however is more power consuming. Typically Flash data is written in clusters of multiple data points and a series of data points must be stored in the MCU RAM. Clever lossless data compression can increase the number of points that can be stored in the memory, e.g. a reduced number of bits are used to indicate a differential change in a parameter when the parameter only changes slowly.

6.1.2 Power budget

The highest volumetric energy density of commercial cells are found for lithium and silver-oxide chemistry cells. Depending on the exact geometry of the cells, the energy density ranges from 0.8 to 1.7 Jmm^{-3} for cells of less than 10 mm in diameter, which is approximately 35% more than for the corresponding Alkaline cells. Additionally, the lithium and silver-oxide cells have a slightly more flat discharge curve than the corresponding alkaline cells. The lithium cells deliver 3 V whereas silver-oxide deliver 1.55 V making two cells in series deliver 3.1 V. However, few of the commercially available lithium batteries have diameters less than 10 mm, and two silver-oxide cells in series are preferred. Silver-oxide cells from Sony of 6.8 mm in diameter and 2.6 mm in height have a nominal capacity of 29 mAh and fit in a package comparable in size to the commercially available DSTs. If the electronics allows for it, the system voltage can be reduced to half by using only one cell.

29 mAh is sufficient to run the electronics for two years and make one million measurements, as seen from the power budget in Table 6.1. The main power consumer is the MCU in operation mode. The operation time is estimated as the sensor sensing time plus two times 100 ms general operation time for power control etc. The sensor power time is limited by the A/D conversion time. When using a sigma-delta ADC, it takes 2^{16} clock cycles for a 16 bit conversion corresponding to 65 ms for an MCU operating at 1 MHz. If the MCU speed is reduced to 100 kHz, the MCU current drainage is reduced to 65 μA and the total MCU consumption is reduced to 16 mAh. However, the ADC sampling time goes up to 650 ms, which increases the total sensor consumption to 19 mAh and the total system consumption to 41 mAh.

Alternatively the resolution of the ADC can be reduced to 12 bits which results in a total system consumption of 27 mAh for 1 MHz and 12 mAh for 100 kHz MCU operation. The power budgets of the four different cases are shown in Appendix C.

The power budget in Table 6.1 shows that sensors can only draw 100 μA for 65 ms for each measurement. This means that resistive sensors should have an overall impedance of 30 kΩ for a 3 V supply voltage. This is met for the pressure sensor, whereas the thermistor and conductivity sensor both use too much power with this electronic setup. Reducing the ADC accuracy will lower

	Current (mA)	Time	Time (h)	CurrentTime mAh
Standby consumption				
- MCU	0.0001	2×365 days	17520	1.8
Flash Writting (2MB)				
- 256 byte pages Flash	17.0000	8192×0.1 s	0.2	3.9
- MCU	0.0650	8192×1 s	2.3	0.1
Operation consumption				
- MCU (1 MHz)	0.2600	10^6×265 ms	77.2	20.1
- Sensors	0.1000	10^6×65 ms	18.9	1.9
Total consumption				28.2

Table 6.1: Power budget - 16 bit ADC - 1 MHz MCU. Additional budgets for 12 and 16 bit ADCs for 1 MHz and 100 kHz MCU operation is found in Appendix C.

the power consumption to a level where the sensor consumption does not drain the system. Flash ADCs can deliver much faster sampling, but the cost is size of the electronics.

Silver-oxide chemistry with NaOH electrolytes are designed for low normal drainage with high drainage peaks, and should easily deliver enough current for peak current consumption. If this is not the case, de-coupling capacitors can be introduced to boost the current delivery. De-coupling capacitors should also be introduced to limit high frequency noise from the power source and electronics.

Both lithium and silver-oxide chemistry cells can operate in the normal temperature interval of -2°C to 20°C. However, in some cases fish are frozen after capture to temperatures as low as -40°C. Lithium cells have a minimum storage temperature of -55°C whereas silver-oxide cells have a minimum storage temperature of -10°C [66]. This means that frozen DSTs with silver-oxide batteries must be powered from external sources during readout of data.

6.1.3 Sensor conditioning circuits

The pressure sensor and the thermistor can both be supplied in very simple ways. Some microcontrollers have a constant voltage reference output. This reference can then be converted into a constant current by using an operational amplifier (Opamp) and a resistor as shown in Figure 6.2. The constant current is supplied to the sensors (the pressure sensor could be bias with the reference voltage directly). The output voltage from the sensors can either be amplified or fed directly to the ADC depending on signal magnitude and ADC precision.

The conductivity sensor is harder to interface. The alternating input signal should be created with very low consumption of power and space, and the microcontroller offers limited sample frequency. Generating arbitrary sensor input signals from the microcontroller output channel can be achieved, although a microcontroller, which is powered by batteries from ground to a positive voltage, can only supply positive voltages on the output pins. A differential signal thus has to be constructed. In order to minimize the number of pins used at the microcontroller, the output reference voltage V_{ref} can be used to make a reference voltage of half the potential $V_h = \frac{1}{2}V_{ref}$ by voltage division and a buffer as shown in Figure 6.3. One output pin of the microcontroller can

be used to create a voltage V_s with small signal variations around the half potential. The resulting differential signal is applied to the conductivity cell through a high precision resistor R_i yielding a near constant current $I = (V_s - \frac{1}{2}V_{ref})/R_i$ through the cell. The sensor output signal and the current through the cell can be determined by two differential measurements of the voltage drops over the cell and the series coupled resistance, respectively. However, the microcontroller has a limited sampling frequency and a precise temporal representation of the output signal is not easily obtainable.
Alternatively the output voltage is fed through a rectifier and a voltage multiplier to yield a DC voltage signal with a magnitude which is proportional to the AC signal amplitude.

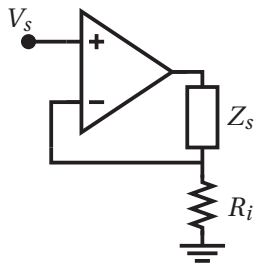

Figure 6.2: Temperature and pressure sensor conditional circuit. The supply voltage V_s is controlled by the microcontroller and the Opamp and the resistor R_i ensures a constant current through the sensor impedance Z_s

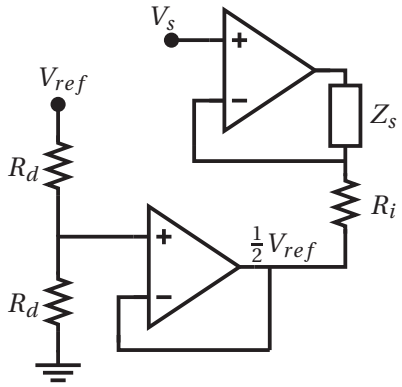

Figure 6.3: Conductivity sensor conditional circuit. A voltage divider and a buffer ensure a current delivering note at half the reference potential ($V_h = \frac{1}{2}V_{ref}$). The supply voltage V_s sets a small signal around the half potential which is converted to a current proportional to the small signal through $I = (V_s - \frac{1}{2}V_{ref})/R_i$. This current is fed through the conductivity cell Z_s.

6.2 Draft of DST electronics

A draft of an SMD PCB is designed. The design accommodates one pressure sensor and is used for testing purposes. The design consists of an MSP430F2013 micro controller from Texas Instruments and an AT45DB041D Serial Flash memory from Atmel. These two components communicate via SPI as shown in Figure 6.4. Pins 2 and 3 of the MCU are used as inputs for the pressure sensor

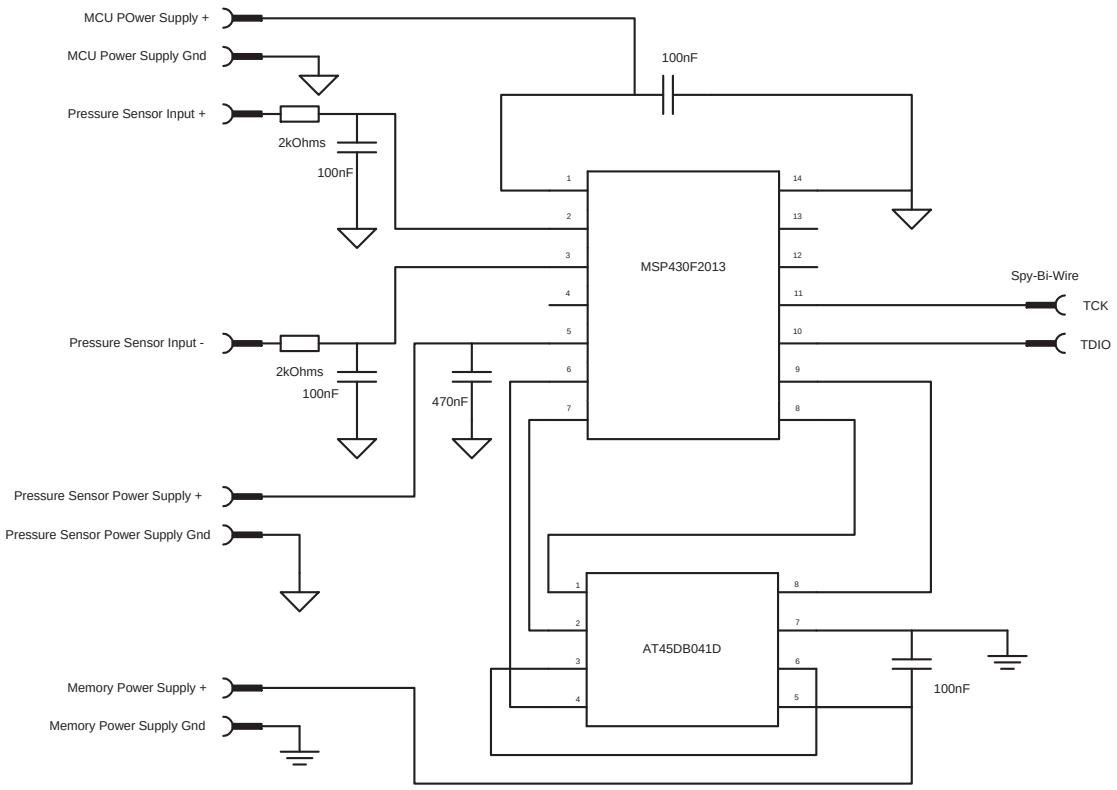

Figure 6.4: Schematic of the simple pressure sensor DST electronics. The design accommodates one pressure sensor and is used for testing purposes. The microcontroller (MSP430F2013) and memory (AT45DB041D) communicates via SPI. The pressure sensor is fed from the MCU low pass filters are applied from the pressure sensor output to the ADC input of the MCU.

signal. This signal is conditioned with two low pass filters with cutoff frequency below 1 kHz. Pin 5 serves as voltage reference output which feeds the sensor.

Both the MCU and the Flash are decoupled with 100nF capacitors. The MCU is programmed by a Spy-Bi-Wire interface (by use of a USB interface).

Figure 6.5 shows the top side of the PCB layout. The designed PCB is a standard FR-4 with two sides and dimensions 9×40 mm^2. All the used components are SMDs (MCU is TSSOP14, Flash is SO8 and passive components are of 0805 type).

The PCB is larger than the packaging size of existing DSTs. However, the layout is not yet optimized for size, and further reduction is expected to be possible. There is free design space on the back side of the PCB where additional components for the salinity sensor can be added.

6.3 Summary

The general considerations on electronics with regards to size, power consumption and sensor interfacing is promising for the feasability of a new DST electronics design made from discrete components. This design will be capable of measuring and storing 1 million data points over a period of two years and of fitting in a packaging of a size comparable to existing DSTs along with two silver-oxide chemistry cells.

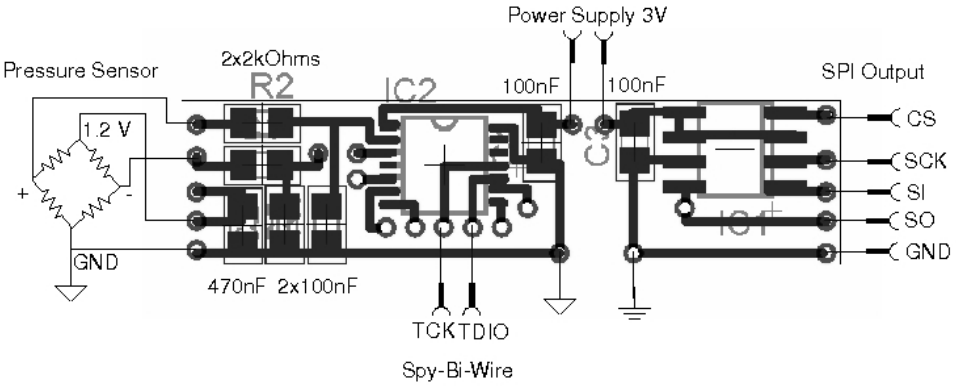

Figure 6.5: PCB frontside layout with connected components. The layout is not yet optimized for size, and an optimized design is expected to fit in a packaging of the size of existing DSTs.

CHAPTER

7 Sensor testing

After fabrication and packaging, the finished chips are tested in a lab environment. Although the chips are ultimately to function in a real-world environment for more than two years without calibration, such a practical test has not been possible within the time frame of this project.

The individual sensors are characterized for sensitivity and resolution and relevant cross sensitivities are investigated, whereas long time accuracy and stability is only sparsely examined.

7.1 Conductivity sensor

When testing the performance of the conductivity electrodes, the packaged sensor is submerged into beakers with samples of dissolved KCl in deionized water at different concentrations. KCl is preferred to standard seawater (where a lot of different salts are present) because the salinity standard is defined from a KCl solution and KCl solutions are made for a fraction of the price of certified standard seawater solutions. The reference conductivities of the saline solutions are measured using the commercial Radiometer CDC749 conductivity probe. A mechanical stirrer ensures a high level of uniformity. A magnetic stirrer is avoided since it affects the measurement. The beakers are placed in an outer salt water thermal reservoir which again is put in a thermo insulating box in order to ensure uniform quasi-equilibrium conditions (see Figure 7.1).

The measurements in Sections 7.1.1 and 7.1.2 are conducted at constant temperature within a short time frame, whereas the temperature dependencies in Section 7.1.3 are carried out at increasing temperatures over several days at quasi equilibrium conditions.

Three sets of electrodes (E_A, E_B and E_C), with different geometries and cell constants are investigated. The cell geometries are listed in Table 7.1.

Design		E_A		E_B		E_C	
Electrode		Current	Voltage	Current	Voltage	Current	Voltage
Width	[μm]	100	50	400	50	970	50
Length	[μm]	400	400	800	800	3200	3200
Centre spacing	[μm]	1500	1200	3500	2800	2830	1770

Table 7.1: Table of electrode dimensions for three different sensor designs E_A, E_B and E_C.

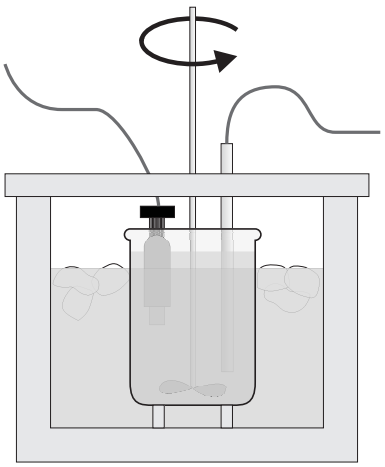

Figure 7.1: Thermobath used for calibration of conductivity and and temperature. The inner beaker with known salinity is placed in an outer saturated saline water thermal reservoir which again is put in a thermo insulating box in order to ensure uniform quasi-equilibrium conditions. The solutions are stirred with a mechanical stirrer and a reference temperature sensor is submerged next to the sensor under calibration.

7.1.1 Two electrode configuration

The simplest measurement of conductivity is made with a set of two electrodes as described in Section 2.1. An AC sine shape voltage of a constant 10 mV peak-to-peak amplitude is applied from an Instek GFG-3015 function generator. The signal goes through a high precision resistor and through the cell, as shown in Figure 2.5 on page 16. The voltages over the cell and the resistor are amplified using two AD524 high input impedance precision instrumentation amplifiers in order to minimize the parasitic conductance through the measurement equipment. The amplified signal is measured using a Keithley 2700 digital multimeter and a Keithley 7700 multiplexer card. The multimeter is also used to log the solution temperature measured with a class-A PT100 temperature probe.

The sensor, which is packaged using epoxy potting (see Chapter 5), is in turn submerged into the saline solutions of different concentrations starting with the lowest salinity. In between submersions, most water residues are removed by shaking the cell in order to minimize concentration or dilution of the saline solutions. The impedance of the two electrode conductivity cell is measured as a function of frequency for different saline solutions. The measured cell impedance for the E_A cell of 400 μm × 100 μm electrodes with a 1500 μm center spacing is shown in Figure 7.2. The impedance profile is very similar to the theoretically predicted profiles in Figure 2.4 on page 2.4. Clearly, the salinity window is quite narrow and the measurement of conductivity with such a cell is influenced either by the double layer capacitance at high conductivities or by the parasitic capacitance at low conductivities for a given frequency. The cell impedance at 18 kHz as a function of water resistivity of the corresponding saline solutions is shown in Figure 7.3. Ideally the impedance is perfectly linearly dependent on the resistivity with a linear slope constant equal to the cell constant K. However, the double layer capacitance introduces a significant offset, and at higher resistivities the parallel parasitic conduction becomes evident.

The actual water impedance is extracted by making a non-linear least squares fit of the model in Figure 2.3 on page 15 to the measured data. The fitted model impedance as a function of frequency is shown in Figure 7.4. Clearly, the model fits very well. The fitted cell water impedance as a function of water resistivity is shown in Figure 7.7. A much higher level of linearity is obtained

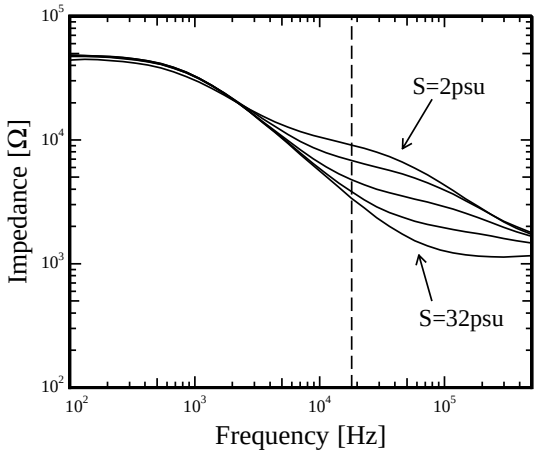

Figure 7.2: Measured 2-electrode cell impedance as a function of frequency for the E_A cell at 5 different salinities (2, 4, 8, 16 and 32 psu). At medium frequencies there is a salinity sensitive window. At low frequencies the electrochemical double layer is not short-circuited. At high frequencies the cell conducts through the substrate loosing sensitivity. The dashed line indicates the single frequency where the correlation between cell impedance and reference water resistivity has the highest degree of linearity. The data at 18 kHz are used to construct Figure 7.3.

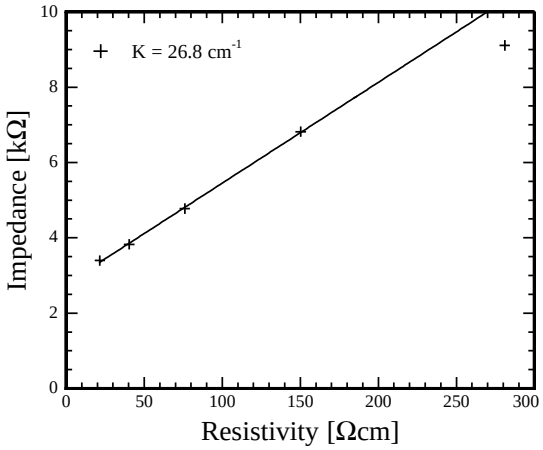

Figure 7.3: Measured 2-electrode cell impedance for the E_A cell as a function of water resistivity measured with a commercial reference sensor. The data is extracted from Figure 7.2 at 18 kHz which yield the highest degree of linearity. The impedance varies linearly with resistivity for low resistivities but suffer from parasitic conductance for higher resistivities.

this way. The model fits the data best when the capacitance and exponents change with salinity. The fitted capacitances and their exponents are shown in Figure 7.5. As expected the double layer capacitance changes with salinity[12] whereas the parasitic capacitance is only slightly dependent on salinity. The parasitic impedance actually functions as a distributed capacitor-resistor network where its time dependence varies with the ratio between the involved components, i.e. the capacitance of the insulating film, the substrate resistivity and the water resistivity.

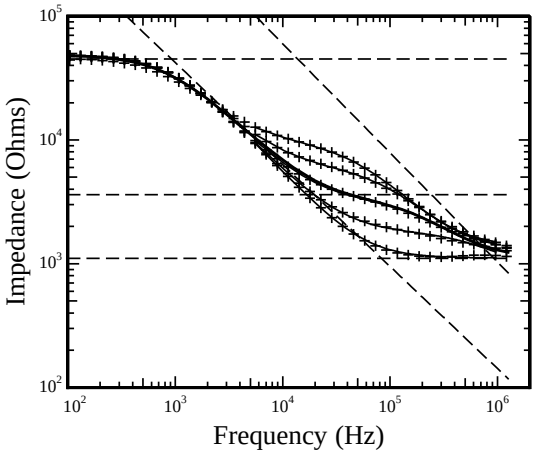

Figure 7.4: Model fit to measured data. The points are measured data from a two electrode conductivity cell. Dashed lines indicate the single parameter contributions to the complete fit indicated by the thick solid line. The model corresponds to the diagram shown in Figure 2.3 in Chapter 2.

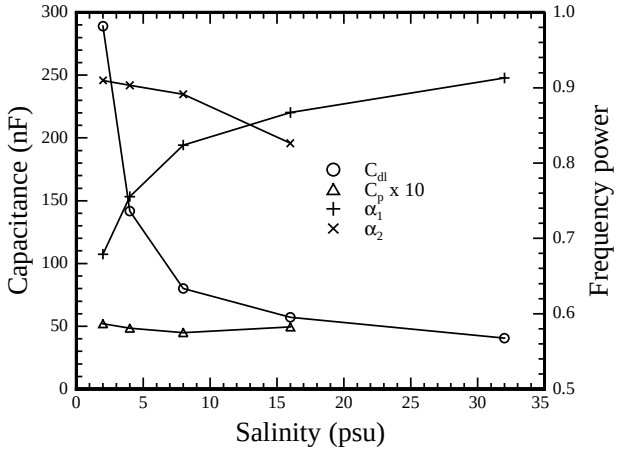

Figure 7.5: Fitted model parameters. The double-layer and parasitic capacitances and their frequency power dependencies as a function of salinity as found from the fits in Figure 7.4.

Although a reasonable correlation between impedance and resistivity is found, the full fit is too computationally demanding for a very small autonomous system.

7.1.1.1 Double layer error elimination

The salinity window is quite narrow and simple offset compensation of the double layer contribution is not sufficient, since the accuracy of salinity sensor suffers if the double layer capacitance changes just slightly. A simple error compensation procedure may be applied to minimize this effect. A first order series expansion of Equation 2.2 will give a simple approximation of the low-

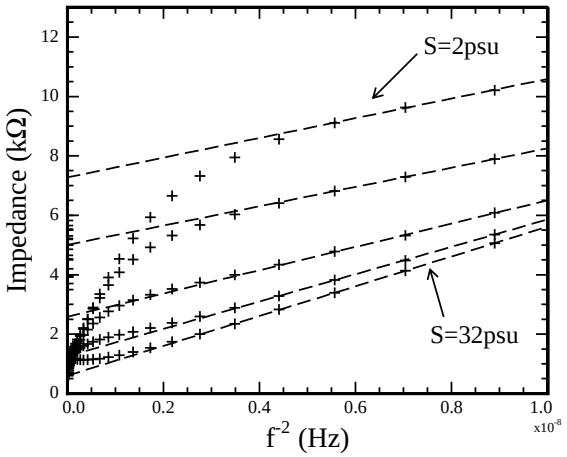

Figure 7.6: Measured 2-electrode cell impedance for the E_A cell as a function of f^{-2} at 5 different salinities (2, 4, 8, 16 and 32 psu). According to Equation 7.1, this relation should be locally linear for frequencies in the salinity window. Making a linear fit and extrapolation to infinite frequency ($f^{-2} = 0$) eliminates the double layer contribution to the impedance.

medium frequency response as

$$|Z| \approx R_w \left(1 + \frac{1}{2\omega^2 C_{dl}^2 R_w^2}\right) \tag{7.1}$$

Thus plotting the impedance as a function of inverse frequency squared (see Figure 7.6) will make the impedance in the salinity window linear with a slope depending on the double layer capacitance and an intersect at ω^{-2}=0 of R_w corresponding to conditions of a short circuited double layer capacitance at infinite frequency. The 18 kHz cell impedance (from Figure 7.2), the full fit impedance (from Figure 7.4) and the extrapolated impedance (from the axis intersection on Figure 7.6) of electrode design E_A are shown in Figure 7.7 as a function of resistivity. In all three cases, the relation is linear at low resistivities (lower than ~150 Ωcm corresponding to salinities higher than 4 psu) but suffers from parasitic conductance for higher resistivities. The relative standard deviation is 2% corresponding to an accuracy of 0.7 psu. Both the full fit and extrapolated cell constants are comparable to the theoretical cell constant determined through FEM simulation. The large offset of the single frequency data indicates that the effects of the double layer and series resistances are not completely avoided. The single frequency data can be used if the offset is zero compensated. The results will however be much more sensitive to changes in double layer capacitance compared to the other methods.

7.1.2 Four electrode configuration

The value of the double layer capacitance and the parasitic capacitance can both be altered by changing the chip design as shown in Section 2.1. However, introducing two more electrodes and measuring using the four electrode configuration improves the determination of the water conductivity significantly. In the following the performance of the three conductivity cell designs E_A, E_B and E_C is evaluated.

Using the four electrode configuration for conductivity measurements at a single frequency makes the measurement more tolerant to changes in double layer capacitance when taking the

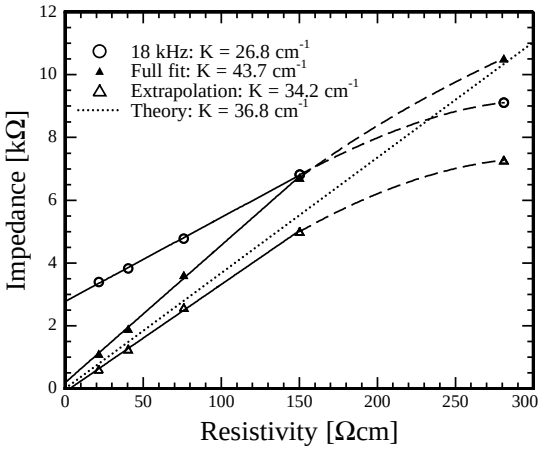

Figure 7.7: Measured 2-electrode cell impedance for the E_A cell as a function of water resistivity, found at 18 kHz single frequency (◯), found from a full fit (▲) and found through extrapolation (△). The reference water resistivities are measured with a commercial reference sensor. The impedance varies linearly with resistivity for all three cases when salinity is higher than 4 psu (Resistivity < ~150 Ωcm), with a relative standard deviation of ≈ 2% for all three cases. This corresponds to an accuracy of 0.7 psu. Both the full fit and extrapolated cell constants are comparable to the theoretical cell constant determined through FEM simulation. The single frequency data can be used if the offset is zero compensated. The results will however be much more sensitive to changes in double layer capacitance compared to the other methods.

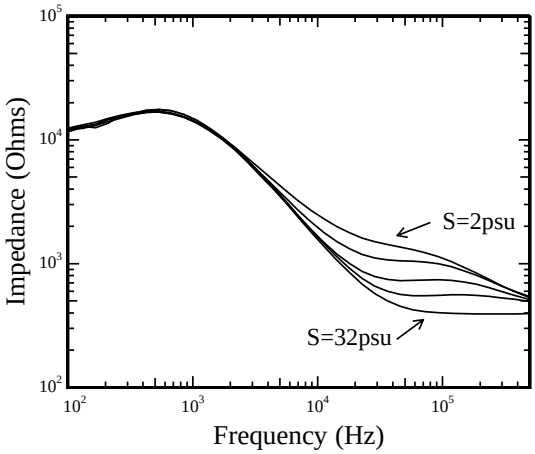

Figure 7.8: Measured 4-electrode cell trans-impedance as a function of frequency for the E_A cell at 5 different salinities (2, 4, 8, 16 and 32 psu). The trans-impedance at 18 kHz is used to construct Figure 7.11.

precautionary measures discussed in Section 2.1. A current is forced through the outer electrodes while measuring the voltage at the inner electrodes. The cell trans-impedance as a function of frequency for the three different geometries, (E_A, E_B and E_C) are shown in Figure 7.8, 7.9 and 7.10. The most linear resulting trans-impedances as functions of reference resistivities are shown in Figure 7.11. As expected the cell constant is much lower in the four electrode case than for the two electrode case, but the linearity is also much better. The measured and simulated cell constants

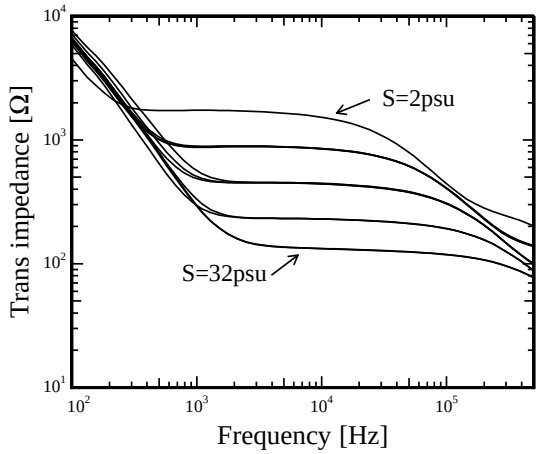

Figure 7.9: Measured 4-electrode cell trans-impedance as a function of frequency for the E_B cell at 5 different salinities (2, 4, 8, 16 and 32 psu). The salinity window is wider compared to E_A shown in Figure 7.2. The trans-impedance at 3.4 kHz is used to construct Figure 7.11.

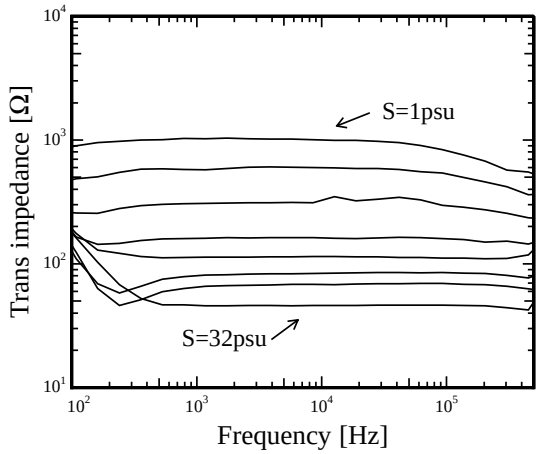

Figure 7.10: Measured 4-electrode cell trans-impedance as a function of frequency for the E_C cell at 8 different salinities (1, 2, 4, 8, 12, 16, 24 and 32 psu). The salinity window extents to fill almost the full frequency range and is wider compared to E_A and E_B shown in Figure 7.2 and 7.9. The trans-impedance at 3.4 kHz is used to construct Figure 7.11.

are summarized in Table 7.2. As seen the cell constants are in very good agreement with theory, except for the E_A four electrode case where the deviation is expected to be due to poor matching of the measurement equipment. Prior to the addition of a high impedance instrumentation amplifier stage the measurement equipment had an input impedance comparable to the voltage electrode contact impedance. The quite low cell constants of the configuration E_B and E_C four electrode measurements are tolerable, and the salinity windows are much wider compared to E_A allowing for a precise determination of conductivity. Figure 7.11 shows the four electrode trans-impedance as a function of reference resistivity for the E_A, E_B and E_C geometries. Clearly E_B and E_C delivers

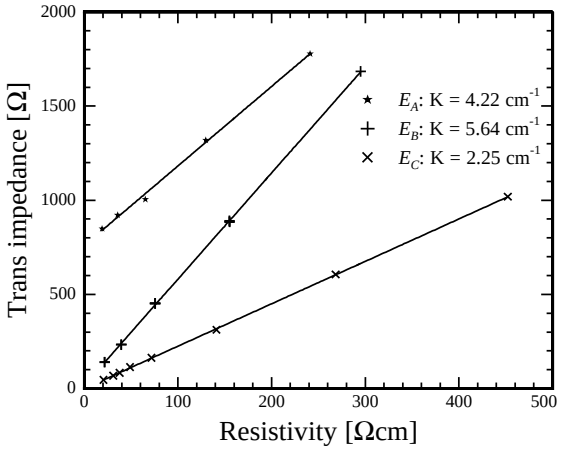

Figure 7.11: Measured 4-electrode conductivity cell trans-impedance as a function of water resistivity for the E_A cell at 18 kHz, the E_B cell at 3.4 kHz, and the E_C at 3.8 kHz. The reference resistivity is measured with a commercial reference sensor. Both E_B and E_C has a negligible offset. The E_C cell shows a linear response with a cell constant of 2.25 cm^{-1} and a low standard deviation which allows for determination of the salinitiy with an accuracy of ±0.1 psu

	K - 2 electrode [cm^{-1}]			K - 4 electrode [cm^{-1}]		
	E_A	E_B	E_C	E_A	E_B	E_C
Theoretical	36.8	14.0	3.4	13.6	6.6	2.8
Measured	26.8-43.7	14.0	6.9	4.2	5.6	2.25
Frequency [kHz]	18	5.6	4.9	18	3.4	3.8

Table 7.2: Table of cell constants for electrode designs E_A, E_B and E_C. The theoretical cell constants are found using FEM and the listed cell constants are measured at the frequency giving the highest degree of linearity (lowest relative standard deviation).

the best results with relative standard deviations of 0.5% and 0.3% respectively compared to 3% for E_A. Additionally the offsets are very close to zero. This means that the salinity can be measured with an accuracy of ±0.1 psu.

7.1.2.1 Evaluation of signal stability

The optimum measurement frequency is found by evaluating the linearity of the resistivity-impedance dependance at every measured frequency. For each frequency the impedance is plotted against the reference resistivity and the cell constant and the relative standard deviation is calculated. The cell constant/sensitivity and standard deviation from these fits as functions of frequency for the three electrode designs are shown in Figures 7.12, 7.13 and 7.14. Clearly E_C is very tolerant to changes in measurement frequency as the cell constant varies less than 2% for frequencies in the interval 2.5 kHz to 8.5 kHz. The relative standard deviation is also very low (~ 0.3%). Conversely, E_A is very sensitive to changes in measurement frequency or double layer capacitance as it is only reasonably linear in a narrow frequency band.

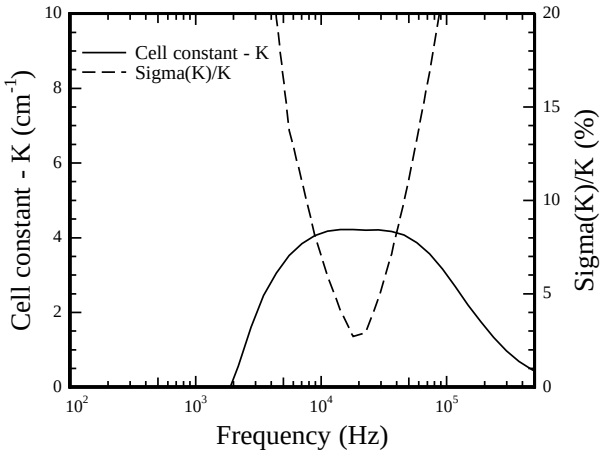

Figure 7.12: 4-electrode cell constant and relative standard deviation from the linear relation between the cell impedance and water resistivity as a function of frequency for the E_A cell design. The fitted cell constant is almost constant for frequencies from 10 kHz to 50 kHz. However, the impedance to resistivity relation is only linear in a very narrow frequency range around 18 kHz.

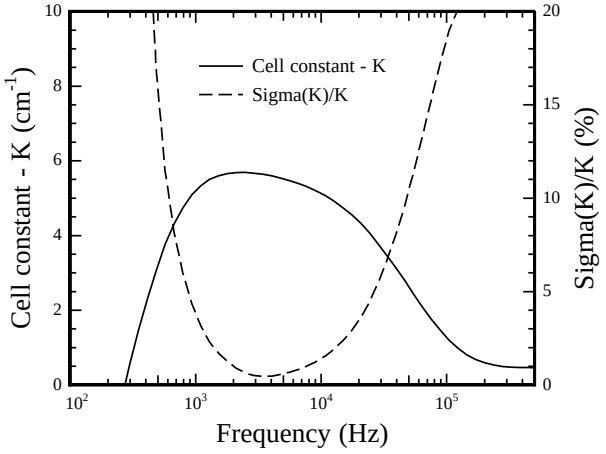

Figure 7.13: 4-electrode cell constant and relative standard deviation from the linear relation between the cell impedance and water resistivity as a function of frequency for the E_B cell design. The fitted cell constant is high but varying in the frequency range from 1 kHz to 10 kHz. However, the linearity of the impedance to resistivity relation is much better than for E_A.

7.1.3 Temperature dependence of conductivity

The above measurements are all performed near room temperature. As shown in Chapter 2 the conductivity changes rapidly with temperature. Therefore, the cell response to changing temperatures is investigated. The temperature effect on conductivity is investigated by cooling the outer reservoir to -2°C and the system is left for the temperature slowly to increase towards room temperature. The rate of the temperature change is less than 0.6°C/hour making the system in quasi-equilibrium. The trans-impedance of the cell at different frequencies is measured during

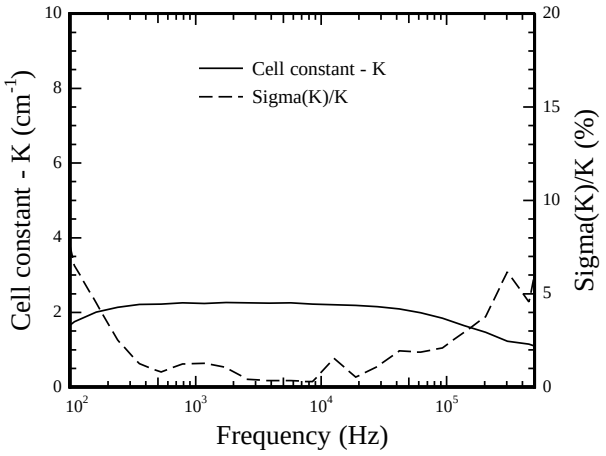

Figure 7.14: 4-electrode cell constant and relative standard deviation from the linear relation between the cell impedance and water resistivity as a function of frequency for the E_C cell design. The fitted cell constant is constant for frequencies from 500 Hz to 30 kHz and the linearity of the impedance to resistivity relation is excellent from 3 kHz to 9 kHz.

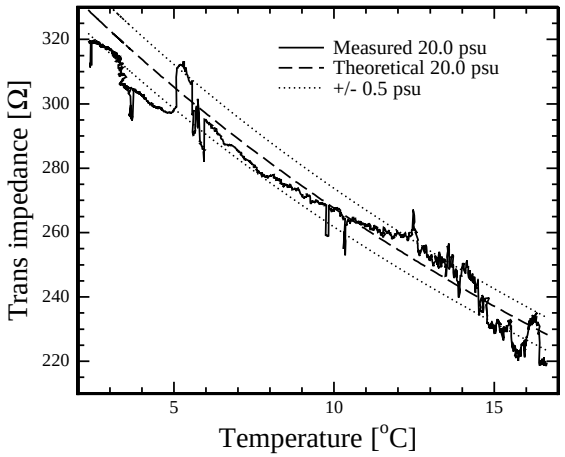

Figure 7.15: Measured and theoretical 3.4 kHz trans-impedance (E_B) as a function of temperature. The sensor has an accuracy of approximately ±0.5 psu. The variations in impedance are probably due to changes in the near electrode conditions such as air-bubbles or salt and organic debris.

the temperature rise. The system temperature is monitored with the chip temperature sensor and an external reference temperature sensor. The measured resulting 3.4 kHz trans-impedance of E_B as a function of temperature is shown in Figure 7.15. The theoretical temperature dependence is found using the cell constant calculated at 15°C. The resolution is 0.1 mScm^{-1}. The variations in impedance are probably due to changes in the near electrode conditions such as air-bubbles. Figure 7.16 shows the 10 kHz trans-impedance of E_C as a function of temperature. Cell design E_C has a 9.7 times larger electrode surface area and it appears to be much less sensitive to changes in the near electrode environment. The impedance of the cell deviates less than 0.1 psu from the impedance calculated from seawater state equations. The slightly different temperature depen-

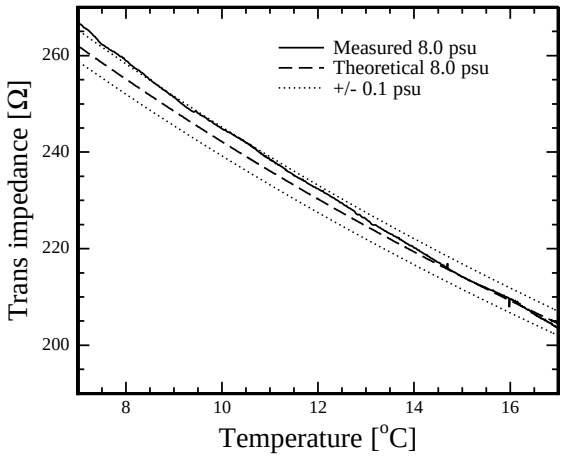

Figure 7.16: Measured and theoretical 10 kHz trans-impedance (E_C) as a function of temperature. The sensor has an accuracy of approximately ±0.1 psu. The lower variations in impedance (compared to electrode design E_B in Figure 7.15) are probably due to the larger electrode area making it less sensitive to changes in the near electrode conditions.

dence may be due to the difference in salt composition between the KCl samples and that of the seawater.

The accuracy of the conductivity determination also depends very much on the long time stability of the electrodes. Initial investigations have shown no significant algae growth or electrode degradation when exposed to an algae fermentation solution for periods of weeks. Therefore the accuracy is expected to be limited by the resolution.

At stabilized temperature the short term repeatability of the measurements is excellent and the long term measurements at varying temperatures indicates that the accuracy is actually as low as ±0.2 psu. Calibration of the cell against standard seawater samples may show an even better accuracy.

7.1.4 Conductivity sensor summary

The 2-electrode configuration has been investigated and small area electrodes without an applied double layer compensation technique shows a poor linearity between cell impedance and reference resistivity. Increasing the electrode size and using a 4-electrode configuration significantly improve the linearity and sensor accuracy while lowering the sensor sensitivity to changes in frequency and double layer capacitance. The E_C cell can thus measure the conductivity with an accuracy corresponding to ±0.2 psu even for varying temperature.

Further investigations of the cell impedance variations in the complete salinity, temperature and pressure parameter space have to be conducted in standard seawater samples. Furthermore, the long time stability of the sensor has to be investigated.

7.2 Temperature sensor

The temperature sensor is tested in a thermobath as shown in Figure 7.1. The large insulated thermal reservoir and continuous stirring ensures a high level of uniformity and quasi equilibrium

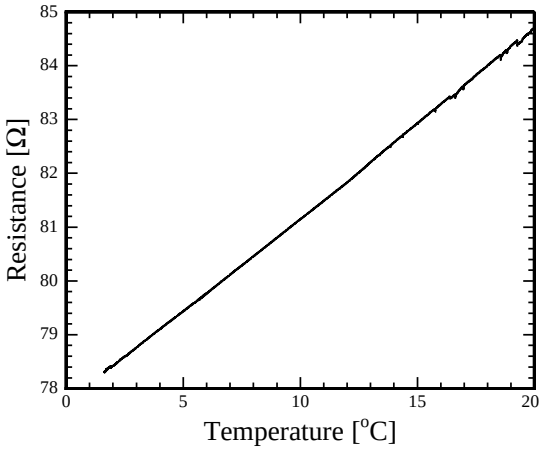

Figure 7.17: Measured thermistor resistance as a function of PT100 reference temperature. The reservoir is cooled to 2°C and the system is left to drift towards room temperature. The signal is more noisy for higher temperatures probably due to increased activity in the laboratory or changes in test equipment measurement range.

conditions. The sensor is placed inside the epoxy packaging in order to limit the sensitivity to fluctuations in the water temperature. In this way the noise within the sensor and from the thermobath is separated. The temperature coefficient of resistance of the $TiSi_2$ thermistor is measured by cooling a saturated saline solution and the outer reservoir to 2°C and letting the temperature rise slowly towards room temperature while monitoring the resistance of the thermistor and a commercial class A certified PT100 sensor. The measured $TiSi_2$ thermistor resistance as a function of PT100 reference temperature is shown in Figure 7.17. It is not immediately apparent whether the relation is slightly exponential or completely linear. For a linear relation the differential change in resistance ($\delta R/\delta T$) is constant whereas the relative differential change in resistance ($\delta R/\delta T/R$) is constant in the exponential case. Figure 7.18 shows the differential change in resistance and the relative differential change in resistance as a function of temperature. Most constant values are found for the exponential case, although the difference is minute. Full linear and exponential fits to the measured data gives standard deviations of 0.101°C and 0.046°C respectively. It is therefore impossible to conclude whether the relation is exponential or linear from this narrow temperature range. The relation can be considered locally linear or represented by an exponential expression, both with a TCR of 4.2×10^{-3} K^{-1}. This is comparable to 3.9×10^{-3} K^{-1} of the widely used platinum thermistors. The first generation doped silicon thermistors have a higher TCR of 7.6×10^{-3} K^{-1}, but also suffer from a much higher sensitivity to light. Figure 7.19 shows the deviation of measured data from the exponential fit for raw data, a 10 point moving average filter and a 10 point repeating average filter respectively. Clearly the noise level is below ±0.005°C, which is sufficient for the DST application.

7.2.1 Temporal response

The response time of the $TiSi_2$ temperature sensor is evaluated by submerging the calibrated chip into saline solutions at two different temperatures, 5°C and 30°C respectively. The calibrated measured temperature as a function of time for a $TiSi_2$ sensor within the epoxy packaging material and

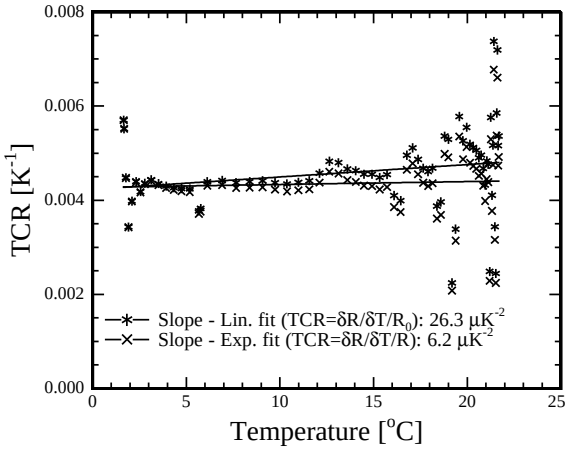

Figure 7.18: Temperature coefficient of resistance as a function of temperature as calculated from the linear and exponential model respectively. A slightly more constant TCR is found with the exponential model indicating that the resistivity dependence of temperature is slightly exponential, but can be considered locally linear in the narrow temperature range.

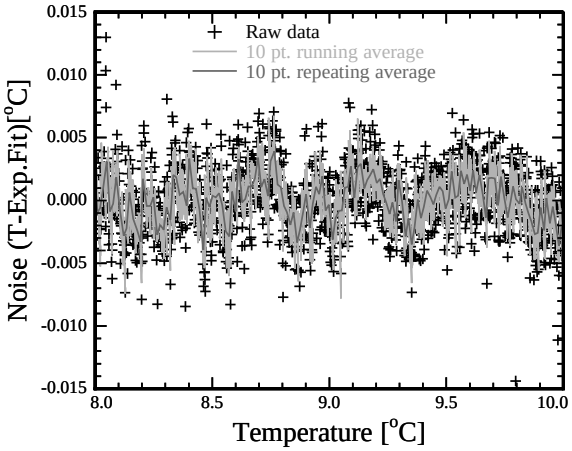

Figure 7.19: Noise in the temperature sensor. The noise is calculated as deviations in sensor reading from the fitted exponential model. It can however not be determined from these data whether the fluctuations stems from noise in the thermistor or it actually represents local temperature fluctuations in the media that the reference sensor is just to slow to detect. Applying various filters will of course reduce the apparent noise.

a fully exposed $TiSi_2$ sensor is shown in Figures 7.20 and 7.21. The encapsulated sensor takes 55 seconds to reach 66% of the temperature step for both heating and cooling. This is comparable to specifications of commercial DSTs. The fully exposed sensor reaches 66% of the temperature step in less than 1 second, which is much faster than the conventional sensors. The small 5°C temperature change of the exposed sensor that follows after 60 seconds, stems from residual heat from the connected packaging which is transported to the chip. The temperature sensor sensitivity to light is handled later in this chapter.

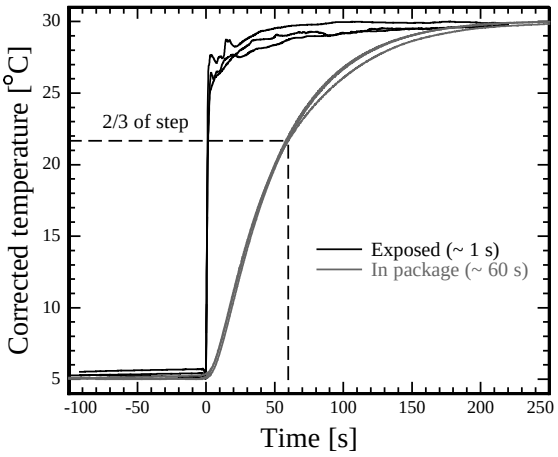

Figure 7.20: Temporal response of the temperature sensor when fully exposed and within the packaging. The sensors are moved from a 5°C thermal reservoir to a 30°C thermal reservoir while the resistance is monitored. The experiment is performed three times. The packaged sensor reaches 2/3 of the temperature step in 60 seconds while the exposed sensor reacts within 1 second. The small 5°C temperature change of the exposed sensor that follows after 60 seconds, stems from residual heat from the connected packaging which is transported to the chip.

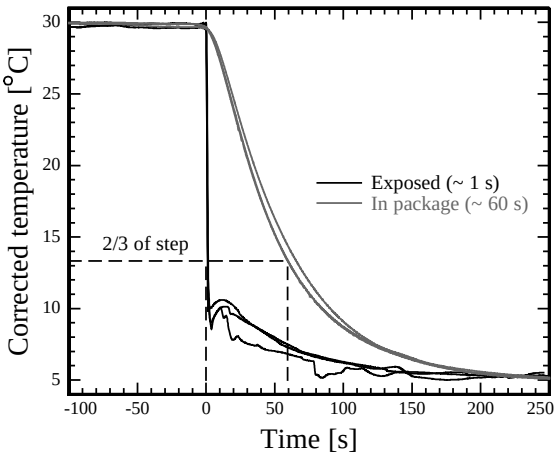

Figure 7.21: Temporal response of the temperature sensor when fully exposed and within the packaging. The sensors are moved from a 30°C thermal reservoir to a 5°C thermal reservoir while the resistance is monitored. The experiment is performed three times. The packaged sensor reaches 2/3 of the temperature step in 60 seconds while the exposed sensor reacts within 1 second. The small 5°C temperature change of the exposed sensor that follows after 60 seconds, stems from residual heat from the connected packaging which is transported to the chip.

7.2.2 Temperature sensor summary

The temperature coefficient of resistance as well as the temporal response of the temperature sensor has been investigated. The TCR is 4.2×10^{-3} K^{-1} and the linearity is excellent between 0°C and 20°C with a resolution of 0.005°C. The fully exposed temperature sensor has a short response time

and reaches 2/3 of a 25°C temperature step in less than 1 second.

Further thermal decoupling of the sensor from the packaging should be investigated in order to further improve the temporal response of the sensor.

7.3 Pressure Sensor

The pressure sensor performance is only sparsely evaluated since fabrication difficulties have resulted in very few devices with functioning pressure sensors. The pressure sensor output signal is tested mounting the sensor in a small pressure chamber fixture and by applying a constant voltage to the bridge while measuring the output voltage. The pressure is controlled using a commercial Druck DPI 510 pressure controller. The output to input ratio (V_{out}/V_{in}) as a function of pressure is shown in Figure 7.22. The sensor is tested up to 10 bar which is the operating range of the available pressure controller. The sensitivity is $S = 1.44 \times 10^{-7}$ Pa^{-1} which is very close to $S = 1.5 \times 10^{-7}$ Pa^{-1} predicted in Section 2.3.2.1 on Page 33. The relation between output voltage and pressure is not completely linear, which is most likely due to the glue that is used to make the reference cavity in absence of a pyrex bonded cavity. A linear fit is accurate to ±57 mbar (0.57% of full scale), which corresponds to 57 cm water column. Not enough measurements have been performed to estimate the resolution. The pressure sensor output is sensitive to changes in temperature. However, this can be compensated by doing a simultaneous measurement of temperature. The pressure sensor sensitivity to light is described in Section 7.5.2.1.

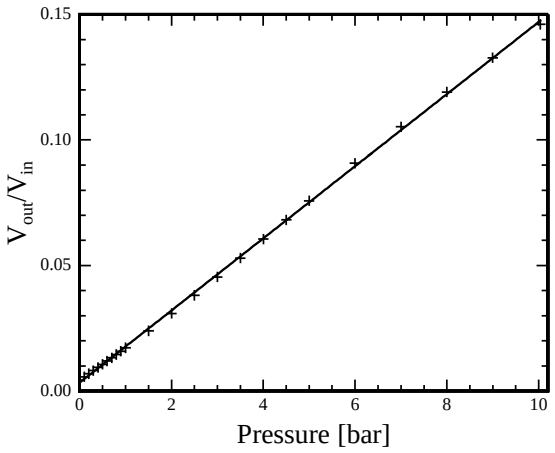

Figure 7.22: Relative pressure sensor voltage output as a function of pressure. The sensor is supplied with a constant current and the resulting bridge voltage is measured. The offset is close to zero and the output voltage is almost linear with pressure. The slight nonlinearity is most likely due to the glue that is used to make the reference cavity in absence of a pyrex bonded cavity.

7.3.1 Pressure sensor summary

The pressure sensor performance has only been sparsely investigated but shows a sensitivity of $S = 1.44 \times 10^{-7}$ Pa^{-1} as theoretically predicted. A number of investigations of the pressure sensor sensitivity, resolution and accuracy have to be performed for the full pressure range and at different temperatures in order to evaluate the performance of the sensor.

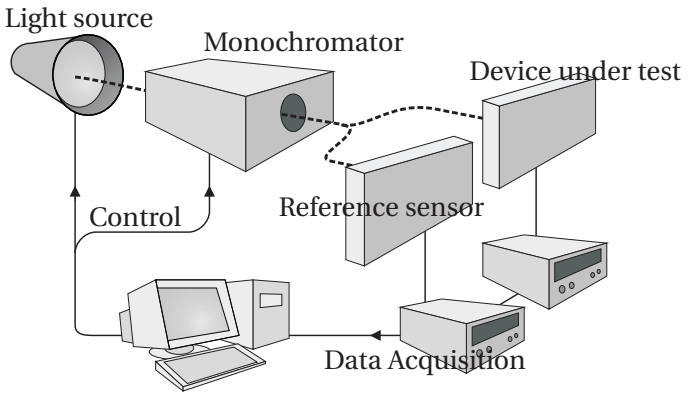

Figure 7.23: Quantum efficiency measurement setup. The light is directed through the monochromator and onto the two sensors. The resulting photogenerated current is detected with the picoammeters and data is collected.

7.4 Light sensor

The light sensor sensitivity is measured using a setup as illustrated in Figure 7.23. Light from a broad-spectrum light source is directed through a Jobyn Yvon monochromator, and the output beam is focussed into a dual core optical fiber with a splitter that divides the signal into two. The two light beams are focussed onto the light sensor under test (DUT) and onto a calibrated reference sensor (REF). It is vital for an accurate determination that the entire beam is within the sensor area. The photoinduced currents are measured using two Keithley 6485 picoammeters. The picoammeters have a bias voltage of less than 200 μV ensuring a low bias current. The photoinduced current, I_{ph}, in the two sensors is expressed as

$$I_{ph,DUT} = \Phi Q E_{DUT} \tag{7.2}$$
$$I_{ph,REF} = \Phi Q E_{REF} K \tag{7.3}$$

where Φ is the photon flux, QE_{DUT} and QE_{REF} is the quantum efficiency of the device under test and the calibrated reference sensor respectively, and K is the fiber splitter splitting ratio. All the above involved factors depend on the wavelength. The quantum efficiency is regarded as constant in the very narrow bandwidth of the light. The splitting ratio K takes into account that K times the flux in the one fiber runs in the other. K is found by measuring the current from two arbitrary sensors whereafter the sensors are interchanged and the measurement is repeated. This will yield the four equations

$$I_{ph,DUT,1} = \Phi Q E_{DUT} \tag{7.4}$$
$$I_{ph,REF,1} = \Phi Q E_{REF} K \tag{7.5}$$
$$I_{ph,REF,2} = \Phi Q E_{REF} \tag{7.6}$$
$$I_{ph,DUT,2} = \Phi Q E_{DUT} K \tag{7.7}$$

with four unknown variables. The splitting ratio is found as a function of the currents as

$$K = \sqrt{\frac{I_{ph,DUT,2} I_{ph,REF,1}}{I_{ph,DUT,1} I_{ph,REF,2}}} \tag{7.8}$$

The quantum efficiency of a device under test is then found as

$$QE_{DUT} = \frac{I_{ph,DUT,1} QE_{REF} K}{I_{ph,DUT,1}} \tag{7.9}$$

The measured quantum efficiency of a 1st generation pn-junction light sensor as a function of wavelength is shown in Figure 7.24 along with two theoretical quantum efficiencies. The theoretical quantum efficiencies are calculated from transfer matrices and a finite element diffusion model as described in Chapter 2. The quantum efficiency ranges between 40% to 70% in the visible domain. The quantum efficiency is however lowest in the blue part of the spectrum where light is predominantly transmitted in water. When comparing the measured quantum efficiency with the theoretical values two conclusions can be drawn. The silicon dioxide surface film appears thinner than the assumed 200 nm seen from the peak frequency positions on the spectrum. This is most likely true since cleaning steps will thin the silicon dioxide slightly during processing (Approx 20 seconds accumulated time in BHF corresponds to 30 nm over etch). If it is assumed that approximately 40% of the carriers created outside the depletion region are lost by surface or bulk recombination processes, the theory fits very well. The theoretically expected sensor current induced by light from sun light transmitted in the ocean as a function of depth is shown in Figure 2.26 on Page 40. The current is calculated on basis of the measured quantum efficiency and the spectral distribution calculated from simple absorption in clear water. This predicts a 50 nA signal at 100 m depth. In reality, a much lower photon flux may be present and the signal will therefore be much lower. The reverse leakage current is below 1 nA for a 1mV reverse bias and 100 nA for a 1 V reverse bias, which should allow for light detection at 100 m water depth.

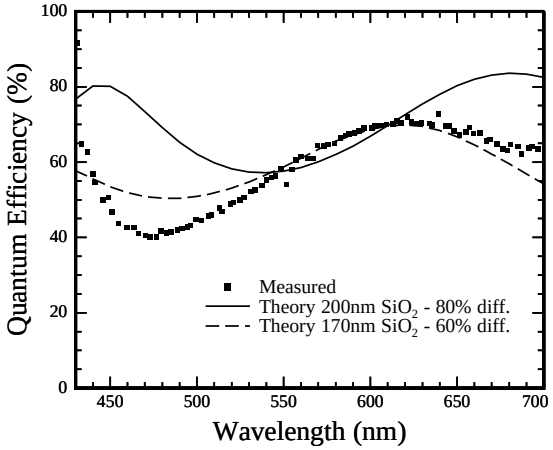

Figure 7.24: Measured quantum efficiency combined with theoretical results as a function of wavelength. The measured quantum efficiency is in very good agreement with a theory when assuming that the surface oxide film is 170 nm in thickness and that 60% of the carriers generated outside the depletion region diffuse and contribute to the current. The design model of 200 nm oxide and higher contribution from diffusion gives a slightly different result.

7.4.1 Light sensor summary

The light sensor quantum efficiency has been measured. The measured values between 40% and 70% and the wavelength dependency are close to the theoretically predicted.

A further verification of the quantum efficiency dependence of surface film composition and an investigation of the quantum efficiency variation over the wafer would yield valuable information on the sensor optimization and reproducibility.

7.5 Cross sensitivity

One problem with making multiple sensors in one chip is crosstalk. In single sensor devices, packaging can limit the influence from parameters other than the sensor parameter. Onesided crosstalk, where parameter A influences the parameter B sensor, but parameter B does not influence the parameter A sensor, can easily be taken into account through simple calibration. Much worse is mutual crosstalk where parameter A influence the parameter B sensor an visa versa. In this case iterative compensation might be necessary. In worst case the cross sensitivity is 1 to 1 and changes in A and B cannot be distinguished.

7.5.1 Conductivity, temperature and pressure

In the third generation multisensor, some crosstalk is present. As shown in Section 2.3, changes in temperature influence the sensitivity of the pressure sensor. The effective piezo coefficient changes with temperature as shown in Figure 2.14 on Page 31. Additionally, the resistance of the unstressed piezoresistors change with temperature (TCR = 6×10^{-4} K^{-1}). This effect is however reduced in the Wheatstone bridge. The temperature influence on pressure sensor output has not been measured. The calibration is however simple as the pressure does not influence the measurement of temperature if the temperature sensor is kept at a distance to the pressure membrane. The light sensor is also unaffected by changes in pressure under the same conditions.

The temperature also influences the measurement of light. The reverse saturation current of the pn-junction which determines the minimum detection limit, is a very strong function of temperature. The saturation current typically changes a factor of 16 for a 20°C change in temperature [16]. By making a dark-current measurement as a function of temperature, this influence can be subtracted. The sensitivity of the light sensor is also sensitive to temperature as the carrier diffusion changes with temperature. However, as the carrier lifetime is already very high compared to the diffusion distances, small changes in temperature have negligible influence.

The measurement of conductivity is not influenced by any of the other parameters, although changes in temperature may influence the performance of the interface electronics. Similarly, a change in conductivity does not influence the measurement of any of the other parameters.

7.5.2 Light

Light has a significant influence on both the measurement of pressure and temperature as the pressure sensor and the earlier version of the temperature sensor rely on pn-junction isolation of the resistors from the substrate. Incoming light generates carriers that contribute to a leakage current to the substrate. Depending on the interface electronics this effect can have a more or less significant effect. Additionally, the light also contributes to local heating in metal or metal silicide layers, which influence the measurement conducted with the $TiSi_2$ temperature sensor.

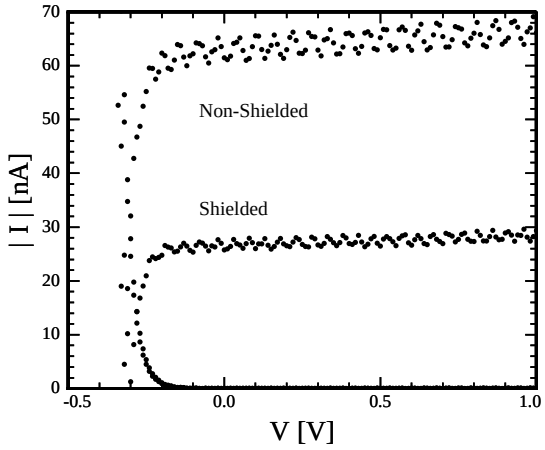

Figure 7.25: Reverse bias current for a pn-junction with and without shielding when illuminated with a broad spectra light source as well as under dark conditions. The reduction in light generated current is 57% when shielding the sensor. The shielding $TiSi_2$ film only covers an area ranging from 10 μm outside the sensor area. The carriers generated outside the shielded surface area can diffuse under the shielding and contribute to the current. The true transmission through the film is thus probably much lower than 57%.

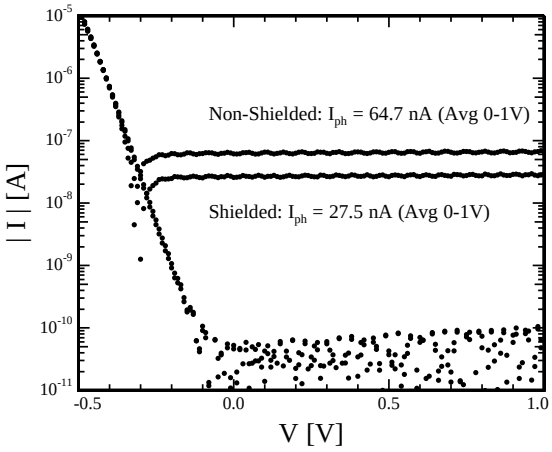

Figure 7.26: Reverse bias current for a pn-junction with and without shielding when illuminated with a broad spectra light source as well as under dark conditions on a logarithmic scale. The reduction in light generated current is 57% when shielding the sensor. The remaining light generated current is however still more than two decades higher than reverse saturation current.

7.5.2.1 Shielding of light

Reflective or absorption films can be fabricated on the surface above vulnerable sensors to shield off light. Figures 7.25 and 7.26 show the absolute reverse bias current from a pn-junction with and without an absorption layer under illumination as well as without illumination. Clearly, a large photocurrent is generated, and introducing a 220 nm $TiSi_2$ absorption layer yields a 57% reduction in reverse bias current. However, the shielding only covers an area ranging from 10 μm

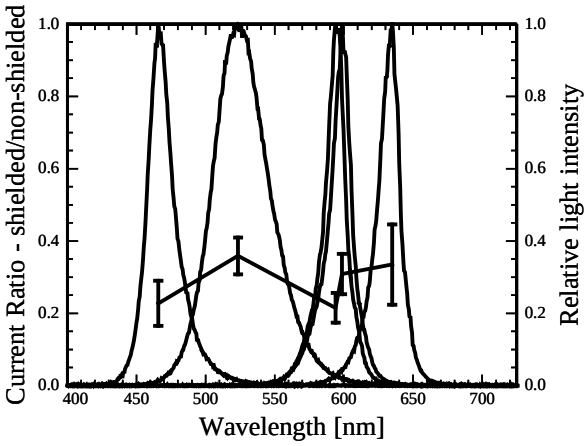

Figure 7.27: Ratio of reverse bias currents for a pn-junction with and without shielding when illuminated with light emitting diodes at different frequencies. The shielding efficiency shows no significant sensitivity to changes in wavelength.

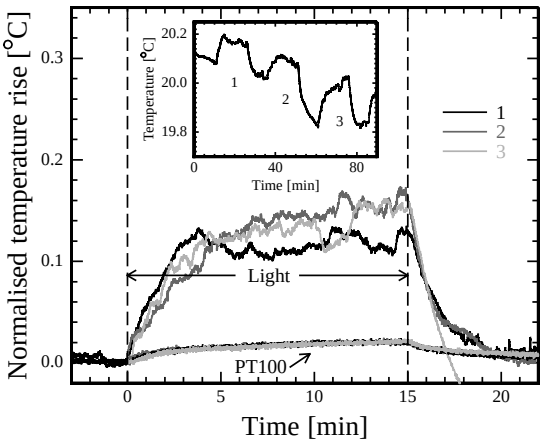

Figure 7.28: Temperature sensor signal rise induced by illumination by light. Three consecutive illumination periods (*insert*) is normalized to eliminate drift. The signal rise in the illumination periods is clearly not immediate and the effect is conclusively not an ionization effect. The signal decay after ended illumination is exponential as expected from thermal diffusion processes.

outside the sensor are, covering the sensor. Carriers generated in the substrate outside the area of the absorption layer can diffuse to the junction, thereby compromising the effectiveness of the absorption film. Furthermore, light of long wavelengths have a high penetration depth, which also limits the effectiveness of the film. The ratio between leakage currents in sensors with and without an absorption film is shown in Figure 7.27. The reverse bias currents are measured in pn-junctions when illuminated with light from four light emitting diodes. The effectiveness of the absorption layer ranges from 60% to 80% for wavelengths between 450 nm and 650 nm.

The temperature rise introduced by incoming light is measured by submerging a $TiSi_2$ temper-

ature sensor along with a PT100 reference sensor into a thermobath without stirring. The resistances are measured while the system is illuminated for 15 minutes at a time. Figure 7.28 shows the temperature rise introduced by light when the general temperature drift in the system has been compensated. Clearly, there is no carrier generation or ionization effect as these would be immediate. The sensor temperature reaches a steady state rise of up to 0.16°C under illumination, whereas the reference sensor only experiences one tenth of that temperature rise. This indicates that much of the light is absorbed directly in sensor resulting in a very local heat dissipation. Introducing stirring to the water and/or facing the sensor away from the light will reduce the photoinduced steady state temperature rise of the temperature sensor.

	Affected sensor			
	Conductivity	Temperature	Pressure	Light
Conductivity	-	No	No	No
Temperature	No	-	Yes	Yes
Pressure	No	No	-	No
Light	No	Yes	Yes	-

Table 7.3: Table of cross sensitivity

7.6 Summary

The individual sensors have been characterized for sensitivity and resolution and the relevant cross sensitivities have been investigated. The conductivities of the water samples are measured with an accuracy of 0.6 $mScm^{-1}$ and the temperature and pressure is measured with an accuracy of ±0.13°C and ±0.05 bar respectively. The salinity can therefore be detected with an accuracy of ±0.2 psu. The quantum efficiency of the light sensor ranges between 40% to 70% in the visible domain. The temporal response of all sensors can be considered as immediate. Additionally, most of the cross sensitivities arising from sensor integration are negligible. However, the signal rise in the temperature sensor under firm light illumination corresponds to approximately 0.01°C and light induced currents in the pn-junctions of the pressure sensor is still an issue that has to be addressed. The long time accuracy and stability has only been sparsely examined.

CHAPTER

8 Conclusion & Outlook

Conclusion

In this project, steps toward a new generation Data Storage Tag (DST) have been taken. The main focus has been on the development of an integrated silicon multi-sensor chip consisting of four sensors that can be directly exposed to the surrounding water. This leads to a very compact system with high accuracy and fast response times. Also three packaging concepts have been designed and evaluated. General aspects of DST electronics have been considered.

The multi-sensor chip consists of four sensors; a conductivity sensor, a thermistor, a pressure sensor and a light sensor. The theoretical aspects of the individual sensor designs have been investigated. A versatile bulk micromachining fabrication process has been designed and sub-steps have been optimized. Based on the theoretical sensor considerations and the designed fabrication process, three generations of multi-sensor chips have been designed and fabricated. The final chip is $3.9 \times 7.3 \times 1.2$ mm^3. The chips have been tested in a laboratory environment.

The electrical conductivity is measured by using four electrodes exposed to the surrounding water. The frequency dependence of the impedance of the electrochemical cell and the low and high cut-off frequencies change with electrode geometry. This has been investigated through analytical and numerical methods and verified through measurements. The frequency range in which conductivity can be measured range from 300 Hz to 300 kHz. In this frequency range the conductivity can be measured with a resolution of 0.14 psu. The expected accuracy when considering long time monitoring with changes in temperature is ±0.2 psu. The low cutoff frequency is obtained by optimizing the cell constant and electrode area product. Consequently the electrodes occupy much (23%) of the chip surface area, and the cell constant is relatively low, 2.25 cm^{-1}. The upper limit cut-off frequency is increased by applying a thick insulating oxide that lowers the parasitic substrate capacitance.

Thermistors are used to measure the temperature and both doped silicon and $TiSi_2$ thermistors have been investigated. Although doped silicon resistors potentially have a higher temperature coefficient of resistance (TCR) compared to metals, the high sensitivity to light makes doped resistors impractical in use on a chip for direct media exposure. $TiSi_2$ thermistors can effortlessly be introduced as $TiSi_2$ layers already function as highly conductive electrical wiring system in the fabrication process. The $TiSi_2$ has a TCR of 4.2×10^{-3} K^{-1} which is comparable to that of commercial resistive thermometers. The resolution is ±0.005°C and the accuracy is expected to be of the same magnitude. The response time of the exposed sensor is 1 second to reach 66% of a temperature

step compared to 20+ seconds of sensors in commercial DSTs.

The pressure sensor is only sparsely investigated as fabrication of piezoresistive pressure sensors is a well known technology. The width to thickness ratio of the flexible membrane is set to 29 which allows for a 20 bar full scale safe operating range with a high sensitivity of $V_{out}/(V_{in}p)$=1.5×10^{-7} Pa^{-1}. The accuracy is ±57 mbar which corresponds to 57 cm water column.

The conductivities of the water samples are measured with an accuracy of 0.6 mScm^{-1} and the temperature and pressure is measured with an accuracy of ±0.13°C and ±0.05 bar respectively. The salinity can therefore be detected with an accuracy of ±0.2 psu.

The light sensor consists of a silicon pn-junction. Due to fabrication constraints the optical transmission is not optimized for blue light transmission. However, the measured quantum efficiency is between 40% and 70% in the visible domain and the reverse saturation current is below 1 nA for a 1mV reverse bias. This means that sunrise and sunset events can be detected even with a very low light transmission through the water.

All the sensors are designed aiming at low power consumption.

The fabrication process is based on commercial bulk micromachined piezoresistive pressure sensor principles. It is extended to include $TiSi_2$ wires, local oxidation and platinum surface electrodes as well as a 3 layer chip stack made from two consecutive anodic bonds. The process substeps are optimized for process stability and adapted towards batch processing. In particular the $TiSi_2$ fabrication process is very dependent on wafer handling and the process parameters. Titanium and polycrystalline silicon, with low oxygen contamination, pre-annealed at 600°C and post-annealed at 850°C - 950°C yields an electrical resistivity of approximately 17 $\mu\Omega$cm. The $TiSi_2$ layer is subsequently covered by a Si_3N_4 film. This makes $TiSi_2$ an attractive alternative to metal wiring systems because of its high thermal stability.

Local oxidation of silicon is successfully used to make differentiated oxide thicknesses for the light sensor (200 nm oxide) and the conductivity sensor (3 μm oxide) as well as to completely isolate the individual sensors on an SOI substrate. Care has however to be taken to ensure that the Si_3N_4 film is of a sufficient thickness and quality to prevent oxidation of underlying silicon.

Careful anodic bonding allows for bonding of silicon wafers on both sides of a pyrex wafer, which effectively double the usable sensor area for a given chip size (not considering the chip thickness). Despite the promising results, a full process run, involving the successful fabrication of all four sensors on a single chip has not yet been performed. The available Si_3N_4 system has delivered films of varying quality resulting in no pressure sensor membranes being realized. Partial runs have though indicated that successful full processing is possible once a stable Si_3N_4 process has been established.

Three different packaging concepts are tested and epoxy potting in a polystyrene tube shows the most promising results for deep sea applications. Investigation of the water penetration processes show that diffusion through the bulk packaging material is sufficiently low for some epoxies. The water uptake by weight and water diffusion of EpoTek 302-3M is 3% and 1.5×10^{-9} cm^{2}s^{-1}, respectively. However, pressurized testing of the packaging reveals that water is creeping along the interface between the chip and the packaging material. Thus, material adhesion to the chip surface is a factor that has to be considered.

The power consumption and draft design of the DST electronics have been investigated. In most cases the power consumption of the sensors take up half the total power budget, and sensor measurement times of less than 100 ms and currents of less than 100 μA are desirable. This is

achievable with all sensors.

In the course of this project, one bachelor of science project and four master of science projects have been carried out with topics related to this project.

The results of the project have been presented at the *IEEE MEMS 2005* conference (poster), the *IEEE Sensors 2005* conference (oral presentation), the *Eurosensors 2006* conference (oral presentation) and the *IEEE MEMS 2007* conference (oral presentation). Additionally, the work has resulted in two publications in *Sensors and Actuators - A physical*.

The accuracy of the sensor is not as high as in macro size CTD profilers (0.2 psu compared to 0.005 psu), and does not yet meet the specification of salinity sensor accuracy proposed by DIFRES (0.01 psu). However, an accuracy of 0.2 psu is sufficiently high for most tracking purposes. The system volume is however much smaller (~5000×). The temperature sensor meets the specified accuracy of 0.01°C, and the pressure sensor meets the accuracy of 1 m (if full scale is 200 m) water column. The integrated salinity multi-sensor is successfully fabricated using conventional silicon micro-fabrication technology and is packaged using a novel Epoxy packaging scheme. The sensor has been used successfully in a lab environment and has proven stable when exposed to water with high concentration of algae culture.

In conclusion, this work shows that single multi-sensor chips for direct exposure with the use of an epoxy potting packaging concept has the potential of revolutionizing the performance of commercial DSTs in the coming years.

Outlook

Throughout this PhD project, profound knowledge has been obtained on multi-sensor integration and the issues of design of autonomous microsystems for operation in harsh environments. This in particular concerns fabrication process optimization and identification of packaging and electronics related challenges, which should all be combined into a full system design approach.

The next step is the final optimization of the multi-sensor containing the four sensors described in this thesis. One route is to exploit the three layered stack as developed in this project to divide the fabrication into two wafer designs each with a reduced fabrication complexity. One silicon wafer contains chips with a conductivity sensor and a temperature sensor. These sensors utilize the $TiSi_2$ wiring system and are completely dielectrically isolated from the substrate. The second wafer is an SOI wafer and contains chips with a pressure sensor and a light sensor. These sensors comprise doped regions in the device layer. The sensors are dielectrically isolated from each other by trenches in the device layer filled with SiO_2. This wafer does not necessarily need $TiSi_2$ wiring. The two wafers are anodically bonded to the same pyrex wafer. Because of the reduced fabrication complexity the yield can be increased, while obtaining the same or better performance.

Once the sensors can be fabricated with reasonable yield and high level of reproducibility, the functionality should be extended to include accelerometers, oxygen sensors or micro-compasses.

Furthermore, the failure mechanisms of the packaging concept should be investigated thoroughly and a completely reliable packaging scheme that is compatible with electronics and batteries should be developed.

Finally, electronics should be developed, which is optimized for space and power consumption and the subcomponents should be assembled to form the full autonomous system. This system needs intense laboratory testing, including testing when mounted on a fish in a controlled and

constrained environment.

Although the marked for data storage tags for fisheries research is relatively limit, the high demands within the field justifies a low volume commercial production. In addition, the lessons learned from the development and maturing of this technology can serve as a basis for autonomous measurement systems for many other applications.

Bibliography

[1] J.E. Steffensen J.C. Svendsen, K. Aarestrup and J. Herskin. A novel acoustic dissolved oxygen transmitter for fish telemetry. Marine Technology Society Journal, 40, 2006.

[2] K.H. Andersen and S. Neuenfeldt. Torskens hemmelige liv (danish: The secret life of the cod). Fisk & Hav (Danish: Fish & Sea), 61, 2006.

[3] J.D. Metcalfe and G.P. Arnold. Tracking fish with electronic tags. Nature, 387(6634):665, 1997.

[4] H. Hinrichsen S. Neuenfeldt and A. Nielsen. A method to geolocate eastern baltic cod by using data storage tags (dsts). In ICES CM, volume 6, 2004.

[5] S.S. Madsen C.J. Brauner, M. Seidelin and F.B. Jensen. Effects of freshwater hyperoxia and hypercapnia and their influences on subsequent seawater transfer in atlantic salmon (salmo salar) smolts. Canadian Journal of Fisheries and Aquatic Sciences, 57:2054–2064, 2000.

[6] J.F. Steffensen nad K. Johansen P.G. Bushnell. Oxygen consumption and swimming performance in hypoxia-acclimated reinbow trout (salmo gairdneri). The Journal of Experimental Biology, 113:225–235, 1984.

[7] S.R. Kerr G. Claireaux, D.M. Webber and R.G. Boutilier. Physiology and behaviour of free-swimming atlantic cod (gadus morhua) facing fluctuating salinity and oxygenation conditions. The Journal of Experimental Biology, 198:61–69, 1995.

[8] N.P. Fofonoff and R.C. Millard Jr. Algorithms for computation of fundamental properties of seawater. UNESCO technical paper in marine science 44, UNESCO, 1983.

[9] CEFAS Technology Ltd. (England). http://www.cefastechnology.co.uk/. Internet.

[10] Star-Oddi. http://www.star-oddi.com/. Internet.

[11] Edward Lyn Lewis. The practical salinity scale 1978 and its antecedents. IEEE Journal Of Oceanic Engineering, OE-5:3–8, 1980.

[12] E. Barsoukov and J.R. Macdonald (Ed.). Impedance Spectroscopy - Theory, Experiment and Applications. Wiley, 2005.

[13] Jeanett Norrbohm Sørensen. Establishment of a primary standard for electrolytic conductivity and new reference solutions. PhD thesis, Technical University of Denmark, April 2000.

[14] T. Van Duzer & J.R. Whinnery S. Ramo. Fields and Waves in Communication Electronics. Wiley, 1984.

[15] COMSOL Multiphysics. http://www.comsol.com/. Internet.

[16] Donald A. Neamen. Semiconductor Physics and Devices. McGraw-Hill, 3 edition, 2003.

[17] E. Obermeier P. Kopystynski. Polysilicon as a meterial for microsensor applications. Sensors and Actuators, A: Physical, 30:149–155, 1992.

[18] G. Schultes, M. Schmitt, D. Goettel, and O. Freitag-Weber. Strain sensitivity of tib2, tisi2, tasi2 and wsi2 thin films as possible candidates for high temperature strain gauges. Sensors & Actuators: A. Physical, 126(2):287–291, 2006.

[19] Simon M. Sze. Semiconductor Devices - Physics and Technology. John Wiley & Sons, 1985.

[20] D.A. Bittle, J.C. Suhling, R.E. Beaty, R.C. Jaeger, and R.W. Johnson. Piezoresistive stress sensors for structural analysis of electronic packages. Transactions of the ASME. Journal of Electronic Packaging, 113(3):203–215, 1991.

[21] Y. Kanda. A graphical representation of the piezoresistance coefficients in silicon. IEEE Transactions on Elctron Devices, pages 64–70, 1982.

[22] Y. Kanda. Piezoresistance effect of silicon. Sensors and Actuators A (Physical) , A28(2):83–91, 1991.

[23] R.J. Roark. Roarks. McGraw-Hill, Inc., 1989.

[24] J. Singh. Semiconductor optoelectronics Physics and technology. McGraw-Hill, 1995.

[25] F.L. Pedrotti & L.S. Pedrotti. Introduction to optics. Prentice Hall, 1993.

[26] J.A. del Alamo and R.M. Swanson. Measurement of steady-state minority-carrier transport parameters in heavily doped n-type silicon. IEEE Transactions on Electron Devices, 34(7):1580–1589, 1987.

[27] M.S. Tyagi and R. Van Overstraeten. Minority carrier recombination in heavily-doped silicon. Solid-State Electronics, 26(6):577–597, 1983.

[28] W. Gerlach, H. Schlangenotto, and H. Maeder. On the radiative recombination rate in silicon. Phys Status Solidi (A) Appl Res, 13(1):277–283, 1972.

[29] Silvaco.
http://www.silvaco.com. Internet, 2007.

[30] R.K. Ulrich, A.J. Phillips, D.H. Yi, W.D. Brown, and S.S. Ang. Mechanical stability of pecvd silicon nitride protective films over bondwires, bonds and bondpads during thermal stress. Microelectronics Reliability, 31(6):1237–1249, 1991.

[31] S.P. Murarka. Silicide films and their applications in microelectronics. Elsevier Science Limited, 1994.

[32] Søren Dahl Petersen. Mems multi sensor for use in greenhouses. Master's thesis, Technical University of Denmark, 2006.

[33] P.B. Griffin J.D. Plummer, M. Deal. Silicon VLSI technology : Fundamentals, practice and modeling. Prentice Hall., 2000.

[34] K. E. Bean W. R. Runyan. Semiconductor Integrated Circuit Processing Technology. Addison Wesley, 1990.

[35] Thomas Pedersen. Corrosion resistant capacitive pressure sensor. Master's thesis, Technical University of Denmark, 2006.

[36] A.J. Walker, K.Y. Le, J. Shearer, and M. Mahajani. Analysis of tungsten and titanium migration during esd contact burnout. IEEE Transactions on Electron Devices, 50(7):1617–1622, 2003.

[37] K. Maex. Silicides for integrated circuits: Tisi2 cosi2. Materials Science and Engineering: R: Reports, 11(2-3):vii–viii+53–153, 1993.

[38] T. Jarmar. High-resolution studies of silicide films for nano ic-components. PhD thesis, Uppsala University, 2005.

[39] Shin ichi Ogawa and T. Yoshida. Dependence of thermal stability of titanium silicide/silicon structure on impurities. Appl. Phys. Lett., 56(8):725–727, 1989.

[40] J P Ponpon and A Saulnier. Comparison of the growth kinetics of titanium silicide obtained by rta and furnace annealing. Semiconductor Science and Technology, 4(7):526–528, 1989.

[41] R.B. Fair. Rapid thermal processing : Science and technology. Academic press, 1993.

[42] A. Kalnitsky, P.K. Hurley, and A. Lepert. Dopants (p, ss, and b) in thee polycrystalline silicon/titanium silicide system: redistribution and activation. Journal of the Electrochemical Society, 144(3):1090–1095, 1997.

[43] Kaustav Banerjee, Ajith Amerasekera, Girish Dixit, and Chenming Hu. Temperature and current effects on small-geometry-contact resistance. Proceedings of the IEEE Hong Kong Electron Devices Meeting, pages 115–118, 1997.

[44] K.R. Williams and R.S. Muller. Etch rates for micromachining processing. Journal of Microelectromechanical Systems, 5(4):256–269, 1996.

[45] Peter A. Rasmussen. Cantilever-based Sensors for Surface Stress Measurements. PhD thesis, Technical University of Denmark, August 2003.

[46] S.M.L. Nai, J. Wei, P.C. Lim, and C.K. Wong. Silicon-to-silicon wafer bonding with gold as intermediate layer. Proceedings of the 5th Electronics Packaging Technology Conference (EPTC 2003), pages 119–24, 2003.

[47] S Weichel. Silicon to silicon wafer bonding for microsystem packaging and formation. PhD thesis, Technical University of Denmark, 2000.

[48] Simon T. Jespersen. Design and packaging concepts for mems pressure sensors. Master's thesis, Technical University of Denmark (DTU) - Department of Micro and Nanotechnology (MIC), August 2003.

[49] Dieter K. Schroder. Semiconductor Material and Device Characterization. John Wiley & Sons, 1990.

[50] R.F. Eduljee M.R. Vanlandingham and Jr. J.W. Gillespie. Moisture diffusion in epoxy systems. Journal of Applied Polymer Science, 71:787–798, 1999.

[51] I. Belov M. Lindgren and P. Leisner. Experimental evaluation of glob-top materials for use in harsh environments. International Microelectronics and Packaging Society, 2-4, 2005.

[52] Xu Chen Y.C. Lin. Investigation of moisture diffusion in epoxy systems: Experiments and molecular dynamics simulations. Chemical Physics Letters, 412:322–326, 2005.

[53] D.P. Seraphim L.L. Marsh, R. Lasky and G.S. Springer. Moisture solubility and diffusion in epoxy and epoxy-glass composites. IBM Journal of Research and Development, 28, 1984.

[54] K.W. Jacobsen J.P. Krog C. Christensen C. Pedersen, S.T. Jespersen and E.V. Thomsen. Combined differential and static pressure sensor based on a double-bridged structure. Sensors and Actuators A, 115:617–627, 2004.

[55] D. Snakenborg, Henning Klank, and J.P. Kutter. Microstructure fabrication with a co/sub 2/ laser system. Journal of Micromechanics and Microengineering, 14(2):182–189, 2004.

[56] Molex.
http://www.molex.com. Internet, 2007.

[57] Christine M. Mahoney, Albert J. Fahey, and Greg Gillen. Temperature-controlled depth profiling of poly(methyl methacrylate) using cluster secondary ion mass spectrometry. 1. investigation of depth profile characteristics. Analytical Chemistry, 79(3):828–836, 2007.

[58] Henkel.
http://henkel.com. Internet, 2007.

[59] P.P. Parlevliet, H.E.N. Bersee, and A. Beukers. Residual stresses in thermoplastic composites-a study of the literature-part i: Formation of residual stresses. Composites Part A, 37(11):1847–1857, 2006.

[60] EpoTek. http://www.epotek.com/. Internet.

[61] J. Comyn R.D. Adams and W.C. Wake. Structural Adhesive Joints in Engineering. Chapman & Hall, 1997.

[62] J. Crank. Mathematics of Diffusion. Oxford University Press, London, 1956.

[63] J. Janting. Sensor packaging for harsh environments. Encyclopedia of Sensors, IN PRESS, 2006.

[64] Ya-Jun Guo Y.J. Weitsman. A correlation between fluid-induced damage and anomalous fluid sorption in polymeric composites. Composites Science and Technology, 62, 2002.

[65] Y.J. Weitsman. Anomalous fluid sorption in polymeric composites and its relation to fluid-induced damage. Composites: Part A, 37, 2006.

[66] VARTA Microbattery GmbH.
http://www.varta-microbattery.com/en/oempages/index.htm. Internet, 2007.

[67] E.V. Thomsen A. Hyldgård, O. Hansen. Fish & chips: Single chip silicon mems ctdl salinity, temperature, pressure and light sensor for use in fisheries research. In IEEE MEMS 2005 proceedings, pages 303–306, 2005.

[68] M. Olesen T. Hedegaard O. Hansen & E.V. Thomsen A. Hyldgård, Í. Olafsdóttir. Fish & chips: Four electrode conductivity / salinity sensor on a silicon multi-sensor chip for fisheries research. In IEEE Sensors 2005 Proceedings, pages 1124–1127, 2005.

[69] J. Janting & E.V. Thomsen A. Hyldgård, K. Birkelund. Direct media exposure of mems multisensor systems using a potted-tube packaging concept. Sensors and Actuators A, IN PRESS, 2007.

[70] Ronald G. Perkin Edward Lyn Lewis. The practical salinity scale 1978: Fitting the data. IEEE Journal Of Oceanic Engineering, OE-5:9–16, 1980.

[71] P. Kopystynski E. Obermeier. Polysilicon as a material for microsensor applications. Sensors and Actuators, A: Physical, 30:149–155, 1992.

[72] Jacob Buur M. Myrup Andreasen. Generel Problemløsning, Konstruktion og Produktudvikling (Danish). Institut for Konstruktionsteknik, DTH, Lyngby, Denmark, 1984.

[73] Scientific United Nations Educational and Cultural Organization (UNESCO).
http://www.unesco.org. Internet.

[74] Microchip Technology Inc. http://www.microchip.com. Internet, 2002.

[75] Sten Munch-Petersen. Fiskebestande og fiskeri i 2003 (danish). Report 115-02, Danmarks Fiskeriundesøgelser, Afd. for Havfiskeri, Charlottenlund Slot, 2920 Charlottenlund, November 2002.

[76] Bo Lundgren. Teknik for fjernmåling af fødeindtag hos fritsvømmende fisk (danish). Fisk og Hav, 45:65–74, 1994.

[77] et. al. John L. Daschbach. Microelectrodes: Theory and Applications, volume 197 of NATO ASI Series. Kluwer Academic Publishers, 1990.

[78] H.D.Abruña. Electrochemical Interfaces, Modern Techniques for In-Situ Interface Characterization. VCH Publishers Inc., 1991.

[79] Jerry Goodisman. Electrochemistry: Theoretical Foundations. John Wiley & Sons, 1987.

[80] Søren P. Rybro Christian B. Nielsen and Erik V. Thomsen. Design Handbook - for the Multiple Project Wafer (MPW). MIC - Deparment of Micro and Nanotechnology, 2003.

[81] Gary S. May and Simon M. Sze. Fundamentals of Semiconductor Fabrication. John Wiley & Sons, 2004.

[82] Stephen D. Senturia. Microsystem Design. Kluwer Academic Publishers, 2002.

[83] Jasprit Singh. Semiconductor Optoelectronics - Physics and Technology. McGraw-Hill, 1995.

[84] Vilhjalmur Thorsteinsson. Tagging methods for stock assessment and research in fisheries. Report of Concerted Action FAIR CT.96.1394, Marine Research Institute, Reykjavik, Iceland, 2002.

[85] Jannik H. Nielsen. Low Power CMOS Interface Circuitry for Sensors and Actuators. PhD thesis, Technical University of Denmark, December 2003.

[86] Jacob Richter & Anders Hyldgård. Design of a generic testchip - for a multi project wafer process. 2002.

[87] W.B. Stine & R.W. Harrigan. Solar Energy Systems Design. John Wiley & Sons, revised for internet edition, 1985. http://www.powerfromthesun.net.

[88] Martin Pumera et al. Contactless conductivity detector for microship capillary electrophoresis. Analytical Chemistry, 74(9), May 2002.

[89] Frederic Laugere et al. On-chip contactless four-electrode conductivity detection for capillary electrophoresis devices. Analytical Chemistry, 75(2), January 2003.

[90] J. Ronald V. Zaneveld W. Scott Pegau, Deric Gray. Absorption and attenuation of visible and near-infrared light in water: dependence on temperature and salinity. Applied Optics, 36(24), August 1997.

[91] M.J. Devlin and M.J. Lourey. Water Quality field and analytical procedures. Australian Institute of Marine Science, Townsville, 2000.

[92] Stein Sandven Johnny A. Johannessen and Dominique Durand. Oceanography - The Century of Space Science, chapter 65, page 1585Ű1622. Kluwer Academic Publishers, 2001.

[93] Anders Hyldgård. Design of a test setup for fluid chips fabricated in the sensonor mpw process. 2003.

[94] J. Bausells. SensoNor Foundry Processes Design Handbook. SensoNor asa, 1999.

[95] Wildlife Computers. http://www.wildlifecomputers.com/. Internet.

[96] C. Vahlas, P.Y. Chevalier, and E. Blanquet. A thermodynamic evaluation of four si-m (m = mo, ta, ti, w) binary systems. Calphad, 13(3):273–292, 1989.

[97] D. D. Denton, D. R. Day, D. F. Priore, S. D. Senturia, E. S. Anolick, and D. Scheider. Moisture diffusion in polyimide films in integrated circuits. Journal of Electronic Materials, 14(2):119–136, 1985.

[98] Texas Instruments.
ez430-f2013 development tool, http://www.ti.com. Internet, 2006.

APPENDIX

A Salinity

A definition of salinity based on the work in several different laboratories [11][70] is stated in the *UNESCO Practical Salinity Scale of 1978-PSS78*:

> "The practical salinity, symbol S, of a sample of sea water, is defined in terms of the ratio K of the electrical conductivity of a sea water sample of 15°C and the pressure of one standard atmosphere, to that of a potassium chloride (KCl) solution, in which the mass fraction of KCl is 0.0324356, at the same temperature and pressure. The K value exactly equal to one corresponds, by definition, to a practical salinity equal to 35."

In Oceanographic applications the salinity is measured using a CTD method, where salinity is deducted from well acknowledged polynomial equations from **C**onductivity, **T**emperature and **D**epth. In most practical oceanographic applications the change in conduction is dominated by the temperature. The *UNESCO* formula for calculating salinity S is given by

$$S = \sum_{i=0}^{5} a_i R_T^{i/2} + \left[\frac{T-15}{1+0.0162(T-15)} \right] \sum_{i=0}^{5} b_i R_T^{i/2} \tag{A.1}$$

valid for

$$\begin{aligned} 2‰ \leq \quad & S \quad \leq 32‰ \\ -2°C \leq \quad & T \quad \leq 35°C \end{aligned}$$

where T is the temperature (°C) and R_T is the temperature and pressure compensated ratio between the measured conductivity and the conductivity of standard seawater. $a_0 - a_5$ and $b_0 - b_5$ are constants:

$a_0 =$ 0.0080	$b_0 =$ 0.0005
$a_1 =$ -0.1692	$b_1 =$ -0.0056
$a_2 =$ 25.3851	$b_2 =$ -0.0066
$a_3 =$ 14.0941	$b_3 =$ -0.0375
$a_4 =$ -7.0261	$b_4 =$ 0.0636
$a_5 =$ 2.7081	$b_5 =$ -0.0144

In practice the conductivity ratio R is measured at some salinity S, temperature T and pressure p in relation to the standard seawater at standard conditions. This relation can be expressed as:

$$\begin{aligned} R &= \frac{C(S,T,p)}{C(35,15,0)} = \frac{C(S,T,p)}{C(S,T,0)} \cdot \frac{C(S,T,0)}{C(35,T,0)} \cdot \frac{C(35,T,0)}{C(35,15,0)} \\ &= R_p \cdot R_T \cdot r_T \end{aligned} \tag{A.2}$$

where R_p is the pressure correction factor (Eq. A.3) and r_T is the temperature correction factor (Eq. A.4). The value of R_T which should be used in (A.1) can be found as

$$R_T = \frac{R}{r_T \cdot R_p} = \frac{R}{r_T(1+\alpha)}$$

where

$$\alpha = \frac{A_1 p + A_2 p^2 + A_3 p^3}{1 + B_1 T + B_2 T^2 + B_3 R + B_4 T R} \tag{A.3}$$

and

$$\begin{aligned} A_1 &= 2.070 \cdot 10^{-5} \\ A_2 &= \text{-}6.370 \cdot 10^{-10} \\ A_3 &= 3.989 \cdot 10^{-15} \\ B_1 &= 3.426 \cdot 10^{-2} \\ B_2 &= 4.464 \cdot 10^{-4} \\ B_3 &= 4.215 \cdot 10^{-1} \\ B_4 &= \text{-}3.107 \cdot 10^{-3} \end{aligned}$$

(using the convention that p is measured in decibar ($p = 0$ at atmospheric) and T in °C)
r_T can be found by means of the following polynomial expression:

$$r_T = \sum_{i=0}^{4} c_i T^i \tag{A.4}$$

where

$$\begin{aligned} c_0 &= 6.766097 \cdot 10^{-1} \\ c_1 &= 2.00564 \cdot 10^{-2} \\ c_2 &= 1.104259 \cdot 10^{-4} \\ c_3 &= \text{-}6.9689 \cdot 10^{-7} \\ c_4 &= 1.0031 \cdot 10^{-9} \end{aligned}$$

(T in °C)

Calculating the Salinity from CTD data

In order to calculate the salinity from measured conductivity, temperature and depth data, the following steps should be followed:

1. Calculate the ratio R between the measured conductivity and that of standard seawater ($C(35, 15, 0) = 42.914$ mS/cm)).

2. Evaluate expression (A.3) and (A.4) for the measured temperature and pressure.

3. Calculate R_T and insert it in expression (A.1) to get the salinity.

Examples

A CTD measurement of $C = 35.73$ mS/cm, $T = 10$°C and $p = 100$ decibar (approx 100 m depth) will lead to the following results:

$$\begin{aligned} R &= \frac{35.730}{42.914} = 0.8326 \\ \alpha &= 0.00121 \\ r_T &= 0.8875 \\ R_T &= 0.9370 \\ S &= 32.554 \end{aligned}$$

If the data is $C = 35.73$ mS/cm, $T = 20$°C and $p = 100$ decibar the result will be:

$$\begin{aligned} R &= \frac{35.730}{42.914} = 0.8326 \\ \alpha &= 0.00095 \\ r_T &= 1.1165 \\ R_T &= 0.7450 \\ S &= 25.212 \end{aligned}$$

Changing the pressure to that of surface water ($p = 0$ decibar) will lead to:

$$\begin{aligned} R &= \frac{35.730}{42.914} = 0.8326 \\ \alpha &= 0 \\ r_T &= 1.1165 \\ R_T &= 0.7457 \\ S &= 25.239 \end{aligned}$$

Thus the most significant influence on the conductivity - salinity relation comes from the temperature, whereas small changes in pressure have little influence.

	$S \sim 35$	$S \sim 7$
$\Delta T \sim 0.005$°C	$\rightarrow \Delta S \sim 0.006$	$\rightarrow \Delta S \sim 0.0009$
$\Delta p \sim 0.1$ decibar	$\rightarrow \Delta S \sim 0.0001$	$\rightarrow \Delta S \sim 0.0000$
$\Delta C \sim 0.01$ mS/cm	$\rightarrow \Delta S \sim 0.015$	$\rightarrow \Delta S \sim 0.008$

Figure A.1: The influence of inaccuracies in the measured data on the calculation of the salinity.

APPENDIX

B

Process flow for the 3rd generation multi-sensor

Equipment used in alphabetic order

- Alcatel: Alcatel SCM 600 E-beam metal deposition system
- EVC Aligner: Electro Vision Contact aligner AL6-2
- EVG NIL: Nano Imprint Lithography and Anodic bonder
- Boron-drive: High temperature annealing and diffusion furnace for boron doped wafers
- Boron-predep: High temperature annealing and diffusion furnace for pre-deposition of boron
- Ion implanter (Smart Implants, England)
- Jipelec RTP: Rapid Thermal Annealing equipment
- LPCVD Nitride: Low Pressure Chemical Vapor Deposition furnace for deposition of silicon nitride
- LPCVD Poly: Low Pressure Chemical Vapor Deposition furnace for deposition of polycrystalline silicon
- HMDS oven: IMTEC Star2000
- Plasma Asher: Model 300 Autoload PC Plasma Processor
- Phosphorus-drive: High temperature annealing and diffusion furnace for phosphorus doped wafers
- Phosphorus-predep: High temperature annealing and diffusion furnace for pre-deposition of phosphorus
- RIE1: Surface Technology System Reactive Ion Etcher
- TEOS oxide: Low Pressure Chemical Vapor Deposition furnace for deposition of TEOS glass
- Track 1: SSI System 150

Terms used in the tables

- SP: Fabrication cost of current step
- ST: Time elapsed during current step
- TP: Total Fabrication cost at given process step
- TT: Total Time elapsed at given process step

All amounts in Danish kroner (DDK) which equals €0.13 (July 2007). Price is excluding labour, ion-implantation and mask-cost. Implantation cost is estimated at €4600.

Step	Description	Parameters	Schematic/notes	Time &Price
0	Silicon wafer	n-type SOI 4" wafer with (100) orientation. Device layer: Thickness: 3μm±1μm Resistivity: 1-20 Ωcm Buried layer: Thickness: 1μm Handle wafer: Thickness: 400μm Resistivity: 1-20 Ωcm Double sided polished.		ST: 0:00 h:m TT: 0:00 h:m SP: 10000DDK TP: 10000DDK
1	**Oxidation**			
1.1	RCA clean		Removes impurities from the surface by Stripping the wafer of its native oxide layer. (optional)	ST: 3:00 h:m TT: 3:00 h:m SP: 0DDK TP: 10000DDK
1.2	SiO_2	Furnace: A1 Boron-drive Recipe: Wet1150 Time: 60 min Temp: 1150°C Thickness: 600nm		ST: 4:00 h:m TT: 7:00 h:m SP: 720DDK TP: 10720DDK
2	**LPCVD Nitride**			
2.1	LPCVD	Furnace: B2 LPCVD Nitride Recipe: NITRIDE Time: 25 min Temp: 850°C Thickness: 120nm		ST: 2:30 h:m TT: 9:30 h:m SP: 1960DDK TP: 12680DDK
3	**TEOS Oxide**			
3.1	TEOS	Furnace: B3 TEOS Oxide Recipe: TEOSPNE Time: 36 min Temp: 725°C Thickness: 400nm		ST: 3:00 h:m TT: 12:30 h:m SP: 2470DDK TP: 15150DDK

Table B.1: Process flow for the 3rd generation multi-sensor (Part I)

Step	Description	Parameters	Schematic/notes	Time &Price
4	**Photolithography**		LOCOS	
4.1	HMDS	Machine: HMDS Recipe: 4 Rest: 10 min	Makes the surface hydrophilic and thereby improving the adhesion of the photoresist.	ST: 0:30 h:m TT: 13:00 h:m SP: 110kry TP: 15260DDK
4.2	Spinner	Machine: Track 1 Recipe: PR1_5 Thickness: 1.5μm Hot plate time: 60s Hot plate temp: 90°C		ST: 0:30 h:m TT: 13:30 h:m SP: 390DDK TP: 15650DDK
4.3	UV exposure	Machine: EV Aligner Mask: LOCOS Mode: Hard contact Exposure: 10s N_2 pressure: 0.5bar		ST: 1:00 h:m TT: 14:30 h:m SP: 260DDK TP: 15910DDK
4.4	Develop	Bench: Dev1 (Dev2) Time: 60s		ST: 0:25 h:m TT: 14:55 h:m SP: 0DDK TP: 15910DDK
4.5	Hardbake	Furnace: 120°C oven Time: 30 min Temp: 120°C	Increases adhesion and chemical stability.	ST: 0:30 h:m TT: 15:25 h:m SP: 0DDK TP: 15910DDK
5	**BHF-etch**			
5.1	BHF-etch	Bench: Oxide Etch 1 Time: 10 min		ST: 0:15 h:m TT: 15:40 h:m SP: 0DDK TP: 15910DDK
5.2	Acetone dip	Bench: Photo strip Bath 1 Time: 30s Bath 2 Time: 3 min +US		ST: 0:15 h:m TT: 15:55 h:m SP: 0DDK TP: 15910DDK
6	**Nitride-etch**			
6.1	H_3PO_4	Bench: Nitride-etch Time: 60 min		ST: 2:30 h:m TT: 18:25 h:m SP: 410DDK TP: 16320DDK
7	**BHF-etch**			
7.1	BHF-etch	Bench: Oxide Etch 1 Time: 15 min		ST: 0:20 h:m TT: 18:45 h:m SP: 0DDK TP: 16320DDK

Table B.2: Process flow for the 3rd generation multi-sensor (Part II)

Step	Description	Parameters	Schematic/notes	Time &Price
8	**LOCOS Oxide**			
8.1	RCA clean	Bench: RCA Temp: 70°C	Removes impurities from the surface by Stripping the wafer of its native oxide layer.	ST: 3:00 h:m TT: 21:45 h:m SP: 0DDK TP: 16320DDK
8.2	Wet SiO_2	Furnace: A1 Boron-drive Recipe: Wet1150 Time: $4\times11 hour$ Temp: 1150°C Thickness: 2.5μm	The LOCOS process consists of a cequence of oxidations followed by a BHFecth. In this way the process time and cost is minimized.	ST: 56:00 h:m TT: 77:45 h:m SP: 10528DDK TP: 26848DDK
9	**Nitride-etch**			
9.1	H_3PO_4	Bench: Nitride-etch Time: 60 min		ST: 2:30 h:m TT: 80:15 h:m SP: 410DDK TP: 27258DDK
10	**Photolithography**		Phosphorus	
10.1	HMDS	Furnace: HMDS Recipe: 4 Rest: 10 min	Makes the surface hydrophilic and thereby improving the adhesion of the photoresist.	ST: 0:30 h:m TT: 80:45 h:m SP: 110DDK TP: 27368DDK
10.2	Spinner	Machine: Track 1 Recipe: PR1_5 Thickness: 1.5μm Hot plate time: 60s Hot plate temp: 90°C		ST: 0:30 h:m TT: 81:15 h:m SP: 390DDK TP: 27758DDK
10.3	UV exposure	Machine: EV Aligner Mask: N-well Mode: Hard contact Time: 10s N_2 pressure: 0.5bar		ST: 1:30 h:m TT: 82:45 h:m SP: 390DDK TP: 28148DDK
10.4	Develop	Bench: Dev1 (Dev2) Time: 60s		ST: 0:25 h:m TT: 83:10 h:m SP: 0DDK TP: 28148DDK
10.5	Hardbake	Furnace: 120°C oven Time: 30 min Temp: 120°C	Increases adhesion and chemical stability.	ST: 0:30 h:m TT: 83:40 h:m SP: 0DDK TP: 28148DDK
11	**BHF-etch**			
11.1	BHF-etch	Bench: Oxide Etch 1 Time: 15 min		ST: 0:20 h:m TT: 84:00 h:m SP: 0DDK TP: 28148DDK
11.2	Acetone dip	Bench: Photo strip Bath 1 Time: 30s Bath 2 Time: 3 min +US		ST: 0:15 h:m TT: 84:15 h:m SP: 0DDK TP: 28148DDK

Table B.3: Process flow for the 3rd generation multi-sensor (Part III)

Step	Description	Parameters	Schematic/notes	Time &Price
12	**n-type Predep**			
12.1	RCA clean	Bench: RCA Temp: 70°C		ST: 3:00 h:m TT: 87:15 h:m SP: 0DDK TP: 28148DDK
12.2	Phosphorus Predep	Furnace: A4 Phosphorus-predep Recipe: POCL 1000 Time: 60 min Temp: 1000°C		ST: 4:00 h:m TT: 91:15 h:m SP: 720sDDK TP: 28868DDK
13	**Re-Oxidize**			
13.1	Phosphorus Drive	Furnace: A3 Phosphorus-drive Recipe: Wet1000 Time: 20 min Temp: 1000°C Thickness: 200nm		ST: 4:00 h:m TT: 95:15 h:m SP: 720DDK TP: 29588DDK
14	**Photolithography**		Phosphorus	
14.1	HMDS	Furnace: HMDS Recipe: 4 Rest: 10 min		ST: 0:30 h:m TT: 95:45 h:m SP: 110DDK TP: 29698DDK
14.2	Spinner	Machine: Track 1 Recipe: PR1_5 Thickness: 1.5μm Hot plate time: 60s Hot plate temp: 90°C Hot plate time: 60s		ST: 0:30 h:m TT: 96:15 h:m SP: 390DDK TP: 30088DDK
14.3	UV exposure	Machine: EV Aligner Mask: Boron Mode: Hard contact Exposure: 10s N_2 pressure: 0.5bar		ST: 1:30 h:m TT: 97:45 h:m SP: 390DDK TP: 30478DDK
14.4	Develop	Bench: Dev1 (Dev2) Time: 60s		ST: 0:25 h:m TT: 98:10 h:m SP: 0DDK TP: 30478DDK
14.5	Hardbake	Furnace: 120°C oven Time: 30 min Temp: 120°C	Increases adhesion and chemical stability.	ST: 0:30 h:m TT: 98:40 h:m SP: 0DDK TP: 30478DDK
15	**BHF-etch**			
15.1	BHF-etch	Bench: Oxide Etch 1 Time: 15 min		ST: 0:20 h:m TT: 99:00 h:m SP: 0DDK TP: 30478DDK
15.2	Acetone dip	Bench: Photo strip Bath 1 Time: 30s Bath 2 Time: 3 min +US		ST: 0:15 h:m TT: 99:15 h:m SP: 0DDK TP: 30478DDK

Table B.4: Process flow for the 3rd generation multi-sensor (Part IV)

Step	Description	Parameters	Schematic/notes	Time &Price
16	**Boron Predep**			
16.1	RCA clean	Bench: RCA Temp: 70°C		ST: 3:00 h:m TT: 102:15 h:m SP: 0DDK TP: 30478DDK
16.2	Boron Pre-dep	Furnace: A2 Boron Predep Recipe: BP975 Time: 60 min Temp: 975°C Gas flow: Process/Cool down (O_2/N_2) 0.2SCCM/5SCCM 0SCCM/5SCCM		ST: 4:00 h:m TT: 106:15 h:m SP: 720DDK TP: 31198DDK
17	**Boron Drive**			
17.1	BHF-etch	Bench: Oxide Etch 1 Time: 15 min		ST: 0:20 h:m TT: 106:35 h:m SP: 0DDK TP: 31198DDK
17.2	Boron Drive	Furnace: A1 Boron Drive Recipe: DRY1000 Time: *?? min* Temp: 1000°C Thickness: 100nm		ST: 3:30 h:m TT: 110:05 h:m SP: 630DDK TP: 31828DDK
18	**Photolithography**		Phosphorus	
18.1	HMDS	Furnace: HMDS Recipe: 4 Rest: 10 min		ST: 0:30 h:m TT: 110:35 h:m SP: 110DDK TP: 31938DDK
18.2	Spinner	Machine: Track 1 Recipe: PR1_5 Thickness: 1.5μm Hot plate time: 60*s* Hot plate temp: 90°C		ST: 0:30 h:m TT: 111:05 h:m SP: 390DDK TP: 32328DDK
18.3	UV exposure	Machine: EV Aligner Mask: Piezo Mode: Hard contact Time: 10*s* N_2 pressure: 0.5bar		ST: 1:30 h:m TT: 112:35 h:m SP: 390DDK TP: 32718DDK
18.4	Develop	Bench: Dev1 (Dev2) Time: 60*s*		ST: 0:25 h:m TT: 113:00 h:m SP: 0DDK TP: 32718DDK
18.5	Plasma Asher	Machine: Asher Recipe: 35 Time: 4 min		ST: 0:30 h:m TT: 113:30 h:m SP: 110DDK TP: 32828DDK
18.6	Hardbake	Furnace: 250°C oven Time: 30 min Temp: 250°C	Increases adhesion and chemical stability.	ST: 0:30 h:m TT: 114:00 h:m SP: 0DDK TP: 32828DDK

Table B.5: Process flow for the 3rd generation multi-sensor (Part V)

Step	Description	Parameters	Schematic/notes	Time &Price
19	**Ion Implanting**			
19.1	Boron Implant	Machine: Implanter Dose: ??? cm^{-2} Beam: 50KeV AC: 100μA		
19.2	Plasma Asher	Machine: Asher Recipe: 35 Time: 10 min		ST: 0:30 h:m TT: 114:15 h:m SP: 110DDK TP: 32828DDK
20	**Re-oxidize**			
20.1	RCA clean	Bench: RCA Temp: 70°C		ST: 3:00 h:m TT: 117:15 h:m SP: 0kr TP: 32828kr
20.2	Boron Drive	Furnace: A1 Boron Drive Recipe: Wet900 Time: 30 min Temp: 900°C Thickness: 200nm total Gas flow: P/C 0.2/5 0/5		ST: 3:30 h:m TT: 120:35 h:m SP: 630kr TP: 33458kr
21	**Photolithography**		Phosphorus	
21.1	HMDS	Furnace: HMDS Recipe: 4 Rest: 10 min	Makes the surface hydrophilic and thereby improving the adhesion of the photoresist.	ST: 0:30 h:m TT: 121:05 h:m SP: 110kr TP: 33568kr
21.2	Spinner	Machine: Track 1 Recipe: PR1_5 Thickness: 1.5μm Hot plate time: 60*s* Hot plate temp: 90°C		ST: 0:30 h:m TT: 121:35 h:m SP: 390kr TP: 33958kr
21.3	UV exposure	Machine: EV Aligner Mask: Oxide contacts Mode: Hard contact Time: 10*s* N_2 pressure: 0.5bar		ST: 1:30 h:m TT: 123:05 h:m SP: 390kr TP: 34348kr
21.4	Develop	Bench: Dev1 (Dev2) Time: 60*s*		ST: 0:25 h:m TT: 123:30 h:m SP: 0kr TP: 34348kr
21.5	Hardbake	Furnace: 120°C oven Time: 30 min Temp: 120°C	Increases adhesion and chemical stability.	ST: 0:30 h:m TT: 124:00 h:m SP: 0kr TP: 34348kr

Table B.6: Process flow for the 3rd generation multi-sensor (Part VI)

Step	Description	Parameters	Schematic/notes	Time &Price
22	**BHF-etch**			
22.1	BHF-etch	Bench: Oxide Etch Time: 7 min		ST: 0:15 h:m TT: 124:15 h:m SP: 0kr TP: 34348kr
22.2	Acetone dip	Bench: Photo strip Bath 1 Time: 30*s* Bath 2 Time: 3 min +US		ST: 0:15 h:m TT: 124:30 h:m SP: 0kr TP: 34348kr
23	**LPCVD POLY**			
23.1	RCA clean	Bench: RCA temp: 70°C	***Parking 5 wafers until the quality of the poly silicon is confirmed***	ST: 3:00 h:m TT: 127:30 h:m SP: 0kr TP: 34348kr
23.2	LPCVD POLY	Furnace: B4 LPCVD Poly Recipe: poly630 Time: 10.5 min Temp: 900°C Thickness: 100nm		ST: 3:00 h:m TT: 130:30 h:m SP: 2360kr TP: 36708kr
24	**Photolithography**		Phosphorus	
24.1	HMDS	Furnace: HMDS Recipe: 4 Rest: 10 min	Makes the surface hydrophilic and thereby improving the adhesion of the photoresist.	ST: 0:30 h:m TT: 131:00 h:m SP: 110kr TP: 36818kr
24.2	Spinner	Machine: Track 1 Recipe: PR1_5 Thickness: 1.5μm Hot plate time: 60*s* Hot plate temp: 90°C		ST: 0:30 h:m TT: 131:30 h:m SP: 390kr TP: 37208kr
24.3	UV exposure	Machine: EV Aligner Mask: Silicide Mode: Hard contact Time: 10*s* N_2 pressure: 0.5bar		ST: 1:30 h:m TT: 133:00 h:m SP: 390kr TP: 37598kr
24.4	Develop	Bench: Dev1 (Dev2) Time: 60*s*		ST: 0:25 h:m TT: 133:25 h:m SP: 0kr TP: 37598kr
24.5	Plasma Asher	Machine: Asher Recipe: 35 Time: 4*s*		ST: 0:30 h:m TT: 133:55 h:m SP: 110kr TP: 37708kr
24.6	Hardbake	Furnace: 120°C oven Time: 30 min Temp: 120°C	Increases adhesion and chemical stability.	ST: 0:30 h:m TT: 134:25 h:m SP: 110kr TP: 37818kr

Table B.7: Process flow for the 3rd generation multi-sensor (Part VII)

Step	Description	Parameters	Schematic/notes	Time &Price
25	**Poly-etch**			
25.1	Poly-etch	Time: 2 min	BHF-etch for 15*s* to improve selectivity to poly silicon (optional)	ST: 0:20 h:m TT: 134:45 h:m SP: 0kr TP: 37818kr
25.2	Acetone dip	Bench: Photo strip Bath 1 Time: 30*s* Bath 2 Time: 3 min +US		ST: 0:15 h:m TT: 135:00 h:m SP: 0kr TP: 37818kr
26	**Silicide**			
26.1	BHF-etch	Bench: Oxide Etch Time: 15*s*	Removal of native oxide for improved silicide quality. Steps 26.1-26.5 must be made in direct sequence.	ST: 0:15 h:m TT: 135:00 h:m SP: 0kr TP: 38958kr
26.2	Ti Deposition	Machine: Alcatel Thickness: 44nm	Steps 26.1-26.5 must be made in direct sequence.	ST: 3:00 h:m TT: 138:00 h:m SP: 1140kr TP: 38958kr
26.3	RTP	Machine: Jipelec RTP Recipe: Ahy_prea Time: 5 min Temp: 650°C	Steps 26.1-26.5 must be made in direct sequence.	ST: 10:00 h:m TT: 148:00 h:m SP: 1370kr TP: 40328kr
26.4	Piranha	Glass Beaker: 7-up H_2O_2(20%):H_2SO_4(80%) Time: 5 min	Steps 26.1-26.5 must be made in direct sequence.	ST: 0:30 h:m TT: 148:30 h:m SP: 0kr TP: 40328kr
26.5	RTP	Machine: Jipelec RTP Recipe: Ahy_anne Time: 1 min Temp: 950°C	Steps 26.1-26.5 must be made in direct sequence. ***Parking 5 wafers until the quality of the nitride is confirmed in KOH-etch***	ST: 5:00 h:m TT: 153:30 h:m SP: 690kr TP: 41018kr
27	**LPCVD Nitride**			
27.1	Piranha	Glass Beaker: 7-up H_2O_2(20%):H_2SO_4(80%) Time: 5 min		ST: 0:30 h:m TT: 154:00 h:m SP: 0kr TP: 41018kr
27.2	LPCVD	Furnace: B2 LPCVD Nitride Recipe: NITRIDE Time: 25 min Temp: 850°C Thickness: 120nm Pressure: 230mTorr		ST: 3:00 h:m TT: 157:00 h:m SP: 2360kr TP: 43378kr

Table B.8: Process flow for the 3rd generation multi-sensor (Part VIII)

Step	Description	Parameters	Schematic/notes	Time &Price
28	**TEOS Oxide**			
28.1	TEOS	Furnace: B3 TEOS Oxide Recipe: TEOSPNE Time: 36 min Temp: 725°C Thickness: 400nm		ST: 3:00 h:m TT: 160:00 h:m SP: 2470 kr TP: 45848kr
29	**Photolithography**		Membrane	
29.1	HMDS	Furnace: HMDS Recipe: 4 Rest: 10 min	Makes the surface hydrophilic and thereby improving the adhesion of the photoresist.	ST: 0:30 h:m TT: 160:30 h:m SP: 110kr TP: 45958kr
29.2	Spinner	Machine: Track 1 Recipe: PR1_5 Thickness: 1.5μm Hot plate time: 60s Hot plate temp: 90°C	Front side	ST: 0:30 h:m TT: 161:00 h:m SP: 390kr TP: 46348kr
29.3	Hardbake	Furnace: 120°C oven Time: 30 min Temp: 120°C	Increases adhesion and chemical stability.	ST: 0:30 h:m TT: 161:30 h:m SP: 0kr TP: 46348kr
29.4	Spinner	Machine: Track 1 Recipe: PR1_5 Thickness: 1.5μm Hot plate time: 60s Hot plate temp: 90°C	Backside	ST: 0:30 h:m TT: 162:00 h:m SP: 390kr TP: 46738kr
29.5	UV exposure	Machine: EV Aligner Mask: Membrane Mode: Hard contact Exposure: 10s N_2 pressure: 0.5bar		ST: 1:30 h:m TT: 163:30 h:m SP: 390kr TP: 47128kr
29.6	Develop	Bench: Dev1 (Dev2) Time: 60s		ST: 0:25 h:m TT: 163:55 h:m SP: 0kr TP: 47128kr
29.7	Hardbake	Furnace: 120°C oven Time: 30 min Temp: 120°C	Increases adhesion and chemical stability.	ST: 0:30 h:m TT: 164:25 h:m SP: 0kr TP: 47128kr
30	**BHF-etch**			
30.1	BHF-etch	Time: 10 min		ST: 0:15 h:m TT: 164:40 h:m SP: 0kr TP: 47128kr
30.2	Acetone dip	Bench: Photo strip Bath 1 Time: 30s Bath 2 Time: 3 min +US		ST: 0:15 h:m TT: 164:55 h:m SP: 0kr TP: 47128kr

Table B.9: Process flow for the 3rd generation multi-sensor (Part IX)

Step	Description	Parameters	Schematic/notes	Time &Price
31	**Nitride-etch**			
31.1	H_3PO_4	Bench: Nitride-etch Time: 60 min		ST: 2:30 h:m TT: 168:25 h:m SP: 410kr TP: 47538kr
32	**KOH-etch**			
32.1	KOH	Bench: KOH1 Time: 4*hour* Temp: 80°C	BHF-etch for 15*s* to improve selectivity to silicon	ST: 5:00 h:m TT: 173:25 h:m SP: 820kr TP: 48358kr
33	**TEOS**			
33.1	RCA clean		Removes impurities from the surface by Stripping the wafer of its native oxide layer.	ST: 3:00 h:m TT: 176:25 h:m SP: 0kr TP: 48358kr
33.2	TEOS Oxide	Furnace: TEOS Oxide Recipe: TEOSPNE Time: 36 min Temp: 725°C Thickness: 400nm		ST: 3:00 h:m TT: 179:25 h:m SP: 2470kr TP: 50828kr
34	**Photolithography**		Front side	
34.1	HMDS	Machine: HMDS Recipe: 4 Rest: 10 min	Makes the surface hydrophilic and thereby improving the adhesion of the photoresist.	ST: 0:30 h:m TT: 179:55 h:m SP: 110kr TP: 50938kr
34.2	Spinner	Machine: Track 1 Recipe: PR1_5 Thickness: 1.5μm Hot plate time: 60*s* Hot plate temp: 90°C		ST: 0:30 h:m TT: 180:25 h:m SP: 390kr TP: 51328kr
34.3	Hardbake	Furnace: 120°C oven Time: 30 min Temp: 120°C	Increases adhesion and chemical stability.	ST: 0:30 h:m TT: 180:55 h:m SP: 0kr TP: 51328kr
35	**BHF-etch**		Backside	
35.1	BHF-etch	Bench: Oxide Etch Time: 10 min		ST: 0:15 h:m TT: 181:10 h:m SP: 0kr TP: 51328kr
35.2	Acetone dip	Bench: Photo strip Bath 1 Time: 30*s* Bath 2 Time: 3 min +US		ST: 0:15 h:m TT: 181:25 h:m SP: 0kr TP: 51328kr

Table B.10: Process flow for the 3rd generation multi-sensor (Part X)

Step	Description	Parameters	Schematic/notes	Time &Price
36	**Nitride-etch**			
36.1	H_3PO_4	Bench: Nitride-etch Time: 60 min		ST: 2:30 h:m TT: 183:55 h:m SP: 410kr TP: 51738kr
37	**BHF-etch**			
37.1	BHF-etch	Bench: Oxide Etch 1 Time: 10 min		ST: 0:15 h:m TT: 184:10 h:m SP: 0kr TP: 51738kr
38	**Photolithography**		Membrane	
38.1	HMDS	Furnace: HMDS Recipe: 4 Rest: 10 min	Makes the surface hydrophilic and thereby improving the adhesion of the photoresist.	ST: 0:30 h:m TT: 184:40 h:m SP: 110kr TP: 51848kr
38.2	Spinner	Machine: Track 1 Recipe: PR1_5 Thickness: 1.5μm Hot plate time: 60s Hot plate temp: 90°C		ST: 0:30 h:m TT: 185:10 h:m SP: 390kr TP: 52238kr
38.3	UV exposure	Machine: EV Aligner Mask: Nitride Mode: Hard contact Time: 10s N_2 pressure: 0.5bar		ST: 1:30 h:m TT: 186:40 h:m SP: 390kr TP: 52628kr
38.4	Develop	Bench: Dev1 (Dev2) Time: 60s		ST: 0:25 h:m TT: 187:05 h:m SP: 0kr TP: 52628kr
38.5	Hardbake	Machine: 120°C oven Time: 30 min Temp: 120°C	Increases adhesion and chemical stability.	ST: 0:30 h:m TT: 187:35 h:m SP: 0kr TP: 52628kr
39	**RIE**			
39.1	RIE	Machine: RIE 1 Recipe: OH_POLYA Time: 2:45 min		ST: 3:00 h:m TT: 190:35 h:m SP: 1750kr TP: 54378kr
39.2	Acetone dip	Bench: Photo strip Bath 1 Time: 30s Bath 2 Time: 3 min +US		ST: 0:15 h:m TT: 190:50 h:m SP: 0kr TP: 54378kr

Table B.11: Process flow for the 3rd generation multi-sensor (Part XI)

Step	Description	Parameters	Schematic/notes	Time &Price
40	**Photolithography**		Contact metal	
40.1	HMDS	Furnace: HMDS Recipe: 4 Rest: 10 min		ST: 0:30 h:m TT: 191:20 h:m SP: 110kr TP: 54488kr
40.2	Spinner	Machine: Track 1 Recipe: PR2_2 Thickness: 2.2μm Hot plate time: 60s Hot plate temp: 90°C		ST: 0:30 h:m TT: 191:50 h:m SP: 390kr TP: 54878kr
40.3	UV exposure	Machine: EV Aligner Mask: Contacts Mode: Hard contact Exposure: 7s N_2 pressure: 0.5bar		ST: 1:30 h:m TT: 193:20 h:m SP: 390kr TP: 55268kr
40.4	Reverse baking	Machine: Track 1 Recipe: REV_100S Time: 100s Temp: 120°C		ST: 0:20 h:m TT: 193:40 h:m SP: 260kr TP: 55528kr
40.5	Flood exposure	Machine: EV Aligner Mode: Exposure only Time: 25-30 s		ST: 0:15 h:m TT: 193:55 h:m SP: 70kr TP: 55598kr
40.6	Develop	Bench: Dev1 (Dev2) Time: 60s		ST: 0:25 h:m TT: 194:20 h:m SP: 0kr TP: 55598kr
40.7	Plasma Asher	Machine: Asher Recipe: 35 Time: 4 min		ST: 0:30 h:m TT: 194:50 h:m SP: 110kr TP: 55708kr
41	**Contact metal**			
41.1	Metal deposition	Machine: Alcatel Ti thichness: 30nm Au thickness: 300nm		ST: 4:00 h:m TT: 198:50 h:m SP: 1520kr TP: 57228kr
41.2	Lift-off	Bench: Lift-off Time: 10-20 min+US		ST: 0:30 h:m TT: 199:20 h:m SP: 0kr TP: 57228kr

Table B.12: Process flow for the 3rd generation multi-sensor (Part XII)

Step	Description	Parameters	Schematic/notes	Time &Price
42	**Photolithography**		Electrode metal	
42.1	HMDS	Furnace: HMDS Recipe: 4 Rest: 10 min		ST: 0:30 h:m TT: 199:50 h:m SP: 110kr TP: 57338kr
42.2	Spinner	Machine: Track 1 Recipe: PR2_2 Thickness: 2.2μm Hot plate time: 60s Hot plate temp: 90°C		ST: 0:30 h:m TT: 200:20 h:m SP: 390kr TP: 57728kr
42.3	UV exposure	Machine: EV Aligner Mask: Electrode Mode: Hard contact Exposure: 7s N_2 pressure: 0.5bar		ST: 1:30 h:m TT: 201:50 h:m SP: 390kr TP: 58118kr
42.4	Reverse baking	Machine: Track 1 Recipe: REV_100S Time: 100s Temp: 120°C		ST: 0:20 h:m TT: 202:10 h:m SP: 260kr TP: 58378kr
42.5	Flood exposure	Machine: EV Aligner Mode: Exposure only Time: 25-30 s		ST: 0:15 h:m TT: 202:25 h:m SP: 70kr TP: 58448kr
42.6	Develop	Bench: Dev1 (Dev2) Time: 60s		ST: 0:25 h:m TT: 202:50 h:m SP: 0kr TP: 58448kr
42.7	Plasma Asher	Machine: Asher Recipe: 35 Time: 4 min		ST: 0:30 h:m TT: 203:20 h:m SP: 110kr TP: 58558kr
43	**Electrode metal**			
43.1	Metal deposition	Machine: Alcatel Ti thichness: 30nm Pt thickness: 300nm		ST: 3:00 h:m TT: 206:20 h:m SP: 1137kr TP: 59695kr
43.2	Lift-off	Bench: Lift-off Time: 10-20 min+US		ST: 0:30 h:m TT: 206:50 h:m SP: 0kr TP: 59695kr

Table B.13: Process flow for the 3rd generation multi-sensor (Part XIII)

Step	Description	Parameters	Schematic/notes	Time &Price
44	**Anodic Bonding**		Single sided	
44.1		Machine: EVG NIL Time: 10/10/10 min Temp: 320°C Voltage: 200V/300V/400V		ST: 10:00 h:m TT: 216:50 h:m SP: 11030kr TP: 70725kr
45	**Anodic Bonding**		Double sided	
45.1		Machine: EVG NIL Time: 10/10/10 min Temp: 320°C Voltage: 200V/300V/400V	For double sidded designs (optional)	ST: 2:00 h:m TT: 218:50 h:m SP: 2206 kr TP: 72931kr

Table B.14: Process flow for the 3rd generation multi-sensor (Part XIV)

APPENDIX

C Power Budgets

16 bit ADC - 100 kHz	Current (mA)	Time	Time (h)	CurrentTime mAh
Standby consumption				
- MCU	0.0001	2*365 days	17520.0	1.8
- Flash	0.0050	0 days	0.0	0.0
Flash Writting (2 MB)				
- 256 byte pages Flash	17.0000	8192*0.1sec	0.2	3.9
- MCU	0.0550	8192*0.3sec	2.3	0.1
Operation consumption				
- MCU (100 kHz)	0.0550	1M*0.85sec	291.3	16.0
- Sensors	0.1000	1M*0.65sec	189.3	18.9
Total consumption				**40.7**

16 bit ADC - 1 MHz	Current (mA)	Time	Time (h)	CurrentTime mAh
Standby consumption				
- MCU	0.0001	2*365 days	17520.0	1.8
- Flash	0.0050	0 days	0.0	0.0
Flash Writting (2 MB)				
- 256 byte pages Flash	17.0000	8192*0.1sec	0.2	3.9
- MCU	0.2600	8192*1sec	2.3	0.6
Operation consumption				
- MCU (1 MHz)	0.2600	1M*0.265sec	77.2	20.1
- Sensors	0.1000	1M*0.065sec	18.9	1.9
Total consumption				**28.2**

12 bit ADC 100 kHz	Current (mA)	Time	Time (h)	CurrentTime mAh
Standby consumption				
- MCU	0.0001	2*365 days	17520.0	1.8
- Flash	0.0050	0 days	0.0	0.0
Flash Writting (2MB)				
- 256 byte pages Flash	17.0000	8192*0.1sec	0.2	3.9
- MCU	0.0550	8192*1sec	2.3	0.1
Operation consumption				
- MCU (100kHz)	0.0550	1.3M*0.24sec	93.0	5.1
- Sensors	0.1000	1.3M*0.04sec	15.5	1.5
Total consumption				**12.4**

12 bit ADC 1 MHz	Current (mA)	Time	Time (h)	CurrentTime mAh
Standby consumption				
- MCU	0.0001	2*365 days	17520.0	1.8
- Flash	0.0050	0 days	0.0	0.0
Flash Writting (2MB)				
- 256 byte pages Flash	17.0000	8192*0.1sec	0.2	3.9
- MCU	0.2600	8192*1sec	2.3	0.6
Operation consumption				
- MCU (1 MHz)	0.2600	1.3M*0.204sec	79.0	20.5
- Sensors	0.1000	1.3M*0.004sec	1.5	0.2
Total consumption				**26.9**

Appendix

D Journal papers

D.1 Sensor and Actuators A: Physical

Available online at www.sciencedirect.com
ScienceDirect
Sensors and Actuators A xxx (2007) xxx–xxx
SENSORS AND ACTUATORS A PHYSICAL
www.elsevier.com/locate/sna

Direct media exposure of MEMS multi-sensor systems using a potted-tube packaging concept

Anders Hyldgård [a,*], Karen Birkelund [a], Jakob Janting [b], Erik V. Thomsen [a]

[a] *MIC-Technical University of Denmark, Building 345 East, DK-2800, Denmark*
[b] *DELTA-Venlighedsvej 4, DK-2970 Hørsholm, Denmark*

Received 30 September 2006; received in revised form 3 January 2007; accepted 25 February 2007

Abstract

A packaging concept for Data Storage Tags is presented. A potted-tube packaging concept, using a polystyrene tube and different epoxies as filling material that allows for direct sensor exposure is investigated. The curing temperature, water uptake and the diffusion coefficient for water in the filling material is measured. The packaging concept is used to encapsulate a microfabricated multi-sensor (measuring temperature, water conductivity, pressure and light intensity). The direct exposure of the sensors results in high sensitivity and fast response time. The design of an elongated multi-sensor is described and effectiveness of the packaging is demonstrated with the precise measurement of water conductivity using the packaged multi-sensor. The packaging concept is very promising for high accuracy measurements in harsh environments.

Keywords: Packaging; Multi-sensor; Direct exposure; Potting; Harsh environment

1. Introduction

Reliable monitoring of individual fish behavior and migration in their natural environment is crucial in order to make accurate population estimations and plans for preservation of the different species. A Data Storage Tag (DST), Fig. 1 is an autonomous system that when sutured onto the back of a fish can measure parameters in the surroundings of the fish and store the data until the fish is re-caught [1].

The Data Storage Tag consists of a microcontroller, which activates sensors and stores measured data in a non-volatile memory. Batteries power the system. When the fish is re-caught, the system can be powered through a wireless interface while data is read out.

In our case, the sensor can measure temperature, pressure, light intensity and electrical conductivity allowing the salinity of the water to be determined. Based on these parameters, the fish migration route can be reconstructed [1].

A very compact and reliable system capable of measuring the parameters very accurately with a high sensitivity and short response time is needed. This calls for a packaging scheme that allows for direct exposure of a silicon sensor to the surrounding environment. Isolating the sensing area from the packaging material also imply that the sensors are stress de-coupled from the packaging. This in turn allows for pre-packaging wafer scale calibration.

We use microtechnology and a potting packaging to make such a system. DST manufacturer CEFAS Technology Ltd. [2] uses a potting packaging system in their G5 tag. This system does not expose the sensors directly but relies on internal sensors coupled to the surrounding environment through the packaging. The G5 tag shows that potting using a two-component fill can be used in yearlong exposure to seawater.

Our system has to be partly sealed off from the surrounding water. This is obtained by placing the sensors, PCB and batteries in a polystyrene tube which is subsequently filled with epoxy leaving one end of the sensor exposed to the surroundings (Figs. 2, 3 and 4). This process is known as potting. Potting with epoxy in a polystyrene tube was chosen because the complete filling leaves no room for water to condense as opposed to an "o"-ring packaging concept that relies on ventilation of the dry side of the packaging to remove water vapor [3]. The silicon–epoxy interface is also very strong which is not always the case for injection-molded thermoplasts, that tends to shrink

* Corresponding author. Tel.: +45 4525 5761; fax: +45 4588 7762.
E-mail address: ahy@mic.dtu.dk (A. Hyldgård).

0924-4247/$ – see front matter © 2007 Elsevier B.V. All rights reserved.
doi:10.1016/j.sna.2007.02.024

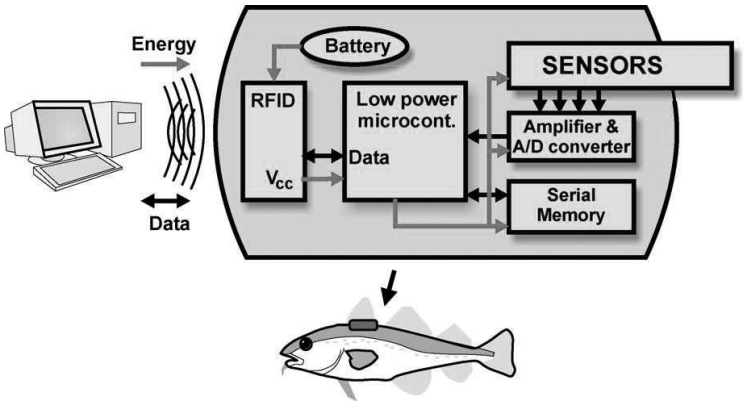

Fig. 1. Data Storage Tag (DST) system overview. A microcontroller manages the power to and data from the sensors and stores the data in the memory. Batteries power the system. When retrieved the system can be powered via the wireless interface while data is read out.

slightly when cooled. The water uptake and diffusion in polymers and epoxies has been investigated in Refs. [4–7] but an investigation of the specific epoxy in this system is needed in order to ensure that it meets all the requirements set by the harsh system environments.

2. Sensor chip design and fabrication

The high demands on the packaging scheme with regards to long-time stability and direct exposure calls for a system design approach. Special care has to be taken in the chip design to ensure that the design facilitates a direct exposure in the predecided packaging scheme. This includes protecting all sensor parts while making good electrical contact to the interface electronics and to distance sensors from bond pads.

The silicon multi-sensor is fabricated using conventional bulk micromachining [8,9] including ion-implantation to functionalize the silicon. Thermally grown SiO_2 and deposited Si_3N_4

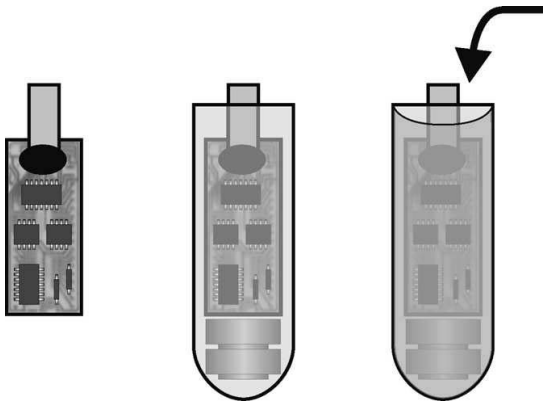

Fig. 2. Packaging scheme. The sensor chip is mounted on the PCB and the wire-bonds are glob-topped. The PCB and batteries are connected and put in a polystyrene tube. The tube is filled with glue (potted) covering the system while leaving one end of the sensor chip exposed.

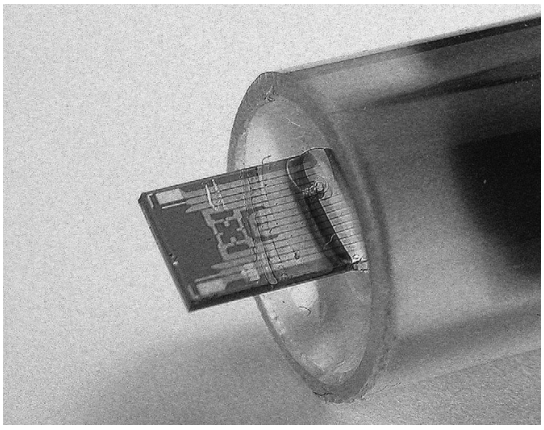

Fig. 3. The exposed sensor chip. The sensors include a piezoresistive pressure sensor, a thermistor temperature sensor, a pn-junction light sensor and a four-electrode conductivity sensor. The sensors are contacted via $TiSi_2$ wires and are protected by a Si_3N_4 film.

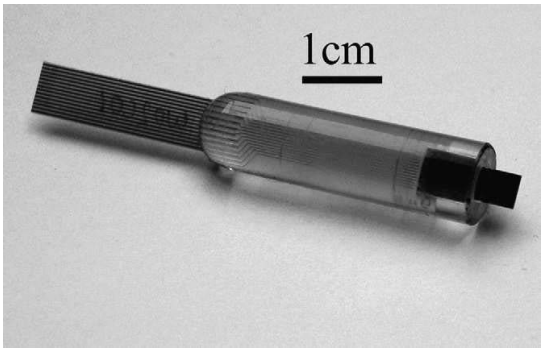

Fig. 4. A packaged multi-sensor. The packaging is made in two versions. One (shown here), where the connector print is exposed on the rear end to allow for online monitoring. And one, where electronics and batteries are potted inside to allow for autonomous measurements in the field.

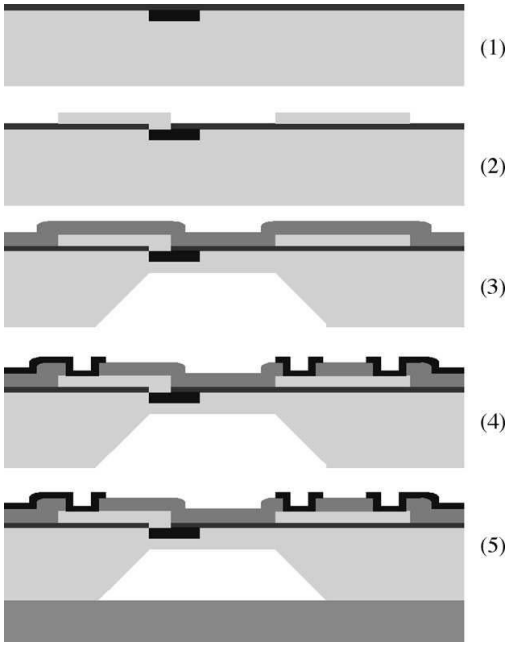

Fig. 5. Chip fabrication sequence. (1) The temperaure, pressure and light sensors are ion implanted. (2) $TiSi_2$ wiring is formed. (3) Si_3N_4 coating is deposited and a membrane is created by etching. (4) Two metallizations form electrodes and contact areas. (5) A Pyrex wafer is anodic bonded to the backside.

layers serve as insulating layer and protective coating, respectively. The process flow is illustrated in Fig. 5.

Interconnects, electrodes and contacts are made of $TiSi_2$, Ti/Pt and Ti/Au, respectively. The membrane of the pressure sensor is released using an anisotropic KOH etch and a reference cavity is formed by bonding Pyrex glass to the backside of the wafer.

The sensor chip is designed so that sensors are placed in one end of the chip and contacts are placed in the other. Contacts and sensors are connected using highly conductive (20 $\mu\Omega$ cm) $TiSi_2$ wire-paths ($R_\square = 1\ \Omega$) that are buried under a protective Si_3N_4 film. The diffusion constant of water through a PECVD Si_3N_4 film is 10^{-18} cm^2 s^{-1} according to Ref. [10]. This means that it will take more than 3 years in order to reach 90% saturation under the film, and even longer for stoichiometric LPCVD nitride as used in the current design. The fabricated chip is shown in Fig. 3, where it is sticking out of the potted tube.

This allows for the sensor end of the chip to be completely exposed to the surrounding environment while the other end is wire-bonded to the electronics and completely sealed in.

The multi-sensor is capable of measuring temperature, pressure, light intensity and electrical conductivity. A thorough description is published in earlier works [8,9]. Fig. 6 shows the conductivity sensor cell trans-impedance as a function of frequency for five different salinities. A clear salinity sensitive interval exists for medium frequencies. Plotting the trans-impedance at a single frequency as a function of the resistivity

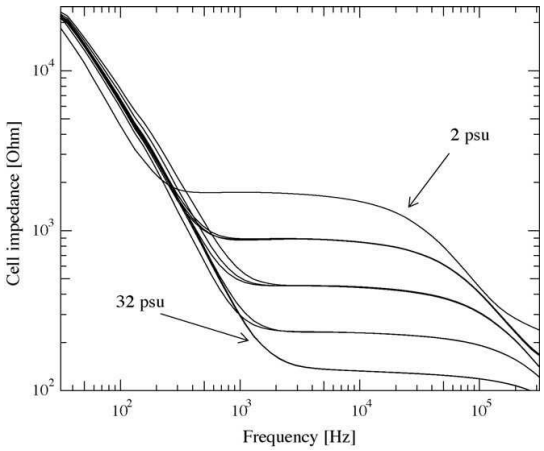

Fig. 6. Conductivity cell trans-impedance as a function of frequency for five different salinities (2, 4, 8, 16 and 32 PSU). At medium frequencies there is a salinity sensitive window. At low frequencies, the Debye layer is not short-circuited. At high frequencies, the cell conducts through the substrate loosing sensitivity. The trans-impedance at 3.4 kHz is used to construct the calibration curve of the sensor as shown in Fig. 7.

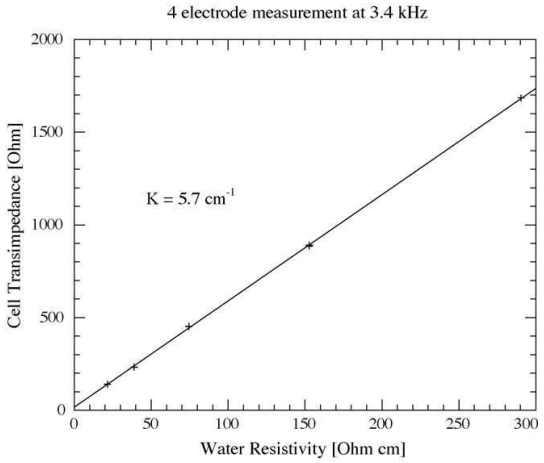

Fig. 7. Conductivity cell trans-impedance as a function of water resistivity measured with a commercial reference sensor. The cell shows a linear response with a cell constant of 5.7 cm^{-1} and a mean deviation of <1% which allows for determination of the salinity with an accuracy of ±0.5 PSU.

corresponding to the respective salinities shows a linear relation (Fig. 7). The repeatability is excellent and the accuracy is better than 1% allowing for the determination of salinity with accuracy better than 0.5 PSU.

3. Experimental evaluation of potting material

The most important requirements for the potting material that has to be considered are

- chemical stability;

Table 1
Key properties of three EpoTek epoxies

Epoxy name (EpoTek)	Supplier values		Measured values			
	Viscosity (cP s)	T_g (°C)	Maximum curing temperature (°C)	Water uptake (weight %)	D_{H_2O}-short (10^{-9} cm^2 s^{-1})	D_{H2O} – long (10^{-9} cm^2 s^{-1})
302-3M	800–1600	65	26.6	2.9	1.6 ± 0.8	1.5 +/− 0.2
301-2FL	125	60	24.1	4.0	4.4 ± 0.4	6.5 +/− 0.2
305	100–300	30	–	14.4	10.0 ± 0.4	10.7 +/− 2.7

The low water uptake and diffusion of EpoTek 302-3M makes it the epoxy of choice. A T_g well above working temperature range, a low curing temperature and a moderate viscosity is also fulfilled.

- adhesion;
- water solubility and diffusion;
- viscosity;
- glass transition temperature (T_g);
- electrical insulation;
- curing temperature.

Additionally, we seek a zero buoyancy mass of the system as well as neutral colors making the fish no more visible than usual.

We consider three transparent epoxies, listed in Table 1, all with a specific weight at approximately 1.1 g cm^{-2}, good electrical insulation properties and a T_g well above the working temperature range.

The potting process is very simple and if the epoxy curing process is kept below 70 °C, then batteries, electronics and sensors will survive the potting process. Many epoxies are typically cured at temperatures above 80 °C for 1–3 h, but when curing larger amounts as we do in our case, the exothermic process plays an important role. To ensure that the temperature does not rise above 70 °C while curing a PT100 element has been encapsulated in test tubes, and the temperature has been monitored while curing. The curing temperature profiles for the different epoxies are shown in Fig. 8. In the case of curing EpoTek 302-3M, the temperature rise is insignificant as long as the epoxy is cured at a temperature below 40 °C. If the curing temperature is increased to 45 °C the temperature inside the tube increases to about 56 °C within 15 min. An alternative to the heat curing epoxies is UV-curing glues. The Dymax 1180 and Dymax 3069 UV-glues show high exothermicity even at constant low power illumination (pot center temperature >80 °C). UV-glues also have to be cured from the bottom and up in order to avoid trapped bubbles in the tube, which further complicates the potting process. Due to the high temperature during curing, the UV-glues are discarded for use in the current application.

Obviously the main purpose of the packaging is to protect the contents of the tag from the surrounding water. A good packaging material is chemically inert and prevents water from being present at critical sites inside the package. In the following, it will become clear that water will diffuse to the center of the package within a limited period of time, and the presence of water will then be limited only by the water saturation level. If the system undergoes temperature changes, the water solubility in the filling will change, and excess water will be transferred to the surface of the filling volume.

The water uptake of most epoxies is listed as being very low (<1%) [11]. The real uptake is however significantly higher and has to be measured. Rough estimates, of how much water can be accepted within the packaging, can be made from assumptions of corrosion mechanisms and water flux consideration [12]. However, the final evaluation should be made empirically and measures of water uptake and diffusion should work as comparison only. The water uptake in the most resistant epoxies is expected to have no significant impact on the performance of the packaging and the embedded system. Completely filling also result in a mechanically robust packaging.

The total water uptake as well as the diffusion coefficient is found by measuring the gain in weight of 50 mm × 50 mm × 1 mm sheets of epoxy after submersion in salt water at room temperature, see Fig. 9. The choice of epoxy obviously has a huge influence on the amount of water that the packaging can contain, for these epoxies a variation from 3 up to 15%. The sample with the highest water uptake, where the EpoTek 305 epoxy was used, got brittle and broke during handling. The amount of water that will condense in possible small cavities within the packaging will be dependent of the water concentration at the cavity interface. The water diffusion into the sheets

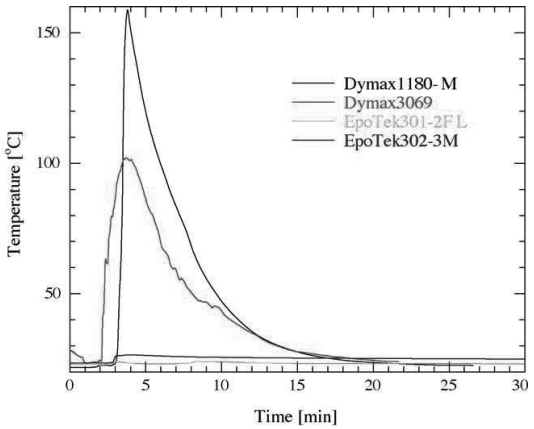

Fig. 8. Encapsulation center temperature as a function of time as measured with potted PT100 elements. For constant low power illumination the Dymax UV-curing glues show high exothermicity giving rice in temperatures to above 100 °C. The heat curing epoxies cures in 24 h without significant temperature rise. Accelerated curing can be performed at intermediate temperatures (∼45°) without compromising the tube content.

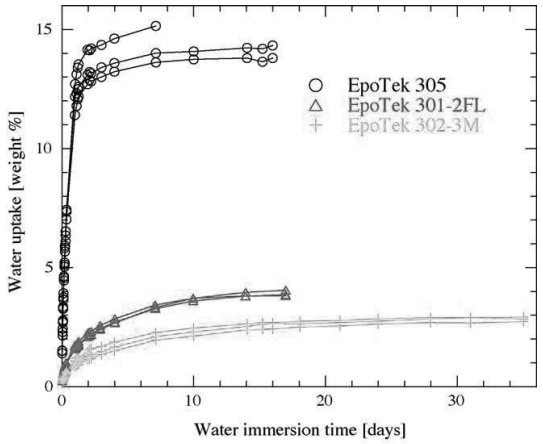

Fig. 9. Relative water uptake (by weight) in three epoxies as a function of time of sample immersion. Three samples are measured for each epoxy. For true Fickian difussion the uptake should saturate when a uniform saturation level is reached through the whole sheet. Non-Fickian diffusion, such as polymer redistribution or reaction with incoming water may make the water uptake continue. The lowest uptake is found in EpoTek 302-3M that saturates at approximately 2.9%.

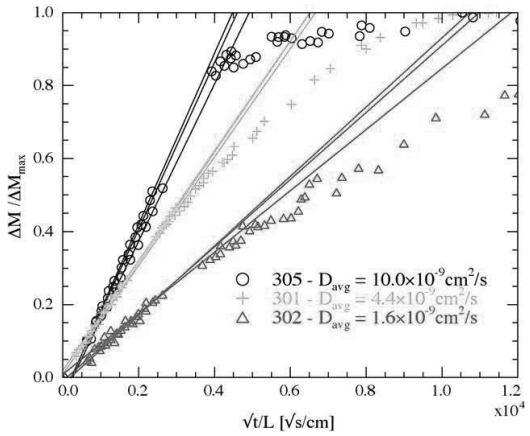

Fig. 10. Relative water saturation (by weight) in three epoxies as a function of the square root of time of sample immersion normalized with the sample thickness. Three samples are measured for each epoxy. For short times, the diffusion coefficient is proportional to the slope of the graph. The diffusion is six times faster in the EpoTek 305 than in the EpoTek 302-3M. Diffusion constants fit very well with literature values [12].

can be considered as a one-dimensional diffusion from two sides. The concentration profile and time development is found from Fick's law under the assumption of a constant diffusion constant

$$\frac{\partial C(x,t)}{\partial t} = D\frac{\partial^2 C(x,t)}{\partial x^2}$$

where C is the concentration, D the diffusion constant, t the time and x is the distance within the sample normal to the surface.

The well known one sided diffusion problem with boundary conditions

$$C(x,0) = 0, \quad C(0,t) = C_s \quad \text{and} \quad C(\infty,t) = 0$$

where C_s is the solid solubility of water in the sample, will yield the error function solution [13]

$$C(x,t) = C_s\left(1 - \text{erf}\left(\frac{x}{2\sqrt{Dt}}\right)\right)$$

As the maximum of absorbed water will be C_sL where L is the thickness of the sample the total water uptake $M(t)$ can be expressed as

$$M(t) = \frac{4}{\sqrt{\pi}}C_s\sqrt{Dt}$$

and the relative water uptake as

$$\frac{M(t)}{M_{\max}} = \frac{4}{L\sqrt{\pi}}\sqrt{Dt} \tag{1}$$

where $M_{\max}$ is the water content at saturation. For short times, where the diffusion from the two sides of the sample is uncoupled, the diffusion constant can be found as from the linear relation between the relative water uptake and square root time as expressed by Eq. (1).

The short time water uptake is shown in Fig. 10. It shows the expected linear relation and the diffusion constants are calculated and listed in Table 1.

To analyze the long-term measurements it is necessary to consider that the diffusion profiles from the two sides overlap. Hence, the exact solution to the double sided diffusion problem must be used. The exact solution can be found with the boundary conditions

$$C(x,0) = 0, \quad C(0,t) = C_s \quad \text{and} \quad C(L,t) = C_s$$

by using the method of separation of variables. The exact one-dimensional solution can then be expressed as an infinite series [13]

$$M(t) = M_{\max}\left(1 - \frac{8}{\pi^2}\sum_{n=0}^{\infty}\frac{1}{(2n+1)^2}\exp\left[\frac{-D(2n+1)^2\pi^2 t}{L^2}\right]\right)$$

For short times, the solution equals the simple solution given by Eq. (1). For long times, the two error functions meet and the water uptake will be approaching total saturation as an exponential decay. All the exponential terms will be dominated by the $n = 0$ term which gives the simple long time expression

$$1 - \frac{M}{M_{\max}} = \frac{8}{\pi^2}\exp\left(-\frac{Dt}{L^2}\pi^2\right) \tag{2}$$

Thus, a logarithmic plot of the long time relative water uptake as a function of time has a slope proportional to the diffusion constant.

Fig. 11 shows such plots for the water uptake of the investigated epoxies. As expected from Eq. (2), straight lines are seen, from which the diffusion coefficients of water is determined and results are listed in Table 1.

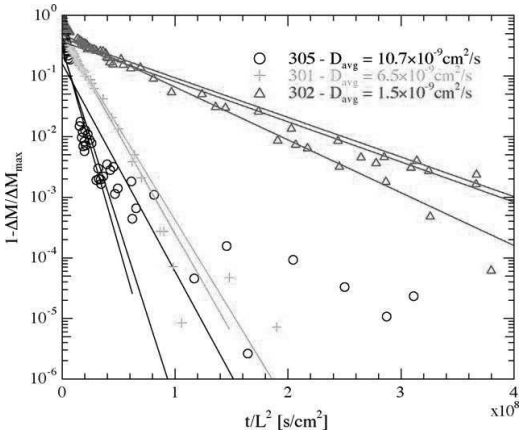

Fig. 11. Logarithm of the relative water saturation (by weight) in three epoxies as a function of time of sample immersion normalized with the sample thickness squared. Three samples are measured for each epoxy. For long times, the diffusion coefficient is proportional to the slope of the graph. The diffusion is six times faster in the EpoTek 305 than in the EpoTek 302-3M. Fitting between 60 and 99.9% saturation gives diffusion constants which matches very well with the short time diffusion values found in Fig. 9.

4. Discussion

A number of properties has to be taken into account when choosing potting material [14]. The low water uptake and diffusion constant of EpoTek 302-3M makes it the epoxy of choice. However, 302-3M has the highest viscosity of the three (0.8–1.6 Pa s compared to 0.1–0.3 Pa s), which again makes the chance of bubble formation higher. However, even with the EpoTek 302-3M bubble formation was not observed.

A T_g well above working temperature range ensures a low plastic deformation over time and a low curing temperature and a moderate viscosity makes the epoxy practical for potting. The electrical insulating properties are not listed by the supplier, but similar epoxies are listed with electrical resistivities higher than $10^{13}\ \Omega$ cm.

In addition to the above investigations, mechanical stress has to be considered as a significant failing process. Stress from the curing process or stress induced by polymer swelling can result in excessive force on wire-bonds or allow water to penetrate along the surface of the chip. This in turn can result in loss of electrical contact as wire-bonds are torn off or etched away.

Choosing an epoxy with low water uptake can minimize problems with polymer swelling. Clever design of the exact shape of the packaging may also limit the stress coupled to the interfaces.

5. Conclusion

A packaging concept for Data Storage Tags is demonstrated. The effectiveness of the packaging is demonstrated with the precise measurement of water conductivity. The packaging concept is very promising for high accuracy measurements in harsh environments.

Acknowledgment

We acknowledge the Danish Institute for Fisheries Research for their help to the completion of this work.

References

[1] J.D. Metcalfe, G.P. Arnold, Tracking fish with electronic tags, Nature 387 (1997) 665–666.
[2] http://www.cefastechnology.co.uk.
[3] C. Pedersen, S.T. Jespersen, K.W. Jacobsen, J.P. Krog, C. Christensen, E.V. Thomsen, Combined Differential, Static pressure sensor based on a double-bridged structure, Sens. Actuators A 115 (2004) 617–627.
[4] M.R. Vanlandingham, R.F. Eduljee, J.W. Gillespie Jr., Moisture diffusion in epoxy systems, J. Appl. Polym. Sci. 71 (1999) 787–798.
[5] M. Lindgren, I. Belov, P. Leisner, Experimental evaluation of glob-top materials for use in harsh environments, Int. Microelectron. Packaging Soc. 2–4 (2005) 253–268.
[6] Y.C. Lin, Xu Chen, Investigation of moisture diffusion in epoxy systems: experiments and molecular dynamics simulations, Chem. Phys. Lett. 412 (2005) 322–326.
[7] L.L. Marsh, R. Lasky, D.P. Seraphim, G.S. Springer, Moisture solubility and diffusion in epoxy and epoxy-glass composites, IBM J. Res. Dev. 28 (1984) 655–661.
[8] A. Hyldgård, O. Hansen, E.V. Thomsen, FISH & CHIPS: single chip silicon MEMS CTDL salinity, temperature, pressure and light sensor fur use in fisheries research, in: IEEE MEMS 2005 Proceedings, Miami Beach, FL, USA, January 30–February 3, 2005, pp. 303–306.
[9] A. Hyldgård, Í. Olfafsdóttir, M. Olesen, T. Hedegaard, O. Hansen, E.V. Thomsen, FISH & CHIPS: four electrode conductivity/salinity sensor on a silicon multi-sensor chip for fisheries research, in: IEEE Sensors 2005 Proceedings, Irvine, CA, USA, October 31–November 3, 2005, pp. 1124–1127.
[10] R.K. Ulrich, A.J. Phillips, D.H. Yi, W.D. Brown, S.S. Ang, Mechanical stability of PECVD silicon nitride protective films over bondwires, bonds and bondpads during thermal stress, Microelectron. Reliability 31 (1991) 1237–1249.
[11] http://www.epotek.com/.
[12] R.D. Adams, J. Comyn, W.C. Wake, Structural Adhesive Joints in Engineering, Chapman & Hall, 1997.
[13] J. Crank, Mathematics of Diffusion, first ed., Oxford University Press, London, 1956.
[14] J. Janting, Sensor Packaging for Harsh Environments, in: C.A. Grimes, E.C. Dickey, M.V. Pishko (Eds.), Encyclopedia of Sensors, vol. 9, American Scientific Publishers, 2006, ISBN 1-58883-065-9, pp. 271–288.

Biographies

Anders Hyldgård received his MSc degree in physics and nanotechnology from the Technical University of Denmark. He is currently employed as a PhD student in the Department of Micro and Nanotechnology at the Technical University of Denmark within the field of microsystem integration and microsystem packaging for harsh environments.

Karen Birkelund received her MSc degree from Roskilde University, Denmark in 1993 and her PhD degree in micro and nanotechnology from the Microelectronics Center of the Technical University of Denmark in 1997. She has worked at Danfoss A/S, TopSpin and Cantion A/S. She is currently employed at the Department of Micro and Nanotechnology at the Technical University of Denmark, where focus of her work is on microsystem encapsulation for harsh environments.

Jakob Janting received his MSc degree in materials science from the University of Aarhus, Denmark in 1991 where he thereafter worked as a research affiliated until 1994. In 1994 he joined Grundfos Research. Since 1998, he has been employed at DELTA, the Department for Microsystems, where focus of his work is on polymer microsystem encapsulation.

Erik V. Thomsen is group leader for the MEMS Applied Sensors activities at the MEMS section at MIC-Department of Micro and Nanotechnology, Technical University of Denmark, DTU, where he is affiliated as associate professor. He holds a MSc in physics from Odense University and a PhD in electrical engineering from DTU. Erik V. Thomsen has been affiliated with MIC since 1992 and has been working with fabrication of semiconductor devices. His current interests include research and teaching within micromechanical multi-sensors, piezo resistivity of strained layers, piezoelectric MEMS devices, and microsystem packaging. He teaches in "Solid State Electronics & Microtechnology" and "Nano & Microfabrication".

D.2 Sensor and Actuators A: Physical

G Model
SNA-6309; No. of Pages 11
ARTICLE IN PRESS

Sensors and Actuators A xxx (2008) xxx–xxx

Contents lists available at ScienceDirect

Sensors and Actuators A: Physical

journal homepage: www.elsevier.com/locate/sna

Autonomous multi-sensor micro-system for measurement of ocean water salinity

A. Hyldgård*, D. Mortensen, K. Birkelund, O. Hansen, E.V. Thomsen

Technical University of Denmark, Department of Micro and Nanotechnology, DTU-Building 345 East, DK-2800 Kgs. Lyngby, Denmark

ARTICLE INFO

Article history:
Received 20 June 2007
Received in revised form 29 April 2008
Accepted 2 June 2008
Available online xxx

Keywords:
Salinity
Micro-system
Conductivity
Temperature
Depth
CTD
Multi-sensor
Silicon

ABSTRACT

This paper describes the design, fabrication and application of a micro-fabricated salinity sensor system. The theoretical electrochemical behaviour is described using electrical equivalent diagrams and simple scaling properties are investigated analytically and numerically using finite element method (FEM). The chip design and fabrication is described and measurement results of two different electrode designs are presented. The 4 mm × 4 mm multi-sensor allows for salinity determination with an accuracy of ±0.5 psu through determination of the electrical conductivity, temperature and pressure with accuracies of ±0.6 mS, ±0.065 ° C and ±0.05 bar, respectively.

1. Introduction

This paper describes the design, fabrication and application of a micro-fabricated salinity sensor system. Determination of salinity is used in various applications within chemical and biological systems, and the determination of salinity through measurement of conductivity, temperature and pressure is well known on the macro-scale. Thus very precise determination of salinity can be made in glass tubes for reference and calibration and high accuracy conductivity, temperature and depth (CTD) profilers are used to investigate seawater parameters at all ocean depths. However, in some applications a complete salinity measurement system of reduced size is needed.

1.1. Data storage tags

Data storage tags (DST) are tiny autonomous measurement systems used in fisheries research to obtain data on the behaviour of fish. These DST's contain sensors, electronics, memory, batteries and, depending on duty cycle, these systems typically operate for around 2 years and store one million measurements. State of the art DST's can measure temperature, depth and salinity. This information can subsequently be used to reconstruct fish migration and patterns of fish behaviour [1,2].

Fish are caught by the researchers, the system is mounted on the fish which is then released to the ocean. When fishermen eventually re-catch the fish, the DST is returned to the fisheries research institution upon a reward. The data are then retrieved from the tag. By fitting the development in time of the CTD data to oceanographic information from other sources the most probable migration route of the fish can be reconstructed.

The performance and usability of current DSTs are limited by the considerable size, low accuracy and/or slow response time of conventional discrete sensor solutions.

State of the art tags, such as the CEFAS G5 [3] tag or StarOddi DST-micro[4] tag, have a diameters of only 8 mm and have lengths of 30 mm or less. These only measure temperature and depth, where as the smallest tag also measuring salinity is 17 mm in diameter and 46 mm long length [4].

Currently, only the conductivity sensor electrodes used in DST's are exposed directly to the water, while the other sensors are placed within the packaging. This leads to long response times and erroneous salinity readings when conditions change rapidly (asynchronous measurement of conductivity and temperature). In order to integrate more sensors in a given volume and to improve the accuracy, we have developed a micro-fabricated multi-sensor chip

* Corresponding author. Tel.: +45 2826 2424.
E-mail address: anders@hyldgaardnet.dk (A. Hyldgård).

0924-4247/$ – see front matter © 2008 Elsevier B.V. All rights reserved.
doi:10.1016/j.sna.2008.06.004

Please cite this article in press as: A. Hyldgård, et al., Autonomous multi-sensor micro-system for measurement of ocean water salinity, Sens. Actuators A: Phys. (2008), doi:10.1016/j.sna.2008.06.004

G Model
SNA-6309; No. of Pages 11
ARTICLE IN PRESS

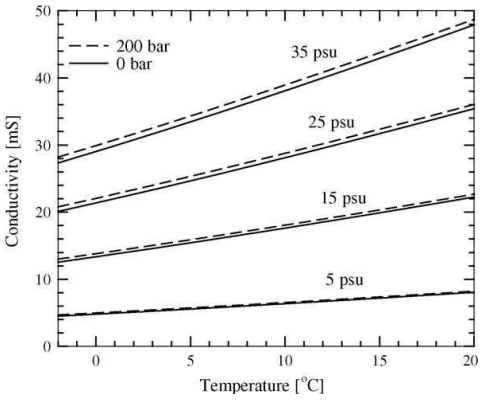

Fig. 1. Conductivity of saline water as a function of temperature at four different salinities and two different pressures. A precise determination of conductivity and temperature is needed for precise determination of salinity, whereas pressure has a less significant influence.

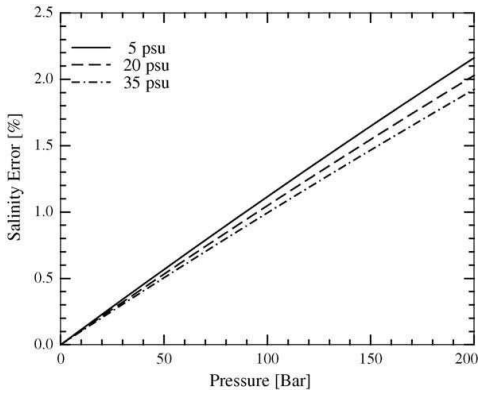

Fig. 2. The error in salinity determination introduced by pressure if the results are not pressure compensated. The error is 1% at approximately 80 bar corresponding to 800 m depth.

that can be exposed directly to the sea. The chip contains a piezoresistive pressure sensor, a thermistor, electrodes for determination of the salinity of the water and a pn-junction light sensor [5,6]. The variation of light intensity during the day can be used to deduct the longitude and latitude for longer migration distances. Shrinking the system will put high demands on the system design and will put constraints on sensor signals, measurement frequency and system lifetime.

Motivated by the need for a CTD system mountable on the back of fish we describe the theory of salinity measurements, including electrochemistry and electrode properties as well as design and fabrication of a silicon-based multi-sensor. Measurement results from the sensor under various conditions are given and constraints on interface electronics are discussed.

1.2. Salinity

Salinity, or dissolved salts, is the amount of salts (by weight) dissolved in the water. Ocean water contains about 32–38 ppt salt of which 90% is NaCl. Oceanographers often refer to the salinity in the unit of psu (practical salinity unit) which is actually equivalent to ppt, thus 32 ppt = 32 psu. The salinity can be determined by drying out samples of seawater and weighing the remaining salts. However, the present, and more practical, salinity definition is based on electrical conductivity, temperature and pressure of the water as defined in UNESCOs "The Practical Salinity Scale" from 1974 [7]. According to this definition the salinity can be calculated from the conductivity, temperature and pressure triplet from well-established polynomial fits to empirical data. Fig. 1 shows relations between salinity, electrical conductivity, temperature and pressure.

At fixed temperature and pressure the conductivity changes almost linearly with salinity. As seen in Fig. 1 the temperature has a significant influence on the conductivity whereas pressure plays a less significant role. Thus in all cases a precise measurement of conductivity and temperature is needed in order to make a precise determination of salinity. Because of linearity a 1% (of full scale) accuracy on conductivity is needed for 1% accuracy in salinity determination. Temperatures should be determined with an accuracy better than 0.5 °C, which corresponds to a maximum of 1% change in conductivity for a fixed salinity. Whether pressure compensation is needed depends on the specific measurement conditions and the needed accuracy. The error in salinity determination as introduced by lack of pressure compensation is shown in Fig. 2. Obviously, if salinity measurements are performed in waters at depths not exceeding 200 m, corresponding to 20 bar, the error would be less than 0.2% which might be precise enough for some applications. In this paper we aim at highest possible accuracy and will thus implement sensors for all three parameters. The pressure sensor is needed anyway, since the pressure must be monitored to infer the precise vertical position. Meeting the requirements for temperature and pressure will not take too much effort, why conductivity will be the main focus of the paper. From the following it will be evident that precise measurements of conductivity will be complicated by system shrinkage.

2. Theory

Measurement of the conductivity of an electrolyte is in principle carried out by forcing a current through a sample of the electrolyte and measuring the resulting potential drop. This is most often done with either two or four electrodes exposed to the electrolyte. A number of electrodes combined with a sample of electrolyte is normally referred to as a cell. In the cell, the electrical conductivity κ is ideally related to the measured current I and voltage V as

$$\frac{V}{I} = \frac{K}{\kappa} \tag{1}$$

where the cell constant K is geometry-dependent. This will be discussed in more detail later. Here it is assumed that the electrolyte is behaving purely ohmic and that the polarization ability is negligible. The charge transfer will be purely electric and independent of ion-transport. Real measurements are complicated by the existence of contact potentials in the electrode–electrolyte interface [8]. Charge transfer to and from the interface is a result of either reduction-oxidation (red-ox) processes at the interface or charging of the electrochemical double layer, the charging behaviour of which is much like in a Schottky diode in semi-conductor physics. These two processes can simply be modeled as a resistive and a capacitive component in parallel. However, the red-ox reaction resistance is highly nonlinear and the impedance of the double layer capacitance is not exactly inversely proportional to the frequency. The reaction resistance is dependent of the ion-concentration in the electrolyte and highly dependent of the applied potential. The higher the potential, the more red-ox processes are possible. The potential should be kept as low as possible so that no red-ox processes involving the electrode material takes place, hereby min-

Please cite this article in press as: A. Hyldgård, et al., Autonomous multi-sensor micro-system for measurement of ocean water salinity, Sens. Actuators A: Phys. (2008), doi:10.1016/j.sna.2008.06.004

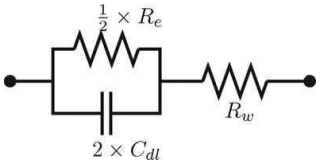

Fig. 3. Equivalent circuit at low frequencies of a cell. The reaction resistance R_e is much higher than the water resistance R_w. At higher frequencies the double layer capacitance C_{dl} short circuits and the impedance converge to R_w. The circuit terminals corresponds to the bulk of the two electrodes.

imizing the corrosion of the electrodes. This is of course of outmost importance in micro-systems where the volume to area ratio of the electrodes is low. In a simple estimation of the corrosion rate at a high applied voltage, it is assumed that all charge transfer is caused by red-ox processes involving electrode material. In this case, every electron passing the interface junction results in the oxidation of one platinum atom, and a 800 μm × 400 μm (4000 nm thick) electrode will dissolve in 16 s, assuming 200 μA for 10 V applied potential. For low voltages, e.g. 10 mV, the reaction resistance is easily above 1 M Ω and the corrosive processes are negligible. The double layer capacitance depends on the electrode material and the electrolyte ion concentration. The area specific capacitance is typically in the range of 10–40 μF cm^{-2} [8]. A simple equivalent circuit of a two electrode cell can be illustrated as in Fig. 3. The contribution from the two electrodes is reduced into one effective reaction resistance $R_e/2$ and one effective double layer capacitance $2 \times C_{dl}$. The impedance Z of the cell at medium frequencies, where the reaction resistance, R_e, is negligible, can be expressed as

$$Z = R_w + \frac{1}{j2\omega^{\alpha} C_{dl}} \tag{2}$$

where R_w is the water contribution to the resistance of the cell, ω is the angular frequency, C_{dl} is the double layer capacitance of one electrode and α is an ideality factor *of the double layer* which is close to 1 [15]. The magnitude of the impedance can be expressed as

$$|Z| = \sqrt{R_w^2 + \frac{1}{4\omega^{2\alpha} C_{dl}^2}} = R_w \sqrt{1 + \frac{1}{4\omega^{2\alpha} C_{dl}^2 R_w^2}} \tag{3}$$

At low frequencies the cell impedance will be dominated by the reaction resistance and the conducted current for fixed voltage amplitude will be very small. A precise determination of the water resistance R_w is thus very difficult. At higher frequencies the double layer capacitance will conduct, short-circuiting R_e, and eventually the cell impedance equals the water resistance. In most systems there are upper limits to the operating frequency determined by parasitic capacitances either to a conducting substrate or in the wiring system and measurement equipment.

A more realistic model of the cell behaviour of electrodes placed on a silicon substrate with an insulator in between is illustrated in Fig. 4. In this case the high frequency impedance will be equal to the impedance of the water and the impedance of the substrate in parallel. A theoretical impedance spectrum with realistic parameters (C_{dl} = 32 nF, C_p = 5 nF, R_e = 50 k Ω, R_p = 600 Ω and R_w = 1.1–10.5 k Ω) is shown in Fig. 5. The values are based on a specific double layer capacitance of 10 μF cm^{-2}, an electrode size of 800 μm × 400 μm and salinities ranging from 1 to 32 psu, and a cell constant found using the finite element method. Obviously a frequency interval exists (hereafter named salinity window) in which the impedance is highly dependent of salinity and where the impedance ideally is inversely proportional to the conductivity. The lower frequency limit for the salinity window is determined by double layer capacitance and water resistance at high salinities. Both

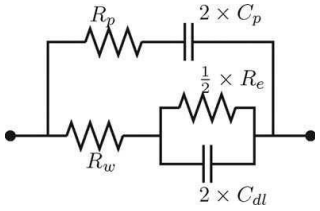

Fig. 4. Equivalent circuit of a cell, including parasitic resistance R_p and capacitance C_p. The electrolysis impedance R_e is much higher than the water resistance R_w. The double layer capacitance C_{dl} is higher than the parasitic capacitance C_p

depend on electrode geometry. The upper frequency limit for the salinity window is determined by the water impedance at low salinities and the parasitic capacitive coupling through the substrate, which is dependent on the dielectric insulation of the electrode system. For metal electrodes placed on silicon dioxide, the upper limit frequency can easily be adjusted by changing the insulating oxide thickness or changing the dimensions of the wiring system. In some cases it is possible to eliminate errors from parasitic or double layer capacitances by calibration. However, the double layer capacitances will most likely change over time due to electrode degradation and/or algae growth. In order to widen the salinity window and increase system stability a four electrode configuration can be used; in this case the transimpedance Z_T is measured by forcing a current through two (most often outer) electrodes, while the potential is measured between two other (most often inner) electrodes. Ideally the system should give a true measurement of the water resistance for all frequencies lower than the upper frequency limit since all current flow is through the water. This is, however, not always the case.

An equivalent circuit of the system including measurement equipment is shown in Fig. 6. An AC power source delivers a constant amplitude voltage. The power source is connected to the outer electrodes of the cell through a high precision series resistor used to monitor the current. The current is coupled to the water through the contact impedance. The water resistance is distributed on three resistors the values of which depend on the cell geometry. Unwanted parasitic coupling of the electrodes takes place either as

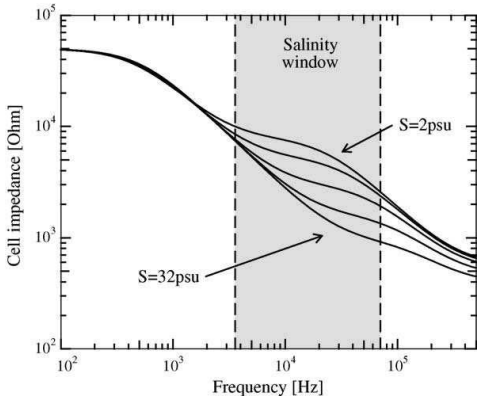

Fig. 5. Theoretical impedance vs. frequency for a two electrode measurement setup for five different salinities (2, 4, 8, 16 and 32 psu) calculated from realistic parameters (C_{dl} = 32 nF, C_p = 5 nF, R_e = 50 k Ω, R_p = 600 Ω and R_w = 1.1–10.5 k Ω). At medium frequency the impedance is strongly dependent of salinity. The lower limit frequency is determined by double layer capacitance and the upper limit frequency is determined by parasitic capacitive coupling in the wiring system and substrate.

Please cite this article in press as: A. Hyldgård, et al., Autonomous multi-sensor micro-system for measurement of ocean water salinity, Sens. Actuators A: Phys. (2008), doi:10.1016/j.sna.2008.06.004

G Model
SNA-6309; No. of Pages 11
ARTICLE IN PRESS

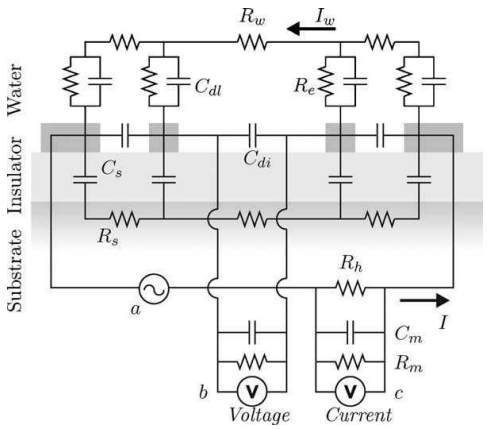

Fig. 6. An electrical equivalent description of the four electrode conductivity measurement, including cell, source (a) and measurement equipment (b and c). The current I is measured as a voltage drop over the high precision resistor R_h with a voltmeter with inner impedance consisting of C_m and R_m. All current should ideally go through the water resistance R_w. The contact impedance at the inner voltage electrodes through C_{dl} and R_e should be much lower than the inner impedance of the measurement equipment. The capacitive coupling to the substrate through C_s and R_s as well as the direct dielectric coupling between the electrodes, C_{di} should be kept to a minimum.

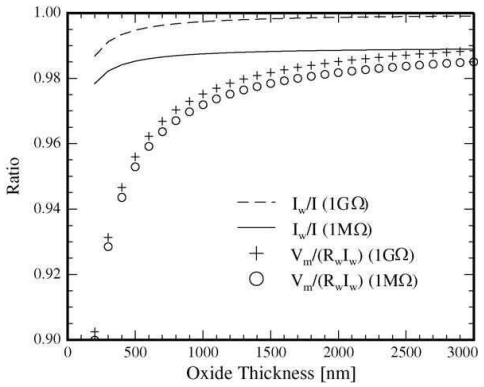

Fig. 7. 18 kHz ratio between measurement current I and water current I_w as well as the ratio between measurement potential V_m and the cell water potential R_wI_w, with (1 G Ω) and without (1 M Ω) high impedance pre-amplification stage as a function of insulator thickness. The model parameters are the same as in Fig. 5.

direct capacitive coupling between the electrodes (minor effect) or as capacitive coupling through the dielectric insulating layer into the resistive substrate. The inner impedance of the equipment measuring the cell current and voltage has to be taken into account. Two preconditions need to be fulfilled in order to get a true and stable measurement of the water resistance in the cell; (1) The current I flowing through the outer wire loop (Fig. 6) should equal the current flowing in the water I_w, and (2) the potential across the voltage measurement equipment b (Fig. 6) should equal the potential I_wR_w in the water at the interface of the voltage electrodes. The first precondition is subject to the same upper limit frequency considerations as in the case of a two terminal setup. The second precondition is met, provided that the impedance across the water–electrode interface (contact impedance) of the voltage electrodes is much smaller than the inner impedance of the measurement equipment and the impedance of the substrate coupling. For submillimeter electrodes at low potentials, the contact impedance will easily exceed 1 M Ω in the low frequency domain. This is comparable to the typical input impedance of the AC voltage stage of digital multimeters, such as the Keithley 2000 series ($R = 1$ M Ω, $C = 100$ pF). Simple voltage division predicts a significant measurement error (¿60%) as a result. This can be counteracted by increasing the electrode size and/or increasing the input impedance of the measurement equipment by use of a high impedance instrumentation pre-amplifier stage (such as AD524 with $R = 1$ G Ω and $C = 10$ pF). At medium frequencies the capacitive coupling through the substrate has a significant influence. Fig. 7 shows the ratio between water current I_w and measurement current P as well as the ratio between cell water potential R_wI_w and measurement potential V_m, with and without instrumental amplifier as a function of insulator thickness (at 3 kHz).

This analysis indicates that a four electrode cell on a 3 μm silicon dioxide insulating layer and a 1 G Ω/10 pF input impedance of the voltage measurement equipments can be used to measure the water resistance with an accuracy better than ±1%. Increasing the size of the voltage electrodes can further improve the accuracy.

3. Design

In order to predict the performance of a conductivity cell, the cell constant has to be determined. This can be done by considering the cell as a purely resistive media without any contact potentials under DC conditions. For very simple electrode geometries, such as hemispheres or parallel semi-infinite radial conductors, the cell constant can be evaluated analytically. This can be used to predict simple scaling properties of the system. For slightly more complicated structures, as generated with planar processing, numerical methods are needed.

3.1. Analytical approximation

A good two electrode model system, representing square planar electrodes, consists of a pair of hemispherical electrodes of radius a separated a distance d, immersed in a semi-infinite conductive medium (such as the ocean) with the electrical resistivity ϱ, as shown in Fig. 8. In a first approximate model the electrodes are considered half space point current sources with the currents $\pm I$. The current density $J(r)$ from a single point source is purely radial,

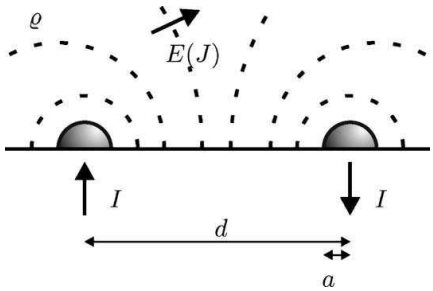

Fig. 8. Simple analytical approximation to planar and hemispherical electrodes. Two hemisphere electrodes in a semi-infinite media of resistivity ϱ. The electrodes carry a current I and $-I$ and the potential drop between the electrodes is found by integrating the resulting electric field distribution $E(J)$ between the electrodes. The approximation is good when the center distance d is much larger than the radius a of the electrodes.

Please cite this article in press as: A. Hyldgård, et al., Autonomous multi-sensor micro-system for measurement of ocean water salinity, Sens. Actuators A: Phys. (2008), doi:10.1016/j.sna.2008.06.004

G Model
SNA-6309; No. of Pages 11
ARTICLE IN PRESS

thus

$$J(r) = \frac{I}{2\pi r^2} \tag{4}$$

where r is the radial distance from the current source. Thus also the electric E field is purely radial:

$$E(r) = -\frac{\partial \Phi}{\partial r} = \varrho J(r) = \frac{\varrho I}{2\pi r^2} \tag{5}$$

Two superimposed point current sources results in the potential Φ:

$$\Phi(r_1, r_2) = \frac{\varrho I}{2\pi}\left(\frac{1}{r_1} - \frac{1}{r_2}\right) \tag{6}$$

where r_1 and r_2 are the distances from the point sources to the point of interest.

A simple approximate expression for the potential difference V between the hemispheres can be obtained by evaluating the potential, Eq. (6), at the facing points of the spheres; the result is

$$V = \frac{\varrho I}{\pi a}\frac{d-2a}{d-a} \tag{7}$$

and thus the cell constant is

$$K = \frac{V}{\varrho I} = \frac{1}{\pi a}\frac{d-2a}{d-a} \tag{8}$$

This simple result is useful for establishing the scaling behaviour, comparison to numerical models, and as an approximate solution to the problem of some planar electrodes separated a large distance. Note, however, that Eqs. (7) and (8) are only approximations since the potential, Eq. (6), does not fulfil the boundary conditions on the hemispherical surfaces.

A potential that fulfil the boundary conditions can be constructed from an infinite sum of point source potentials using the method of images [9]. A set of primary point sources $\pm I_0$ at the centre of the hemispheres must be combined with image point sources $\pm I_1 = \pm I_0 a/d$ displaced a distance $\lambda_1 = a^2/d$ from the centre in order to fulfil the boundary condition on the opposing hemisphere. Now to fulfil the boundary conditions on the opposing hemisphere, these image sources again must be combined with new image sources $\pm I_2 = \pm I_1 a/d_1$ displaced $\lambda_2 = a^2/d_1$ from the centre, and so on *ad infinitum*. Here $d_i = d - \lambda_i$ is the distance from the centre of one sphere to image i in the opposing sphere. The resulting total current becomes $I = \sum_{i=0}^{\infty} I_i$ a sum that converges rapidly except when the spheres nearly touch (it diverges when they touch). The resulting potential difference between the spheres becomes $V = 2\varrho I_0/(2\pi a)$ since the images are arranged for zero potential on the sphere. Finally, the cell constant becomes:

$$K = \frac{V}{\varrho I} = \frac{1}{\pi a}\frac{I_0}{I} = \frac{1}{\pi a}\frac{I_0}{\sum_{i=0}^{\infty} I_i} = \frac{1}{\pi a}F\left(\frac{a}{d}\right) \tag{9}$$

where $F(a/d)$ is a function exclusively of the ratio a/d. The general trends of the exact and the approximate expressions for the cell constant Eqs. (9) and (8) against variation of the geometry are quite similar as seen in Fig. 9, thus the simple approximate expression serves as a useful design tool, while the exact solution provides an excellent tool for verification of the accuracy of numerical modeling.

The cutoff frequency of the cell, f_{th}, can be expressed as (using Eq. (2) with $\alpha = 1$):

$$\begin{aligned} &\left|R_{\text{w,min}}\right| = \left|\varrho_{\text{min}} K\right| = \left|\frac{1}{j2\omega_{\text{th}} C_{\text{dl}}}\right| = \left|\frac{1}{j4\pi f_{\text{th}} c'_{\text{dl}} A}\right| \\ &\Leftrightarrow f_{\text{th}} = \frac{1}{4\pi c'_{\text{dl}} A \varrho_{\text{min}} K} \end{aligned} \tag{10}$$

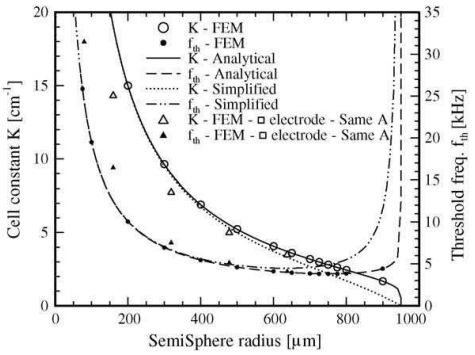

Fig. 9. FEM verification. The cell constant and corresponding threshold frequency for the hemisphere electrodes and for square planar electrodes with the same area. All have same outer distance of 3.8 mm limited by the chip size. The hemisphere FEM results are in good agreement with the analytical solution (Eq. (9)). The approximate solution is only good for electrode radius much smaller than the spacing (Eq. (8)). Medium sized square planar electrodes can be well represented by sphere electrodes of equivalent surface area.

where $R_{\text{w,min}}$ and ϱ_{min} are the water resistance and resistivity at the highest detectable salinity, c'_{dl} is the specific double layer capacitance and A is the electrode surface area. The lowest cutoff frequency is found when the $K \times A$ product is highest. Thus, for semi-spherical electrodes, solving:

$$\frac{\partial(K(a,d) \times (2\pi a^2))}{\partial a} = 0 \tag{11}$$

gives the best electrode radius (or equivalent square side length) for a given electrode spacing. For a constant outer distance of the electrode of 3800 μm, the lowest cutoff frequency is found at $a \approx 750\,\mu$m which corresponds to $0.33d$.

In the case where the electrodes are elongated rectangular shaped and planar, the cell can be approximated using two pieces of semi-infinite cylindrical electrodes of radius a separated the distance d. In this case the potential from two off centre line current sources fulfil the boundary conditions on the cylinder surfaces; this results in the simple exact expression:

$$K = \frac{2}{\pi \ell}\operatorname{arccosh}\frac{d}{2a} \tag{12}$$

for the cell constant of a cylinder pair of length ℓ. These electrodes each have the area

$$A = \pi a \ell \tag{13}$$

The cylindrical electrode model is a good approximation to long, narrow planar electrodes. Thus it is clear that for these electrodes the product $K \times A$ and hereby the cutoff frequency becomes independent on the electrode length ℓ.

It must be noted that even though Eq. (11) will result in the lowest cutoff frequency, increasing the electrode area will also decrease the cell constant and thereby the water resistance. At some point, problems with noise or instrumentation might discourage further enlargement.

3.2. FEM analysis

In cases where the electrodes have odd shapes or dimensions that are not easily approximated by simple analytical expressions, a numerical simulation is useful. The cell constants are found numerically using the finite element method (FEM) in the commercial

Please cite this article in press as: A. Hyldgård, et al., Autonomous multi-sensor micro-system for measurement of ocean water salinity, Sens. Actuators A: Phys. (2008), doi:10.1016/j.sna.2008.06.004

G Model
SNA-6309; No. of Pages 11
ARTICLE IN PRESS

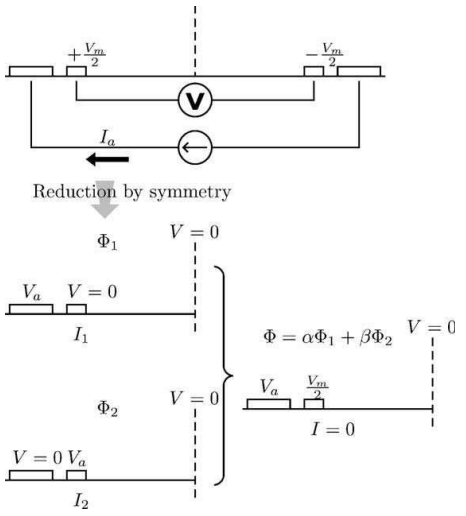

Fig. 10. Determination of cell transimpedance using FEM. The electrostatic solution is found in two cases; V_a on the outer electrode and $V = 0$ on the inner and then the potentials interchanged. A linear combination of the solutions are found, which fulfills V_a at the outer electrode and $I = 0$ at the inner. The corresponding current in the cell is found by integrating the current density.

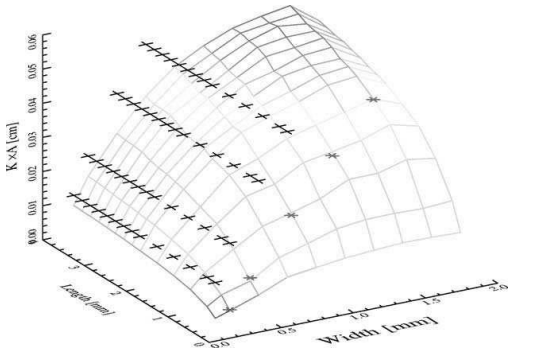

Fig. 11. $K \times A$ as a function of electrode width and length for and outer electrode spacing of 3.8 mm. High $K \times A$ results in low cutoff frequency. The full mesh is FEM results, and the discrete points are the analytical solutions for the hemisphere (Eq. (9)= ⋆) and semi-infinite conductor (Eq. (12)= ×) cases for the same electrode area. Clearly the hemisphere solution fits very well whereas the semi-infinite conductor approximation only gives accurate results for electrodes that are very long and thin compared to their spacing.

software COMSOL [10]. Generally the potential distribution Φ is found in a cell by solving Laplace's equation:

$$\nabla^2\Phi = 0 \tag{14}$$

when applying a current I_a through the outer electrodes while measuring the potential drop V_m on the outer (two electrode configuration) or inner electrodes (four electrode configuration). For unit resistivity the cell constant is equal to the inverse impedance or the inverse transimpedance, respectively, e.g.

$$K = Z_T = \frac{V_m}{I_a} \tag{15}$$

By means of symmetry the cell is reduced into a half cell, as illustrated in Fig. 10. The solution to the two electrode configuration problem is easily found by applying a voltage to the electrode and finding the resulting current by integrating the current density across the electrode interface. For the four electrode configuration the solution is found in three steps.

First, the potential distribution Φ_1 is found for a cell with a voltage V_a applied to the outer electrode ($2V_a$ in a full cell) and 0 V applied to the inner electrode. The currents $I_{in,1}$ and $I_{out,1}$ are found for the inner and outer electrode by integrating the current density at the interface of the electrodes.

Similarly Φ_2, $I_{in,2}$ and $I_{out,2}$ are found for a case where the electrode voltages are interchanged.

Last, the real solution is found as a linear combination $\Phi = \alpha\Phi_1 + \beta\Phi_2$ which also fulfils Laplace's equation. In order to meet the conditions of V_a on the outer electrode and zero current at the inner electrodes it is clear that $\alpha = 1$ and $\beta = -\alpha I_{in,1}/I_{in,2} = -I_{in,1}/I_{in,2}$. Thus the potential measured at the inner electrode is

$$V_m = -2V_a\frac{I_{in,1}}{I_{in,2}} \tag{16}$$

and the current flowing in the outer electrode

$$I_a = I_{out,1} - I_{out,2}\frac{I_{in,1}}{I_{in,2}} \tag{17}$$

which gives a cell constant of

$$K = \frac{V_m}{I_a} = \frac{-2V_a}{I_{out,1}(I_{in,2}/I_{in,1}) - I_{out,2}} \tag{18}$$

The FEM model is verified by comparing the analytical determined cell constant for the hemispherical electrodes with the FEM calculated cell constant (Fig. 9). The hemisphere FEM results are in very good agreement with the analytical solution. The approximate solution is only good for electrode radius much smaller than the spacing. The analysis also show that moderately sized square planar electrodes can be described with an accuracy within 15% by using results from hemispherical electrodes of the same surface area.

Fig. 11 shows the FEM simulated $K \times A$ product of rectangular planar electrodes as a function of the electrode width and length. In conclusion the electrodes should occupy all available space on a chip of limited size in order to lower the cutoff frequency. However, too closely spaced electrodes will result in an increase in cutoff frequency due to very low cell constants.

For the four electrode setup all the above considerations are also valid, and the voltage electrode should be placed as close to the current electrodes as possible. In the upper limit the four electrode cell constant becomes equal to the two electrode cell constant. The size of the voltage electrodes is not important unless the contact impedance becomes comparable to the inner impedance of the measurement equipment as discussed in Section 2.

3.3. Process design

The sensor is fabricated on a silicon substrate where conventional fabrication processes can be used. When choosing the fabrication technology, the main concerns are the surrounding media and the sensor integration. The sensor system is exposed directly to the seawater which calls for a protective coating. In our case a LPCVD Si_3N_4 film is chosen because of its excellent chemical stability, its low water diffusivity (less than 10^{-18} cm^2 s^{-1}[11]) and its well established fabrication technology. In order to electrically connect the sensors to the electronics, a wiring system, which is isolated from the water as well, has to be applied. Because of the high thermal budget of the Si_3N_4 fabrication, a metal film is not an option. Highly doped silicon paths can be used, but the high density of wires, the relatively high resistivity (compared to met-

Please cite this article in press as: A. Hyldgård, et al., Autonomous multi-sensor micro-system for measurement of ocean water salinity, Sens. Actuators A: Phys. (2008), doi:10.1016/j.sna.2008.06.004

G Model
SNA-6309; No. of Pages 11
ARTICLE IN PRESS

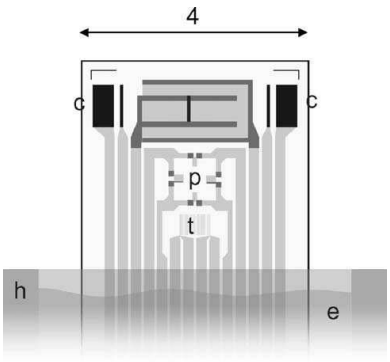

Fig. 12. Chip layout. Pressure sensor (P), $TiSi_2$ wiring and temperature sensor (T), pn-junction light sensor (L), four conductivity electrodes (C), polystyrene housing (H) and Epoxy (E).

als) and the high capacitance to the substrate makes doped silicon wires unattractive. An excellent alternative is titanium disilicide ($TiSi_2$)[12] which offers high thermal stability, a low resistivity (~ 10 times lower than highly doped silicon) and manageable processing. In addition the $TiSi_2$ can be used as thermistor material with a relatively high sensitivity to temperature and insignificant sensitivity to light (compared to doped silicon thermistors). The electrode material should be chosen from criteria of good electrochemical coupling to the electrolyte and chemical inertness. Platinum electrodes are preferred in many applications, and are also used in our sensor. In some cases the platinum surface is processed to form a porous structure, so-called platinum black, in order to increase the effective area. However, this method is unfit for marine applications since the rough surface is a catalyst for bio-fowling, e.g. algae growth.

3.4. Sensor layout

A central square membrane with piezoresistors centered on the membrane perimeter lines connected in a Wheatstone bridge configuration, serves as the pressure sensor (see Fig. 12). A meander structure $TiSi_2$ four point thermistor serves as an accurate, local and fast temperature sensor. The piezo resistors have a resistance of approximately 30 k Ω and the $TiSi_2$ thermistor 1 k Ω. The power consumption of the sensor is inversely proportional to the resistance while the thermal noise is proportional to the square root of the resistance [14]. The resistor values are therefore chosen as a tradeoff between power consumption and signal to noise ratio. A pn-junction measures light. The four platinum electrodes are placed in pairs on two sides of the pressure sensor membrane and light sensor. The whole sensor area is exposed directly to the seawater while a low resistance $TiSi_2$ wiring system connects the sensors to contacts in the other end of the chip. The electrodes, the thermistor and the wiring system are isolated from the substrate by a silicon dioxide film and protected from the seawater by a silicon nitride film (electrodes are exposed). Ideally, the silicon dioxide under the electrodes should be as thick as possible. However, the oxide layer is shared by the pressure sensor where only a limited silicon dioxide layer thickness can be used on the membrane. Alternatively a local oxidation step can assure different silicon dioxide layer thicknesses allowing good capacitive isolation of the electrodes from the substrate. The contacts are sealed off from the water with an Epoxy [13].

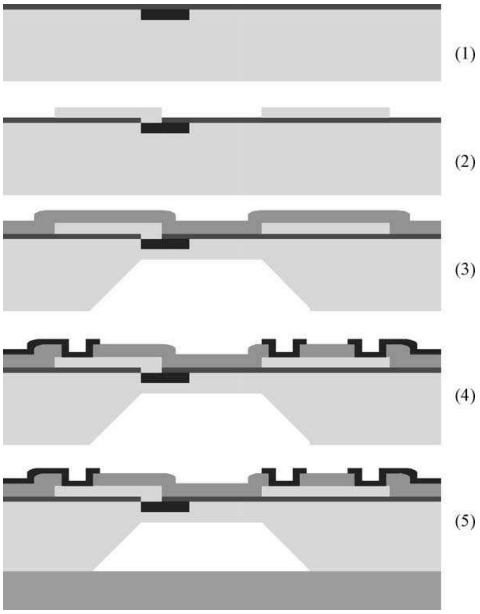

Fig. 13. Chip fabrication sequence. (1) Piezo resistors for the pressure sensor are ion implanted. (2) $TiSi_2$ wiring and temperature sensor are formed. (3) Si_3N_4 coating is applied and a membrane etched out. (4) Two metallizations form electrodes and contact areas. (5) A Pyrex wafer is anodic bonded to the backside.

4. Fabrication

An outline of the fabrication process is shown on Fig. 13. The detailed process proceeds as follows:

(1a) A 100 nm thick wet thermal oxide is grown ($T = 1150\,^{\circ}C$) on a 350 μm thick double polished (1 0 0) Si n-type (10 Ω-cm) substrate. Alignment marks are made by opening windows in the oxide followed by further thermal oxidation resulting in 200 nm oxide.
(1b) Ion implantation masked with a 2.2 μm thick AZ5214e resist is used to form the piezoresistors (^{11}B, 5×10^{14} cm^{-2}, 50 keV), the substrate conductor (^{11}B, 10^{15} cm^{-2}, 150 keV) and the substrate contact (^{31}P, 6×10^{15} cm^{-2}, 150 keV).
(2a) The implanted resistors are contacted via a self-aligned $TiSi_2$ wiring system[12]. This is done by deposition and structuring of 100 nm polysilicon (LPCVD at 620 ° C and wet etch in HF and HNO_3) followed by deposition of 44 nm Ti and a two step RTP annealing process at 600 ° C for 5 min and 850 ° C for 60 s to form the stable C54 phase of $TiSi_2$.
(3a) Both sides of the wafer are coated with a 120 nm thick LPCVD silicon nitride deposited at 800°C.
(3b) Holes are opened in the nitride using Reactive Ion Etching in a SF_6/O_2 plasma (32:8 sccm, 80 mTorr). Holes are opened in the underlying oxide in HF and a timed KOH etch is performed to form the 30 μm thick membrane of the pressure sensor.
(3c) The nitride on the backside is then removed in H_3PO_4. The nitride on the front side works as a protective coating for the sensors and is thus protected by a PECVD oxide during the etch. This oxide is subsequently removed.
(4a) Contact holes through the nitride is formed by reactive ion etching in a SF_6/O_2 plasma.

Please cite this article in press as: A. Hyldgård, et al., Autonomous multi-sensor micro-system for measurement of ocean water salinity, Sens. Actuators A: Phys. (2008), doi:10.1016/j.sna.2008.06.004

G Model
SNA-6309; No. of Pages 11
ARTICLE IN PRESS

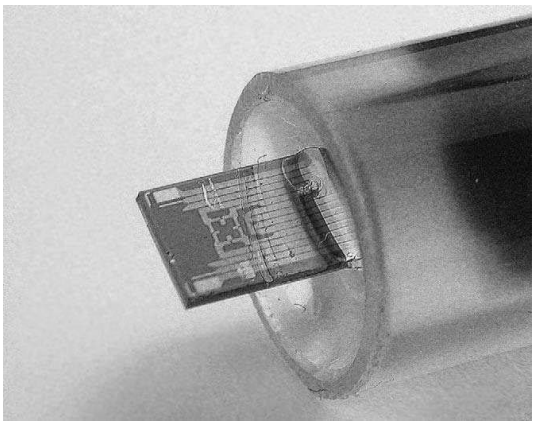

Fig. 14. Photograph of finished chip sticking out of a polystyrene tube filled with Epoxy. Sensors and wires are protected from the sea water by a Si_3N_4 film, and the bonding pads, electronics and battery is inside the Epoxy packaging.

(4b) A lift off process is used to define the 100/10 nm Pt/Ti layer used for the conductivity electrodes.
(4c) And another lift off process defines the 200/10 nm Au/Ti layer used for the bonding pads.
(5a) Finally, a 500 μm pyrex wafer is anodically bonded to the backside of the wafer (at 375 °C) at low pressure forming the reference cavity for the pressure sensor.

The chip is packaged using a potted tube packaging concept. The sensors and PCB is placed in a Polystyrene tube which is subsequently filled with two component *EpoTek 302-3M* [16] epoxy leaving one end of the sensor exposed to the surroundings (Fig. 14). This process is known as potting. Potting is a compact and reliable packaging scheme that allows for direct yearlong exposure of a silicon sensor to the surrounding environment with a high degree of protection of the vulnerable parts of the system [13].

5. Results

The finished salinity sensors are tested in a lab environment. The pressure sensor is calibrated in an air-pressurized chamber whereas the conductivity and temperature sensors are tested in samples of dissolved KCl in water at different saline concentrations. The sensors are submerged in beakers of saline water and a mechanical stirrer ensures high level of uniformity (A magnetic stirrer has been avoided since it affects the measurement).

The beakers are placed in an outer salt water thermal reservoir which again is put in a thermo insulating box in order to ensure uniform quasi-equilibrium conditions.

5.1. Conductivity sensor

The conductivity is measured using two sets of electrodes of different dimensions as listed in Table 1. The two sets illustrates how the cell constant and salinity window width change with geometry. The measured cell impedance for (400 μm × 100 μm × 1500 μm center spacing) E_A electrodes as a function of frequency is shown in Fig. 15. The response is very much like the theoretically predicted in Fig. 5. The salinity window is quite narrow and the accuracy of salinity sensor will suffer if the double layer capacitance changes just slightly. An error compensation procedure may be applied to minimize this effect. A first order series expansion of Eq. (2) will give

Table 1
Table of electrode dimensions

Design electrode	E_A		E_B	
	Current	Voltage	Current	Voltage
Width (μm)	100	50	400	50
Length (μm)	400	400	800	800
Centre spacing (μm)	1500	1200	3500	2800

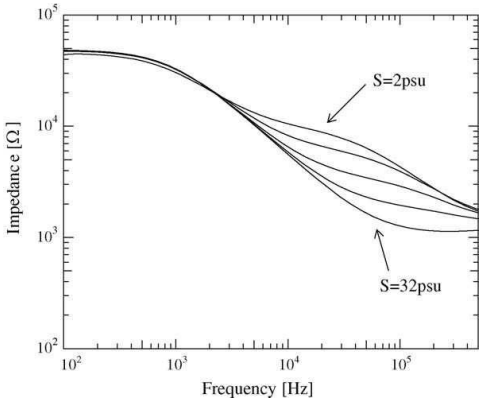

Fig. 15. Measured cell impedance as a function of frequency for a two electrode cell at five different salinities (2, 4, 8, 16 and 32 psu). At medium frequencies there is a salinity sensitive window. At low frequencies the Debye layer is not short-circuited. At high frequencies the cell conducts through the substrate loosing sensitivity.

a simple approximation of the low-medium frequency response as

$$|Z| \approx R_w \left(1 + \frac{1}{2\omega^2 C_{dl}^2 R_w^2}\right) \quad (19)$$

Thus plotting the impedance as a function of inverse frequency squared (see Fig. 16) will make the impedance in the salinity window linear with a slope depending on the double layer capacitance and an intersect at $\omega^{-2} = 0$ of R_w corresponding to conditions of a short circuited double layer capacitance at infinite frequency. The 18 kHz cell impedance (From Fig. 15) and the extrapolated impedance (from Fig. 16) of E_A are shown in Fig. 17 as a function of

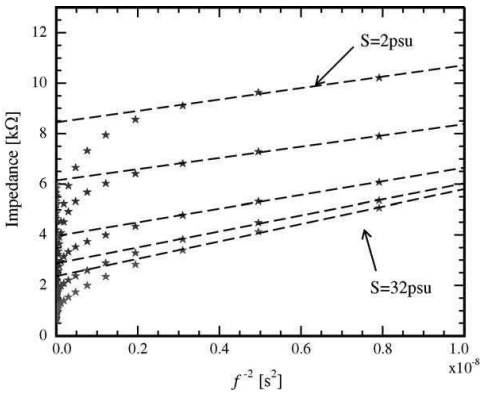

Fig. 16. Measured cell impedance as a function of f^{-2} at five different salinities (2, 4, 8, 16 and 32 psu). According to Eq. (19) this relation should be locally linear for frequencies in the salinity window. Making a linear fit and extrapolation to infinite frequency ($f^{-2} = 0$) eliminates the double layer contribution to the impedance.

Please cite this article in press as: A. Hyldgård, et al., Autonomous multi-sensor micro-system for measurement of ocean water salinity, Sens. Actuators A: Phys. (2008), doi:10.1016/j.sna.2008.06.004

G Model
SNA-6309; No. of Pages 11
ARTICLE IN PRESS

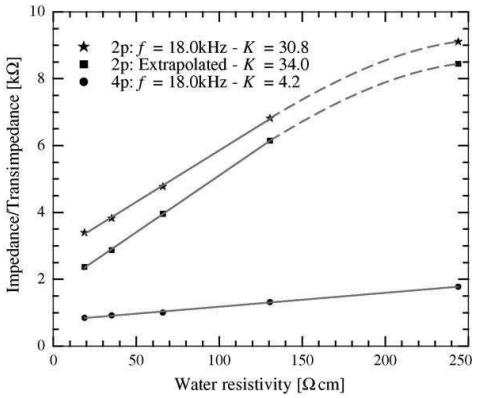

Fig. 17. 18 kHz and extrapolated (E_A) conductivity cell impedance as a function of water resistivity measured with a commercial reference sensor. The two electrode impedance varies linearly with resistivity for low resistivities but suffer from parasitic conductance for higher resistivities. The extrapolated results will however be much more tolerant to changes in double layer capacitance. The four electrode trans-impedance response is more linear but still has a large offset.

reference resistivity. In both cases the relation is linear at low resistivities but suffer from parasitic conductance for higher resistivities. The extrapolated results will however be much more tolerant to changes in double layer capacitance. In both cases a large offset indicates that the effects of the double layer and series resistances are not completely avoided.

The four electrode configuration further reduces this problem. In this case the conductivity measurements at a single frequency should be possible even with changes in double layer capacitance. A current is forced through the outer electrodes while measuring the voltage at the inner electrodes. The cell trans-impedance as a function of frequency is shown in Fig. 18. The resulting trans-impedance as a function of reference resistivity is shown in Fig. 17 for comparison. Evidently the cell constant is much lower in the four electrode case, but the linearity is much better.

Similar measurements are carried out for electrode configuration E_B and the results are summarized in Table 2. As seen the cell constants are in very good agreement with theory, except for

Table 2
Table of cell constants

	K—2 electrode (cm^{-1})		K—4 electrode (cm^{-1})	
	E_A	E_B	E_A	E_B
Theoretical	36.8	14.0	13.6	6.6
Measured	34	–	4.2	5.7

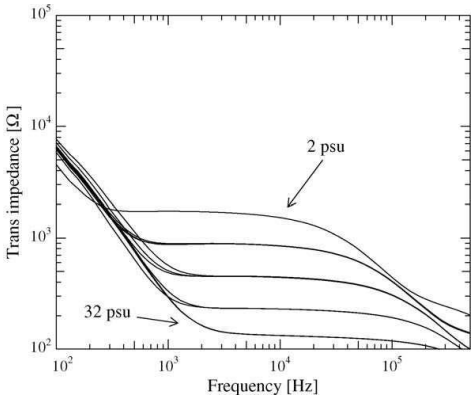

Fig. 19. Measured E_B cell trans-impedance as a function of frequency for five different salinities (2, 4, 8, 16 and 32 psu). The salinity window is wider compared to E_A shown in Fig. 15. The trans-impedance at 3.4 kHz is used to construct Fig. 20.

E_A four electrode case where the deviation is expected to be due to poor matching of the measurement equipment (too low input impedance). The quite low cell constant of the configuration E_A four electrode measurements is tolerable, and the salinity window is much wider compared to E_A (See Fig. 19) allowing for a precise determination of conductivity. Fig. 20 shows the four electrode trans-impedance as a function of reference resistivity for the E_A and E_B configuration. Clearly E_B delivers the best results.

The temperature effect on conductivity is investigated by cooling the outer reservoir to -2° C and the system is left for the temperature slowly to increase towards room temperature. The trans-impedance of the cell at different frequencies is measured

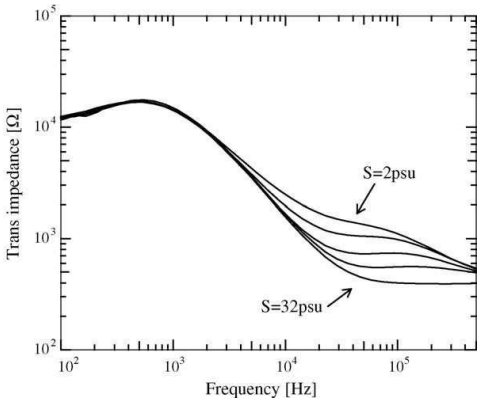

Fig. 18. Measured trans-impedance as a function of frequency for a four electrode cell at five different salinities (2, 4, 8, 16 and 32 psu). The trans-impedance at 18 kHz is used to construct Fig. 20.

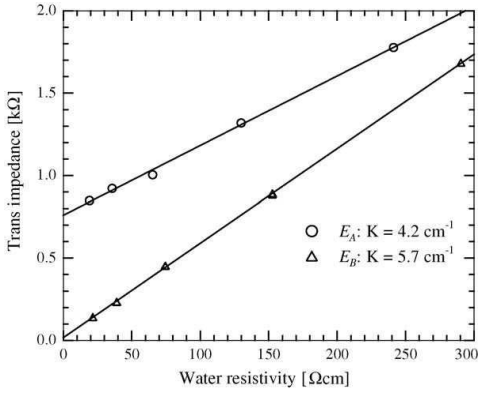

Fig. 20. 18 kHz (E_A) and 3.4 kHz(E_B) conductivity cell trans-impedance as a function of water resistivity measured with a commercial reference sensor. The E_B cell shows a linear response with a cell constant of 5.7 cm^{-1} and negligible offset which allows for determination of the salinitiy with an accuracy of ±0.5 psu.

Please cite this article in press as: A. Hyldgård, et al., Autonomous multi-sensor micro-system for measurement of ocean water salinity, Sens. Actuators A: Phys. (2008), doi:10.1016/j.sna.2008.06.004

G Model
SNA-6309; No. of Pages 11
ARTICLE IN PRESS

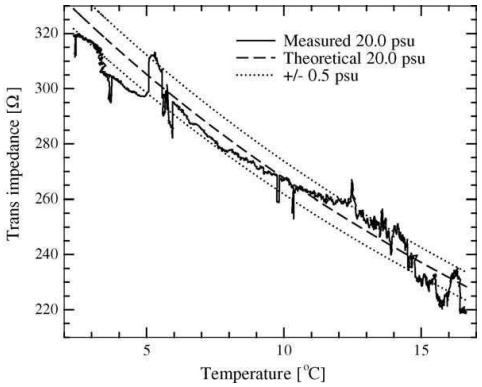

Fig. 21. Measured and theoretical 3.4 kHz trans-impedance (E_B) as a function of temperature. The sensor has an accuracy of approximately ±0.5 psu. The variations in impedance are probably due to changes in the near electrode conditions such as air-bubbles or salt and organic debris.

during the temperature rise. The system temperature is monitored with the chip temperature sensor and an external reference temperature sensor. The measured resulting 3.4 kHz trans-impedance of E_B as a function of temperature is shown in Fig. 21. The theoretical temperature dependence is found using the cell constant calculated at 15 °C. The resolution is 0.1 mS cm^{-1}. The variations in impedance are probably due to changes in the near electrode conditions such as air-bubbles. The accuracy of the conductivity determination will also depend very much on the long time stability of the electrodes. Initial investigations have shown no significant algae growth or electrode degradation when exposed to an algae fermentation solution for periods of weeks. Therefore the accuracy is expected to be limited by the resolution.

At stabilized temperature the short term repeatability of the measurements is excellent and the accuracy is better than 0.2 mS cm^{-1} allowing for the determination of salinity with accuracy better than 0.2 psu. However the long term measurements at varying temperatures indicates that the accuracy is actually as low as ±0.5 psu. If this inaccuracy is due to changes in the conditions at the water–electrode interface, such as bubbles or residues of salt or organic debris, the accuracy might increase with increase in electrode size as the average influence will be smaller.

5.2. Temperature sensor

The thermistor is calibrated against a commercial class A certified PT100 sensor. The repeatability at numerous temperature cycles is excellent. A temperature coefficient of resistance of 4.2×10^{-3} K^{-1} is achieved with a resolution of 0.01 ° C and an accuracy of 0.13 °C. The temporal response of the sensor is evaluated by submerging the calibrated chip into saline solutions at two different temperatures. This experiment is carried out for a sensor within the packaging material and a fully exposed sensor. The encapsulated sensor takes 55 s to reach 66% of the temperature step which is comparable to specifications of commercial DSTs. The fully exposed sensor reaches 77% of the temperature step in less than 1 s. Layers in the ocean with rapid changes in temperature (thermocline) and/or rapid changes in salinity (halocline) exist, e.g. where fresh water stream into ocean water or where the sun heats up the upper stagnant layer of water. A fast response time will increase the reliability of measurements in the presence of such phenomena.

5.3. Pressure sensor

The pressure sensor Wheatstone bridge shows a linear response with a sensitivity of $V_{out}/V_{in} = 0.014$ bar^{-1} and a accuracy of 0.1 bar (0.5% of full scale) when an air pressure is applied.

6. Conclusion

The conductivities of the water samples are measured with an accuracy of 0.6 mS cm^{-1} and the temperature and pressure is measured with an accuracy of ±0.13 ° C and ±0.05 bar, respectively. The salinity can therefore be detected with an accuracy of ±0.5 psu.

The accuracy of the sensor is not as high as in macro-size CTD profilers (0.5 psu compared to 0.005 psu) but it is sufficiently accurate for tracking purposes. The system volume is however much smaller (∼ 5000 ×). The integrated salinity multi-sensor is successfully fabricated using conventional silicon micro-fabrication technology and is packaged using a novel Epoxy packaging scheme. The sensor has been used successfully in a lab environment and has proven stable when exposed to water with high concentration of algae culture. This is, to our knowledge, the first published application of a micro-scale integrated CTD profiler.

Acknowledgment

The authors would like to thank the Danish Institute for Fisheries Research (DIFRES) who supported this work.

References

[1] J.D. Metcalfe, G.P. Arnold, Nature 387 (1997), 665–662.
[2] S. Neuenfeldt, H. Hinrichsen, A. Nielsen, A method to geolocate eastern Baltic cod by using Data Storage Tags (DSTs), ICES CM 2004/L:06.
[3] http://www.cefastechnology.co.uk.
[4] http://www.star-oddi.com.
[5] A. Hyldgård, O. Hansen, E.V. Thomsen, Fish & chips: single chip silicon MEMS CTDL salinity, temperature, pressure and light sensor for use in fisheries research, in: IEEE MEMS 2005 proceedings, 2005, pp. 303–306.
[6] A. Hyldgård, Í. Olafsdóttir, M. Olesen, T. Hedegaard, O. Hansen, E.V. Thomsen, IEEE Sensors 2005 Proceedings, 2005, pp. 1124–1127.
[7] E.L. Lewis, The practical salinity scale 1978 and its antecedents, IEEE Journal of Oceanic Engineering (1980).
[8] E. Barsoukov, J.R. Macdonald, (Ed.), Impedance Spectroscopy—Theory, Experiment and Applications, Wiley (2005).
[9] S. Ramo, T. Van Duzer, J.R. Whinnery, Fields and Waves in Communication Electronics, Wiley, 1984.
[10] http://www.comsol.com.
[11] R.K. Ulrich, A.J. Phillips, D.H. Yi, W.D. Brown, S.S. Ang, Microelectronics and Reliability 31 (1991) 1237–1249.
[12] S.P. Murarka, Silicide Films and their Applications in Microelectronics, Elsevier Science Limited, 1994.
[13] A. Hyldgård, K. Birkelund, J. Janting, E.V. Thomsen, Direct media exposure of MEMS multi-sensor systems using a potted-tube packaging concept, Sensors and Actuators A, doi:10.1016/j.sna.2007.02.024, in press.
[14] S.D. Senturia, Microsystem Design, Kluwer Academic Publishers, 2002.
[15] J. N. Sœrensen, Establishment of a Primary Standard for Electrolytic Conductivity and New Reference Solutions, Ph.D. thesis, Technical University of Denmark (2000).
[16] http://www.epotek.com.

Biographies

Anders Hyldgård received his M.Sc. (2004) and Ph.D. (2008) degrees in Physics and Nanotechnology from the Technical University of Denmark. He is currently employed as a development engineer at SunSil A/S working with crystalline solar cells and high efficiency solar cell systems.

Dennis Mortensen received his M.Sc. degree in Physics and Nanotechnology from the Technical University of Denmark in 2007. He is currently employed as an R&D engineer at Sonion A/S within the field of micro-sensors for hearing aids.

Karen Birkelund received her M.Sc. degree from Roskilde University, Denmark in 1994 and her Ph.D. degree in Micro and Nanotechnology from the Microelectronics

Please cite this article in press as: A. Hyldgård, et al., Autonomous multi-sensor micro-system for measurement of ocean water salinity, Sens. Actuators A: Phys. (2008), doi:10.1016/j.sna.2008.06.004

G Model
SNA-6309; No. of Pages 11

Center of the Technical University of Denmark in 1997. She has worked at Danfoss A/S, TopSpin and Cantion A/S. She is currently employed at the Department of Micro and Nanotechnology at the Technical University of Denmark, where focus of her work is on microsystem encapsulation for harsh environments.

Ole Hansen received the M.Sc. degree from the Semiconductor Laboratory, DTU, in 1977. Since then he has done research in silicon-based micro- and nanotechnology and its applications, first at the Semiconductor Laboratory, and later at the Department of Micro and Nanotechnology, MIC. Current research interests include Deep Reactive Ion Etching of silicon, $Si_{1-x}Ge_x$/Si heterostructures, microreactors for catalysis, and cantilever-based microprobes for nano-science. He is presently teaching three lecture courses: Semiconductor Technology, Semiconductor Devices and Microelectromechanical Systems. Since 1990 he has been an Associate Professor at MIC.

Erik V. Thomsen is group leader for the MEMS Applied Sensors activities at the MEMS section at the Department of Micro and Nanotechnology, Technical University of Denmark, DTU, where he is affiliated as associate professor. He holds a M.Sc. in physics from Odense University and a Ph.D. in electrical engineering from DTU. Erik V. Thomsen has been affiliated with MIC since 1992 and has been working with fabrication of semi-conductor devices. His current interests include research and teaching within micromechanical multi-sensors, piezo resistivity of strained layers, piezoelectric MEMS devices, and micro-system packaging. He teaches classes in solid-state electronics, microtechnology and nano- & microfabrication".

Please cite this article in press as: A. Hyldgård, et al., Autonomous multi-sensor micro-system for measurement of ocean water salinity, Sens. Actuators A: Phys. (2008), doi:10.1016/j.sna.2008.06.004

APPENDIX

E Conference Proceedings

E.1 IEEE MEMS 2005 - Miami Beach, Florida, USA

FISH & CHIPS: SINGLE CHIP SILICON MEMS CTDL SALINITY, TEMPERATURE, PRESSURE AND LIGHT SENSOR FOR USE IN FISHERIES RESEARCH

A. Hyldgård, O. Hansen, and E.V. Thomsen
Technical University of Denmark, Dept. of Micro and Nanotechnology (MIC), Lyngby, Denmark

ABSTRACT

A single-chip silicon MEMS CTDL multi sensor for use in aqueous environments is presented. The new sensor chip consists of a conductivity sensor based on platinum electrodes (C), an ion-implanted thermistor temperature sensor (T), a piezo resistive pressure sensor (D for depth/pressure) and an ion-implanted p-n junction light sensor (L). The design and fabrication process is described. A temperature sensitivity of $0.8\times10^{-3}K^{-1}$ has been measured and detailed analysis of conductivity measurement data shows a cell constant of $81cm^{-1}$.

1. INTRODUCTION

In recent time a significant focus has been set on fish behaviour and fish population estimations due to the expected endangerment of certain species of fish mainly as a result of excessive fishing activity. Reliable monitoring of individual fish behaviour and migration in their natural environment is crucial in order to make accurate population estimations and plans for preservation of the different species.

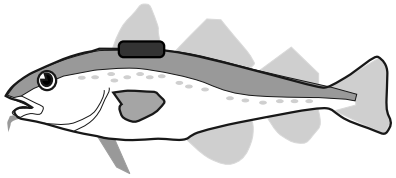

Figure 1: A cod with a Data Storage Tag sutured onto its back. The considerable size of current tags sets the lower limit for the size of the fish that can be tagged.

Data Storage Tags (DSTs) are small autonomous measuring systems that offer to deliver precise information about the fish surroundings. When a fish is caught the DST is sutured to its back (see Figure 1) and the fish is released. For a period of time the DST measures parameters in the fish surroundings and stores the data in an internal memory. When fishermen re-catch the fish, an award is offered for the return of the DST, and researchers can then retrieve the measured data.

The usefulness of current DSTs is strongly limited by the size, price and limited measuring capabilities. The DSTs comprise of a sensor part, interface electronics, a non-volatile memory and a energy source as depicted in Figure 2. The aim of our project is to increase measuring capabilities and to shrink the system size while keeping in mind that the design is only a complete success if tags can be produced at a price comparable or preferably lower than that of the DSTs available today.

By making an integrated multi-sensor and applying custom made electronics and packaging concept the total system size can be shrunk to a size mainly limited by the size of the needed energy source. The emphasis of this paper is on the design and fabrication of multi-sensor chips capable of measuring depth, temperature, salinity and light intensity. From well-established polynomial fits to empirical data of the conductivity, temperature and pressure, the salinity can be calculated [1]. The light intensity day variation can be used to deduct the longitude and latitude. This information can be used to reconstruct fish migration and fish patterns of behaviour.

The new multi-sensor chip implements, unlike conventional sensor systems, all sensors needed to make salinity measurements at high-pressure (e.g. at deep-sea), where the conductivity data has to be pressure compensated to ensure accurate salinity results.

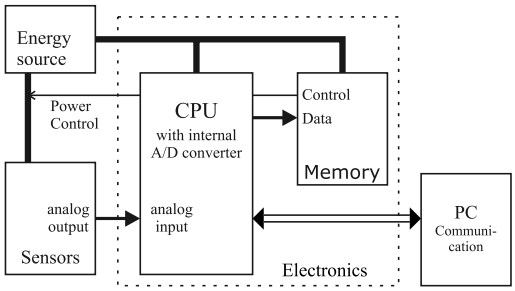

Figure 2: Schematics of the Data Storage Tag subparts. The sensors can be integrated into one chip and the electronics on another. The volume of a complete system will ultimately be limited by the onboard energy source.

2. DESIGN

The chip has been designed so that it can be exposed directly to the seawater in order to gain a high level of accuracy and low response times. A reliable O-ring packaging concept as depicted in Figure 3 is used, and a protective film is applied to the chip surface. The chip packaging concept with a compressed O-ring and a protective film has proven very reliable in other harsh environments [2] and should offer excellent protection.

The chip size is $4\times6mm^2$ and the sensors are placed as central on the chip as possible in order to minimize the influence from stress that unavoidably will be introduced from the packaging. The chip can easily be shrunk to $4\times4mm^2$ in final production by rearranging the contact areas to the corners of the square chip.

The pressure sensor consists of a 50 μm thick, 800 μm square membrane with four piezo resistors

(N_A=2.2×10^{18}cm^{-3}) arranged in a Wheatstone bridge configuration. The resistors are placed so that the resistor value will pair wise increase and decrease to give a linear bridge output signal from 0-20 bar with a resolution of about 0.1 bar.

The temperature sensor is also made as a Wheatstone resistor bridge with the resistor doping concentration tuned to give a negative and positive temperature response. N_A=5×10^{16}cm^{-3} gives a temperature coefficient of resistance (TCR) of 3.6×10^{-3}K^{-1} and N_A=2.2×10^{18}cm^{-3} gives a TCR of -0.5×10^{-3}K^{-1}. The output to input signal ratio will thus have a sensitivity of approx. 2×10^{-3}K^{-1}. This results in a possible resolution of at least 0.01K for a 3V input voltage.

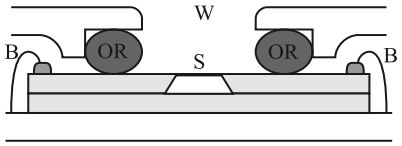

Figure 3: Cross-section of the O-ring packaging concept. The sensor-chip area (S) is exposed directly to the water (W) though the O-ring (OR). Wire-bonds (B) make electrical connections to the interface electronics.

A set of electrodes exposed directly to the seawater functions as an electrical conduction sensor cell. To measure the conductivity of an electrolyte it is nescessary to use AC voltages, because of dominant capacitances at the electrode-electrolyte interface. The electrodes are dimensioned on the basis of a FEM model and capacitive considerations in order to ensure that a change in electrical conductivity in the water can be observed at medium frequencies as described in the results section. The design allows for both two- and four-probe measurements.

The light sensor is a p-n junction diode with a 0.37 mm^2 junction area. Fortunately, silicon is a strong absorber at the blue wavelengths where seawater transmits light. This makes light measurements possible at a depth lower than 100m in *clear* seawater.

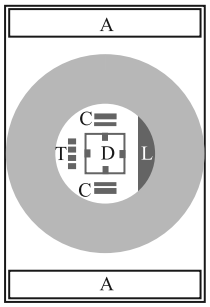

Figure 4: Chip design layout. The sensors; Temperature (T), Pressure (D), Electrical conductivity (C) and Light intensity (L), are centred with respect to the interface O-ring. The contact areas (A) are placed on the dry ends of the chip.

All sensors are electrically connected to contact pads at the edge of the chip. The very compact placement of the sensors yields a need for low sheet resistance interconnects that can be placed under a protective film. A silicide serves this purpose as well as light shielding of the sensor areas, to eliminate light sensitivity for the implanted pressure and temperature sensors. Furthermore, silicide combined with implanted conductors allows for crossover of electrical interconnects. The chip layout is depicted in Figure 4.

3. FABRICATION

Figure 5 shows a cross-sectional fabrication sequence for the multi-sensor chip. Different resistors optimized for piezo resistivity, thermal sensitivity and high conductivity, respectively, are ion-implanted through a silicon dioxide layer into the single crystal silicon (100) substrate. The resistive sensors have a resistance of approx. 30kΩ to yield low power consumption while keeping a high signal to noise ratio.

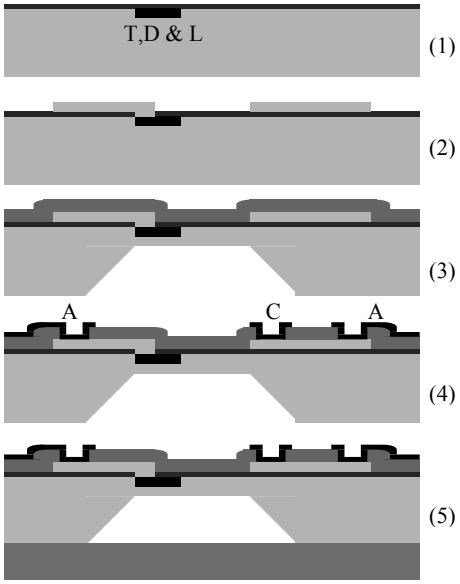

Figure 5: Chip fabrication sequence. (1) Sensors (T,D & L) are ion implanted. (2) $TiSi_2$ wiring is formed. (3) Si_3N_4 coating is applied and a membrane etched out. (4) Two metallizations form electrodes (C) and contact areas (A). (5) A Pyrex wafer is anodic bonded to the backside.

The implanted resistors are contacted via a $TiSi_2$ wiring system made by RTP annealing of titanium and polysilicon. The low sheet resistance of the $TiSi_2$ wiring ensures low parasitic series resistances between sensors and contacts even in long conductor paths ($R_{\square}$=1Ω).

Both sides of the wafer are coated with a LPCVD silicon nitride. The nitride is used as masking material in the subsequent KOH bulk silicon etch that forms the pressure sensor membrane. The backside nitride is then removed

whereas the front-side nitride is kept as the protective coating of the sensors. Contact holes are made through the nitride by reactive ion etching.

The chips are metallized by platinum and gold to form electrodes and contact pads respectively as the demands for corrosion inertness and wire bonding compatibility are not met by a single metal. The backside of the chip is anodic bonded to a Pyrex wafer to form a low-pressure reference cavity and add mechanical stability to the chip.

The complete process is only slightly more complex than processes used in commercial pressure sensor fabrication, and is well suited for batch processing. A finished chip is shown in Figure 6.

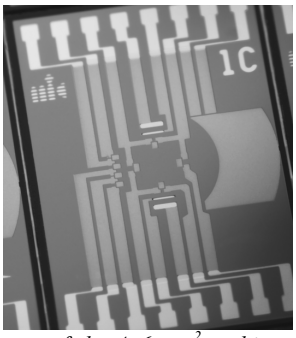

Figure 6: Picture of the 4×6 mm^2 multi-sensor chip. The dark paths are titanium silicide conductors and the light areas are gold used for bonding-pads and electrodes. The front-side is protected by a Si_3N_4 film.

4. RESULTS

Piezo resistive pressure sensors and p-n junction photo diodes are well described in literature and the performance is well known. The light sensor shows a linear response to light intensity but a measure of noise and quantum efficiency is needed to evaluate the performance of the sensor. The emphasis here will be on the electrical conductivity measurements and the temperature sensor. These are also the most important parameters when determining the salinity.

Temperature

The temperature sensor has been tested in an air heated oven using a K-type thermo couple (TC) for the reference temperature probe. The measured temperature range is higher than the expected working range, but it shows that leakage currents are not a problem. As the data in Figure 7 indicates there must be a slight time delay between the TC and the chip sensor as the heating and cooling curve differ. The results were reproducible so the difference is not drift related.

The slight non-linearity is partly due to the change in temperature coefficient of resistance of the sensor with temperature and partly due to a slightly unbalanced Wheatstone bridge. For sea investigations the above deviations should give no problems, since the expected temperature variations are limited and the heat transport more efficient. The sensor sensitivity of $0.8\times10^{-3}K^{-1}$ is approximately 40% of the expected value. This could be caused by a deviation in actual doping level from the design value or that the temperature model is not accurate enough in this range.

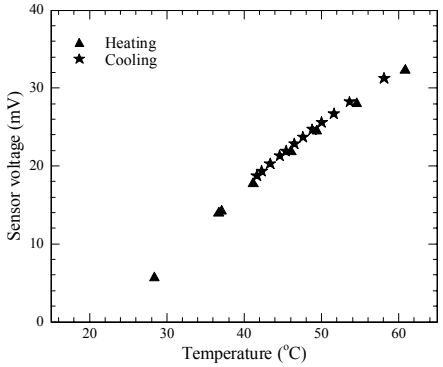

Figure 7: The temperature sensor voltage as a function of refererence temperature measured with a thermocouple. For small changes in temperature the dependence is almost linear.

Electrical conductivity

In the ideal case the cell impedance Z is related to the water conductivity κ through the equation

$$Z = \frac{K}{\kappa}$$

where the cell constant K depends on the cell geometry. However, due to parasitic capacitances in the substrate and electrolytic double layer capacitances forming in the water at the electrode interface [3], the measured cell impedance has to be compensated. A simplified equivalent circuit of Z is shown in Figure 8. Z_E expresses the electrolysis process and is much higher than the water impedance Z_W. Z_W and the double layer capacitance C_{DL} depend on the electrode area. The cell is designed to make C_{DL} and Z_W high while keeping the parasitic capacitance C_P low.

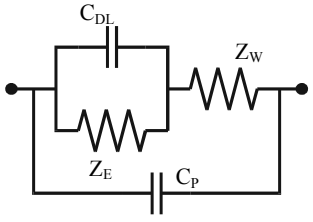

Figure 8: Conductance cell equivalent circuit. The electrolysis impedance Z_E is much higher than the water impedance Z_W. The double layer capacitance C_{DL} is higher than the parasitic capacitance C_P.

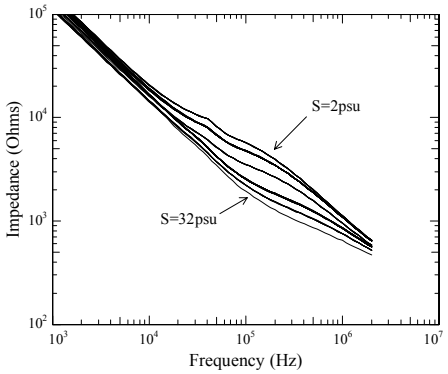

Figure 9: Cell impedance at 6 different salinities (2, 4, 8, 16, 24 and 32psu) as a function of frequency. For each salinity value approx 10 measurements are super-imposed.

Figure 9 shows the cell impedance vs. frequency for 6 different salinities. The impedance depends strongly on salinity at frequencies between 50kHz and 500kHz. By plotting the cell impedance vs. $1/f^2$ and extrapolating to infinite frequency the water impedance (Z_w) can be deducted from the intersection with the impedance axis (Figure 10). The deducted water conductance ($1/Z_w$) shows a linear dependence on the reference conductivity measured with a Radiometer CDC749 probe, as depicted in Figure 11. The offset stems from the parasitic conductance that is also experienced with no water in the cell. The deducted cell constant K for extrapolated data is 81cm^{-1} which compares well with FEM results. The cell conductance is also linear dependent on water conductivity when measured at a single frequency. The best sensitivity is found at f=493kHz giving an effective K of 68cm^{-1}. The extrapolation method should deliver accurate results even when the capacitance changes due to algae growth etc.

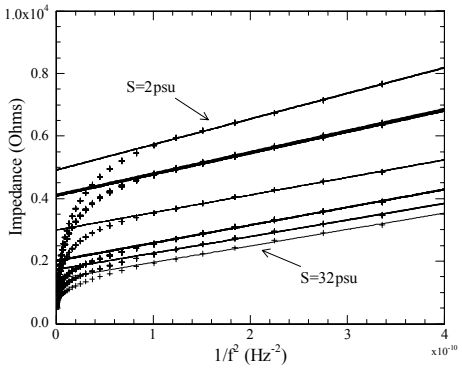

Figure 10: Measured cell impedance as a function of $1/f^2$ at 6 different salinities (2, 4, 8, 16, 24 and 32psu). For each salinity value approx 10 measurements are super-imposed. Extrapolation to infinite frequency eliminates the double layer contribution.

A PSpice model (Figure 8) is fitted to the experimental data and the extracted capacitances are in good agreement with the expected theoretical values. The extracted double layer capacitance C_{DL} is 1μF which compares well with an estimate of 3μF based on typical values [3]. An extracted parasitic capacitance C_P of 170pF compares well with 70pF estimated from device geometry.

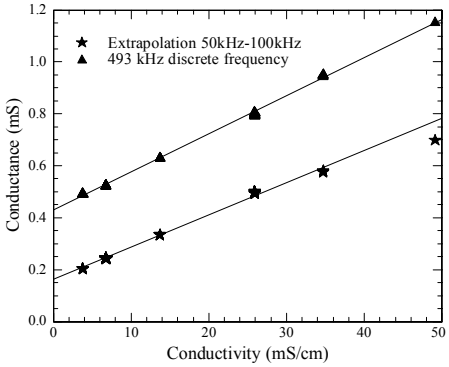

Figure 11: Measured cell conductance as a function of conductivity measured with a Radiometer CDC749 probe. Good linearity is found at a single frequency measurement (▲) as well as by extrapolating to infinite frequency (★).

5. CONCLUSIONS

The temperature sensor shows a linear response with a high signal to noise ratio. As expected, the p-n junction short circuit current is also linear with the light intensity. The conductivity sensor shows a linear response for both single frequencies and for extrapolation compensation. In conclusion, the multi-sensor chip offers precise determination of salinity, temperature, pressure and light intensity, and is a major step towards a new generation of miniturized DSTs.

Acknowledgements

This work is supported by *The Danish Institute for Fisheries Research*.

6. REFERENCES

[1] E. L. Lewis, "The Practical Salinity Scale 1978 and its antecedents", *IEEE Journal of Oceanic Engineering*, OE4:3-8, 1980

[2] C. Pedersen, S. T. Jespersen, K. W. Jacobsen, J. P. Krog, C. Christensen, and E. V. Thomsen, "Highly Reliable O-ring Packaging Concept for MEMS Pressure Sensors", *Sensors and Actuators A* 115 (2004) 617-627

[3] M. I. Montenegro et al, "Microelectrodes: Theory and applications", Kluwer Academic Publishers

[4] E. Hunter et al, "Geolocation of free-ranging fish on the European continental shelf as determined from environmental variables", *Marine Biology*, 142-3 (2003), pp 601-609

E.2 IEEE Sensors 2005 - Irvine, California, USA

FISH & CHIPS: Four Electrode Conductivity / Salinity Sensor on a Silicon Multi-sensor Chip for Fisheries Research

A. Hyldgård, Í. Ólafsdóttir, M. Olesen, T. Hedegaard, O. Hansen & E. V. Thomsen
Department of Micro and Nanotechnology (MIC)
Technical University of Denmark (DTU)
Kgs. Lyngby, Denmark
ahy@mic.dtu.dk

***Abstract*— The design and fabrication of a single chip silicon salinity, temperature, pressure and light multi-sensor is presented. The behavior 2- and 4-electrode conductivity micro-sensors is described, and methods for precise determination of water conductivity is given.**

I. INTRODUCTION

In recent time a significant focus has been set on fish behavior and fish population estimations due to the expected endangerment of certain species of fish mainly as a result of excessive fishing activity. Reliable monitoring of individual fish behavior and migration in their natural environment is crucial in order to make accurate population estimations and plans for preservation of the different species.

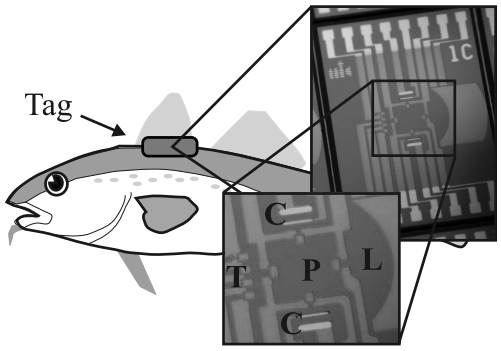

Figure 1. The sensor is placed on the back of a fish and is exposed directly to the seawater. On-board electronics stores the measured data. The sensor measures Temperature (T), Pressure (P), Light Intensity (L) and electrical conductivity (C).

A Data Storage Tag is an autonomous measurement system that, when sutured onto the back of a fish, can collect information about the fish surroundings. When the fish are re-caught the data can be retrieved. The salinity can be calculated from the conductivity, temperature and pressure triplet from well-established polynomial fits to empirical data [1]. Comparison with data of local variations can be used to estimate the local movement of the fish. The variation of light intensity during the day can be used to deduct the longitude and latitude. This information can be used to reconstruct fish migration and fish patterns of behavior [2]. Today, research on fish behavior is strongly limited by the considerable size of conventional discrete sensors. The aim is thus to make a microscale multi-sensor package that, when combined with suitable electronics and a compact packaging, will allow for a significantly smaller tag.

II. DESIGN

A multi-sensor (see Fig. 1) consisting of a piezoresistive Wheatstone bridge pressure sensor, a doped silicon thermistor, a pn-junction photodiode and a 4-electrode array, is arranged on the central 1.5x1.5mm^2 part of a 4x6mm^2 silicon chip. The contacts are placed on the ends of the chip and the sensors are contacted via a buried silicide layer in order to allow for direct exposure of the sensors to the water, while keeping the contacts dry. An O-ring packaging system is used to seal out the water [3].

III. FABRICATION

Fig. 2 shows a cross-sectional fabrication sequence for the multi-sensor chip. Different p-type resistors optimized for piezo resistivity, thermal sensitivity and high conductivity, are ion-implanted through a 100nm silicon dioxide layer into the single crystal n-type silicon (100) substrate. The resistive sensors have a resistance of approx.

This work is supported by *The Danish Institute for Fisheries Research http://www.dfu.min.dk*

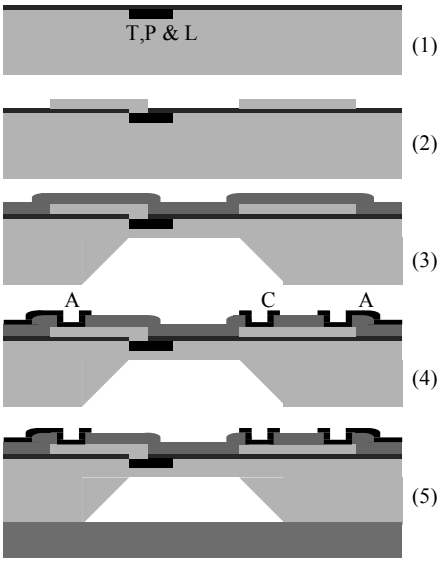

Figure 2. Chip fabrication sequence. (1) Sensors (T,P & L) are ion implanted. (2) $TiSi_2$ wiring is formed. (3) Si_3N_4 coating is deposited and a membrane is etched out. (4) Two metallizations form electrodes (C) and contact areas (A). (5) A Pyrex wafer is anodic bonded to the backside.

30kΩ to yield low power consumption while keeping a high signal to noise ratio.

The implanted resistors are contacted via a $TiSi_2$ wiring system made by RTP annealing of titanium and polysilicon at 800°C for 30s. The low sheet resistance of the 250nm $TiSi_2$ wiring ensures low parasitic series resistances between sensors and contacts even in long conductor paths ($R_{\square}$=1Ω).

Both sides of the wafer are coated with a 120nm LPCVD silicon nitride. The nitride is used as masking material in the subsequent KOH bulk silicon etch that forms the pressure sensor membrane. The backside nitride is then removed whereas the front-side nitride is kept as the protective coating of the sensors. Contact holes are made through the nitride by reactive ion etching in a SF_6/O_2 plasma.

The chips are metallized by platinum and gold to form electrodes and contact pads as the demands for corrosion inertness and wire bonding compatibility are not met by a single metal. The backside of the chip is anodic bonded to a Pyrex wafer to form a low-pressure reference cavity and add mechanical stability to the chip.

The complete process is only slightly more complex than processes used in commercial pressure sensor fabrication, and is well suited for batch processing.

IV. Results

Although the salinity is expressed by the conductivity, temperature and pressure triplet, it varies most with the conductivity [4]. A precise determination of conductivity is thus essential. Therefore the main focus is on the conductivity results.

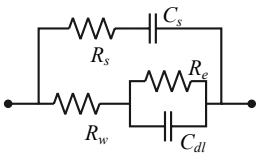

Figure 3. Conductance cell equivalent circuit. The electrolysis impedance R_e is much higher than the water impedance R_w. The double layer capacitance C_{dl} is higher than the parasitic capacitance C_s.

A. Conductivity

The electrical conductivity of the seawater is determined by measuring the impedance between 2 or 4 electrodes. Ideally the conductivity κ is related to the impedance Z through the relation $\kappa = K/Z$, where K is the geometrically determined cell constant. In reality, the relation is complicated by the presence of an electrochemical double layer capacitance (DLC) at the electrode-water interface and a parasitic conductance in the substrate. An equivalent model for the 2-electrode system is shown in Fig. 3 and the corresponding impedance can be expressed as

$$Z = \frac{1}{\dfrac{1}{R_w + \dfrac{1}{1/R_e + j\omega^{\alpha_1} C_{dl}}} + \dfrac{1}{R_s + \dfrac{1}{j\omega^{\alpha_2} C_s}}}.$$

For low frequencies the current is due to charge transfer by electrolysis. This gives an effectively high resistance R_e compared to the water resistance R_w. For medium frequencies the double layer capacitance C_{dl} starts conducting and changes in water conductivity due to changes in salinity can be observed.

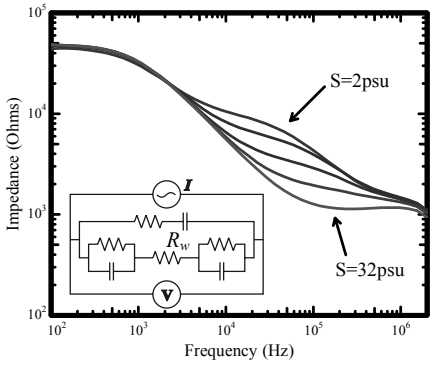

Figure 4. Impedance as a function of frequency for a 2-electrode cell at 5 different salinities (2, 4, 8, 16 and 32 psu). The double layer capacitance can be eliminated by extrapolation of the impedance to infinite frequency. Thus, the water resistance, R_w, can be determined.

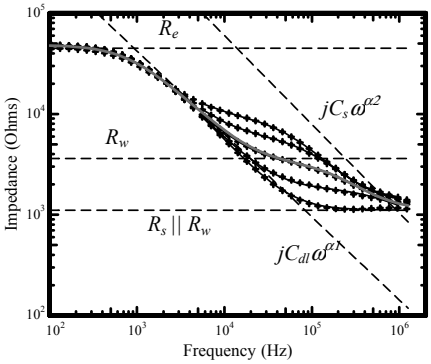

Figure 5. Model fit to the measured data. Dashed lines indicate the contributions to the complete fit indicated by the thick solid line.

Table 1. Parameters from model fit to measured data

Sal.	R_w (Ω)	R_e (Ω)	R_p (Ω)	C_{dl} (nF)	α_1	C_p (nF)	α_2
2	10517	50k	1.5k	289	0.68	5.2	0.91
4	6726	51k	1.7k	142	0.76	4.8	0.90
8	3618	49k	2.0k	80	0.82	4.5	0.89
16	1906	49k	3.1k	57	0.86	4.9	0.83
32	1116	49k	-	41	0.91	-	-

For high frequencies, the impedance is dominated by the parasitic conductance expressed by the substrate capacitance C_s and the substrate resistance R_s. Fig. 4 shows the impedance as a function of frequency measured with 2 electrodes at 5 different salinities. The model is fitted to the measured data as shown in Fig. 5 and the extracted parameters are presented in Table 1. The impedance behaves as expected and the slopes of the capacitances are numerically smaller than 1, which would be expected for normal capacitances.

For the DLC this is predicted in electrochemistry where the impedance is known to be proportional to $\omega^{-\alpha}$ where $\alpha < 1$. Both C_{dl} and α_1 changes with salinity which is in good agreement with the behavior of permanent and diffusive double layers. Fig. 6 shows the capacitances and the related power coefficients. For high salinities C_{dl} converges as the diffusive double layer becomes negligible. The slope of the parasitic transient can be explained by expanding the simple parasitic substrate capacitance with a distributed capacitance network as shown in Fig. 7. A simple distributed network has a typical frequency relation of $\omega^{-1/2}$. For that reason the more complex system at hand is modeled by $\omega^{-\alpha}$.

The extracted water conductance as a function of salinity is shown in Fig. 8. The almost linear relation is in good agreement with theory.

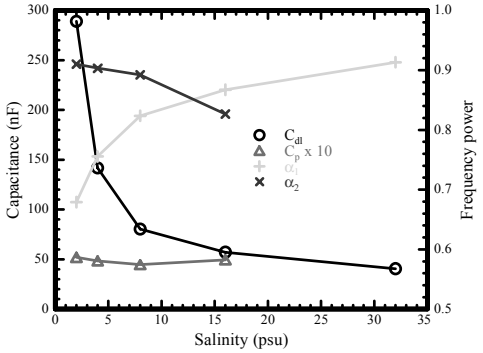

Figure 6. Model capacitances and the related power coefficients. For high salinities C_{dl} converges as the diffusive double layer becomes negligible.

In real applications, a simpler and more direct determination of the water conductivity is desirable. Determining the water conductivity directly from the impedance will introduce an error caused by the DLC. This can be eliminated by extrapolation to infinite frequency as described in [4]. Alternatively a 4-electrode configuration can be used. The transimpedance as a function of frequency for a 4-electrode cell is shown in Fig. 9. The DLC is not as evident at the measurement electrodes. However, a medium frequency AC current still has to run in the current electrodes in order to ensure a significant potential drop across the water.

For the simple 2-electrode and 4-electrode configuration there is a linear relation between the salinity and the water resistance extrapolated at a single frequency.

Fig. 10 shows the cell constant K and the standard deviation of the impedance/salinity linear fit as a function of frequency for the 2-electrode (extrapolated) and the 4-electrode configuration respectively.

Clearly the cell constant is higher for the 2-electrodes than for 4-electrodes. However, a higher impedance offset for the 2-electrode makes the difference in relative sensitivity less evident, as shown in Fig. 11. The peak in cell constant is also much wider and the 4-electrode configuration must be considered as being less sensitive to variations in frequency and DLC.

In order to optimize the conductivity cell the ratio between the upper and lower frequencies limiting the salinity window must be as high as possible, widening the frequency band in which impedance is strongly dependent of salinity.

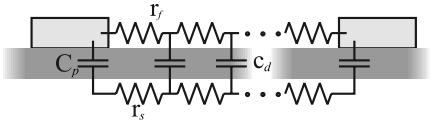

Figure 7. Distributed capacitance network. The dielectric film will serve as a capacitor stretching between the two electrodes. The impedance typically varies with $\omega^{-1/2}$. rf and cd represents the distributed parameters.

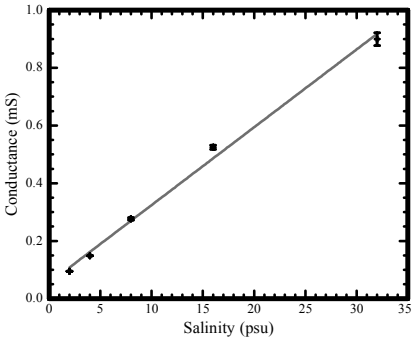

Figure 8. The inverse of the fitted water resistance as a function of salinity. The almost linear relation is in good agreement with theory.

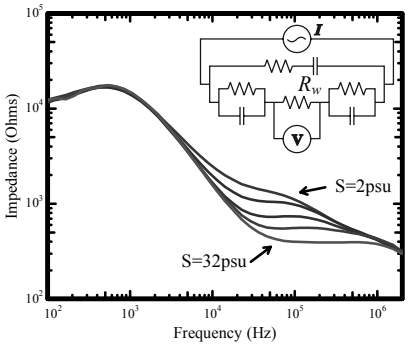

Figure 9. Transimpedance as a function of frequency for a 4-electrode cell at 5 different salinities (2, 4, 8, 16 and 32 psu). For medium to high frequencies the impedance is independent of the double layer when neglecting the parasitic impedance in the substrate.

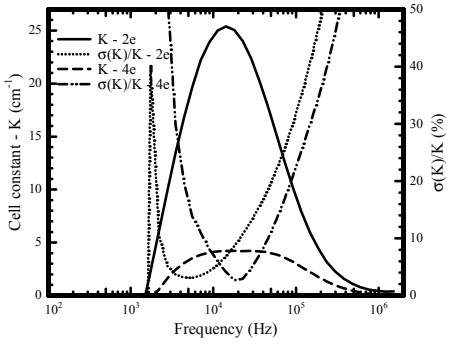

Figure 10. The 2-electrode and 4-electrode cell-constants as a function of frequency. σ represents the relative standard deviation of the cell constant as obtained from the linear regression. The 2-electrode has a high cell constant whereas the 4-electrode has a flat profile with K and σ peeks at the same frequency.

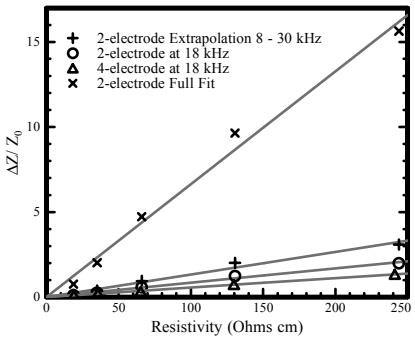

Figure 11. Relative change in cell impedance vs. saltwater resistivity. For simple extractions, the sensitivity (slope of fit) is higher for 2-electrode than for 4-electrode. 4-electrode signals are more stable for changes in electrode double layer capacitance. The optimum determination of water conductance comes from a complete fit.

Merely increasing the electrode area will not lower the low-end frequency as this will both increase the DLC and decrease K. Analytical approximations and FEM analysis indicates that thin long electrodes are the best solution for microsystems with limited electrode spacing. The high-end frequency scales with the inverse substrate capacitance. The capacitance can be lowered by limiting the area of the conducting paths, by increasing the dielectric thickness, and/or by increasing the substrate resistance.

B. Temperature and Light

The temperature sensor shows a high degree of linearity between thermistor resistance and reference temperature measured with a commercial PT100 element. There is no measurable time delay between the two temperature readings when submerged in liquid. The light sensor quantum efficiency (QE) is measured against a calibrated photodiode. The light sensor has a QE of 40-70% in the visible domain.

V. SUMMARY

The water conductivity and thereby the water salinity can be determined in different ways. A precise determination calls for a frequency scan whereas different methods allow for determination from few single frequencies. A wider frequency band can be obtained by changing the substrate capacitance.

REFERENCES

[1] E. L. Lewis, "The Practical Salinity Scale 1978 and its antecedents", IEEE Journal of Oceanic Engineering, 1980S.

[2] Neuenfeldt , H. Hinrichsen and A. Nielsen, "A method to geolocate eastern Baltic cod by using Data Storage Tags (DSTs)", ICES CM 2004/L:06

[3] C. Pedersen, S. T. Jespersen, K. W. Jacobsen, J. P. Krog, C. Christensen, and E. V. Thomsen, "Highly Reliable O-ring Packaging Concept for MEMS Pressure Sensors", Sensors and Actuators A 115 (2004) 617-627

[4] A. Hyldgård, O. Hansen, E.V. Thomsen, "Fish & Chips: Single Chip Silicon MEMS CTDL Salinity, Temperature, Pressure and Light Sensor for Use in Fisheries Research. IEEE MEMS 2005 proceedings, p. 303

E.3 Eurosensors 2006 - Göteborg, Sweden

DIRECT EXPOSURE OF MEMS MULTI-SENSOR SYSTEMS USING A POTTED-TUBE PACKAGING CONCEPT

Anders Hyldgård[1*], Karen Birkelund[1], Jakob Janting[2] & Erik V. Thomsen[1]
[1] MIC - Technical University of Denmark, Building 345East, DK-2800, Denmark
[2] DELTA - Venlighedsvej 4, DK-2970 Hørsholm, Denmark
*Corresponding author: Anders Hyldgård, Tel: +45 4525 5761, Fax: +45 4588 7762, E-mail: ahy@mic.dtu.dk

Abstract: A potted-tube packaging concept that allows for direct sensor exposure is presented. This results in high sensitivity and fast response time of the sensors. The design of an elongated multi-sensor is described and salinity measurement results from the packaged multi-sensor chip are given.

Keywords: packaging, multi-sensor, exposure

INTRODUCTION

Reliable monitoring of individual fish behavior and migration in their natural environment is crucial in order to make accurate population estimations and plans for preservation of the different species. A Data Storage Tag (DST) is an autonomous system that when sutured onto the back of a fish can measure parameters in the surroundings of the fish and store the data until the fish is re-caught [1].

The data storage tag consists of a microcontroller, which activates sensors and stores measured data in a non-volatile memory. Batteries power the system. When the fish is re-caught, the system can be powered through a wireless interface while data is read out.

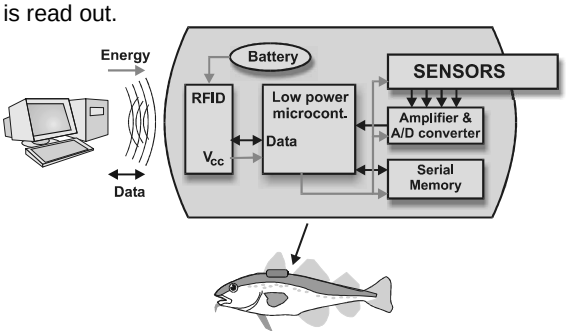

Figure 1. Data Storage Tag (DST) system overview. A microcontroller manages the power to and data from the sensors and stores the data in the memory. Batteries power the system. When retrieved the system can be powered via the wireless interface while data is read out.

In our case the sensor can measure temperature, pressure, light intensity and electrical conductivity.
A very compact and reliable system capable of measuring the parameters very accurately with a high sensitivity and short response time is needed. This calls for a packaging scheme that allows for direct exposure of a silicon sensor to the surrounding environment. Isolating the sensing area from the packaging material also imply that the sensors are stress de-coupled from the packaging. This in turn allows for pre-packaging calibration.
We use microtechnology and a potting packaging to make such a system. DST manufacturer CEFAS Technology Ltd.[2], uses a potting packaging system in their G5 tag. However, this system does not expose the sensors directly but relies on internal sensors coupled to the surrounding environment through the packaging. The G5 tag shows that potting using a two-component fill can be used in yearlong exposure to seawater.

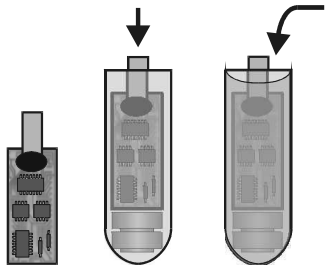

Figure 2. Packaging scheme. The sensor chip is mounted on the PCB and the wire-bonds are glob-topped. The PCB and batteries are connected and put in a tube. The tube is filled with glue (potted) covering the system while leaving one end of the sensor chip exposed.

Our system has to be partly sealed off from the surrounding water. Potting with epoxy in a tube (Figure 2, 3 and 7) has been chosen because the complete filling leave no room for water to condense as opposed to an "o"-ring packaging concept that relies on ventilation of the dry side of the packaging to remove water vapor [3]. The silicon-epoxy interface is also very strong which is not always the case for injection-molded thermoplasts, which tends to shrink slightly when cooled.

SENSOR-CHIP DESIGN

The high demands on the packaging scheme with regards to longtime stability and direct exposure calls for a system design approach. Special care has to be taken in the chip design to ensure that the design facilitates a direct exposure in the pre-decided packaging scheme. This includes protecting all sensor parts while making good electrical contact to the interface electronics and to distance sensors from bond pads.

The silicon multi-sensor is fabricated using conventional bulk micromachining [4,5] including ion-implantation to functionalize the silicon. Grown SiO_2 and deposited Si_3N_4 layers serve as insulating layer and protective coating respectively.

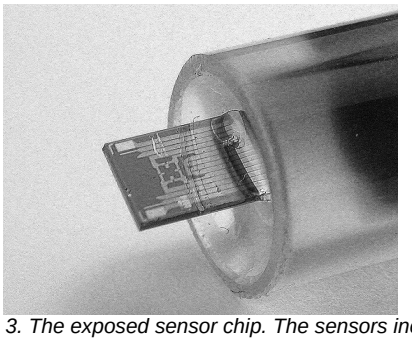

Figure 3. The exposed sensor chip. The sensors include a piezoresistive pressure sensor, a thermistor temperature sensor, a pn-junction light sensor and a four-electrode conductivity sensor. The sensors are contacted via $TiSi_2$ wires and are protected by a Si_3N_4 film.

Interconnects, electrodes and contacts are made of $TiSi_2$, Ti/Pt and Ti/Au respectively. The membrane of the pressure sensor is released using an anisotropic KOH etch and a reference cavity is formed by bonding Pyrex glass to the backside of the wafer.

The sensor chip is designed so that sensors are placed in one end of the chip and contacts are placed in the other. Contacts and sensors are connected using highly conductive $TiSi_2$ wire-paths ($R_{\square}$=1Ω) that are buried under a protective Si_3N_4 film. The diffusion constant of water through a PECVD Si_3N_4 film is 10^{-18} cm^2 s^{-1} according to [6]. This means that it will take more than 3years in order to reach 90% saturation under the film, and even longer for stoichiometric LPCVD nitride. The fabricated chip is shown in Figure 3, where it is sticking out of the potted tube.

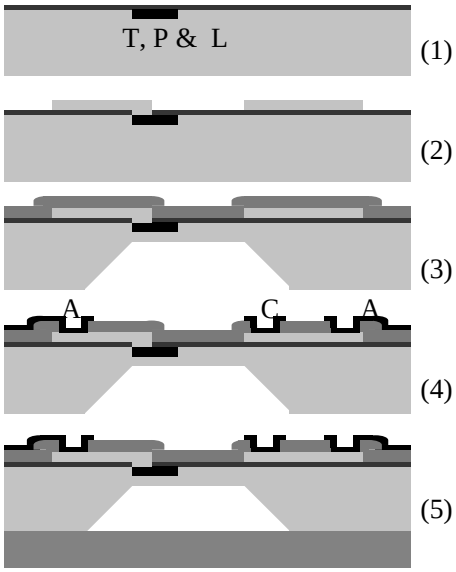

Figure 4. Chip fabrication sequence. (1) The Temperaure (T), Pressure (P) and Light (L) sensors are ion implanted. (2) $TiSi_2$ wiring is formed. (3) Si_3N_4 coating is deposited and a membrane is created by etching. (4) Two metallizations form electrodes (C) and contact areas (A). (5) A Pyrex wafer is anodic bonded to the backside.

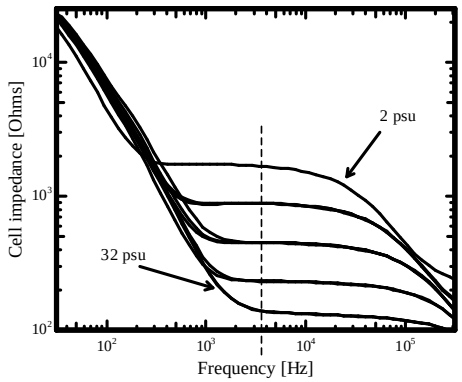

Figure 5. Conductivity cell trans-impedance as a function of frequency for 5 different salinities (2, 4, 8, 16 & 32 PSU). At medium frequencies there is a salinity sensitive window. At low frequencies the Debye layer is not short-circuited. At high frequencies the cell conducts through the substrate loosing sensitivity. The trans-impedance at 3.4kHz (slashed line) is used to construct Figure 6.

This allows for the sensor end of the chip to be completely exposed to the surrounding environment while the other end is wire-bonded to the electronics and completely sealed in.

The multi-sensor is capable of measuring temperature, pressure, light intensity and electrical conductivity. A thorough description is published in earlier works [4,5]. Figure 5 shows the conductivity sensor cell trans-impedance as a function of frequency for 5 different salinities. A clear salinity sensitive interval exists for medium frequencies. Plotting the trans-impedance at a single frequency as a function of the resistivity corresponding to the respective salinities shows a linear relation (Figure 6). The repeatability is excellent and the accuracy is better than 1% allowing for the determination of salinity with accuracy better than 0.5 PSU.

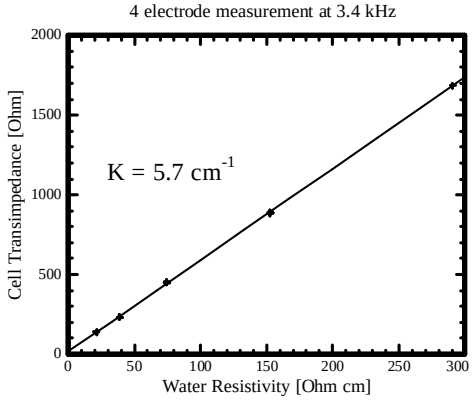

Figure 6. Conductivity cell trans-impdance as a function of water resistivity measured with a commercial reference sensor. The cell shows a linear response with a cell constant of 5.7cm^{-1} and a mean deviation of <1% which allows for determination of the salinitiy with an accuracy of +/- 0.5 PSU.

EVALUATION OF POTTING MATERIAL

The most important requirements for the potting material that has to be considered are

- Chemical stability
- Adhesion
- Water solubility & diffusion
- Viscosity
- Glass transition temperature (T_g)
- Electrical insulation
- Curing temperature

Additionally we seek a zero buoyancy mass of the system as well as neutral colors making the fish no more visible than usual.

We consider three transparent expoies, all with a specific weight at approx 1.1g/cm^2, good electrical insulation properties and a T_g well above the working temperature range.

The potting process is very simple and if the epoxy curing process is kept below 70℃, then batteries, electronics and sensors will survive the potting process. Many epoxies are typically cured at temperatures above 80℃ for 1-3 hours, but when curing larger amounts as we do in our case, the exothermic process plays an important role. To ensure that the temperature does not rise above 70℃ while curing a PT100 element has been encapsulated in test tubes, and the temperature has been monitored while curing. In the case of curing EpoTek 302-3M the temperature rise is insignificant as long as the epoxy is cured at a temperature below 40℃. If the curing temperature is rised to 45℃ the temperature inside the tube increases to about 56℃ within 15 min. An alternative to the heat curing epoxies is uv-curing glues. The Dymax 1180 and Dymax 3069 uv-glues show high exothermicity even at low power illumination (pot center temperature > 80℃). Uv-glues also have to be cured from the bottom and up in order to avoid trapped bubbles in the tube, which further complicates the potting process.

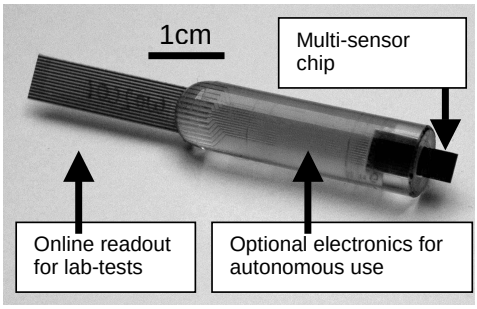

Figure 7. A packaged multi-sensor. The packaging is made in two versions. One (shown here), where the connector print is exposed on the rear end to allow for online monitoring. And one, where electronics and batteries are potted inside to allow for autonomous measurements in the field.

Obviously the main purpose of the packaging is to protect the contents of the tag from the surrounding water. A good packaging material is chemically inert and prevents water from being present at critical sites inside the package. In the following it will become clear that water will diffuse to the center of the package within a limited period of time, and the presence of water will then be limited only by the water saturation level. The amount of water repelled to the surface when a saturated polymer is cooled will also depend on the saturation level.

The water uptake of most epoxies is listed as being very low (<1%) [7]. The real uptake is however significantly higher and has to be measured. Rough estimates, of how much water can be accepted within the packaging, can be made from assumptions of corrosion mechanisms and water flux consideration [8]. However, the final evaluation should be made empirically and measures of water uptake and diffusion should work as comparison only. The water uptake in the most resistant epoxies is expected to have no significant impact on the performance of the packaging and the embedded system. Completely filling also result in a mechanically robust packaging.

The total water uptake as well as the diffusion coefficient is found by measuring the gain in weight of 50x50x1mm^3 sheets of epoxy after submersion in salt water at room temperature, see Figure 8. The choice of epoxy obviously has a huge influence on the amount of water that the packaging can contain, for these epoxies a variation from 3% up to 15%. The sample with the highest water uptake got brittle and broke in handling. The amount of water that will condense in possible small cavities within the packaging will be dependent of the water concentration at the cavity interface. The water diffusion into the sheets can be considered as a one-dimensional diffusion from two sides. The exact one-dimensional solution can be expressed as

$$m(t) = m_\infty \left(1 - \frac{8}{\pi^2} \sum_{n=0}^{\infty} \frac{1}{(2n+1)^2} \exp\left[\frac{-D(2n+1)^2 \pi^2 t}{l^2} \right] \right)$$

where $m(t)$ and m_∞ is the moisture content at the time t and at saturation respectively, D is the diffusion constant and l is the thickness of the sheet [8,9,10].

For short times the solution is simple, the concentration profile is a Gaussian and the water uptake proportional to the square root of time.
For long times the two Gaussians meet and the water uptake will be approaching total saturation as an exponential decay.

The short time results and the calculated diffusion constants are shown in Figure 9. The low water-

uptake and diffusion constant of EpoTek 302-3M makes it the epoxy of choice. However, 302-3M has the highest viscosity of the three (0.8-1.6 Pa·s compared to 0.1-0.3 Pa·s), which again makes the chance of bubble formation higher.

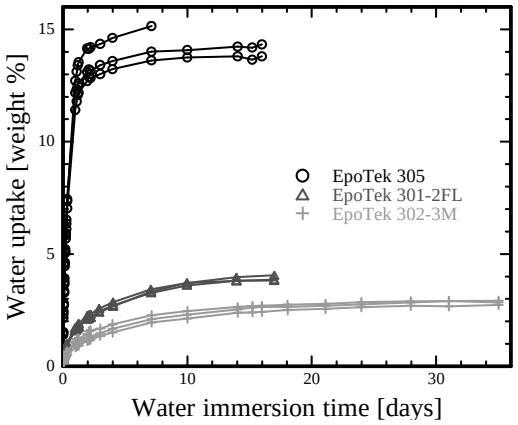

Figure 8. Relative water uptake (by weight) in three epoxies as a function of time of sample immersion. For true Fickian difussion the uptake should saturate when a uniform saturation level is reached through the whole sheet. Non-Fickian diffusion, such as polymer redistribution or reaction with incoming water may make the water uptake continue. The lowest uptake is found in EpoTek 302-3M that saturates at approx 2.9%

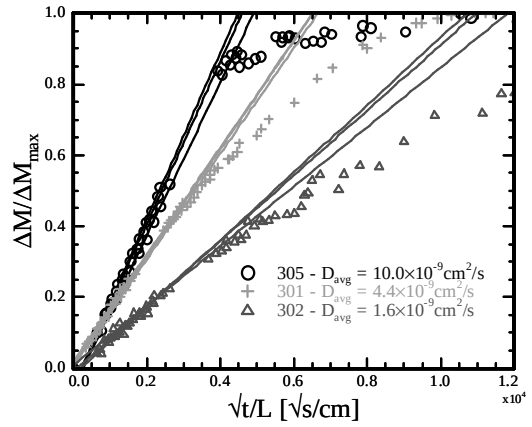

Figure 9. Relative water saturation (by weight) in three epoxies as a function of the square root of time of sample immersion normalized with the sample thickness. For short times, the diffusion coefficient is proportional to the slope of the graph. The diffusion is 6 times faster in the EpoTek 305 than in the EpoTek 302-3M. Diffusion constants fit very well with literature values [8].

OUTLOOK

In addition to the above investigations, stress has to be considered as a significant failing process. Stress from the curing process or stress induced by polymer swelling can result in excessive force on wire-bonds or allow water to penetrate along the surface of the chip. This in turn can result in loss of electrical contact as wire-bonds are torn off or etched away.

Choosing an epoxy with low water-uptake can minimize problems with polymer swelling. Clever design of the exact shape of the packaging may also limit the stress coupled to the interfaces. Preliminary tests are made to measure the packaging induced three-dimensional stress by using a piezo-coefficient mapping device [11]. This will in time allow for optimization of the potting process for low curing stress. We have measured the in-plane stress as approx. 30 MPa and the normal-stress as approx. 190 MPa.

Test of failure due to water penetrating along the interface of the chip will be investigated using a test-chip with a sacrificial aluminum wire network on the surface. These wires will etch away in approx. 40 min in a bulk $32^{oo}/_{o}$ KCl solution, which can easily be detected electrically. The chips will be potted and exposed to a 20 bar pressure for long periods of time while monitoring the resistance of the wire network.

A sensor-interface ASIC is currently undergoing electronic testing and autonomous measurements will also be part of near future work.

CONCLUSION

A packaging concept for data storage tags is demonstrated. The effectiveness of the packaging is demonstrated with the precise measurement of water conductivity. The packaging concept is very promising for high accuracy measurements in harsh environments.

REFERENCES

1. J.D. Metcalfe and G.P. Arnold; *Nature*, (1997) 387:665-6
2. http://www.cefastechnology.co.uk
3. C. Pedersen, S.T. Jespersen, K.W. Jacobsen, J.P. Krog, C. Christensen and E.V. Thomsen; *Sensors and Actuators A*, 115 (2004), pp 617-627.
4. A. Hyldgård, O. Hansen and E. V. Thomsen, IEEE MEMS 2005 proceedings, (2005), 303-306
5. A. Hyldgård, Í. Olfafsdóttir, M. Olesen, T. Hedegaard, O. Hansen & E.V. Thomsen; *IEEE Sensors 2005 Proceedings*, (2005), pp 1124-1127
6. R.K.Ulrich, A.J.Phillips, D.H.Yi, W.D.Brown and S.S.Ang, *Microelectronics and reliability*, (1991), Vol 31, 1237-1249
7. http://www.epotek.com/
8. R.D. Adams, J. Comyn, W.C. Wake, *Chapman & Hall*, (1997)
9. M.R.Vanlandingham, R.F. Eduljee, J.W. Gillespie, Jr, *Journal of Applied Polymer Science*, Vol 71, 787-798 (1999)
10. J. Janting; *Encyclopedia of Sensors*, in press (2006)
11. J. Bartholomeyczik, M. Doelle, P. Ruther, O. Paul, *Sensors & Actuators: A. Physical*, (2006) Vol 127, 255-260

E.4 IEEE MEMS 2007 - Kobe, Japan

DETERMINATION OF PACKAGING INDUCED 3D STRESS UTILIZING A PIEZOCOEFFICIENT MAPPING DEVICE

J. Richter, A. Hyldgård, K. Birkelund, M.B. Arnoldus, O. Hansen, and E.V. Thomsen
Technical University of Denmark
Department of Micro and Nanotechnology
Building 345east, DK-2800 Kgs. Lyngby
Telephone: +45 4525 5700. E-mail: jar@mic.dtu.dk

ABSTRACT

This paper presents a novel method to determine 3D stress in microsystem packaging. The stress components σ_{xx}, σ_{yy}, σ_{zz}, and σ_{xy} are found in an epoxy package using a piezocoefficient mapping device as stress sensor. We spin the current 360° in a circular *n*-type (001) Si piezoresistor by contacts located near the perimeter of the resistor and do high impedance voltage measurements on contacts located near the centre of the resistor. By measuring the potential drops in these contacts we can determine the stress in the chip. The epoxy is potted in a polystyrene tube using the same concept as in [1] used for chip packaging for fisheries research. We investigate the EpoTek 305 epoxy and find stress values of $\sigma_{xx} \approx$ -23 MPa, $\sigma_{yy} \approx$ -1 MPa, $\sigma_{xy} \approx$ 0.3 MPa, and $\sigma_{zz} \approx$ 40 MPa. The presented method can be used for 3D stress measurements of various packaging concepts.

INTRODUCTION

The last step to commercialisation of a MEMS device is often related to packaging. Packaging protects the device from the surroundings. A difficult task is to protect the device and not affect the performance of the device at the same time. The performance of an electrical component can be highly influenced by packaging induced stress. Stress sensors are used to measure the stress and thus explain the performance of the device. In ref. [2] a CMOS integrated stress sensor for packaged integrated circuit dies is presented, and ref. [3] shows a van der Pauw structure used for stress sensing.

In this paper we present a method to measure four components of the stress, σ_{xx}, σ_{yy}, σ_{zz}, and σ_{xy}. This method makes complex stress analysis possible in microscale packaging. The packaging concept analysed is used to protect chip and electronics in a multisensor system developed for fisheries research [4].

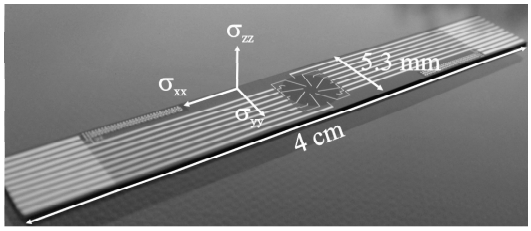

Figure 1 Presentation of stress sensor. The chip is cut along the direction directed 22.5° with respect to the [100] direction. In the centre region of the chip a single circular *n*-type resistor is implemented. A current is forced through the resistor by contacts near the perimeter and 8 contacts placed in a radius of 100 µm with respect to the resistor centre measure 4 potential drops.

THEORY

Inspired by the work of Bartholomeyczik [5] and Steiner [6] we have designed a (001) *n*-type Si circular piezoresistor. The piezoresistor is placed in the centre region of a long thin chip. The chip is dimensioned to fit in a four point bending (4PB) fixture [7]. Figure 1 shows a photograph of the chip. The chip is cut along the direction of 22.5° with respect to the [100] direction. A conceptual drawing of the device is shown in Figure 2. We direct the current, $I(\phi)$, at an angle ϕ by using four outer contacts placed near the resistor perimeter. Thus, in the centre of the circular piezoresistor we spin the current 360°.

In the centre of the resistor at a radius of 100 µm eight contacts are placed. The potential drops, $V_i = V_{ia} - V_{ib}$, are measured across the inner contacts where i=1,2,3,4, see Figure 2. Thus, for each current direction four potential drops are measured. To a first order approximation the relative change, $\Delta V_i/V_{i,0}$, where $V_{i,0}$ is the potential drop V_i at zero stress, is equal to a linear combination of the stress components. Defining two fictive voltage drops, V_p and V_t in Figure 2, as linear combinations of the four potential drops we obtain a condensed linear system where the number of current directions determines the number of equations

$$\begin{aligned} V_p = \; & \tfrac{1}{2}(\cos(\phi)\cdot V_1 + \cos(\phi-\tfrac{\pi}{4})\cdot V_2 \\ & + \sin(\phi)\cdot V_3 + \sin(\phi-\tfrac{\pi}{4})\cdot V_4) \\ V_t = \; & \tfrac{1}{2}(\sin(\phi)\cdot V_1 + \sin(\phi-\tfrac{\pi}{4})\cdot V_2 \\ & - \cos(\phi)\cdot V_3 - \cos(\phi-\tfrac{\pi}{4})\cdot V_4) \end{aligned} \qquad (1)$$

Table 1 Relations of selected relative potential drops. For $\Delta V_2/V_{2,0}$ and $\Delta V_4/V_{4,0}$ similar equations are valid.

$\frac{\Delta V_1}{V_{1,0}} =$	$\frac{\sigma_{xx}}{4}(3\pi_{11}+\pi_{12}+\pi_{44}+(-\pi_{11}+\pi_{12}+\pi_{44})\tan(\phi))$ $+\frac{\sigma_{yy}}{4}(\pi_{11}+3\pi_{12}-\pi_{44}+(\pi_{11}-\pi_{12}-\pi_{44})\tan(\phi))$ $+\frac{\sigma_{xy}}{2}(\pi_{11}+\pi_{12}+\pi_{44}+(\pi_{11}-\pi_{12}+\pi_{44})\tan(\phi))$ $+\sigma_{zz}\pi_{12}$
$\frac{\Delta V_3}{V_{3,0}} =$	$\frac{\sigma_{xx}}{4}(\pi_{11}+3\pi_{12}-\pi_{44}-(\pi_{11}-\pi_{12}-\pi_{44})\cot(\phi))$ $+\frac{\sigma_{yy}}{4}(3\pi_{11}+\pi_{12}+\pi_{44}+(\pi_{11}-\pi_{12}-\pi_{44})\cot(\phi))$ $+\frac{\sigma_{xy}}{2}(\pi_{11}-\pi_{12}-\pi_{44}+(\pi_{11}-\pi_{12}+\pi_{44})\cot(\phi))$ $+\sigma_{zz}\pi_{12}$
$\frac{V_t}{V_{t,0}} =$	$\frac{\sigma_{xx}}{4}(\pi_{11}(\sin(2\phi)+\cos(2\phi))-\pi_{12}(\sin(2\phi)+\cos(2\phi))+\pi_{44}(\sin(2\phi)-\cos(2\phi)))$ $+\frac{\sigma_{yy}}{4}(\pi_{11}(-\cos(2\phi)-\sin(2\phi))+\pi_{12}(\cos(2\phi)+\sin(2\phi))+\pi_{44}(\cos(2\phi)-\sin(2\phi)))$ $+\frac{\sigma_{xy}}{2}(\pi_{11}(-\cos(2\phi)-\sin(2\phi))+\pi_{12}(\cos(2\phi)+\sin(2\phi))+\pi_{44}(-\cos(2\phi)+\sin(2\phi)))$
$\frac{\Delta V_p}{V_{p,0}} =$	$\frac{\sigma_{xx}}{4}(\pi_{11}(2+\cos(2\phi)-\sin(2\phi))+\pi_{12}(2-\cos(2\phi)+\sin(2\phi))+\pi_{44}(\cos(2\phi)+\sin(2\phi)))$ $+\frac{\sigma_{yy}}{4}(\pi_{11}(2-\cos(2\phi)+\sin(2\phi))+\pi_{12}(2+\cos(2\phi)-\sin(2\phi))-\pi_{44}(\cos(2\phi)-\sin(2\phi)))$ $+\frac{\sigma_{xy}}{2}(\pi_{11}(\cos(2\phi)+\sin(2\phi))+\pi_{12}(\cos(2\phi)-\sin(2\phi))+\pi_{44}(\cos(2\phi)+\sin(2\phi)))$ $+\sigma_{zz}\pi_{12}$

where ϕ is the angle between the current direction and the chip-axis. Table 1 shows the expected relations of $\Delta V_1/V_{1,0}$, $\Delta V_3/V_{3,0}$, $\Delta V_p/V_{p,0}$, and $\Delta V_t/V_{p,0}$. Similar equations are valid for $\Delta V_2/V_{2,0}$, and $\Delta V_4/V_{4,0}$.

As seen in Table 1 the relative voltage changes depend on the angle ϕ, the stress components σ_{xx}, σ_{yy}, σ_{xy}, and σ_{zz}, and the piezocoefficients π_{11}, π_{12}, and π_{44}. Performing the measurements when the chip is located in the 4PB fixture we can determine the three piezocoefficients. This can be done since the 4PB fixture applies a well-defined uniform and uniaxial stress, $\sigma_{xx} \neq 0$, to the centre region of the chip where the resistor is placed [7].

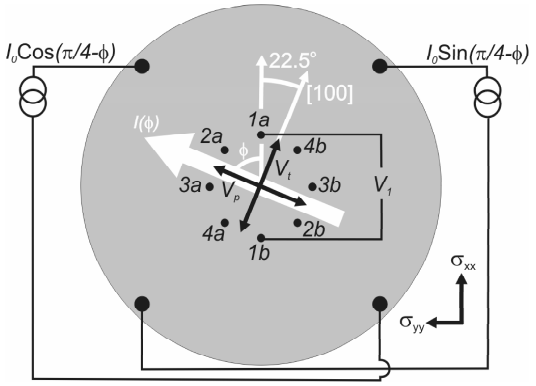

Figure 2 Schematic of the circular piezoresistor. The illustration is not to scale. The resistor diameter is 1700 μm and the inner contacts are placed in a circle with a radius of 100 μm. The four outer contacts spin the current 360° in the centre of the resistor. The fictive voltage drops, V_p and V_t, are linear combinations of all measured potential drops, $V_i = V_{ia} - V_{ib}$ where i=1,2,3,4. The potential drop V_1 is showed as an example.

After this calibration step the chip is packaged and the measurements are performed again. Setting up the linear equation system of V_p and V_t we can determine the four stress components

$$\frac{\Delta V}{V_0} = \sigma_{xx}\cdot a(\phi)+\sigma_{yy}\cdot b(\phi)+\sigma_{xy}\cdot c(\phi)+\sigma_{zz}\cdot d(\phi) \quad (2)$$

where a, b, c, and d are functions of ϕ and contains linear combinations of π_{11}, π_{12}, and π_{44}. The number of equations is determined by the number of spinning angles, ϕ.

EXPERIMENTAL

The stress sensor chip is fabricated in a cleanroom environment using microtechnology. A crosssection of the device is shown in Figure 3. The resistors contain a doping concentration of $N_D=10^{18}$ cm^{-3} implemented by phosphorous ion implantation on a p-type (001) silicon substrate. The resistors are defined using a reactive ion etch and a thermal oxidation activates the donors and ensures isolation between resistor and metal. The metallization occurs in a lift-off process with a multi layer of Ti and Al. The final fabrication step separates the chips using advanced silicon etch. This allows for off-axis dicing.

The electrical measurements are performed with a four point measurement. In Figure 3 it is illustrated how the current is forced through the contacts near the resistor perimeter while performing a high impedance voltage measurement on the contacts localized close to the centre of the resistor. The inner contacts are placed in a radius of 100 μm with respect to the resistor centre ensuring a uniform current distribution in the area of the contacts.

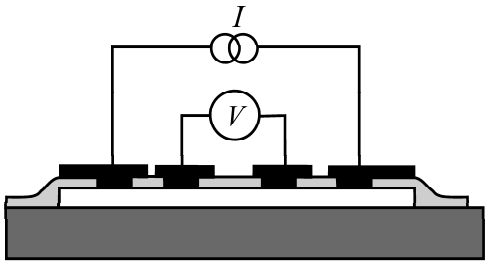

Figure 3 Illustration of stress sensor cross section and measurement principle. The *n*-type resistor (white color) is fabricated by phosphorous implantation on a *p*-type substrate (dark grey). The metal contacts (black) consist of a Ti/Al multi layer and a thermal oxide (light grey) is used for isolation. The current is forced through the resistor from contacts near the resistor perimeter and a high impedance voltage measurement is performed on the contacts near the resistor centre.

Calibration

The original use of the chip is to map the piezocoefficients by spinning the current on a resistor exposed to a defined uniaxial and uniform stress [7]. This is done in a state-of-the-art 4PB fixture shown in Figure 4. Figure 5 shows the relative change in voltage V_1 divided by the applied stress, σ_{xx}, as a function of $\tan(\phi)$. From Table 1 we find that the slope and the offset of the linear fit are related to the three piezocoefficients.

We determine π_{11}, π_{12}, and π_{44} from the overdetermined linear equation system obtained by the relations for the other potential drops in Table 1.

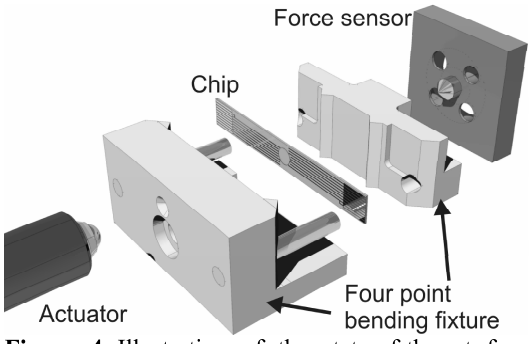

Figure 4 Illustration of the state-of-the-art four point bending fixture used for calibration of the piezocoefficient mapping device. The chip is placed in between the two sets of blades and an actuator is pushing the two parts together. The force on the chip is measured by a highly sensitive force sensor. The fixture applies a uniaxial and uniform stress in the centre region of the chip.

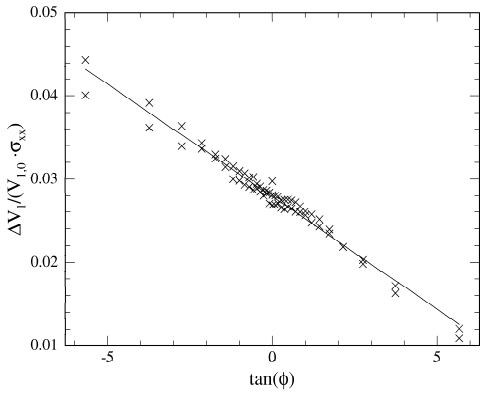

Figure 5 Data of the relative voltage drop measured on V_1, $\Delta V_1 / V_{1,0}$, divided by the applied stress, σ_{xx} . Using the relation in Table 1 and the fitted values of the slope and the offset we can determine the three piezocoefficients by including a second equation, e.g. the relation for $\Delta V_p/V_{p,0}$.

Packaging

After the piezocoefficients have been determined, the chip is potted with EpoTek 305 two-component epoxy in a polystyrene tube. Figure 6 is a photograph of the packaged chip after curing. We perform the same electrical measurements on the packaged chip as performed in the four point bending fixture. Figure 7 shows the relative voltage change $\Delta V_3/V_{3,0}$ as a function of $\cot(\phi)$.

The fictive voltages V_p and V_t are calculated as shown in Equation (1). The linear equation system in Equation (2) can then be written for both voltages with the relations in Table 1 and the stress components are extracted.

RESULTS

The stress has been measured in three samples. The results are presented in Table 2. The largest stress component is the stress normal to the surface plane, $\sigma_{zz} \approx 40$ MPa with an ucertainty of $\Delta\sigma_{zz} \approx 1.5$ MPa. The stress component along the chip edge is $\sigma_{xx} \approx -23$ MPa. The two other stress components $\sigma_{yy} \approx 1$ MPa and $\sigma_{xy} \approx -0.3$ MPa are small compared to these values. Although the uncertainty is comparable to the measured stress values we conclude that σ_{yy} and σ_{xy} are small compared to σ_{xx} and σ_{zz}. The fact that σ_{xx} is much larger than σ_{yy} can be explained by the asymmetry of the polystyrene tube and the shape of the chip.

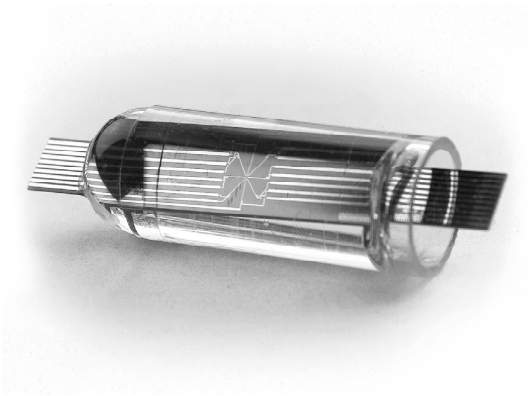

Figure 6 Photograph of the packaged device. The circular piezoresistor is placed in the centre region of the chip. A two-component epoxy is potted in a polystyrene tube. The packaging concept is used in ref. [1] for fisheries research and allows direct exposure of one end of a chip while sealing the other end (along with electronics, battery, etc.) from the surroundings.

The σ_{xx} component depends on the placement of the chip in the tube. This explains the relative large variation in the measured values.
In the hardening process the epoxy is contracted. This contraction contributes to the value of σ_{zz}. The variation of the measured value of this component is small since the same epoxy was used for all samples.

CONCLUSION

We have presented a method which enables 3D stress characterization. To show the concept the stress sensors have been tested in a polystyrene tube potted with the two-component epoxy, EpoTek 305. The results show large stress components along and normal to the chip, $\sigma_{xx} \approx$ -23 MPa and $\sigma_{zz} \approx$40 MPa. The two other components, $\sigma_{yy} \approx$ 1 MPa and $\sigma_{xy} \approx$ -0.3 MPa, are small compared to these values and lies within the uncertainty interval.

The method has proven to extract the four stress components, σ_{xx}, σ_{yy}, σ_{zz}, and σ_{xy}. For future stress analysis we are thus able to perform detailed 3D measurements of packaging induced stress in microsystems.

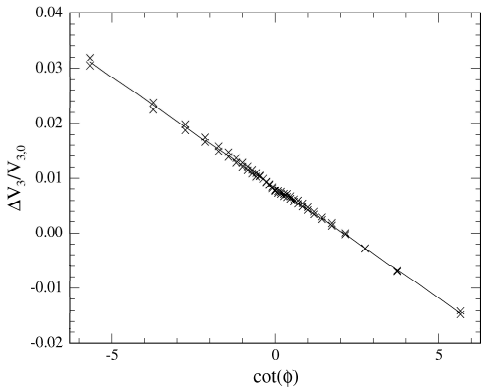

Figure 7 The relative voltage change of V_3 as a function of cot(ϕ). The slope and the offset of the linear fit are related to the stress components as listed in Table 1.

REFERENCES

[1] A. Hyldgård, *et al*, *Proc. Eurosensors 2006*, pp. 262-263.
[2] P. Ruther, *et al*, *Proc. IEEE Sensors 2006*, pp. 314.
[3] A. Mian, J.C. Suhling, R.C. Jaeger, *IEEE Sensors Journal*, 6-2 (2006), pp. 340-356.
[4] A. Hyldgård, O. Hansen and E. V. Thomsen, *Proc. IEEE MEMS 2005*, pp. 303-306.
[5] J. Bartholomeyczik, *et al*, *Proc. IEEE MEMS 2004*, pp. 263-266.
[6] R. Steiner, *et al*, *Sensors and Actuators A*, 66 (1998), pp. 167-172.
[7] M.B. Arnoldus, *et al*, *Proc. Eurosensors 2006*, pp. 378-379.

Table 2 Measured values of the stress components, σ_{xx}, σ_{yy}, σ_{zz}, and σ_{xy} induced by epoxy and the estimated uncertainties.

Type	σ_{xx} [MPa]	$\Delta\sigma_{xx}$ [MPa]	σ_{yy} [MPa]	$\Delta\sigma_{yy}$ [MPa]	σ_{zz} [MPa]	$\Delta\sigma_{zz}$ [MPa]	σ_{xy} [MPa]	$\Delta\sigma_{xy}$ [MPa]
EpoTek 305	-26.9	1.2	-0.7	1.2	39.7	1.4	-0.4	0.2
EpoTek 305	-20.1	0.8	-0.4	0.7	40.5	0.9	-0.2	0.2
EpoTek 305	-23.1	3.2	2.4	2.8	38.6	3.5	0.5	0.6